Development of Bulk and Thin Films of Mg_2TiO_4 Based Ceramics for Microwave Applications

A Thesis Submitted to
Indian Institute of Technology Guwahati
For the Degree of

Doctor of Philosophy

By

Ranjan Kumar Bhuyan

Department of Physics
Indian Institute of Technology Guwahati,
Guwahati- 781039, India

Development of Bulk and Thin Films of Mg_2TiO_4 Based Ceramics for Microwave Applications

A Thesis Submitted to
Indian Institute of Technology Guwahati
For the Degree of

Doctor of Philosophy

By

Ranjan Kumar Bhuyan

Department of Physics
Indian Institute of Technology Guwahati,
Guwahati- 781039, India

Statement

The work contained in the thesis entitled **"Development of bulk and thin films of Mg_2TiO_4 based ceramics for microwave applications"** has been carried out by me under the supervisions of Dr. D. Pamu and Prof. A. Perumal, Department of Physics, Indian Institute of Technology Guwahati. This work has not been submitted elsewhere for the award of any degree.

August - 2015

(**Ranjan Kr. Bhuyan**)
Department of Physics,
Indian Institute of Technology Guwahati,
Guwahati – 781 039

Certificate

This is certify that the work described in this thesis entitled "**Development of bulk and thin films of Mg_2TiO_4 based ceramics for microwave applications**", done by **Mr. Ranjan Kumar Bhuyan**, a Ph.D. student of Department of Physics, Indian Institute of Technology Guwahati, for the award of degree of *Doctor of Philosophy* is a bonafide record of research work has been carried out by him under our supervision and guidance. This thesis work has not been submitted elsewhere for the award of any other degree.

(Dr. D. Pamu)
Department of Physics,
Indian Institute of Technology Guwahati,
Guwahati – 781 039

(Prof. A. Perumal)
Department of Physics,
Indian Institute of Technology Guwahati,
Guwahati – 781 039

Dedicated

to my family

Acknowledgement

Mere words can never suffice to express the sense of gratitude to those whose assistance was indispensable for the completion of my **Ph.D**. thesis. So, it is my pleasure to take this opportunity to thank all of them who helped me in the way of my Ph. D. life.

At the outset, I would like to express my deepest sense of gratitude from the core of my heart to **Dr. D. Pamu** and **Prof. A. Perumal**, Department of Physics, IIT-Guwahati, for their unparalleled guidance, valuable discussion, honest criticism, constant encouragement and expert advice. I am deeply indebted to them for providing me excellent freedom to work on whatever I was interested in.

I am grateful to my doctoral committee members, **Prof. A. Srinivasan (Chairman), Dr. Subhash Thota and Dr. Ravi Shankar** for regular review of my research work and their constructive suggestions and fruitful discussions at various stages of my research work. I express my sincere thanks to the present and former Heads of the Department of Physics **Dr. Poulose** and **Prof. Saurabh Basu,** for their encouragement and allowing me to use departmental facilities throughout the course of my research work. I am also thankful to all other faculty members of the physics department.

I extended my heart-felt thanks to **Prof. S. Ravi** for extending lab space and lab facilities and as well helping me in various ways by treating as one of his student. I am also thankful to **Dr. S. Kanagaraj** (Department of Mechanical Engineering) and **Dr. A. R. James** (DMRL, Hyderabad) for extending lab facilities. I wish to express my heartiest thanks to **Prof. M. V Jacob** (Electronics Materials Lab, School of Engineering and Physical Sciences, James Cook University, Townsville, Australia) and his research groups, for helping me to measure low temperature microwave dielectric behavior of some samples.

My special thanks to **Prof. Ratnajit Bhattacharjee**, Head, Department of Electronics and Electrical Engineering and **Prof. A. Mahanta** for extending network analyzer facility. My sincere thanks to **Mrs. S. Josephine** (Scientific officer, Dept. of Electronics and Electrical Engineering) and **Mr. Dayananda Goswami** for their better co-operation and helping me in doing microwave dielectric measurements. I would like to thank **Dr. Sidananda Sarma** (Scientific officer, Dept. of Physics) for helping me and giving some ideas to complete few experiments. I am also thankful to all staff members of my department and scientific officers of **CIF** for their expertise in handling various

instruments that I have used for my thesis work. I specially thank to **Dr. Biswanath Samantaray,** one of my beloved senior as well as good friend, for helping me in various ways. I cannot repay the help and enjoyment which I have received from him.

I gratefully acknowledge to **Defense Research and Development Organization** (**DRDO**), New Delhi; for providing me the research fellowship to carry out the present thesis work. I would like to thanks **Indian Institute of Technology Guwahati**, for providing me good accommodation in this beautiful campus to carry out my thesis work. I also thanks to **Department of Science and Technology** (**DST**), New Delhi; **Board of Research in Nuclear Sciences**, Mumbai; and **Board of Research in Fusion Science and Technology**, Gandhinagar, Gujarat for financial support through research projects for various experimental facilities. Infrastructure facility (XRD) by DST, New Delhi, through FIST program [SR/FST/PSII-020/2009] is also acknowledged.

I am very much thankful to **Prof. Udai Pratap Singh** (Dept. of Electronics and Telecommunication, KIIT University, Bhubaneswar), **Prof. Pushpa Khare,** my **M. Phil**. supervisor and **Prof. N. C. Mishra** (Department of Physics, Utkal University, Bhubaneswar) for their encouragement and to give me a platform in the field of research.

My sincere thanks to my senior cum friend **Dr. T. Santhosh Kumar** and **Dr**. **Sunita Mohanty** for their help and good company. Thanks to my labmates; **Mahesh, Anil, Pallabi, Srinivas, Dr. Padam, Dr. Tribedi, Junmoni, Bipul, Bibhuti, Pratap, Bhargab, Ranga and Anabil** for their better suggestions, good cooperation and enjoyable company and help in various ways throughout my research. I express my special thanks to **Bata**, **Bhagban** and **Brahmananda** for their friendly company and sharing successes and for all the physics and non-physics discussions during my stay at IIT Guwahati. I would like to thank **Shiba**, **Omkar** and all of my Research Colleagues in the Department of Physics for their help, cooperation and pleasant company during my stay in the campus.

I owe an unlimited debt of gratitude to my parents, **Mr. Panchanan Bhuyan** and **Mrs. Indumati Bhuyan** and my family members for their endless love, blessings and constant encouragement to pursue higher studies. Their hard work and dedication in helping me to pursue higher studies is the strongest source of inspiration for me. My special thanks to my elder brother, **Rajendra Kumar Bhuyan**, who is an inspiring mile stone for all walks of my life. Without his moral support and constant encouragement, I cannot go ahead for higher studies.

Lastly, I thank my lovely wife (**Pinky**) for her indefinable patience, love and the support during the final stage of my Ph.D work. I also thank my father-in- laws family for their moral support and ceaseless inspiration for successful completion of my thesis work.

Thanks to the Almighty "**GOD**" for blessings me a son (**Prince)** and have always enabled me to perceive and pursue higher studies in my life and proceeding strength to take up and complete the task successfully.

Ranjan Kumar Bhuyan

IIT Guwahati

Preface

Demand for electroceramics in the field of wireless-communications industries is growing rapidly, due to their excellent physical, electrical and dielectric properties with advanced technological applications such as microwave oscillators, amplifiers, filters, etc. Although the demands for dielectric materials in different areas are increased considerably, one of the major needs have low loss materials with higher permittivity to miniaturize the device. However, as the carrier frequency of communication systems is extended to higher frequency regions, materials with high dielectric constant has become of less interest. On the other hand, a high quality factor ($Q \times f_o$) would play a more prominent role as $Q \times f_o = (\gamma\omega_o)^{-2}$, where γ is a damping factor and ω_o is an angular frequency, is almost constant in the microwave and millimeter wave regions. At the same time, low dielectric constant (< 15) allows a fast time for electronic signal transition at ultrahigh frequencies. Therefore, in order to work with high efficiency and stability, many researchers have been focusing on developing new dielectric materials with high quality factor (*low loss*) and near zero temperature coefficient of resonant frequency (τ_f). Reduction of the dielectric loss is one of the important tasks for improving the materials performance; thus, for understanding the fundamental mechanism of the dielectric loss, research at microwave frequencies has been attracting more and more attention.

In a similar approach, medium to high dielectric constant thin films turned out to be important in microelectronics. This is due to the fact that for charge storage over an ever decreasing area, materials with higher dielectric constant are essential. As the device dimensions reduce, the frequency of operation of the microelectronic devices goes up and energy dissipation per unit area increases. Hence, thin films with high dielectric constant and low dielectric loss even at higher frequencies and with low temperature dependence are important for such microelectronic applications, i.e., if one can make thin films of materials for DR application, then such materials are expected to serve for this purpose as well. Therefore, a suitable composition was identified in this thesis work to make DRs in both bulk and thin film form. The bulk and thin films are characterized in the microwave frequency range to investigate the possibility of retaining the bulk characteristics in thin films as well.

Most of the current low loss dielectrics are made from complex perovskites requiring high sintering temperatures and compatibly high cost. Moreover, their structures and dielectric properties are quite difficult to predict because there are too many cations

(at least four) involved. Consequently, the search for low-loss and low cost dielectric ceramics has become a primary issue in the last few years. In the meantime, spinel-based medium to high permittivity (k) materials have attracted considerable attention in the field of microwave industry. Among various low loss dielectric materials exhibiting medium to high-k values, Mg_2TiO_4 (MTO) ceramic is considered to be one of the excellent low loss material for the applications discussed above in bulk form. MTO ceramic also exhibits good optical and electrical properties, which could be used for other electronic, photonic and microwave applications. Bulk MTO has an excellent dielectric property such as high quality factor ($Q \times f_o$) ~150,000 GHz, modest dielectric constant (ε_r) ~ 14 and a negative temperature coefficient of resonant frequency (τ_f) ~ - 50 ppm/^oC and its low cost has attracted significant attention recently. Nevertheless, the major disadvantage in preparing such materials is the requirement of very high sintering temperature (above 1420 ^oC). Therefore, it is interesting to seek for the ways to reduce its sintering temperature and the effect of such a process on the resulting microwave dielectric properties.

MTO is an excellent microwave dielectric material with wide band gap and high refractive index suitable for optical and electronic applications. Therefore, its practical applications in optical response are very promissory. Recently, MTO thin films have attracted much attention due to its applications in (i) optical modulation and protective layer of plasma display panels and in the monolithic microwave integrated circuit technologies (MMIC) and (ii) as a buffer layer. In addition, MTO based thin films are used as a substrate for growing high temperature superconductor (HTSC) films due to their high chemical, mechanical properties and thermal stability. Basically, MTO ceramics are being used as a novel substrate for HTSC thin films due to its low loss and well defined surface structure. Recently, thin film technology has become a major requirement for integration since the integrated circuits have been applied in microwave communication systems. Even though the considerable amount of study has gone into the bulk MTO, studies on thin film are rather a few. To the best of our knowledge, the growth of thin films using Mg_2TiO_4 microwave dielectric ceramics as a target material by magnetron sputtering technique has not been reported so far. Therefore, this work also aims to attempt in growing MTO films by a cost effective process and to compare their properties with that of their bulk counterpart.

As a continuing effort in our laboratory on microwave materials, we have chosen to investigate MTO ceramics in the bulk form prepared by mechanical alloying and solid state reaction method and in thin film form prepared by RF magnetron sputtering technique. We have investigated various methods to reduce the sintering temperature of

bulk MTO. The primary motivation was to improve the microwave dielectric properties of the bulk samples by understanding the microstructure and property correlation with different additives, doping and temperature treatments. Another interest is to compare microwave properties of MTO in bulk and thin film form to seek whether the properties are improved in thin film or not. The thesis is divided into seven chapters and the contents of each chapter are briefly summarized below:

Chapter 1 provides a brief introduction to dielectric materials, DRs and related areas. The historical perspective and the devolvement of DRs from the physics and device points of view are also discussed. The basic requirements of a material to be used as DR and its mode characteristics are summarized briefly. The factors affecting the microwave dielectric properties and the applications of DR are also described. Furthermore, the importance of spinel compounds used for DR applications is summarized. The importance of high dielectric constant and low loss films, the characteristics of SiO_2 in CMOS devices and the difficulties in replacing them are discussed. The basic applications of dielectric thin films were also discussed briefly. The importance of MTO as a DR, its crystal structure and a brief overview on microwave dielectric properties along with the motivation behind choosing MTO ceramic as DRs are discussed in detail.

Chapter 2 deals with the synthesis and characterization techniques used for both bulk and thin films of MTO ceramics. The synthesis methods such as mechanical alloying and solid-state reaction method and RF magnetron sputtering technique and characterization techniques (crystal structure, surface morphology, microstructure, relative density, optical properties, thermal decomposition properties, microwave properties) used for analyzing the properties of both bulk and thin films of MTO ceramics in this chapter.

Chapter 3 presents the preparation of MTO nanopowders by the mechanical alloying method under different processing conditions. Moreover, it deals with the impact of mechanical alloying on the crystal structure, sintering temperature, densification, microstructure and microwave dielectric properties of MTO ceramics. In addition, the effect of milling time on particle size, crystal structure and the microstructure were studied through XRD, SEM and TEM analysis. Williamson-Hall (W-H) method was carried out in order to understand the origin of the broadening in the XRD peaks. Since, the sintering temperature of MTO ceramics is about 1450 ^{o}C, therefore, the efforts are made to decrease the sintering temperature by reducing the initial particle size. With the help of this technique, the particle sizes are reduced to 60-100 nm. As a result, the sintering temperature is significantly reduced from 1450 to 1325 ^{o}C with improved microwave dielectric properties. The dielectric loss mechanisms are discussed on the basis of

densification and microstructure of the MTO ceramics and the obtained results are compared with the earlier reports. A maximum relative density of 97.75% was obtained for the MTO sample sintered at 1325 ^{o}C for 3 hr. The best microwave dielectric properties of ε_r ~ 13.68, $Q \times f_o$ ~ 155,000 GHz (measured at 10.4 GHz) were obtained for the pure MTO ceramics, sintered at 1325 ^{o}C. Further, the low frequency dielectric behaviors of MTO ceramics measured in the frequency range of 10 kHz to 1 MHz from room temperature to 500 ^{o}C were also discussed.

Chapter 4 deals with a systematic study on the structural, microstructural and the microwave dielectric properties of pure MTO and MTO ceramics added with CeO_2 nanoparticles prepared by solid state reaction method. Since, the sintering temperature of pure MTO ceramics is about 1450 ^{o}C, therefore, the efforts were made to improve the densification by reducing the initial particle size and by the addition of different concentrations (0.5 - 1.5 wt.%) of CeO_2 nanoparticles as sintering aid. With the addition of CeO_2 nanoparticles, the sintering temperature of MTO ceramics is effectively reduced from 1450 to 1300 ^{o}C along with the significant improvement in the density, uniform microstructure and microwave dielectric properties. It was found that the MTO sample added with 1.5 wt.% of CeO_2 showed highest density of 98.7% with maximum microwave dielectric properties of $Q \times f_o$ ~167000 GHz (at 10.4 GHz) and ε_r ~14.6. These results are promising and enabling the materials for various microwave communication applications. The microwave dielectric properties of the MTO ceramics were also measured at cryogenic temperatures (6.5-295 K). The results indicate that the loss tangent (tan δ) of all the samples enhances with increasing temperature. The loss tangents of the pure MTO ceramics and MTO ceramics added with 1.5 wt.% of CeO_2 nanoparticles, measured at 6.5 K are found to be 6.6×10^{-5} and 5.4×10^{-5}, respectively. The addition of CeO_2 nanoparticles in MTO ceramics reduces the loss tangent significantly. Further, the addition of CeO_2 nanoparticles did not cause any changes on the temperature stability of the MTO ceramics. However, the temperature coefficient of the permittivity improves with the increase in temperature and with CeO_2 content. In addition, the frequency dependence broadband dielectric properties at room temperature was also discussed.

In Chapter 5 a systematic study of the effect of different concentrations of La_2O_3, V_2O_5 and Bi_2O_3 on the crystal structure, densification, microstructure and microwave dielectric properties of MTO ceramics are investigated. The purpose of these additives chosen as sintering aid to MTO ceramics is also discussed. The sintering temperatures and durations were optimized in each case to get uniform microstructure and higher densification. It was found that the increment of these additives, the sintering temperature

of MTO ceramics significantly reduced without affecting the microwave dielectric properties. With low concentrations of these additives, the microstructure of the MTO ceramics has been improved. Further, relative density and dielectric constant follows the same trend as a function of temperature as well as the amount of additives for all the cases. MTO ceramics added with 0.5 wt.% of La_2O_3 or V_2O_5 possessed excellent microwave dielectric properties: ε_r = 14.3, $Q \times f_o$ = 157,550 (at 10 GHz) and ε_r = 14.4, $Q \times f_o$ = 168,000 (at 10 GHz), sintered at 1300 ^oC and 1250 ^oC for 3 hr, respectively. In case of MTO ceramics added with 1.0 wt.% of Bi_2O_3, exhibited best microwave dielectric properties: ε_r = 13.2, $Q \times f_o$ = 160,500 (at 10.48 GHz), sintered at 1250 ^oC. With these additives, it was found that there is not much variation in the dielectric constant, whereas the quality factor is found to be a significant variable. These observations are discussed in this chapter. Furthermore, microwave dielectric properties of pure MTO and MTO ceramics added with different concentrations (0.5 and 1.0 wt.%) of V_2O_5 were measured at cryogenic temperatures (6.5 K to 295 K). It was observed that loss tangent of pure MTO increases with temperature, whereas for V_2O_5 added samples, it decreases with a rise in temperature. However, MTO ceramics added with 0.5 and 1.0 wt.% of V_2O_5 manifested slightly higher loss tangents as compared to the pure MTO ceramics. The mechanism of the microwave loss is in agreement with the theory of intrinsic dielectric loss derived from the two phonon difference process. Further, the addition of V_2O_5 did not cause any changes on the temperature stability of the MTO ceramics, whereas the temperature coefficient of the permittivity improves with the increase in temperature.

Chapter 6 describes the optimization of processing conditions of the MTO thin films prepared by RF magnetron sputtering. MTO thin films were deposited on various substrates like, Si (100), quartz and on platinized silicon ($Pt/TiO_2/SiO_2/Si$)) from the homemade sputtering target, which is prepared from mechanical alloying method. All the films are deposited at an ambient temperatures under different oxygen gas pressure (in a standard cubic centimeters per minute (SCCM)). The impacts of processing parameters (Ar/O_2 ratio) and post deposition annealing on structural, microstructural, optical and dielectric properties of MTO films were investigated. For the first time MTO films were deposited in pure oxygen atmosphere. Interestingly, the as-deposited films on Si substrates are crystalline, while film deposited on the quartz substrate showed amorphous nature. Surface morphology and optical transmittance spectra studies revealed that the average particle size in the film enhances with increasing O_2 SCCM, and the films deposited at higher O_2 SCCM exhibit lower transmittance. In addition, both the refractive index and packing density improves with increasing O_2 SCCM, leading to a decrease in the optical band gap from 4.62 to 4.48 eV. Further, the post - deposition annealing (at 500°C for 1 hr)

resulted in an amorphous – crystalline phase transition in the films (deposited on quartz substrate), which is accompanied by an increase in the refractive index and decrease in the optical bandgap. The annealed films exhibited a refractive index of 1.98-2.03 (at 600 nm) with optical bandgap values between 4.44 and 4.58eV. The O_2 SCCM and annealing are also significantly affected the photoluminescence spectra. Metal-Insulator-Metal (MIM) capacitors were fabricated under different O_2 SCCM for the films deposited on platinized silicon substrates. The dielectric properties of MTO films were measured in the frequency range of 10 kHz to 1MHz as a function of O_2 SCCM. The films deposited in pure oxygen atmosphere showed the highest dielectric constant with low loss at 1MHz. The dielectric constant of each film is close to the bulk value whereas the dielectric losses of the films are observed to be higher than the bulk value. The detailed observations, discussion and possible explanations are presented in this chapter. Further, for the first time the microwave dielectric properties (5 to 15 GHz) of MTO ceramics in thin film form was reported.

Chapter 7 describes an attempt to find the correlations between bulk and thin film properties of MTO. Furthermore, this chapter highlights the summary of the research work and the major conclusions drawn from each chapter. At the end of this chapter, a brief report on the scope for future work is discussed.

Abbreviations

Units of Measurement

m	meter
µm	Micrometer
nm	Nanometer
Å	Angstrom
MHz	Mega hertz
GHz	Giga hertz (frequency)
ppm	Parts per million
hr	Hours
SCCM	Standard cubic centimeter per minute

Dielectric Measurements

ε_r	Dielectric constant
ε_m	Porosity corrected dielectric constant
tan δ	Loss tangent
f_o	Resonant frequency
Q	Quality factor
Q_u	Unloaded quality factor
$Q \times f_o$	Product of Q and resonant frequency
τ_f **(TCF)**	Temperature co-efficient of resonant frequency
τ_ε **(TCP)**	Temperature co-efficient permittivity
σ_{ac}	AC conductivity

Characterization Techniques

XRD	X-ray Diffraction
FWHM	Full width at half maximum (β)
EDS	Energy dispersive spectroscopy
AFM	Atomic force microscopy
TEM	Transmission electron microscopy

HR-TEM	High resolution transmission electron microscopy
SEM	Scanning electron microscopy
FE-SEM	Field emission scanning electron microscopy
TGA	Thermo-gravimetric analyser
DSC	Differential scanning calorimeter
PL	Photoluminescence

Other Parameters

MTO	Magnesium Ortho Titanate (Mg_2TiO_4)
DR	Dielectric resonator
MA	Mechanical alloying
Wt.%	Weight percentage
χ^2	Reduces chi-square
R_p	Profile factor
R_B	Bragg factor
k_B	Boltzmann constant
α	Absorption co-efficient
D	Average crystallite size
E_g	Bandgap
P	Fractional porosity
η	Lattice strain
hv	Photon energy
n	Refractive index

Contents

Chapter 1

Introduction

1.1 Introduction

Over the last two decades, the revolution in wireless communications and information access is one of the most dramatic changes in modern technology. These revolutionary changes in the field of all technological systems are due to advancement in developing smart materials. Novel approaches have been adopted for processing the functional ceramics. However, among the various branches of functional ceramics, the electronic ceramic industry is of primary interest due to their tremendous physical properties and immense technological applications. Further, utilization of microwave frequency has also increased from microwave to millimetre range in order to transmit large quantity of information with high speed. Today, microwaves are used by telecommunication industries in the form of both terrestrial relays and satellite communications. The first microwave message was sent in 1945 from towers located in New York and Philadelphia. Following this successful attempt, microwave communication became the most commonly used data transmission method for telecommunications service providers. Frequencies ranging from 300 MHz- 30 GHz are usually called "**microwaves**". Because of their high frequencies, microwaves have the advantages of being able to carry more information than ordinary radio waves and are capable of being beamed directly from one point to another. So, in order to meet the specifications of the current and future systems, improved or new microwave components based dielectric materials are required. As a result, a large number of dielectric ceramic materials have been developed for the use as resonators, capacitors, substrates, oscillators, electronic package, etc. in various electronics applications.

Recently, dielectric oxide ceramics have revolutionized the microwave wireless communication industry by reducing the size and cost of electronic devices. The advantages of these materials are that they are relatively cheaper as compared with some of the compounds currently utilized and in the future they can be improved even further by suitable additives and by optimizing the processing conditions. Moreover, with the rapid development in mobile phone and satellite communication systems using

microwave as carrier has resulted in an increasing demand of dielectric resonators (DRs). DR is an inevitable component in microwave telecommunication devices and is extensively used in filters, oscillators and dielectric resonator antennas (DRAs). They can be applied for the purpose of cellular phones, wireless local - area networks (WLAN), 3G filters and global positioning systems (GPS) [1, 2]. Therefore, microwave dielectric materials are continuing to play a very important role in the microwave communication industry. To meet the requirements for use in such practical applications, the materials should posses three critical properties: (i) high dielectric constant (ε_r) for miniaturization, (ii) high quality factor ($Q \times f_o$) or low dielectric loss for better selectivity and (iii) low temperature coefficient of resonant frequency (τ_f) for better temperature stability. This helps to use the devices in any environment without detrimental effects on the signal [3-5]. However, as the operating frequency of communication systems being extended from microwave (MW) [ISM (industrial, scientific and medical)] bands to millimeter wave range, materials with high dielectric constant tend to become a less of interest [1, 2], but materials with high quality factor ($Q \times f_o$) are essential [6-12], as $Q \times f_o = (\gamma \omega_o)^{-2}$ (where γ is a damping factor and ω_o is an angular frequency) is almost constant in the MW and millimeter wave regions. Furthermore, high quality factor can significantly reduce the dielectric loss and degree of noise. Low dielectric constant ($\varepsilon_r < 15$) not only minimize the cross coupling with conductors but also shorten the time for the electronic signal transition at ultra - high frequencies. Therefore, the low ε_r ceramics are used for millimeter wave communication and also as substrates for MW integrated circuits. In this regard, new varieties of low - cost dielectric materials with dielectric constant in the range of 10 to 20 and extremely low dielectric losses are urgently required [6-12].

In this chapter, a brief introduction and historical development of DRs with their technological importance are discussed. The fundamental physical aspects of DRs and the factors affecting the microwave dielectric properties are also presented. The working principle and the potential use in different practical applications are discussed. Further, the scientific and electronic applications of thin films with their importance in various areas of interest in the present technological world are also reviewed. Finally, the crystal structure of Mg_2TiO_4 ceramics and the motivation behind this present thesis work are presented.

1.2 Microwave dielectric resonators

1.2.1 Introduction to dielectric resonator

A **Dielectric Resonator** (DR) is an electromagnetic component which functions as a resonant device by reflections at the high (ε_r) dielectric - air interface.

In the early microwave systems, quartz, metallic and microstrip resonators were used. However, the quartz resonators are not attractive at microwave frequencies due to small signal - to - noise ratio available with frequency multiplication to microwave frequencies and their bulky nature. Subsequently, the metallic cavity resonators were developed. This was also proved to be bulky and difficult to integrate with the microwave integrated circuits (MICs). Later, microstrip resonators were developed. However, this one had high dielectric loss and poor temperature stability resulting in the instability of the circuit. Next attempt was the use of ceramic pieces in the form of dielectric resonators, which are resonating at the frequency of the carrier signal to allow that signal to be efficiently separated from other signals in the microwave band. This led to a booming development of novel ceramic microwave DRs.

There are many advantages of microwave dielectric resonators compared to traditional resonators. DRs are much smaller in size and have greater degree of circuit and sub system integration with better circuit performance (with regard to temperature changes and losses). They have the advantage of being more miniaturized as compared to traditional microwave cavities and have a significant higher quality factor. DRs have replaced cavity resonators in most microwave applications due to cost, dimension, mass, stability, efficiency, ruggedness and ease of use. Also, the temperature coefficient of resonant frequency can be engineered to a desired value to meet circuit designer's requirement.

1.2.2 Historical perspective of dielectric resonator from literature review

Before discussing about specific materials, it is worthwhile to review the historical development and the requirements of the materials simply from the application point of view of microwave dielectric properties.

In 1939, Ritchtmeyer (from Stanford University) [13] first introduced the term "**Dielectric Resonator**" and he showed that a suitably shaped dielectric piece (toroid) can function as a microwave resonator. However, from his theoretical work, it was failed to generate significant interest and practically nothing happened in this area for over 25 years. Later, in 1953, Schlicke [14] reported on super - high dielectric constant materials (~ 1000) and their applications as capacitors in low radio frequencies. In the early 1960s, Okaya and Barash from Columbia University [15] rediscovered DRs, while working on

single crystal rutile (TiO_2) and their related literature provided the first analysis of modes and resonator design. Although TiO_2 has high dielectric constant (≈ 100) and low dielectric losses, but it was not put into practical use due to of its poor temperature stability (+450 ppm/^oC). This causes large variation in resonant frequency. Later, in 1968 Bolton [16] reported a temperature stable with maximum dielectric constants around 60 - 80 was achieved for tungsten bronze structured $BaTiO_3$ - Ln_2O_3 - TiO_2. Later, Negas et al. [17] noted that the work of Bolton is rarely acknowledged in subsequent literature, but provided the technical foundation for a host of investigations of tungsten bronze structure materials.

By the late 1970s and early 1980s, a real breakthrough in ceramic technology occurred when Masse et al. [18] developed the first temperature stable low loss barium - tetratitanate ($Ba_2Ti_4O_9$) including $(Mg,Ca)TiO_3$ and $ZrTiO_4$ ceramics. Further, temperature stable microwave DRs were developed by Konishi [19] and Ploudre [20] utilizing the composite structure of positive and negative temperature coefficients. Later, a modified barium tetratitanate with improved performance was reported from Bell Laboratories [21]. The materials, however, were in scarce supply and thus, were not commercially available. The next major breakthrough was came from Japan when the Murata Manufacturing Company produced $(Zr,Sn)TiO_4$ ceramics [22]. They offered adjustable compositions so that the temperature coefficient could be varied between +10 and -10 ppm/^oC. These devices became commercially available at reasonable prices. Afterwards, extensive theoretical and experimental works were performed and the use of DR was expanded rapidly.

At the start of the 1990s, the growth of the mobile communications market was stimulated the research in microwave dielectrics, particularly for high relative permittivity materials (ε_r = 70 - 120) for mobile telephone handset applications and very high Q - materials (40,000 < $Q \times f_o$ < 250,000) with medium relative permittivity (ε_r = 25 - 50) for base station applications [23]. For the former group, the high ε_r tungsten bronze structured materials (for example $BaTiO_3$-Nd_2O_3-TiO_3) remained the primary choice, whilst complex perovskites (e.g. $BaMg_{1/3}Ta_{2/3}O_3$, with ε_r = 24 - 29) provided the highest Q - values for the base stations. A striking feature is the gap in the available materials with ε_r in the range 45 -75. Reaney and Iddles [23] highlighted the fact that materials with ε_r in the range of 45 -75, with high Q - value and zero τ_f do not currently exists. Further, they [23] have plotted a graph between $\log_{10} Q \times f_o$ verses ε_r for commercially available

DR ceramics resulting a straight line. This illustrates the fundamental physical principle that the dielectric loss and dielectric constant are not independent variables. Now-a-days about more than 1500 microwave dielectric ceramics have been investigated for dielectric resonator applications [24]. Research is still continuing to find new materials with enhanced properties.

1.2.3 Current state of materials developed for DR applications

Currently, there are number of new ceramic materials have been developed with improved dielectric properties for practical purposes. A summary of typical materials available presently are discussed in the following section. $(Mg,Ca)TiO_3$ [20, 25] has been attempted as DR materials. Complex perovskites [26 -29] materials showed excellent microwave dielectric properties. For instance, $Ba(Mg_{1/3}Ta_{2/3})O_3$ showed high dielectric constant of 25 with high $Q\times f_o$ of 350000 GHz and near zero τ_f [26]. Similarly, $Ba(Zn_{1/3}Ta_{2/3})O_3$ showed ε_r of 29 with excellent $Q\times f_o$ of 150000 GHz and near zero τ_f (+ 2 ppm/^oC) [27]. $(Zr,Sn)TiO_4$ [28], $Ba_2Ti_9O_{20}$ [29] and $BaO\text{-}Pb0\text{-}Nd_2O_3\text{-}TiO_2$ [30] ceramics also gained commercial acceptance. Currently, $Ba_4Nd_{9.33}Tu_{18}O_{54}$ (BNT) based compounds are used primarily for digital television receivers and it possesses high ε_r of 80 with good $Q\times f_o$ value of 10000 GHz [23]. Similarly, $CaTiO_3$ - $NdAlO_3$ (CTNA) and $ZrTiO_4$ - $ZnNb_2O_6$ (ZT - ZN) based ceramics dominates the base station resonator market. Recently, $Ba(Co, Zn)_{1/3}Nb_{2/3}O_3$ (BCZN) based ceramics are newly developed, which are cheaper and replacing the more expensive $Ba(Zn_{1/3}Ta_{2/3})O_3$ based - materials [23].

1.2.3.1 Importance of spinel compounds used for DR applications

Compounds with the general formula AB_2O_4 or A_2BO_4 are referred to as spinel [31]. A_2BO_4 spinels comprise a broad group of chalcogenides containing two metal atoms (A and B), being either III - valent and II - valent cations (giving the III_2-II-VI_4 spinel group, e.g. Al_2MgO_4) or II - valent and IV - valent cations (giving the II_2-IV-VI_4 spinel group, e.g. Mg_2TiO_4) [32]. There are about 1000 known spinels including - 130 oxides, some of them explored previously with diverse physical properties such as ferromagnetic ordering, metal -insulator transition, superconductivity, heat resistant pigments, gas sensors, catalysts, and magnetic materials [31, 32]. Only recently, this large group of materials have been tapped for their potential in electronic, optoelectronic [33, 34] and microwave applications [35 - 44]. More recently, the high - Q and low permittivity Mg_2TiO_4 (MTO) spinel based materials played an important role in the field of microwave and millimeter wireless communication industry. This is due to their excellent

dielectric properties and cost effectiveness [36]. Careful literature surveys of MTO - based spinel are discussed in the motivation section.

In AB_2O_4 group, the $MgAl_2O_4$ is the parent compound and due to its low electrical loss and high mechanical strength at elevated temperature, it was proposed for microwave applications [37]. It finds applications ranging from traditional refractories to some advanced usage like infrared and humidity sensors, armour materials, excellent transparent material for arc - enclosing envelopes and alkali - metal vapour discharge devices. Surendran et al. [37] studied the microwave dielectric properties of $MgAl_2O_4$ ceramics ($\varepsilon_r \approx 8.75$, $Q \times f_o \approx 69{,}000$ GHz and $\tau_f = -75$ ppm/^oC) in the microwave frequency range. Huang et al. [38] studied the microwave dielectric properties of $(Mg_{1-x}\ Ni_x)Al_2O_4$ spinel compound. They found that the substitution of Mg by Ni significantly promoted the $Q \times f_o$ value up to 130,000 GHz (measured at 15.4 GHz) at $x = 0.25$.

Further, Zinc aluminate spinels are also finding applications for industrial purposes [39]. Surendran et al. [40] reported the low loss $ZnAl_2O_4$ based ceramic system exhibits ideal characteristics for potential applications as microwave substrates and microelectronic packing materials. $ZnAl_2O_4$ also showed a fascinating microwave dielectric properties of $\varepsilon_r \approx 8.5$ with $Q \times f_o$ value of 60,000 GHz and $\tau_f = -79$ ppm/^oC. Further, to compensate the high negative τ_f, they prepared $ZnAl_2O_4$ - x TiO_2 composite ceramics [40]. However, Li. et al. [41] found the $\tau_f = 0$ for this composition close to $x = 0.21$. $ZnAl_2O_4$ - 0.17 TiO_2 composite has a thermal expansion coefficient of 6.3 ppm/^oC which is comparable to that of silicon [42]. Lei et al. [43] found that when the (1- x) $ZnAl_2O_4$ - x Mg_2TiO_4 ($x = 0.21$ and 0.92) spinel - based composite ceramics sintered between 1450 - 1500 ^oC, was showed an extra high $Q \times f_o$ value of 160,000 GHz and 256,810 GHz, respectively. Recently, Huang et al. [44] reported the microwave dielectric properties of spinel - based $(Mg_{1-x}\ Zn_x)Al_2O_4$ ceramic system. They found that with increasing x, the $Q \times f_o$ of $(Mg_{1-x}\ Zn_x)Al_2O_4$ can be tremendously boosted from 82,000 GHz at $x = 0$ to a maximum of 156,000 GHz at $x = 0.05$. All these properties are suitable for millimeter wave communication and as microwave substrates. Further, it is also found that these materials are highly resistant at elevated temperature and highly reflective for wavelengths in UV region, which make them suitable materials for reflective optical coatings in aerospace applications.

1.2.4 Future requirements of the DR materials

The next generation designs, spectral crowding and commercial realities create a continuous need to increase the Q and saving the cost of ceramic resonators and filters. This presents important challenges to materials scientists because the fundamental physics that give rise to the desired properties, especially dielectric loss, is not well understood. Therefore, fundamental understanding of microwave ceramics is needed to improve existing materials and discover new materials for advanced applications.

In order for microwave dielectric ceramics to be used in base stations, they must inevitably offer a commercial advantage over competing technologies. In particular, metal cavities offer an alternative to ceramic resonators. The $Q \times f_o$ factors of metal cavities are considerably lower (~ 6000 GHz) but they are two orders of magnitude cheaper. The high cost of ceramics comes from the often - expensive raw materials such as Nb_2O_5 and Ta_2O_5, and the complex manufacturing processes needed to ensure optimum properties. Therefore, ceramics are only used where high Q is paramount and miniaturization is necessary. At the same time, the efforts are focused on to improve Q particularly by minimizing the extrinsic losses of the microwave ceramics.

Ceramics offer a distinct advantage over competing technologies in the use of irregular geometries to induce multimode resonance and thereby saving space and cost. The unusual shapes and designs also lay down new challenges to ceramists to control Q, ε_r and τ_f during ceramic processing [23]. The microwave ceramic resonator market for base station technology has matured and industry is focusing primarily on improvement on Q and saving its cost [23]. New applications for low loss microwave ceramics are constantly emerging such as global positioning systems, low temperature co - fired ceramics for embedded microwave circuitry, tunable filters and higher frequency applications for advanced radar technology [23]. In addition, as we are moving towards 21st century, environmental considerations are big issues. As a result, microwave ceramics need to be environmentally friendly and recyclable.

1.3 Physics of DR materials

1.3.1 Polarization mechanisms in dielectrics

Polarization is an ordering in space of an electrically charged unit under the influence of an external electric field. This causes the formation of an electric moment in the entire volume of the dielectric and in each separate polarizing unit (atom, ion or molecule). Linear dielectrics show a direct proportionality between the induced electric dipole moment p acquired by the polarizable unit during the process of polarization and the

intensity E of the field acting on it as given by, $\boldsymbol{p} = \boldsymbol{\alpha}\ \boldsymbol{E}$, where, α is known as polarizability reflecting the properties of individual polarizable unit, which is the most important microscopic electrical parameter of a dielectric. There are essentially four basic kinds of polarization mechanisms viz. space charge / interfacial, dipolar, ionic and electronic. Each dielectric mechanism has a characteristic "cut off frequency". The magnitude and "cut off frequency" of each mechanism is unique for different materials.

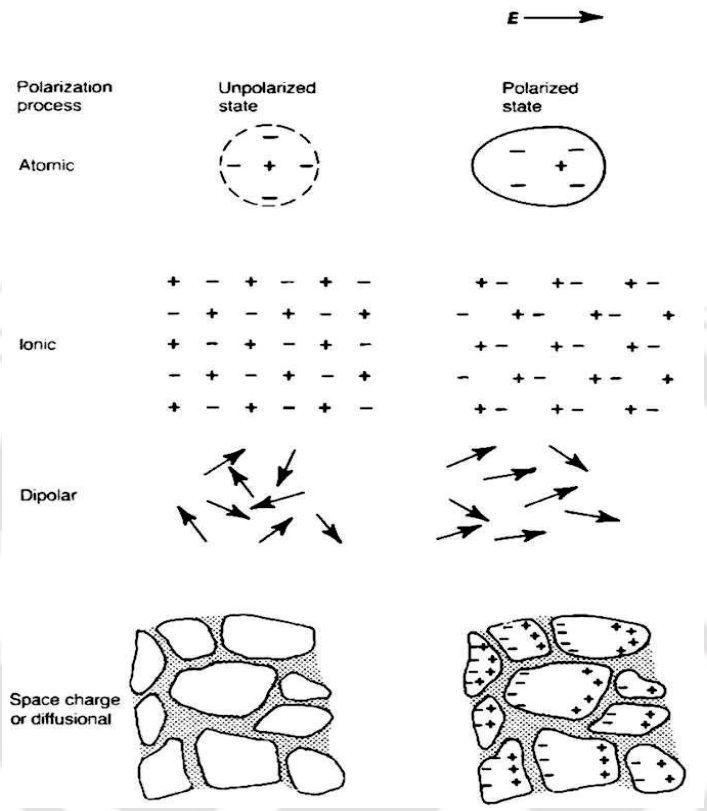

Fig. 1.1: *Different types of polarization mechanisms appear in a dielectric [46].*

During polarization, the charges that are displaceable will be brought in to motion. When the charge carriers are impeded by physical barriers such as grain boundary, inter phase boundary etc. that inhibits charge migration leading to piling up of charges at these boundaries, which causes interfacial polarization or space charge polarization. At low frequencies (~ 1 kHz), this mechanism gives rise to a very large capacitance and high dielectric constant. Dipolar polarization, otherwise known as orientational polarization occurs due to the molecules containing permanent dipole moment or by the rotation of dipoles between two equilibrium positions. In the absence of electric field, the dipoles will be randomly orientated, as result the net polarization is zero. When an electric field is applied, the dipoles will tend align in the direction of the applied field and the materials will acquire a net moment. This type of polarization occurs only in polar molecules, but

relaxes around 10^3 to 10^6 Hz. The ionic polarization occurs due to the relative displacement of the positive and negative ions in a material with respect to each other in the presence of electric field. In this case, material should have ionic character and it relaxes in the frequency range of 10^{12} to 10^{13} Hz (infrared region). Electronic polarization is present in all materials and it does not contribute to conductivity or dielectric loss in most dielectrics. This mechanism arises due to shift electron clouds with respect to the atomic nucleus under the influence of an electric field. This occurs at high frequencies (~ 10^{15} Hz). The relative permittivity at optical frequencies arises entirely from the electronic polarizability. These four polarization mechanisms are illustrated schematically in Fig. 1.1. Each of these involves a short - range motion of charge and contributes to the total polarization of the material. At microwave frequencies, ionic and electronic polarizations contribute to the dielectric properties [45].

1.3.2 Theory of intrinsic dielectric losses

One of the most persistent problems in materials science is dielectric loss. Recently, there have been some attempts to use far infrared spectroscopy to help in the characterization of the dielectric properties of some low loss materials in the microwave region [26, 47, 48]. At present the existing concepts of dielectric losses in microwave dielectrics can be classified in to two categories: (i) intrinsic and (ii) extrinsic. Intrinsic dielectric losses arise due to the interaction of the alternating current electric field with the phonons of the crystal lattice leading to the damping on the optical phonon modes and lattice imperfections. This mechanism is dependent on the composition and the crystal structure of the material and independent of the processing conditions and microstructure. Conversely, extrinsic dielectric losses in materials are arises because of defects such as point defects, domain boundaries, grain boundaries, porosity, impurities, dislocations, secondary phases, etc. and which can be minimized by the careful material processing. In the far infrared region the intrinsic factors play a fundamental role since the intrinsic dielectric losses are much stronger than the extrinsic ones [49, 50]. In principle, it should therefore be possible to extract the value of intrinsic losses in the microwave region from the infrared data if the extrapolation law is known. In the following section a complete theory of intrinsic dielectric losses is discussed.

Almost 30 years ago, Wakino et al. [47, 48] proposed infrared (IR) reflectivity spectroscopy as a tool for investigating the intrinsic microwave (MW) dielectric

properties of dielectric resonators. It is well known that the main infrared dispersion of the permittivity is given by the sum of polar phonon contributions,

$$\varepsilon^*(\omega) = \varepsilon'(\omega) - i\varepsilon''(\omega) = \varepsilon_\infty + \sum_{j=1}^{n} \frac{\Delta\varepsilon_j \omega_j^2}{\omega_j^2 - \omega^2 + i\omega\gamma_j} \tag{1.1}$$

where ε_∞ is the permittivity at optical frequencies, ω_j and γ_j are the frequency and damping constant of the j^{th} polar phonon, respectively; $\Delta\varepsilon_j$ denotes the mode contribution to the static permittivity $\varepsilon'(0)$ of the j^{th} polar lattice mode. Wakino et al. [47, 48] mentioned that extrapolating this model from IR down to MW range, i.e., at $\omega << \omega_j$ gives constant real part of the permittivity,

$$\varepsilon'(\omega) = \varepsilon_\infty + \sum_{j=1}^{n} \Delta\varepsilon_j \tag{1.2}$$

while the dielectric losses ε'' are proportional to frequency,

$$\varepsilon'' = \tan\delta = \omega \sum_{j=1}^{n} \frac{\Delta\varepsilon_j \gamma_j}{\omega_j^4} \tag{1.3}$$

At high temperatures (around and above room temperature) the phonon damping should be linearly temperature dependent, i.e,

$$\varepsilon''(\omega, T) \propto \omega \times T \tag{1.4}$$

This implies that the dielectric loss could be linearly extrapolated from the IR range down to MW region. The method described above was used in the study of many MW ceramics and it was shown that it gives rather good estimation of intrinsic MW losses, although Eq. (1.1) is valid only in the range near phonon frequencies and the use of this formula is not theoretically justified for frequencies much lower than ω_j, i.e., in MW range.

Later, Gurevich and Tagantsev [49, 50] developed a comprehensive microscopic phonon transport theory and have shown that depending on crystalline symmetry, temperature interval, frequency range and some parameters of the phonon spectrum, the temperature and frequency dependence of intrinsic dielectric loss can be described by a power law [50].

$$\varepsilon''(\omega, T) \approx \omega^n \times T^m \tag{1.5}$$

where n = 1 - 5 and m = 1 - 9. In the MW range far below the frequencies of the mean phonon damping, two - phonon difference decay process dominated at room and medium -high temperatures and the theory predicts,

$$\varepsilon''(\omega,T) \approx \omega \times T^2 \tag{1.6}$$

We note that at low temperatures Eq. (1.6) is not valid, but Eq. (1.5) with steeper temperature dependences is theoretically expected. Eq. (1.3) shows that in case of dominating intrinsic losses, the product of quality factor (Q) and frequency f ($\omega = 2\pi f$) is expected to be constant, a rule which holds, at least approximately for many ceramics. Further, it is widely accepted that the intrinsic dielectric losses can be estimated by spectroscopic methods such as Fourier Transform Infrared Spectroscopy (FTIR) [51] and therefore this method is now often is used for the characterization of classical microwave ceramics and related compounds [52].

1.3.3 Modes in a dielectric resonator

There are infinite numbers of resonant modes for a dielectric resonator, each of them corresponding to a particular resonant frequency, at which the electric stored energy is equal to the magnetic one. The excited modes can be classified into three distinct families:

i. Transverse Electric Modes (TE)
ii. Transverse Magnetic Modes (TM)
iii. Hybrid Electromagnetic Modes (HEM)

Among these the lowest hybrid mode is $HEM_{11\delta}$. Its resonant frequency can come even lower than that of the widely used $TE_{01\delta}$ mode. Its proximity to $TE_{01\delta}$ mode is governed by the aspect ratio of the DR and the proximity of perturbing metallic surfaces to the DR. Proximity of $HEM_{11\delta}$ mode to $TE_{01\delta}$ mode is not preferred as the former exhibit a very low value of Q. The $HEM_{21\delta}$ mode also has lower resonant frequency, which falls right between $TE_{01\delta}$ and $TM_{01\delta}$ modes. Thus, when operating in either of these modes, $HEM_{21\delta}$ modes can cause difficulties. Coupling to TM modes needs different arrangement compared to TE modes. However, HEM modes can get coupled to both the TE and TM coupling arrangements, as they have both components. HEM modes are highly leaky (i.e. radiative) and can cause difficulties in using TE and TM modes with their inherent Q values. The complexity of HEM modes increases as the integer's m and n take higher values. An aspect ratio of 2.5 makes $TE_{01\delta}$ well separated from all the neighboring modes.

According to the mode nomenclature described by Kobayashi et al. [53], the variations of fields along the azimuthal, radial and Z - direction inside the resonator, are denoted by adding mode indices as subscripts to each family of modes. The fields for TE and TM modes are axisymmetric whereas hybrid modes are azimuthally dependent. The resonant modes of a cylindrical resonator can be divided into constituent modes with azimuthal variation given by $\cos(m\varphi)$ or $\sin(m\varphi)$, (where $m = 0, 1, 2, 3\ldots$). For $m = 0$, the set of modes can be divided into TE_{mnp} and TM_{mnp}. The first subscript m refers to azimuthal dependence of modes in φ. Second subscript n is radial mode number and the third subscript p denotes the axial mode number. They refer to the field extremes within the DR in the radial and axial directions. Due to the evanescent field effects in a DR, it is customary to replace p with $\ell + \delta$, (where $\ell = 0, 1, 2, 3\ldots$) and $0 < \delta < \ell$ which means that there are ℓ number of half period variations and a fraction of a period of field variation in the DR along the axial direction.

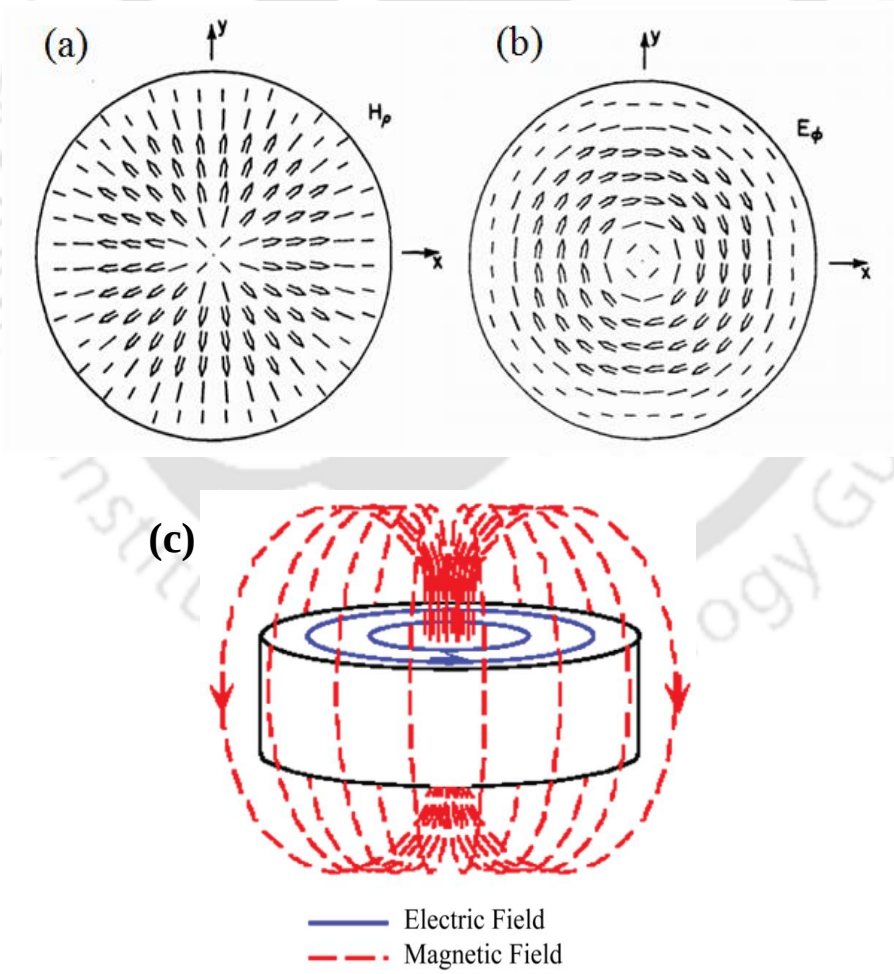

Fig 1.2: (a) *Magnetic field in equatorial plane of the $TE_{01\delta}$ mode.* ***(b)*** *Electric field in equatorial plane of the $TE_{01\delta}$ Mode [22] and* ***(c):*** *Interaction of electric and Magnetic field lines with a cylindrical DR [54].*

The mode which is most commonly used for material characterization is $TE_{01\delta}$ mode. Fig.1.2 displays the magnetic and electric field lines for $TE_{01\delta}$ mode and the side view of a cylindrical DR together with magnetic and electric fields for this mode. The electric field lines are simple circles concentric with the axis of the cylinder. When the relative dielectric constant is around 40, more than 95% of the electric energy of the $TE_{01\delta}$ mode as well as more than 60% of the magnetic energy is stored inside the DR. The remaining energy is distributed in the air around the DR, decaying rapidly with distance away from the DR vicinity. Although the geometrical form of a dielectric resonator is extremely simple, an exact solution of the Maxwell's equations is considerably more difficult for an isolated DR.

To find out the resonant frequencies of a DR with known value of dielectric constant and having a diameter (D) to the height (L) ratio ***D*/*L*** (aspect ratio), standard mode charts are available. In 1980, Kobayashi and Tanaka [53] reported a mode chart for a dielectric rod resonator short circuited at both ends. Mode chart graphically represents the variation of the factor $\varepsilon_r (D/\lambda_0)^2$ as a function of $(D/L)^2$ for all the resonant modes, where λ_0 is the free space wavelength corresponding to the resonant frequency of the mode. From the mode chart, the resonant frequencies of all the resonant modes of a DR can be found using its ε_r, D and L values. Furthermore, one can find out the order in which various modes appear in frequency spectrum. This is important because the proximity of some leaky modes to the mode which is being used can lead to degradation of its performance. From the mode chart, one can find out the aspect ratio that can be used for a DR with a given value of ε_r, to get maximum isolation for the mode of interest. For an approximate estimation of the resonant frequency of the isolated DR, the following simple equation can be used [55].

$$f_{GHz} = \frac{34}{D_{mn}\sqrt{\varepsilon}}\left[\frac{D}{L} + 3.45\right] \tag{1.7}$$

where D is the radius and L is the height of the DR.

Dielectric resonators are simple in concept but controlling their dimensions and precise phase assemblage during processing is difficult. Any slight differences from batch to batch or within a batch may alter their resonant frequency and temperature stability. Ceramic resonators can be made into different geometries (examples: cylindrical, tubular, toroids, spheres, parallelepiped and cubes etc.) to suit the purpose of the component and

are shown in Fig. 1.3 (a). In order to function the DR, conventionally puts within a silver-coated square cavity, as illustrated in Fig. 1.3 (b). Typically, many hundreds of these cavities will reside in the base stations of cellular network.

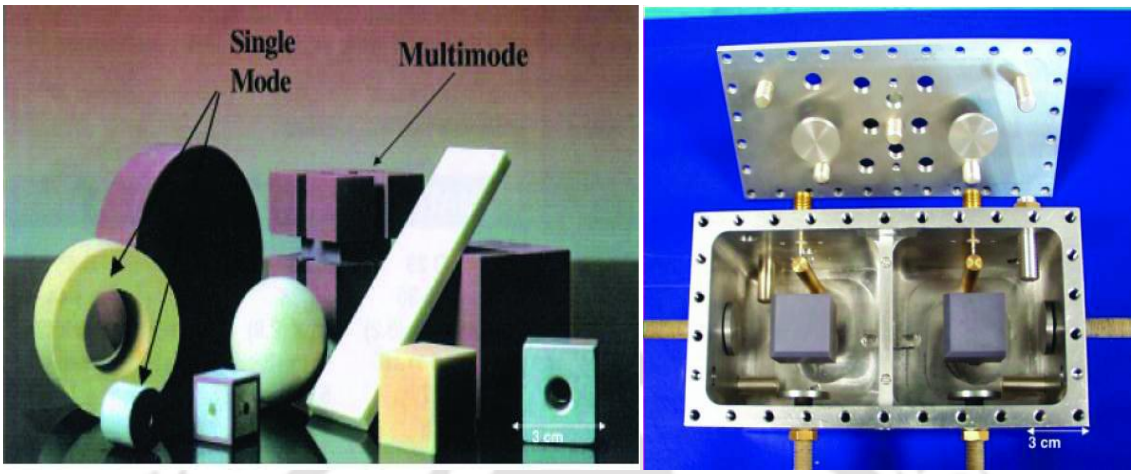

Fig. 1.3: *(a) Various geometries of microwave dielectric resonators and filters and (b) DRs in a silver – coated air filled cavity [23].*

1.3.4 Working principle of a dielectric resonator

The main reason for confinement of microwaves in and in the vicinity of a DR is its large value of dielectric constant (ε_r). As the dielectric constant increases the impedance offered by the dielectric - air boundary also increases to allow better confinement of energy within the dielectric body. The dielectric - air boundary will act as a perfect reflector of microwaves if the angle of incidence is greater than the critical angle $\theta_c = \sin^{-1}(1/\varepsilon_r)$. For large values of ε_r, the electromagnetic waves are internally reflected. Depending on the geometry, the waves undergo multiple total internal reflections. The reflection coefficient approaches unity when the dielectric constant approaches infinity. The trapped electromagnetic waves will form standing waves to generate resonance. A high dielectric constant material can confine most of the standing electromagnetic wave within its volume. If the transverse dimensions of the dielectric are comparable to the wavelength of the microwave, then certain field distributions or modes will satisfy Maxwell's equations and boundary conditions [55] and only those modes satisfying this condition will be excited.

The frequency of the generated resonating modes depends on the dimensions and dielectric constant of the dielectric specimen. The electromagnetic fields outside the dielectric sample decay rapidly. One can prevent radiation losses by placing the DR in a

small metallic enclosure. Since only a small radiation field sees the metallic surface, the resulting conduction loss will be too small and can be neglected. The field confined inside the DR is susceptible to intrinsic losses arising from the imaginary part of the dielectric constant (ε_r'') of the material. Thus, the unloaded quality factor Q_u is limited by the losses in the dielectric resonator. Hence, only a low loss material can be used for DR application.

For microwaves, the free space wavelength (λ_o) is of the order of a few centimetres and on entering into the materials with ε_r in the range of 10 -100, the wavelength (λ_d) inside the dielectric will be in millimetre [55], because, $\lambda_d \approx \frac{c}{f_0 \varepsilon_r^{1/2}}$. i.e., when microwaves, enter a dielectric materials, they are slowed down by a factor roughly equal to the square root of the permittivity. Ultimately, the permittivity of a material determines the relative speed that an electrical signal can travel in that material.

1.4 Material requirements for DR applications

Development of electronic industry demand high performance dielectric materials which have their own specialized requirements and functions. The microwave characterization of dielectric materials is vital to implement the material in communication devices and circuits. There are basically three important characteristic parameters for a dielectric resonator to be used for the said purposes and in the following section we have discussed in detail.

1.4.1 Relative permittivity (ε_r)

The relative permittivity (ε_r) is an important parameter because it will ultimately determine the size and application of the DR. A cylindrically shaped DR sustains an electromagnetic standing wave within its volume because of the total multiple internal reflections at the dielectric air interface. The wavelength of the standing wave is about equal to the diameter of the cylinder and is given by [55],

$$\lambda_d \approx D_r \approx \frac{c}{f_o \varepsilon_r^{1/2}} \tag{1.8}$$

where λ_d is the wavelength of the standing wave along the diameter (D_r) of the resonator, c is the velocity of the electromagnetic waves in vacuum; f_o is the resonant frequency in GHz and ε_r is the relative permittivity of the resonator. Consequently, if the relative permittivity is increased, the size of the resonator may be decreased while still

maintaining a specific resonant frequency, i. e., larger dielectric constants enable miniaturization.

The low relative permittivity ceramics in the range of 4 -12 are used for millimeter - wave communications and also as substrates for microwave integrated circuits. The medium ε_r materials with permittivity in the range of 20 - 50 are used as satellite communications and in cell phone base stations. The high ε_r materials are used in mobile phones, where miniaturization of the device is very important. High speed signal propagation with minimum attenuation is an important aspect which is a direct function of the relative permittivity. In these applications the relative permittivity (ε_r) governs the propagation delay t_d, which is given by the relation [56]: $t_d = (\sqrt{\varepsilon_r}/c)$, where c is the speed of light in vacuum. Thus the materials with low permittivity are required to increase the speed of the signal.

1.4.2 Low dielectric losses ($Q \times f_o$)

One of the most important characteristic required for dielectric a material is of low dielectric loss (tan δ) or high quality factor (Q). The quality factor is defined as $\boldsymbol{Q = 1/\tan\delta}$, which is used as figure of merit in assessing the performance or quality of a microwave devices. Ideally, larger the value of Q, better is the device performance. It is the efficiency of a resonant circuit to confine electromagnetic energy. Further, it can be defined as the measure of energy loss or dissipation per cycle with respect to the energy stored in the fields inside the resonator and is given by [57],

$$Q = 2\pi \frac{\text{maximum energy stored per cycle}}{\text{average energy dissipated per cycle}}$$

$$Q = \frac{2\pi W_o}{PT} = \frac{\omega_o W_o}{P} \tag{1.9}$$

where W_o is stored energy, P is power dissipation and ω_o is the resonant angular frequency and $T = 2\pi/\omega_o$ is the time period.

In case of a homogeneous dielectric material, the quality factor is roughly the inverse of dielectric loss (tan δ) of the material. While in case of an electrically resonant system, the Q factor represents the effect of electrical resistance and for electromechanical resonators such as quartz crystals it represents the mechanical friction. When a resonant circuit or cavity is used as a load in a microwave circuit, the quality factor is called loaded Q - factor, which can be determined by the ratio of resonant

frequency (f_o) to the half power bandwidth (Δf_o), measured at 3dB below the maximum height at resonance [58], by using following relation,

$$Q_l = \frac{f_o}{\Delta f_o} \tag{1.10}$$

It is therefore a direct measure of the ability of the resonating body to select a given frequency. Higher the Q value, better is the signal to noise ratio, so that the risk of cross talk within a given frequency range reduces.

The loaded - Q factor (Q_l) arises, when a dielectric resonator is connected to some external circuit. This is the overall Q - factor of the material including both internal losses [called as unloaded Q - factor (Q_u)] and external losses. For cavity resonators, the power loss due to conductors, dielectric fills and radiation can be contributed to Q_u as given by,

$$\frac{1}{Q_u} = \frac{1}{Q_d} + \frac{1}{Q_c} + \frac{1}{Q_r} \tag{1.11}$$

where $1/ Q_d$ is the dielectric loss, $1/ Q_c$ is the loss due to conductivity of the metallic plates and $1/ Q_r$ is the loss due to radiation. Most of the resonant cavities are completely shielded, so that there is no radiation effect, and hence this term can be neglected. Therefore, the total loss of the system is given by,

$$\frac{1}{Q_l} = \frac{1}{Q_o} + \frac{1}{Q_{ext}} \tag{1.12}$$

where $1/ Q_l$ is the total loss of the system, $1/ Q_o$ is the total internal loss and $1/ Q_{ext}$ is the loss due to external coupling. However, the quality factor of a DR can only be measured as the loaded value (Q_l) by keeping in an external circuit. Therefore, it is necessary to have a relation between the two forms of quality factor (Q_l and Q_u) and is given by,

$$Q_u = \frac{Q_l}{(1-\beta_c)} \tag{1.13}$$

where β_c is the coupling coefficient. To get accurate value of Q_u, weakly coupled case ($\beta_c < 1$) is preferred [23]. The value of coupling constant can be calculated,

$$\beta_c = 10^{\frac{-S_{21}}{20}} \tag{1.14}$$

where S_{21} is the insertion loss of the resonating system.

According to the Classical dispersion theory [47], the dielectric loss can be expressed in terms of the resonant frequency of the ceramics and is given by,

$$\tan\delta = \left(\frac{\gamma}{\omega^2_T}\right) f \tag{1.15}$$

where γ is the damping constant and ω_T is the resonant frequency of the transverse optical mode and f is the angular frequency. Analysis of this equation suggests that as the resonant frequency increases the value of tan δ is observed to decrease, whilst dielectric constant of the ceramic does not change with frequency [58]. The decrease of the tan δ as a function of frequency means that the product of the Q value (1/tan δ) and the resonant frequency (f_o), is approximately constant (known as the figure of merit) over a wide range of frequencies. Therefore, $Q \times f_o$ is often quoted while comparing with different ceramics [58].

1.4.3 Small temperature coefficient of the resonant frequency (τ_f)

Temperature stability is another significant advantage of ceramic dielectric resonators. The resonant frequency of the circuit will tend to shift over temperature as a result of environment factors such as the size and linear thermal expansion coefficient of the metal DR enclosure, the position of the resonator within the cavity, type of resonator support, temperature dependence of other circuit elements, etc. This shifting in resonant frequency can be greatly affected by the DR's intrinsic temperature coefficient of resonant frequency (τ_f). Hence, the temperature coefficient of resonant frequency (τ_f) can be defined as the drift in the resonant frequency with respect to temperature. This ultimately determines how well a resonator will function when there is fluctuation in temperature.

The τ_f is related to the temperature coefficient of relative permittivity (τ_ε) and the coefficient of thermal expansion of the material (α_L) by the relation [55, 58],

$$\tau_f = -\alpha_L - \frac{1}{2}\tau_\varepsilon \tag{1.16}$$

Using the Clausius - Mosotti equation, Bosman and Havinga [59] derived an expression for τ_ε at a constant pressure, as follows:

$$\tau_\varepsilon = \frac{1}{\varepsilon_r}\left(\frac{\partial\varepsilon_r}{\partial T}\right)_P = \frac{(\varepsilon_r - 1)(\varepsilon_r + 2)}{\varepsilon_r}(A + B + C) = \left(\varepsilon_r - \frac{2}{\varepsilon_r} + 1\right)(A + B + C) \tag{1.17}$$

where $A = \frac{1}{3V}\left(\frac{\partial V}{\partial T}\right)_P$, $B = \frac{1}{3\alpha_m}\left(\frac{\partial \alpha_m}{\partial V}\right)_T\left(\frac{\partial V}{\partial T}\right)_P$ and $C = \frac{1}{3\alpha_m}\left(\frac{\partial \alpha_m}{\partial T}\right)_V$ and α_m = total polarizability, V = volume, T = temperature, P = pressure, and ε_r = relative permittivity.

Each of the terms in this equation describes a change in dielectric behaviour as a function of temperature. As a result of the thermal expansion of the lattice, there is a reduction in the concentration of bonds that can become dipoles and this is described by term *A* in the equation. Although there is a reduction in the concentration of particles available for polarization as the lattice expands, the increase in volume enables an increase in the polarizability of a given bond (term *B*). The final term *C*, represents the change in polarizability as a function of temperature.

Further, the τ_f is related to the temperature coefficient of capacitance (τ_c) by the following relation [56],

$$\tau_f = \frac{1}{2}(\tau_C - \alpha_L) \tag{1.18}$$

Experimentally, τ_f is measured by following the drift in the resonance peak frequency (f_o) as the temperature is slowly varied. One can also calculate the τ_f value in terms of resonant frequency and temperature by using following equation:

$$\tau_f = \frac{1}{f_o} \times \frac{\Delta f}{\Delta T}\ ppm/^oC \tag{1.19}$$

where Δf is the change in resonant frequency over a temperature difference of ΔT and f_o is the resonant frequency at room temperature (25 ^{o}C).

It is evident that a material with a significantly large τ_f is not useful in a microwave circuit as it cannot maintain its resonant frequency with changes in the operating temperature [58]. It is therefore important to have a τ_f value that is as close to 0 ppm / ^{o}C, so that the signal does not change during device operation. However, in reality a small non zero value of τ_f (± 2 ppm/^{o}C) is required to compensate for thermal expansion of the microwave cavity and other components in the circuit. A material with a small positive value of τ_f variation can often be combined with another material with a small negative τ_f variation to make the resonator temperature stable.

1.5 Factors affecting microwave dielectric properties

In general, microwave dielectric properties are influenced by a number of factors such as permittivity [60], onset of phase transitions [61], processing conditions and raw material purities [62] and order/disorder behavior and porosity [63]. It is least understood of the three important parameters (ε_r, $Q \times f_o$ and τ_f) and is composition, processing, structure and microstructure dependent. The dielectric loss originates due to the extrinsic and intrinsic factors. From a physical prospective, intrinsic losses are controlled by anharmonicity and damping of the phonon modes of the fundamental lattice [49, 50] and they may be estimated from infrared spectroscopy in a manner as discussed in the section 1.3.2. However, in reality, extrinsic losses dominate Q value and optimization usually refers to the minimization of as many extrinsic loss mechanisms as possible [23]. The following sections present an overview of some of the known mechanisms by which the microwave dielectric properties are affected.

The dielectric loss is the result of a combined contribution of the degree of crystal structure imperfection, microstructural inhomogenity and interaction of phonons with crystal lattice. To obtain a low loss a high purity and good microstructures are required. Ceramics with microstructural inhomogenities such as space charges or dipoles, which lie either between matrix grains and inclusions or at grain boundaries, have higher losses. Such inhomogenities may arise due to secondary phases, impurity segregation, incomplete densification etc. It is evident that the quality factor of a ceramic is increased with an increase in bulk density, provided the densification is promoted by solid state diffusion mechanism. Hence, secondary phase formation should be avoided during sintering to get high quality factor.

1.5.1 Effect of porosity

(a) On dielectric constant (ε_r)

Various approximations [64] have been considered to study the change in dielectric constant with porosity. The models consider the dielectrics as a composite system of two phases (dielectric material and porosity) with different dielectric constants. Consider the dielectrics as parallel layers of two dielectrics having volume fractions V_1 and V_2 and dielectric constants ε_1 ($\varepsilon_1 = \varepsilon_m$, dielectric phase) and ε_2 ($\varepsilon_2 = 1$, porosity), respectively. There are two possible configurations:

(i) If electric field is perpendicular to the plane of the plates [64], then the following equation applies:

$$\varepsilon' = \varepsilon_m - P(\varepsilon_m - 1) \tag{1.20}$$

(ii) If electric field is parallel to the plane of the plates, then

$$\varepsilon' = \frac{\varepsilon_m}{P(\varepsilon_m - 1) + 1} \tag{1.21}$$

Physically, these approximations are not realistic and as a result these models do not fit the data well. Later, Maxwell [64] derived a more realistic model of spherical particles of dielectric constant ε_d in a dielectric matrix of ε_m. The dielectric constant of the mixture is given by,

$$\varepsilon' = \frac{V_m \varepsilon_m \left(\frac{2}{3} + \frac{\varepsilon_d}{3\varepsilon_m}\right) + V_d \varepsilon_d}{V_m \left(\frac{2}{3} + \frac{\varepsilon_d}{3\varepsilon_m}\right) + V_d} \tag{1.22}$$

If the spheres are pores and by applying a linearized approximation [65] for $\varepsilon_m - \varepsilon << \varepsilon_m$, then the Eq. (1.22) becomes,

$$\varepsilon' = \varepsilon_m \left(1 - \frac{3P(\varepsilon_m - 1)}{2\varepsilon_m + 1}\right) \tag{1.23}$$

(b) On dielectric loss (tan δ)

The complex permittivity of a material is given by,

$$\varepsilon = \varepsilon' - i\varepsilon'' \tag{1.24}$$

The real component ε' is the dielectric constant and imaginary component ε'' describes the dissipation of the electric field. Then,

Dielectric loss tangent (tan δ) is given by,

$$\tan\delta = \frac{\varepsilon''}{\varepsilon'} \tag{1.25}$$

and the quality factor is given by,

$$Q = \frac{1}{\tan\delta} \tag{1.26}$$

However, the loss increases with porosity, i.e., porosity adds an additional term to the loss, hence it is easier to determine the functional dependence of *P*. Plot of tan δ against porosity on a log-log plot suggested a straight line, which would give a dependence of the form,

$$\tan\delta = (1-P)\tan\delta_0 + AP^n \tag{1.27}$$

where, $\tan\delta_0$ is the loss tangent of the fully dense material, which depend on the amount of material present, i.e., it should depend on the porosity. It was seen that there is a very little difference between the fits. So, for better fit the above equation can be put into the form of mixture law as follows,

$$\tan\delta = (1-P)\tan\delta_0 + P(AP^{n-1}) \tag{1.28}$$

The loss may be related to the surface area of the pore volume, S and is given by,

$$\tan\delta = (1-P)\tan\delta_0 + P(A'S) \tag{1.29}$$

According to sintering theory, a more accurate relationship between porosity and pore surface area can be determined. It can be written as,

$$S \propto \left(\frac{P}{1-P}\right)^{2/3} \tag{1.30}$$

Thus, by substituting the above equation in Eq. (1.29), we get [66],

$$\tan\delta = (1-P)\tan\delta_0 + A'P\left(\frac{P}{1-P}\right)^{2/3} \tag{1.31}$$

It was found that Eq. (1.31) is a good fit to the data and gives a fully density $\tan\delta$, which is higher than of the single crystal [66].

1.5.2 Effect of grain size

Considerable research has been performed over whether the grain size affects the microwave dielectric properties or not [66-70]. It was suggested that grain size should affect the dielectric properties as the boundary could reasonably be expected to scatter phonons and hence increases the dielectric loss [50, 51]. It is well - known that the *Q* - factor of a composition is highest in its single crystal form compare to polycrystalline, as it will be free from many of the imperfections of a ceramic and this is due to grain size of the materials [69, 70]. For instance, in single crystals of Al_2O_3 , the $Q \times f_o$ value in the

direction perpendicular to [001] plane is 1170,000 GHz and parallel to the [001] direction it is 1890,000 GHz [69]. However, the $Q \times f_o$ value of polycrystalline Al_2O_3 ceramic is 370,000 GHz [70].

Other ceramic materials have been observed to show a grain size - loss relationship to support the idea that with the increase in grain size the dielectric loss reduces. Kim et al. [71] in a study of $Ba(Mg_{1/3}Ta_{2/3})O_3$ doped with nickel found that as the grain size decreased, the loss increased. However, the system was complicated by the fact that there were porosity variations, ordering parameter variations and the possible presence of a liquid phase. Kucheiko et al. [72] found that in ZnO doped $CaTi_{1-x}(Fe_{0.5}Nb_{0.5})_xO_3$ ceramic system the tanδ decreased with increasing grain size but in the undoped material the grain size did not influence tanδ. In these materials, it is not clear whether the reduction in the loss with increasing grain size is due to loss of ZnO during the longer sintering times required to achieve larger grains. Kim et al. [73] found that ordering played a dominant role in the dielectric loss of $Ba(Ni_{1/3}Nb_{2/3})O_3$, so that again, grain size effects were masked. The problem with such perovskite systems is that the interplay of so many parameters (grain size, porosity, ordering and presence of liquid phases) makes it difficult to make definite remarks on grain size loss tangent relationship. Further, in the study of $BiVO_5$ ceramic, Prasad et al. [74] found that dielectric constant and dielectric loss (at 100 kHz) increased with increasing grain size. However, the density also varied significantly, making a firm correlation between grain size and dielectric properties unreliable. In the study of sintered Al_2O_3, Penn et al. [66] found that the density remains constant and there is no issue of ordering or any liquid phase at grain boundaries. Therefore, they suggested that the dielectric loss observed in the sintered alumina are due to coarser - grain microstructure.

1.5.3 Effect of humidity

The dielectric loss tangent increases with increasing porosity due to collection of moisture in the pores. It was reported that humidity effects on the low frequency dielectric properties of porous materials [75]. Jonscher [76] identified low frequency loss mechanism in porous materials in the presence of moisture. Similarly, Tinga et al. [77] studied the effect of humidity in some materials at microwaves frequency. It was evidenced that the relaxation process centred at low frequency is responsible for high dielectric loss over a wide frequency range extending into the microwave frequency range.

1.6 Applications of microwave dielectric ceramics

Microwave dielectric ceramics are crucial components in mobile telephone systems and over last few years there has been a rapid development in this field of technologies. Currently available mobile phone devices include a wide variety of applications in addition to the traditional function of making telephone calls. In the form of dielectric resonators (DRs) they enable the filter units in the mobile telephone base stations to remove unwanted sidebands and secondary signals, ensuring transmission of high quality primary signals with minimum interferences. DRs are also used as a resonating element, feedback element or as radiating elements in various applications. The microwave circuits are primarily oscillators, filters, duplexers and miniature radiating elements. These circuits are key elements in systems used for microwave communications, radar, navigation, electronic warfare systems, cellular telephones, base stations, hand held radio transmitters, speed guns and automatic door openers etc. Further, radiating DRs are being used in superconducting testing and antenna applications. A typical microwave oscillator consists of an active device (a diode or transistor) and a passive frequency determining resonate element (see Fig. 1.4 (a)). Its major applications include mobile - phone communication and satellite television receivers (TVRO and DBS). While DR filter (see Fig. 1.4(b)) consists of ceramic resonator discs mounted in a particular way inside a metal cavity and are frequently used in radar and communication systems.

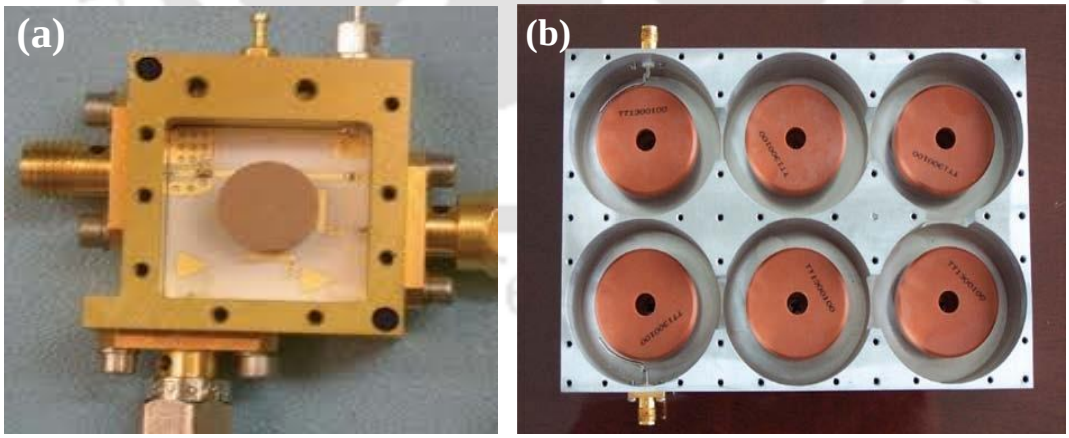

Fig.1.4: *(a) Tuneable dielectric resonator oscillator and (b) Dielectric resonator filter (BL Microwave Ltd.).*

Miniature dielectric filled coaxial resonators are commonly used in wireless handsets such as cellular phones and personal communication systems (PCS) [77]. Other

typical applications include: internet browsing capability, wireless FAX, video recording devices, short messaging service (SMS), motion sensors, video games, high memory capacity for storage of personal media such as downloaded music and movies and personal organizer. It has only been possible to add all of these applications due to the materials development that has led to the miniaturization of device components. Recently, DRs are also widely used in the range of 1 to 60 GHz [78]. Due to this extension of carrier frequency the research of ultrahigh speed communication system has been ongoing. For example, 60 GHz carrier frequency will be used soon for next generation AV centre at home. This will focus on the importance of materials with high quality factor rather than high dielectric constant.

Further, due to small size, light weight, low cost along with enhanced features like low loss, temperature compensated performance with good coupling and frequency tunability characteristics, DRs are being used in making an important device in microwave integrated circuits. Currently, new applications such as, intelligent transport system (ITS), direct broadcasting satellite (DBS), ultra high speed wireless local - area networks, 3G filters, low temperature co - fired ceramics (LTCC) for embedded microwave circuitry and higher frequency applications for advanced radar technology as well as for high frequency temperature compensating capacitors [23] for DRs are constantly emerging.

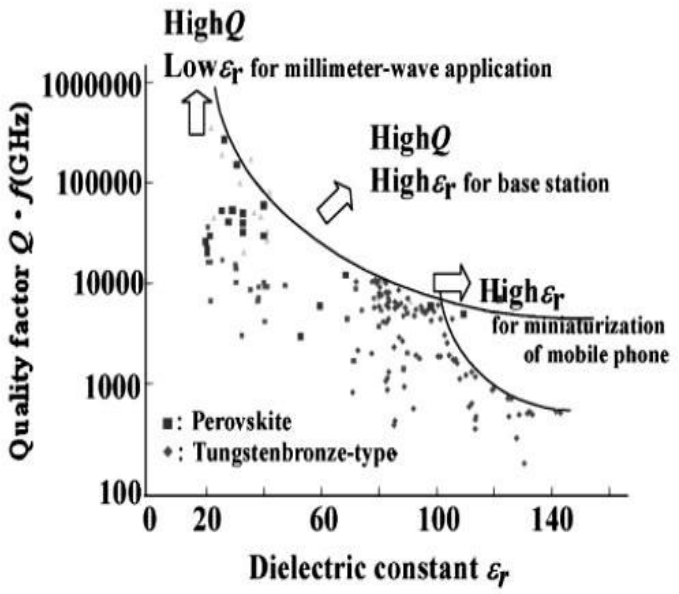

Fig. 1.5: *Variation of $Q \times f_o$ as a function of dielectric constants for different microwave dielectric ceramics [79].*

From application point of view, Ohsato [79] has plotted the quality factor ($Q \times f_o$) as a function of dielectric constant values for many of the published properties of tungsten - bronze and perovskite microwave dielectric ceramics and is illustrated in Fig.1.5. In addition, to compare with this raw data, an approximate specification for millimetre - wave, base stations and mobile telephone handset were also plotted. Dielectric resonator materials used for millimetre - wave applications are required to have ultra high quality factor ($Q \times f_o$), low dielectric constant (ε_r <15) and small temperature coefficient of resonant frequency (τ_f). In this perspective, many aluminate, forsterite and willemite based dielectric ceramics have attracted much attention due to their ultrahigh - Q and low ε_r. Common examples: Al_2O_3 [80], Mg_2SiO_4 [81] and Zn_2SiO_4 [82] with typical microwave dielectric properties of dielectric constants between 5 - 10 and high $Q \times f_o$ of 150,000 - 400,000 GHz.

Another family of microwave dielectric ceramics with slightly higher dielectric constant ($\varepsilon_r \approx$ 13-16) than the silicate ceramics are Mg_2TiO_4 and $MgTiO_3$. Mg_2TiO_4 ceramics have moderate dielectric constant ε_r of 12 - 14 and high $Q \times f_o$ of around 150,000 GHz, but can be tremendously boosted to 318,000 GHz [83] with the partial replacement of Ti^{4+} site by Sn^{4+} and by varying other processing conditions. Similarly, the typical microwave dielectric properties of $MgTiO_3$ are ε_r of 16 -17 and $Q \times f_o$ of 160,000 but can be greatly improved by substituting Sn^{4+} in the Ti^{4+} site to around 328,500 GHz [84]. These materials are being used in today's global positioning systems (GPS), patch antennas, wireless local - area networks (WLAN) band pass filters and even for 5.8 GHz industrial, scientific and medical applications (ISM) band pass filters [85]. Some other major class of microwave dielectric ceramics that cover a wide variety of microwave dielectric properties are based on the mineral perovskite. This types of materials basically used in the base stations for telecommunication purpose and expected to reduce the size for installation and maintenance. The dielectric constant of such ceramic systems can range from low - moderate of 20 for the rare Earth aluminates [86] to 180 for $CaTiO_3$ [87]. Similarly, $Q \times f_o$ shows a wide variety of values ranging from 6000 GHz for $CaTiO_3$ to 56000 GHz for rare earth aluminates.

Finally, in the handsets of the mobile telephone systems, it is more important to reduce the size of the component in order to minimize the size of the device at the expense of frequency selectivity. This needs a material with high dielectric constant of approximately 80 - 100 and with high Q value. An example of a material which meets

such requirement is $Ba_4Nd_{9.33}Ti_{18}O_{54}$ [88]. Similar requirements are needed for the satellite communication system such as GPS. The mass of the components must be minimized in order to save on the fuel getting the satellite into orbit via a spacecraft and to reduce the fuel consumption to keep the satellite into the orbit [89]. Moreover, higher ε_r materials pose problems in base station cavities as the electromagnetic (EM) field is effectively retained within the ceramics. Retention of the fields prevents coupling between pucks, thereby affecting filter performance, i.e. the filter frequency window is narrowed [23].

1.7 Electronic applications of high ε_r and low loss materials in thin film form

Thin film science and technology play an important role in the present - day electronic industries. Thin film technology has been developed primarily for the need of the integrated circuit industry. The demand for development of smaller and smaller devices with higher speed, especially in new generation of integrated circuits requires advanced materials and modern processing techniques suitable for future giga scale integration (GSI) technology. In this regard, physics and technology of thin films can play an important role to achieve this goal. Thin films as a two - dimensional system are important to many real - world problems. Their material costs are very small as compared to the corresponding bulk material and they perform the same function when it comes to surface processes. Thus, knowledge and determination of the nature, functions and properties of thin films can be used for the development of new technologies for future applications. Thin film technology is based on three foundations: fabrication, characterization and applications. Some of the important applications of thin films are in microelectronics, communication, optical electronics, catalysis, surface coating of all kinds and in energy generation and conservation strategies.

Since 1997, a consortium of industry representatives has developed and customized the International Technology Roadmap on Semiconductors (ITRS): a publication on the projected equipment, design and material requirements needed to maintain the rapid evolution of integrated circuit (IC) technology. The 1999 ITRS publication projected the need for superior high dielectric constant (ε_r), low leakage current materials to replace SiO_2 in gate stacks in complementary metal - oxide semiconductor (CMOS) and dynamic random - access memory (DRAM) devices by the year 2005. Since then, it has become apparent that advanced high speed ICs are being developed much faster than the ITRS forecasts. The revised 2000 roadmap stated that “while developmental progress in this

area has been significant, it becomes increasingly probable that chip production with high - ε_r gate stacks will be very difficult to achieve (even) in the 2005 time frame and therefore, appears unlikely in the more accelerated time frames suggested by the new proposed gate length scaling forecasts. Consequently, a major 2001 task is the analysis of the current quickened trend, and the identification of design, device and material alternatives imposed by the difficulties of accelerated high ε_r / dual metal gate CMOS integration" [90].

For 40 years, SiO_2 has been used as a gate dielectric material in silicon based CMOS devices. Demand for greater speed and increased storage capacity has driven the feature size shrinkage of CMOS based circuits and storage devices. With the shrinkage of metal - oxide semiconductor field effect transistor (MOSFET) devices, channel lengths and gate dielectric thickness have been scaled to maintain performance and turn - on voltage characteristics. SiO_2 has been scaled down to attain the desired capacitance, but a roadblock exists in how thin the SiO_2 layer can be made without exceeding the leakage current requirements. The leakage current is particularly significant for logic devices, which must maintain tightly controlled turn - on and turn - off voltages. The leakage current, although prominent for storage devices, does not require a stringent design rule for dynamic memory devices since the data must be periodically re-written to the bit in the operation. Data is re - written on the order of every two to three hundred milliseconds [91]. Leakage current is considerably more important for static memory devices. New high ε_r materials that meet varying requirements are fervently being sought to replace SiO_2 by the projected time frames for the production of future generation devices. With higher dielectric materials, the required capacitance can be maintained with thicker gate layers thereby keeping leakage current under control.

1.8 Efforts to replace SiO_2

Table 1.1 lists several materials and their properties including dielectric constants that have been studied as possible replacement for SiO_2. Before the discussion begins, it is important to understand the requirements for differing device applications. For memory / storage applications, significant attention has been focused on Ta_2O_5, $SrTiO_3$ and Al_2O_3. Static memory applications require a very low leakage current ($J < 10^{-8} A/cm^2$) and high charge storage density. In this case, thermodynamic stability of the high - ε_r material on silicon is not as critical since the dielectric material is sandwiched by the electrodes, poly - Si or metal. It attempts to minimize interfacial reactions which are solely to maximize

charge density storage capacity [92]. Additionally, unlike MOSFET applications, no electric field penetration below the bottom electrode is required allowing the use of metal or heavily doped poly - Si as the lower electrode. Furthermore, current transport along the dielectric interface is not important as in MOSFET applications. Ultimately, the bottom dielectric interface is not as critical in storage applications. A significant research has been done on the materials listed in Table 1.1, but these materials don't possess all the requirements needed for the replacement of SiO_2. Studies of ternary and quaternary oxides and silicates have been the next frontier for finding an adequate replacement.

Table 1.1: *List of medium to high - ε_r material candidates.*

Material	ε_r	Bandgap (eV)	Crystal Structure
TiO_2	100	3.4	Tetragonal (Rutile, Anatase)
La_2O_3	30	4.3	Hexagonal, Cubic
Ta_2O_5	26	4.5	Orthorhombic
HfO_2	25	5.7	Monoclinic, Tetragonal, Cubic
ZrO_2	25	5.9	Monoclinic, Tetragonal, Cubic
Pr_2O_3	26	3.5	Amorphous
$MgTiO_3$	17	4.0	Rhombhohedral
Y_2O_3	15	5.6	Cubic
Al_2O_3	9	8.7	Amorphous
Si_3N_4	7	5.1	Amorphous
SiO_2	3.9	8.9	Amorphous

1.9 Magnesium ortho-titanate [Mg_2TiO_4 (MTO)]: An interesting system in both bulk and thin film forms

1.9.1 Bulk MTO for microwave applications

Recently, dielectric materials based on the MgO - TiO_2 binary system, has brought much more attention in the field of microwave engineering. Among these compositions, Mg_2TiO_4 and $MgTiO_3$ are recognized as good candidates for high frequency applications. This is due to their extremely low dielectric loss, medium to high dielectric constant and

low temperature coefficient of the permittivity. Even their low cost bought much more attention. Therefore, they offer a great stability to specific applications such as frequency discriminators, low phase - noise dielectric resonator oscillators, duplexers, filters and other applications. Moreover, MTO based ceramics have wide applications such as heat resistor, microwave integrated circuit, waveguides and capacitors for temperature compensation. The more detail about its bulk form is discussed in the motivation section.

1.9.2 MTO thin film as a possible gate oxide in electronic applications

The search for materials with high dielectric constant as an alternative to SiO_2 in CMOS gate oxide and ULSI (Ultra Large Scale Integrated) dynamic random - access memory (DRAM) applications have been the subject of intense research in recent years. In the past, selection of gate oxides has mostly focused on few metal oxides such as Sc_2O_3, MgO, Ga_2O_3, Al_2O_3 and HfO_2. However, most of these studies have yielded deep depletion behavior only. Therefore, the need for gate oxide with high permittivity, high thermal stability and low leakage current has become urgent.

As mentioned in the previous section, the physical and electrical properties of MTO thin films as reported by other researchers have good characteristics such as a moderate dielectric constant, low dielectric loss and high temperature stability. These properties make MTO thin film a noteworthy material in integrated electronics as well as in high frequency applications.

1.9.3 Crystal structure of Mg_2TiO_4

Mg_2TiO_4 has an inverse cubic spinel structure having general formula A_2BO_4. The sites can be written as $(A_{1-x}B_x)^{tet.}(A_xB_{2-x})^{oct.}O_4$, where x is called as the inversion parameter. In the present case, the spinel is called inverse since x is equal to 1 [93]. It belongs to O^7_h (*Fd-3m*) (227) space group. The structural formula of Mg_2TiO_4 can be represented as $(Mg)^{2+}[Mg^{2+}Ti^{4+}]O_4$ in which magnesium occupies both tetrahedral (8a) and octahedral (16d) sites but titanium occupies only octahedral (16d) sites. The oxygen atoms are in (32e) site symmetry positions. The schematic representation of Mg_2TiO_4 unit cell is shown in Fig. 1.6. The unit cell of Mg_2TiO_4 consists of eight formula unit (Z = 8), each of which consist of 32 anions and 24 cations, for a total of 56 atoms. The smallest Bravais cell contains only 14 atoms (Z = 2). The typical lattice parameters of MTO ceramics are $a = b = c = 8.451$ Å. The Wyckoff position, atomic coordinates and occupancy of the MTO systems are given in the **Table 1.2**.

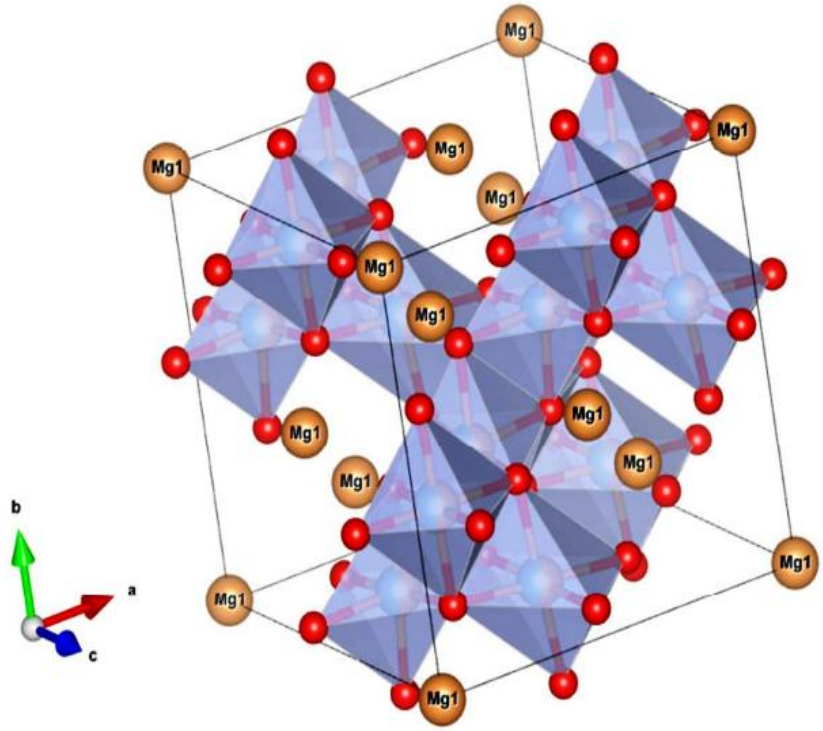

Fig.1.6: *Schematic representation of one unit cell Mg_2TiO_4 [94]. The Mg^{2+} ions occupy at the tetrahedral positions are represented as separate spheres; the octahedral coordination of the Mg^{2+} / Ti^{4+} ions are also shown at the six-fold coordinated.*

Table 1.2: *Occupied Wyckoff position, atomic coordinates and occupancy of MTO system.*

Atoms	Wyckoff positions	*x*	*y*	*Z*	Occupancy
Mg1	8a	0.125	0.125	0.125	0.9970
Ti1	8a	0.125	0.125	0.125	0.0033
Ti2	16d	0.5	0.5	0.5	0.4985
Mg2	16d	0.5	0.5	0.5	0.5015
O1	32e	0.2611	0.2611	0.2611	1

1.10 Motivation of the present thesis work

Most of the currently low loss dielectrics made from complex perovskites are required high sintering temperatures and comparatively high cost. Moreover, their structures and dielectric properties are difficult to predict because there are too many cations (at least four) involved. Recently, spinel - based low permittivity materials have attracted more

attention in the field of science. This is due to extension of carrier frequency from microwave to millimeter - wave range. As a result materials with high dielectric constant have become of less interest. Among many medium to high - K low loss dielectric materials, Mg_2TiO_4 ceramics has been found to be an excellent material for the applications discussed in bulk form. Moreover, it has good optical and electrical properties which could be used for other electronic, photonic and microwave applications.

The microwave dielectric property of the MTO ceramic was first reported by Belous et al. [95]. It has an excellent dielectric properties such as high quality factor ($Q \times f_o$) ~150,000 GHz, modest dielectric constant (ε_r) ~ 14 and a negative temperature coefficient of resonant frequency (τ_f) ~ - 50 ppm/^{o}C). Moreover, its low cost has attracted much more attention. But the major disadvantage in preparing such materials by solid state reaction method is the requirement of very high sintering temperature (above 1420 ^{o}C). Therefore, it is interesting to look for ways to reduce its sintering temperature and the effect of such process for improving the microwave dielectric properties. Another important aspect in the study of DR materials is to understand the factors which influence Q value and look for the ways to improve it. Huang et al. [12] reported the sintering temperature of $Mg_2(Ti_{0.95}Sn_{0.05})O_4$ ceramics as 1300 ^{o}C with the addition of $CaTiO_3$ ceramics. Li et al. [36] reported the preparation of 0.92 $(Mg_{0.95}Co_{0.05})_2TiO_4$ - 0.08$(Ca_{0.8}Sr_{0.2})TiO_3$ ceramics with the addition of 0.5 wt.% B_2O_3 sintered at 1200 ^{o}C. Huang et al. [96] reported the sintering temperature of $(Mg_{0.95}Co_{0.05})_2TiO_4$ was reduced to 1300 ^{o}C with the addition of $SrTiO_3$ ceramics. Nonetheless, the microwave dielectric properties, especially $Q \times f_o$ values are significantly degraded with the additives. On the other hand, few studies were reported on improving the dielectric properties of Mg_2TiO_4 ceramics by partial substitution of Mg by Zn, Co, Mn or Ni: $(Mg_{0.95}Zn_{0.05})_2TiO_4$ (ε_r ~ 15.48, $Q \times f_o$ ~ 275,300 GHz and τ_f = -34 ppm/ ^{o}C) [97], $(Mg_{0.95}Co_{0.05})_2TiO_4$ (ε_r ~ 15.7, $Q \times f_o$ ~ 286,000 GHz and τ_f = -52.5 ppm/ ^{o}C) [98], $(Mg_{0.95}Mn_{0.05})_2TiO_4$ (ε_r ~ 15.69, $Q \times f_o$ ~ 276,200 GHz and τ_f = -52.6 ppm/ ^{o}C) [83], $(Mg_{0.95}Ni_{0.05})_2TiO_4$ (ε_r ~ 16.43, $Q \times f_o$ ~ 238,000 GHz and τ_f = -55 ppm/ ^{o}C) [99], However, the sintering temperature was reported to be always higher than 1350 ^{o}C.

MTO is an excellent microwave dielectric material with wide bandgap and high refractive index suitable for optical and electronic applications. Therefore, its practical applications in optical response are very promise. Recently, MTO thin films have attracted much attention due to its applications in (i) optical modulation and protective

layer of plasma display panels and in the monolithic microwave integrated circuit technologies (MMIC) [30], and (ii) as buffer layer [100]. In addition, MTO based thin films are used as a substrate for growing high temperature superconductor (HTSC) films due to their high chemical, mechanical and thermal stability properties [101]. Basically, MTO ceramic used as a novel substrate for HTSC thin films due to its low microwave loss and well defined surface structure [102]. In addition, they are capable in reducing the dimension of a device in communication integration density. Moreover, thin film technology has become a major requirement for integration since the integrated circuits have been applied in microwave communication systems. Even though the considerable amount of study has gone into bulk MTO, studies on thin film are rather few. To the best of our knowledge, the growth of thin films using Mg_2TiO_4 microwave dielectric ceramics as target materials by RF sputtering has not been reported so far. This motivated the author to make an attempt in that direction by growing MTO films by a cost effective process and to compare their properties with that of their bulk counterpart.

As a continuing effort in our laboratory on microwave materials, we have chosen to investigate Mg_2TiO_4 ceramics in the bulk form prepared by mechanical synthesis, solid state reaction method, and thin film prepared by RF magnetron sputtering technique. We have tried different approaches to reduce the sintering temperature of bulk MTO and have been successful to some extent. The primary motivation was to improve the microwave dielectric properties of the bulk samples by understanding the microstructure and property correlation with different additives, doping and temperature treatments.

The overall main effort in this study is to prepare pure MTO and MTO with different additives to enhance the microwave dielectric properties of the bulk samples by improving the microstructure and relative density and microwave dielectric properties. Another interest is to compare microwave properties of MTO in bulk as well as in thin film form in order to see whether these properties could be enhanced or not. In addition, we have also investigated their optical, electrical properties and impedance spectroscopy, which could not only be useful in other applications but also helps in arriving at a comprehensive picture of the physics in these materials, and the results were compared with the existing literature.

1.11 References

[1] C. L. Huang, C. F. Tseng, W. R. Yang, T. J. Yang, *J. Am. Ceram. Soc.*, **91** (2008) 2201.

[2] C. L. Huang, J. J. Wange, Y. P. Chang, *J. Am. Ceram. Soc.*, **90** (2007) 858.

[3] C. L. Huang, J. F. Tseng, *Mater. Letts*., **58** (2004) 3732.

[4] R. J. Cava, *J. Mater. Chem.*, **11** (2001) 54.

[5] D. Pamu, G. L. Narayana Rao, K. C. James Raju, *J. Alloy. Compd*., **475** (2009) 745.

[6] P. S. Anjana, M. T. Sebastain, M. N. Suma, *Int. J. Appl. Ceram. Technol*., **5** (2008) 325.

[7] B. L. Liang, X. H. Zheng, D. P. Tang, *J. Alloys Compd*., **488** (2009) 409.

[8] Y. B. Chen, *J. Alloys Compd*., **513** (2012) 481.

[9] L. Fang, H. Su, Q. Yu, H. Zhang, B. Wu, *J. Am. Ceram. Soc.*, **9** (2008) 2769.

[10] C.L. Huang, J. Y. Chen, *J. Am. Ceram. Soc.*, **93** (2010) 470.

[11] C.H. Hsu, Y.S. Chang, *J. Alloys Compd*., **479** (2009) 714.

[12] C.L. Huang, J. Y. Chen, B. J. Li, *J. Alloys Compd*., **509** (2011) 4247.

[13] R.D. Ritchtmeyer, *J. Appl. Phys*., **10** (1939) 391.

[14] H.M. Schlicke, *J. Appl. Phys.*, 24 (1953) 187.

[15] A. Okaya, L. F. Barash. *Proc. IRE*., **50** (1962) 2081.

[16] R.L. Bolton, Ph.D Thesis, *University of Illinois, Urbana-Champaign, IL*, (1968).

[17] T. Negas, G. Yeager, S. Bell and R. Amren, *Proc. Int. Conf. Chem. Electron. Ceram. Mater*., NIST Special Publication, **804** (1990).

[18] D.J. Masse, R. Readey, C. Hatwig, *Proc. IEEE.*, **59** (1971) 1628.

[19] Y. Konishi, *Techn. Rep. NHK*, Tokyo, Japan, **111** (1971).

[20] J. K. Plourde, *IEEE MTT-S Digest*, **202** (1973).

[21] J. K. Plourde, D. F. Linn, H. M. O. Jr., J. T. Jr., *J. Am. Ceram. Soc.*, **58** (1975) 418.

[22] K. Wakino, M. Katsube, H. Tamura, T. Nishikawa and Y. Ishikawa, *IEEE Four Joint Conv. Rec*., **235** (1977).

[23] M. Reaney, and D. Iddles, *J. Am. Ceram. Soc.*, **89** (2006) 2063.

[24] M.T. Sebastian, "*Dielectric Materials for Wireless Communications*", Elsevier Science Publishers, Oxford (2008).

[25] K. Wakino, *Ferroelectrics*, **91** (1989) 69.

[26] V. M. Ferreira, F. Azhough, J. L. Baptista and R. Freer, *Ferroelectrics*, **133** (1992) 127.

[27] S. Kawashima, M. Nishida, I. Ueda, K. Wakino, *J. Am. Ceram. Soc.*, **66** (1983) 421.

[28] R. B. Von Dover, L. F. Schneemeyer, and R. M. Fleming, *Nature*, **392** (1998) 162.

[29] H. M. O'Bryan, and J. Thomson, *J. Am. Ceram. Soc.*, **66** (1983) 66.

[30] K. Wakino, K. Minai, H. Tamura, *J. Am. Ceram. Soc.*, **67** (1984) 278.

[31] H. M. Buschbaum, *J. Alloys Compd*., **349** (2003) 49.

[32] T. R. Paudel, A. Zakutyev, S. Lany, M. d'Avezac, A. Zunger, *Adv. Funct. Mater*., **21** (2011) 4493.

[33] N. Ueda, T. Omata, N. Hikuma, K. Ueda, H. Mizoguchi, T. Hasimoto, H. Kawazoe, T. Hashimoto, *Appl. Phys. Lett.*, **61** (1992**)** 1954.

[34] T. Omata, N. Ueda, N. Hikuma, K. Ueda, H. Mizoguchi, T. Hashimoto, H. Kawazoe, *Appl. Phys. Lett.*, **62** (1993**)** 499.

[35] E. R. Leite, C. M. G. Souza, E. Longo, J. A. Varela, *Ceram. Int*., **21** (1995) 143.

[36] B. J. Li, J. Y. Chen, G. S. Huang, C. Y. Jiang, C. L. Huang, *J. Alloys Compd*., **505** (2010) 291.

[37] K. P. Surendran, P. V. Bijumon, P. Mohanan, M. T. Sebastian, *Appl. Phys., A*., **81** (2005) 823.

[38] C. L. Huang, C. Y. Tai, C. Y. Huang, Y. H. Chen, *J. Am. Ceram. Soc.*, **93** (2010) 1999.

[39] A. Escardino, J. L. Amoros, A. Gozalbo, M. J. Orts, A. Moreno., *J. Am. Ceram. Soc*., **83** (2000) 2938.

[40] K. P. Surendran, N. Santha, P. Mohanan, M. T. Sebastian, *Eur. Phys. J. B*., **41** (2004) 301.

[41] W. Lei, W.-Z. Lu, J. H. Zhu, X.-H. Wang, *Mater. Lett*., **61** (2007) 4066.

[42] K. P. Surendran, M. T. Sebastian, M. V. Manjusha, J. Philip, *J. Appl. Phys*., **98** (2005) 044101.

[43] W. Lei, W.-Z. Lu, D. Liu, J.-H. Zhu, *J. Am. Ceram. Soc.*, **92** (2009) 105.

[44] C.L. Huang, Y. H. Chen, C. Y. Tai, C. Y. Huang, *J. Alloys Compd*., **509** (2011) L150.

[45] B. Tareev, "*Physics of dielectric materials*" Mir Publishers, Moscow (1975).

[46] A. J. Moulson and J. M. Herbert, "*Electroceramics Materials, Properties and Applications*", Champman and Hall, London, 1st Edition (1991).

[47] K. Wakino, M. Murata, H. Tamura, *J. Am. Ceram. Soc.*, **69** (1986) 34.

[48] H. Tamura, D. A. Sagala, K. Wakino, *Jpn. J. Appl. Phys.*, **25** (1986) 787.

[49] V. L. Gurevich, Transport in Phonon Systems, North Holland, Amsterdam, 1986.

[50] V. L. Gurevich, and A. K. Tagantsev, *Adv. Phys*., **40** (1991) 719.

[51] J. Petzelt, S. Pecesova, J. Fousek, S. Kamba, V. Zeleny, *Ferroelectrics*, **93** (1989) 77.

[52] R. Kudesia, A. E. Mc Hale, R. A. Condrate, R. L. Synder, *J. Mater. Sci*., **28** (1993) 5569.

[53] Y. Kobayashi, and S.Tanaka, *IEEE Trans. Microw. Theory Techol.*, **28** (1980) 1077.

[54] Rayleigh, *Phil. Mag*., **43** (1892) 123.

[55] D. Kajfez, "*Dielectric resonators*", Chapter 4, Artech House, Norwood (1986).

[56] R. C. Buchanan, "*Ceramic Materials for Electronics*", Marcel Dekker, New York, 1986.

[57] J. Bahl and P. Bhartia, "*Microwave Solid State Circuit Design"*, Wiley, New York, (1988).

[58] A.J. Moulson and J. M. Herbert, "*Electroceramics*", Champman and Hall, London, 1990.

[59] A.J. Bosman, E. E. Havinga, *Phys. Rev*., **129** (1963) 1593.

[60] P. J. Harrop, *J. Mater. Sci.*, **4** (1969) 370.

[61] E. L. Colla, I. M. Reaney, N. Setter, *J. Appl. Phys.*, **74** (1993) 3414.

[62] A. Templeton, X. R. Wang, S. J. Penn, S. J. Webb, L. F. Cohen and N. M. Alford, *J. Am. Ceram. Soc.*, **83** (2000) 95.

[63] D. A. Sagala and S. Nambu, *J. Am. Ceram. Soc.*, **75** (1992) 2573.

[64] W. D. Kingery, H. K. Bowen, and D.R. Uhlmann, *Introduction to Ceramics*, 2nd ed. Wiley, New York, 1976.

[65] R. Heidinger and S. Nazare, *Powder Metall. Int*., **20** (1988) 30.

[66] S. J. Penn, N. M. Alford, A. Templeton, X. Wang, M. Xu, M. Reece, and K. Schrapel, *J. Am. Ceram. Soc.*, **80** (1997) 1885.

[67] J. D. Breeze, J. M. Perkins, D. W. McComb, N. M. Alford, *J. Am. Ceram.Soc.*, **92** (2009) 671.

[68] D. Pamu, G. Lakshmi Narayana Rao, K. C. James Raju, *J. Am. Ceram. Soc.*, **95** (2012) 126.

[69] J. Krupka, K. Derzakowskiz, M. E. Tobar, A. Abramowicz, R. G. Geyer, *IEEE Trans. Microw. Theory Technol.*, **47** (1999) 752.

[70] N. M. Alford and S. J. Penn, *J. Appl. Phys.*, **80** (1996) 5895.

[71] E. S. Kim and K. H. Yoon, *J. Mater. Sci.*, **29** (1994) 830.

[72] S. Kucheiko, H. J. Kim, S. J. Yoon, H. J. Jung, *Jpn. J. Appl. Phys.*, **36** (1997) 198.

[73] T. Kim, Y. Kim, S. J. Chung, *Jpn. J. Appl. Phys.*, **34** (1995) 4096.

[74] K.V.R. Prasad, A. R. Raju and K. B. R. Varma, *J. Mater. Sci.*, **29** (1994) 2691.

[75] R. F. Field, *J. Appl. Phys.*, **17** (1946) 318.

[76] A. K. Jonscher, "*Universal relaxation law*", Chelsea Dielectric, London (1996).

[77] S. R. Fiedziuszko, I. C. Hunter, T. Itoh, Y. Kobayashi, T. Nishiwaka, S. N. Stilzer, K. Wakino, *IEEE Trans. Microw. Theory Technol*., **50** (2002) 706.

[78] A. P. S. Khanna, *Dielectric Resonators*, Chapter 10, D. Kajfez and P. Guillon (Eds.) Artech House, Norwood (1986).

[79] H. Ohsato, *J. Ceram. Soc. Jpn.*, **113** (2005) 703.

[80] C. L. Huang, J. J. Wange, and C. Y. Huang, *J. Am. Ceram. Soc.*, **90** (2007)1487.

[81] H. Ohsato, T. Tsunooka, T. Sugiyama, K. I. Kakimoto, H. Ogawa, *J. Electroceram.*, **17** (2006) 445.

[82] Y. Guo, H. Ohsato, K. I. Kakimoto *J. Eur. Ceram. Soc.*, **26** (2006)1827.

[83] C. L. Huang, J. Y. Chen, *J. Am. Ceram. Soc.*, **92** (2009) 2237.

[84] Z. Gong, Z. Wang, L. Wang, Z. Fu, W. Han, Q. Zhang, *Electr. Mater. Lett.*, **3** (2013) 331.

[85] C. L. Huang, J. J. Wang, B. J. Li, C. F. Shih, *Mater. Lett*., **62** (2008) 2516.

[86] S. Y. Cho, I. T. Kim, and K. S. Hong, *J. Mate. Res*., **14** (1999) 253.

[87] H. F. Kay, P. C. Bailey, *Acta. Cryst*., **10** (1957) 219.

[88] H. Ohsato, T. Ohhashi, H. Kato, S. Nishigaki, T. Okuda, *Jpn. J. Appl. Phys.*, **34** (1995) 187.

[89] A. Hunter, *IEEE Trans. Microw. Theory Technol*., **50** (2002) 794.

[90] Semiconductors Industry Association, "*International Technology Roadmap for Semiconductors*" (2001).

[91] A. I. Kingon, J. P. Maria, S. K. Streiffer, *Nature*, **406** (2000) 1032.

[92] G. D. Wilk, R. M. Wallace, J. M. Anthony, *J. Appl. Phys*., **89** (2001) 5243.

[93] G. Pfaff, *Ceram. Int*., **20** (1994)111.

[94] K. Momma and F. Izumi, *J. Appl. Cryst*., **44** (2011) 1272.

[95] A. Belous, O. Ovchar, D. Durilin, M.M. Krzmanc, M. Valant, D. Suvorov, *J. Am. Ceram. Soc*., **89** (2006) 3441.

[96] C. L. Huang, J. Y. Chen, *J. Alloys Compd*., **485** (2009) 706.

[97] C. L. Huang, S. S. Liu, J. *Am. Ceram. Soc*., **91** (2008) 3428.

[98] C. L. Huang, J. Y. Chen, *J. Am. Ceram. Soc*., **92** (2009) 379.

[99] C. L. Huang, C. En. Ho. *J. Am. Ceram. Soc*., **7** (2010) E163.

[100] C. H. Lee, J. H. Yeom, *Jpn. J. Appl. Phys*., **39** (2000) 6716.

[101] H. Haefke, H. P. Lang, R. Sum, H. J. Guntherodt, L. Berthold, D. Hesse, *Appl. Phys. Lett*., **61** (1992) 2359.

[102] Hesse, *Patent*, DD 0151828 (1981).

Chapter 2

Experimental and characterization techniques

In the course of present investigation, several experimental techniques were used for the preparation and characterization of the samples. This chapter basically provides a brief description of the synthesis methodology and characterization techniques used for both bulk and thin films of Mg_2TiO_4 ceramics.

2. (A) Synthesis of bulk Mg_2TiO_4 ceramics

2.1 Sample preparation

Ceramics are polycrystalline materials having fine crystalline grains and imperfections like grain boundaries, pores, etc. Since they are brittle refractories, shaping them and densifying without cracks and deformation is a challenge. This section deals with the preparation techniques being used for the bulk Mg_2TiO_4 (MTO) ceramics. In order to prepare these materials with highest possible densification for the use in microwave applications, the available methods for the preparation are (a) mechanical alloying (b) solid state reaction (or ceramic method) and (c) chemical methods [1-3]. High purity materials and precise methods of production must be employed to ensure that the desire properties of these advanced materials are achieved in final product. For the present thesis work, mechanical alloying and solid state reaction methods were used for the preparation of MTO ceramics in bulk form.

2.1.1 Mechanical alloying

Mechanical alloying (MA) technique was developed around 1966 by Benjamin and his co-workers [4] as a part of the program to produce oxide dispersion strengthened Ni based super alloys for gas turbine applications. The process of production of alloys by high energy ball milling was initially referred to as milling / mixing. Actually, the term mechanical alloying was coined by Ewan C. Mc Queen [5]. It is a convenient and inexpensive method for the synthesis of wide range of nanosized metallic, amorphous alloys, intermetallic compounds, nanocomposites and ceramic powders in an efficient and economical manner [6]. The most valuable advantage of this technique is that the solid -

state reaction is activated via mechanical energy instead of thermal energy (high temperature). Hence, this method skips the calcination step, which is necessary in the conventional solid - state method, and the initial reaction takes place at a temperature close to room temperature in a sealed container. Furthermore, the mechanically derived powders possess a higher sinterability than those synthesized by the conventional solid - state reaction and most of the wet - chemical processes [7]. This is mainly due to the repeated cold welding and fracturing of powder particles. This in turn increases the area of contact between the reactant powder particles by repeatedly forming new surfaces into contact due to a reduction in particle size during milling. This allows the reaction to proceed without the necessity for diffusion through the product layer. As a consequence, reactions that normally require high temperatures occur at lower temperatures during MA.

MA not only makes the material finer but also includes structural changes, phase transformations and even solid - state reactions among the solid reagents. These physicochemical changes occur due to the efficient transformation of the mechanical energy of the grinding media to the material particles and the intensive mechanical force during the milling process [6]. One of the major advantages of this technique is to produce novel alloys, i.e., alloying of normally immiscible elements, which are not possible by any other technique. The planetary ball mills are generally used for MA processes. The photographic view of a planetary ball mill and the schematic view of MA process are shown in Fig. 2.1. The planetary ball mill owes its name to the planet like movement of its vials. These are arranged on a rotating support disk and a special drive mechanism causing them to rotate around their own axes while revolving in a circle. The centrifugal force produced by the vials rotating around their own axes and that produced by the rotating support disk, both act on the vial contents, consisting of material to be ground and grinding balls added inside the vial.

There are several processing variables to determine the final size of the particles, i.e., type of mill, milling vial, milling speed, milling time, size distribution of the milling medium, ball – to - powder ratio, extent of filling of a vial, milling atmosphere, process control agent and temperature of milling [6, 8]. In the present study, planetary ball mill (M/s Fritsch Pelverisette 6, Germany) was employed for MA process. The zirconium and tungsten carbide vials and different diameters of spherical 5 and 10 mm zirconium / tungsten carbide balls are used. The ball-to-powder weight ratio of 10:1 and rotating

speed 400 rpm maintained during the milling process. In order to avoid excess heating, it is programmed to stop for 10 minutes after every 15 minutes of continuous milling.

Though mechanical treatment of ceramics powders can reduce particle size and enables to produce nanocrystalline powders, but this method lacks the synthesis of phase pure ceramics, which is essential for the fabrication of dielectric ceramics with optimum dielectric properties. Hence, we have chosen the solid - state reaction method as an alternative process for the preparation of MTO based ceramics.

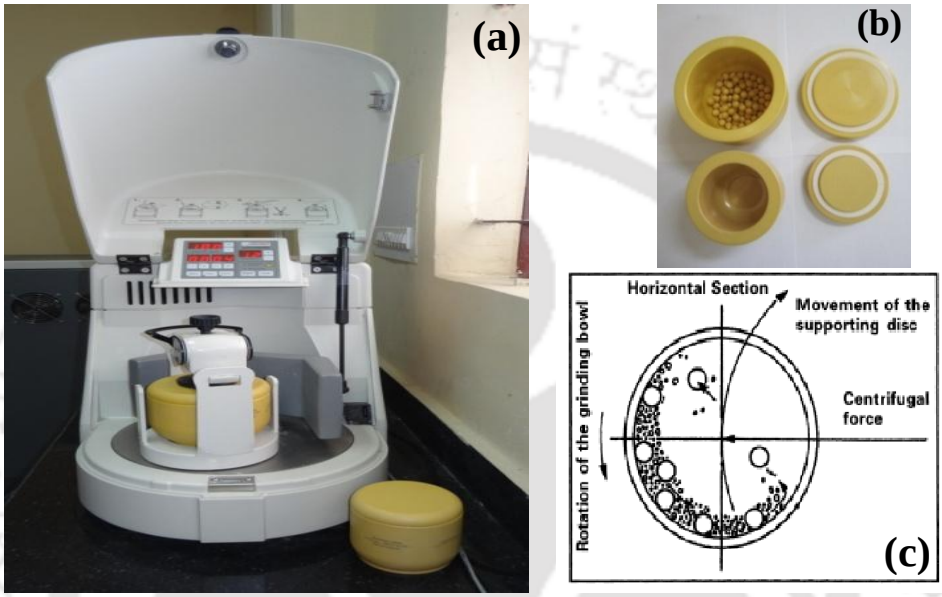

Fig. 2.1 *(a) Photographic view of planetary ball mill (b) Zirconia / tungsten carbide jars with zirconia balls and (c) Schematic view of the mechanical milling process* [6].

2.1.2 Solid state reaction method

The most realistic method of preparing ceramic powders is by solid state reaction method, as this is the simplest and cost - effectiveness method for producing bulk ceramics. However, one of the main disadvantages is the need of high processing temperatures to achieve best properties. Both thermodynamics and kinetic factors are important in solid - state reactions since solids react together only at higher temperatures. The conventional solid state reaction method employed here involves the following steps [9]: (a) powder preparation (b) high temperature calcination (c) green body preparation and (d) sintering. As each of these steps affects the final ceramic properties, they must all be understood clearly.

2.1.2.1 Powder preparation

(a) Stoichiometric weighing of reagents

The most common route is the mixed oxide route, where oxides of the constituent cations are weighed in stoichiometric proportions.

$$2MgO + TiO_2 \rightarrow Mg_2TiO_4 \quad (2.1)$$

The required ratios of the reagents as per the above chemical equation are weighed. The purity greater than 99.99%, (M/s Sigma Aldrich, USA) of the initial reagents is important to achieve phase pure compounds and to maintain reproducible microwave dielectric properties. Electronic balance (M/s Mettler Toledo, Model AG135) with accuracy up to four decimal places is used to weigh the reagents.

(b) Uniform mixing of reagents

The individual reagents are to be mixed uniformly in order to increase the point of contacts between the reagents, which will act as product layer formation centers. The mixing and milling eliminates agglomeration and reduces particle sizes. If agglomerates are present, then they densify more rapidly resulting in pores. During the mixing process, agglomerates are broken and defects are introduced into the grains that enhance the diffusion mechanism. Therefore, the initial stoichiometric reagents mixture must be mixed uniformly with a suitable mixing medium. In the present study, the mixture of constituent powders were mixed (at speed of 150 rotations per minute) using a planetary ball mill (M/s Fritsch, Pelverisette 6, Germany) for 5 - 15 hr in distilled water medium using zirconium / tungsten jar with 5 and 10 mm diameter of zirconium / tungsten balls.

2.1.2.2 Calcination

Calcination is the intermediate heat treatment of a substance below the melting or fusing point to bring about thermal decomposition or a phase transition in the physical or chemical constitution. The modifications achieved by calcination are: coarsening, decomposition, reaction and dehydration. Coarsening involves crystallite growth or fusing or bonding small particles together to produce larger particles. Decomposition involves converting compositions such as carbonates, nitrates, sulphates and acetate to a solid oxide and a gas. The parameters of calcination stage such as temperature, duration of heating and atmosphere are important factors influencing shrinkage during sintering. In the present case, the reagents being oxides do not undergo any decomposition. With the help of the X - ray diffraction pattern (XRD) of the calcinated products, the completion of reaction, desired phase formation and presence of impurity or secondary phases are identified.

2.1.2.3 Green body preparation

(a) Particle size reduction

The particle size reduction of the complex oxides after the calcination stage is important to homogenize the formed phase. It is well - known that the smaller initial particle size reduces the sintering temperature and enhances the density of the ceramics. The planetary ball mills are generally used for milling the powders to achieve particle size reduction. In the present study, planetary ball mill was employed to achieve the initial stoichiometric mixing before the calcination and to reduce the particle size of the calcined ceramic powders. Zirconia / tungsten vials and different diameters of spherical 5 and 10 mm diameter zirconia / tungsten balls are used. All the processing parameters were optimized to achieve smaller particle sizes. In the milling process, the particle experiences mechanical stresses at their contact points due to compression, shear with the milling medium or with other particles. The mechanical stress leads to elastic and inelastic deformation. If the stress is exceeding the ultimate strength of the particle, it will fracture the particles.

(b) Addition of polymeric binder

Binders are particles, which form bridges between flocculated ceramic grains. The binder allows the powder particles to slide past each other to rearrange in the closest possible packing by forming temporary bonds. Binders have strong influence on the properties of granules, such as bulk density, flow rate and compaction behaviour [10]. A good binder for ceramic applications should provide high green strength and appropriate elastic properties for handling and shaping during the post forming stage [11]. The two most popular binders for dry pressed ceramics are polyvinyl alcohol (PVA) and polyethylene glycol (PEG). The research trends suggest that 3 - 4 wt. % of PVA or PEG which are water thinnable polymeric dispersions are ideal binders for the fabrication of microwave dielectric ceramics. PVA binders generally provide high green strength while PEG binders provide high green density. PVA at low level of usage of the binder will not affect the dielectric properties as it evaporates around 400 ^{o}C.

(c) Powder compaction

After reducing the particle size of the calcined powder, the fine powder is compacted into cylindrical specimens (green pellets). The main objective is usually to achieve the greatest degree of particle packing and a high degree of homogeneity. The most common and widely used method of powder compaction is uniaxial pressing. It involves the

compaction of powder into a rigid die by applying pressure in a single axial direction through a rigid punch or piston. The press is usually mechanical or hydraulic. The compaction of the powder should be done slowly to facilitate the escape of the entrapped air. To make the green pellets of the ceramic powder, rust free rigid dies are used. To make the inner walls of the die smooth, stearic acid is used as an internal lubricant. The pressure gradient on the die as a function of the distance from the upper punch is given by the equation,

$$P_X = P_a e^{\frac{-4\mu KL}{D}} \tag{2.2}$$

where, μ is the coefficient of friction, P_a is the applied pressure, L is the length and D is the diameter of the powder compact and K is a constant [12]. It is evident that the pressure distribution of a powder compact is more uniform when length to diameter ratio is smaller. For the microwave dielectric measurements, we prepare samples with the D/L ratio ≈ 2.0 and hence the pressure distribution is quite uniform in the powder compact. Pressure of 50 - 150 MPa is more ideal for ceramic processing.

2.1.2.4 Sintering

The sintering or firing process is usually the final stage in the ceramic manufacturing. It is the process of heating a powder compact to a temperature between ½ to ¾ of the absolute melting point by which particles are formed into a coherent body to achieve higher strength and density. The criteria that should be met before sintering can occur are (1) a mechanism for material transport must be present (2) a source of energy to activate and sustain this material transport must be given. The primary mechanism for transport is diffusion and viscous flow. Heat is the primary source of energy in conjunction with energy gradients due to particle - particle contact and surface tension. Thermodynamically, sintering is an irreversible process in which a free energy decrease is brought about by a decrease in surface area. In ceramics, porosity is an important parameter, which governs many of its properties. For maximizing properties such as the dielectric constant, quality factor, mechanical strength, translucency and thermal conductivity, it is desirable to minimize porosity as low as possible. Therefore, the principal goal of sintering is the reduction of compact porosity. The development of microstructure and densification during sintering is a direct consequence of mass transport through several possible paths and one of these paths is usually predominant at

any given stage of sintering [13]. They are (i) evaporation / condensation (ii) solution / precipitation (iii) lattice diffusion and (iv) surface diffusion or grain boundary diffusion.

Sintering can occur in the presence or absence of a liquid phase. In solid state sintering, densification is achieved through changes in particle shape without particle rearrangement or the presence of the liquid. In liquid phase sintering, the compositions and firing temperatures are chosen such that some liquid is formed during processing which aids compaction.

(a) Solid state sintering

Solid state sintering is the process in which fine particles agglomerate when heated to a suitable temperature, leading to a reduction in porosity. It involves materials transport by volume diffusion. Diffusion may consist of movement of atoms or vacancies along a surface or grain boundary or through the volume of material. Surface diffusion (vapor - phase transport) does not result in shrinkage, whereas volume diffusion along grain boundaries or through lattice dislocations results in shrinkage [13]. The driving force for solid state sintering is the difference in free energy or chemical potential between the free surfaces of particles and the points of contact between adjacent particles.

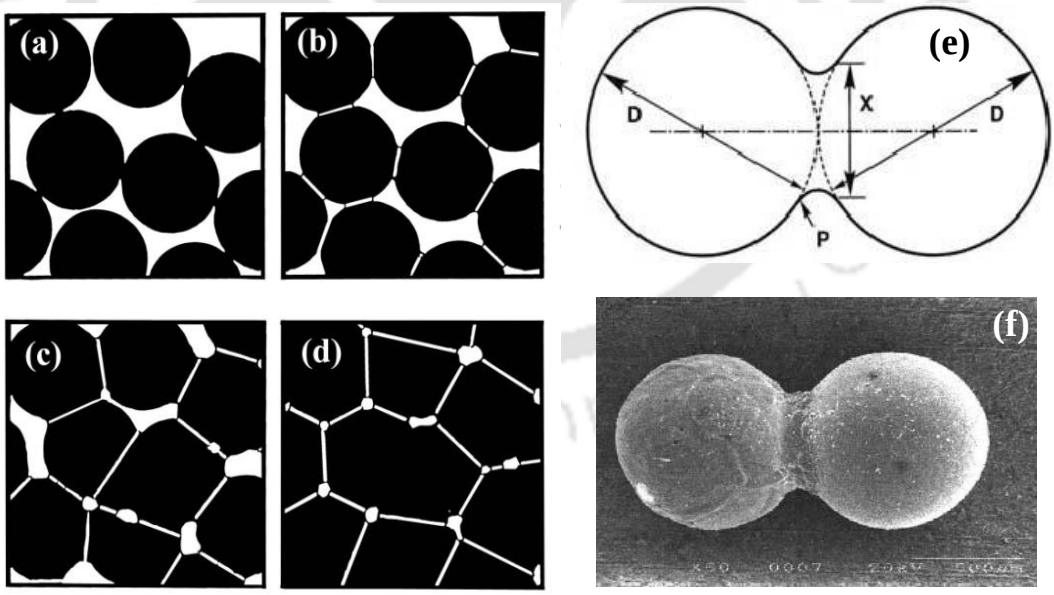

Fig. 2.2 (a - b)Initial stage, (c) Intermediate stage and (d)Final stage of sintering, (e)Neck formation during first stage and (f) SEM picture of neck formation in sintered alumina [14].

The linear shrinkage of the material caused by the lattice diffusion from line of contact between two particles to the neck region can be expressed as:

$$\frac{\Delta L}{L_o} = \left[\frac{K\gamma a^3 Dt}{kTd^n}\right] \tag{2.3}$$

where $\Delta L/L_o$ is linear shrinkage (equivalent to the sintering rate); γ is surface energy; a^3 is atomic volume of the diffusing vacancy; D is self - diffusion coefficient; k is Boltzmann constant; T is temperature; d is particle diameter; t is time and K is a constant dependent on geometry. The exponent n is close to 3. But from Eq. (2.2) it can be clearly understood that the particle diameter has a major effect on the rate of sintering. Hence, the smaller the particles, greater is the sintering rate. Therefore, finer sized particles can be sintered more rapidly at a lower temperature than coarser powder. There are three major stages in sintering as shown in Fig.2.2.

Initial stage of sintering: In the initial stage, there is a rearrangement of surface smoothening of the particles, neck growth and rounding of interconnected open pores (Fig. 2.2 (e)). The rearrangement consists of slight movement or rotation of adjacent particles to increase the number of points of contact. Bonding occurs at the points of contact where materials transport can happen and surface energy is highest. During this stage, the porosity decreases by about 12 % and the initial density of the green ceramics is around 60 %. After the initial stage, the density will be around 70% of theoretical density. However, in the initial stage, the 10 % densification spreads quickly in few minutes after reaching to higher sintering temperature due to large surface area and high driving force for sintering [15]. Fig. 2.2 (*f*) depicts the SEM micrograph of neck formation in sintered alumina.

Intermediate stage of sintering: The second stage of sintering is referred to as intermediate sintering. In the intermediate stage, there is a formation of neck growth as densification proceeds and particle centers approach one another resulting in further shrinkage of the compact. The grain boundaries begin to move so that one grain begins to grow while the adjacent grain is consumed. Intermediate sintering continues as long as pore channels are interconnected and ends when pores become isolated. Most of the shrinkage during sintering occurs in this stage. The shrinkage in this stage can result in about 90 % of theoretical density.

Final stage of sintering: In the final stage of sintering, isolated pores are eliminated by mass transport from the grain boundary at the pore and the uniform grain growth takes place. Pore on a grain boundary gets eliminated by grain boundary or lattice diffusion, but

pores within the grains can be eliminated by lattice diffusion only. This creates a problem, since volume diffusion often has higher activation energy. The complete elimination of porosity in the final stage of sintering can at most happen when all openings are connected to fast and short diffusion paths along the grain boundaries. In most ceramics, the lattice diffusivity of the slower rate limiting constituent is eventually too slow for effective annihilation of pores that got trapped in grains. Therefore, to achieve higher densities, the elimination of pores attached at the grain boundary is important. The final stage sintering begins at about 93 - 95 % of theoretical density, when porosity is already isolated. Ideally, at the end of this stage all porosity must be eliminated.

Solid state sintering involves movement of atoms that in turn is dependent on temperature and concentration of structural imperfections such as vacancies and interstitials. The process variables in sintering are (a) sintering temperature (b) sintering time (c) sintering atmosphere. The factors affecting solid state sintering are (a) particle size and particle size distribution (b) particle shape (c) uniformity of green microstructure (d) particle composition and (e) green density [15]. Solid state sintering of mixed cation oxides that are used in DRs is an ambipolar diffusion process in which anions and cations must be transported from the source to sink without kinetic de - mixing. The rate limiting mechanism will be slowest moving species along the fast path. Therefore, the rate of sintering depends on the diffusivities and additives that influence diffusion. Additives often help to decrease the rate of coarsening in the earlier stages of sintering, increase the rate of densification and decrease the rate of grain growth.

Recrystallization and grain growth

In general, two types of recrystallization processes occur: primary and secondary recrystallization processes. Primary recrystallization is the process by which nucleation and growth of a new generation of strain - free grains occur in a matrix which has been plastically deformed [16]. Grain growth is the process by which the average grain size of the strain released or nearly strain free material increases continuously during heat treatment without change in the grain size distribution. Secondary recrystallization, sometimes called abnormal or discontinuous grain growth, is the process by which a few large grains are nucleated and enlarge at the expanse of fine grained, but essentially strain free matrix.

Primary recrystallization process has its driving force in the increased energy of a matrix which has been plastically deformed. If the isothermal change in grain size of

strain free crystals in a deformed matrix is measured after an initial induction period, there is a constant rate of grain growth for the new strain free grains. If the grain size is *d* [16], then

$$d = U(t - t_0) \tag{2.4}$$

where *U* is the growth rate (cm / sec), *t* is the time and t_o is the induction period. The induction period corresponds to the time required for unstable embryos present to grow to the size of a stable nucleus. For a nucleus to be steady, its size must be larger than some critical diameter at which the lowered free energy of the new grain is equal to the increased surface free energy. If an unlimited number of sites are available, the rate of nucleation increases to some constant rate after an initial induction period. As the temperature increases, the rate of nucleation increases exponentially.

The growth rate remains constant until the grains begin to impinge on one another. The growth rate becoming constant results from the constant driving force. The final grain size is determined by the number of nuclei formed, i.e., the number of grains presents when they finally impinge on one another. Since both the nucleation and growth rate are strongly temperature dependent, the overall recrystallization changes quickly with temperature. With increasing temperature, the final grain size is larger, due to the increased growth rate. However, at higher temperatures, recrystallization is completed more rapidly so that the greater grain size observed can be due to the greater time available for grain growth following the recrystallization [16].

In general, it is observed that (1) some minimum deformation is required for recrystallization, (2) with the small degree of deformation a higher temperature is required for recrystallization to occur, (3) an increased annealing time lowers the temperature of recrystallization and (4) the final grain size depends on the degree of deformation, the initial grain size and the temperature of recrystallization. In addition, continued heat after the completion of recrystallization leads to the prolongation of grain growth [16].

Grain growth

Whether or not primary recrystallization occurs, an aggregate of fine - grained crystals increases in average grain size when heated at elevated temperatures. As the grain size increases, it is obvious that some grains must shrink and disappear. An equivalent way of looking at grain growth is the rate of disappearance of small grains. Subsequently, the

driving force for the process is the difference in energy between the fine - grained material and the larger grain size product resulting from the decrease in grain boundary area and the total boundary energy [16].

(b) Liquid phase sintering

Liquid phase sintering (LPS) is a sub - class of the sintering process, which involves the presence of viscous liquid during the sintering process. The major advantages of LPS over solid state sintering that has enhanced sintering kinetics to tailor the microstructure and density. The disadvantages of LPS are that ceramics densified by this technique has a susceptibility to shape deformation and it may be difficult to control the sintering parameters due to additional complications from the liquid phase. In order to attain the densification by LPS certain criteria [14, 16] must be satisfied: (i) a liquid must be present at the sintering temperature (ii) good wetting of the liquid on solid or the contact angle must be low, (iii) there must be appreciable solubility of solid in liquid. The presence of a liquid phase greatly enhances grain boundary diffusion and grain boundary sliding. When solids and liquids are present together, capillary forces that result from the surface tension are generated. These forces can give rise to strong attractive forces between neighbouring particles and lead to very rapid and significant particle rearrangement and densification. Upon melting, a wetting liquid will penetrate between grains and exert an attractive force, pulling them together.

When liquid coats at each grain, the material shows higher density at lower temperatures with a less tendency for exaggerated grain growth. If the liquid is distributed uniformly and the grain size is about 1 μm, one needs less than one volume percentage liquid phase to coat the grains. The wetting liquid concentrates at the particle contacts and forms a meniscus, which exerts an effective compressive pressure on the compact. There is a rapid rearrangement of particles into higher density configuration. After the initial rearrangements, further densification takes place as particle contacts flatten under the compressive stress applied to the point contacts by capillary pressure. The contact flattening occurs through dissolution at the particle contacts and transport of the materials towards stress free interfaces. This leads to appreciable grain growth compared to solid state sintering.

2.1.3 High temperature sintering furnace

High temperature furnaces were used for the sintering of the samples to obtain highly densified materials and to optimize desired dielectric properties. In the present study,

commercial high temperature sintering furnace (M/s Lenton, UAF 16/5, UK) with the maximum operating temperature of 1650 ^{o}C was used to sinter the samples. All the MTO based samples were sintered within the given temperature for 3 - 4 hr with heating and cooling rates of 10 ^{o}C/min and 2 ^{o}C/min, respectively. To control the set temperature (the heating rate and time duration of heating at a particular temperature), the furnace is connected to programmable controller. The insulated door opens upwards and outwards keeping the hot face insulation away from the operator. The photograph of high temperature sintering furnace being used to prepare the samples is shown in Fig. 2.3.

Fig. 2.3 *Photographic view of high temperature sintering furnace.*

2.2 Characterization Techniques

Experimental tools are the backbone of an experimentalist. Therefore, it is essential to understand the mechanism and operational details of equipment to extract best experimental data. Several experimental tools are used to study the characteristic properties of the different samples. Crystal structure of the samples was analyzed using X - ray diffractometer (Rigaku, TTRAX III, 18 kW) XRD with Cu-Kα (λ = 1.5406 Å) radiation. Morphological and microstructural characterizations were performed by scanning electron microscope (SEM, Leo 1430VP), field - emission scanning electron microscopy (FE - SEM, ΣIGMA - ZEISS), Atomic force microscopy (AFM, Agilent, Model: 5500) and transmission electron microscopy (TEM, JEOL, Model: JEM 2100) techniques. These studies help to learn about the crystal structure, surface morphology and microstructure of the samples. For optical characterizations, UV- Visible - near infrared (UV -Vis - NIR) optical absorption and steady state photoluminescence (PL)

techniques are used. The thermal decomposition behaviour of the dried powder was examined by a thermogravimetric analyser (TGA, NETZSCH, STA 449- F3, Jupiter) and a differential scanning calorimeter (DSC, NETZSCH, STA 449- F3, Jupiter) at a heating rate of 10 ^{o}C/min in argon atmosphere. The dielectric properties of the samples were analyzed using Vector Network Analyzer (VNA, Rohde and Schwarz, Model no: ZVA24) and Impedance analyzer (Agilent E 4991A equipped with BDS 2200, 2300, Concept 7, M/s Novocontrol (GMbH).

2.2.1 X - ray diffraction

XRD is a versatile and non - destructive technique revealing detailed information about the crystallographic structure of materials. XRD results from the scattering of X - rays by the atomic arrangement. Depending on the atomic arrangement, interference between the scattered rays is constructive when the path difference between two diffracted rays differs by an integral number of wavelengths. This is described by the Bragg's equation (Bragg's law):

$$2d\sin\theta = n\lambda \tag{2.5}$$

where λ is the wavelength, d is the spacing between the planes and θ is the Bragg angle [17]. The instrument is based on the Bragg - Brentano geometry as shown in Fig. 2.4. In this geometry, the source to sample distance and the sample to detector distance are kept equal. A Perspex sheet with rectangular groove was used for sample mount, where the powder sample was filled uniformly in the groove.

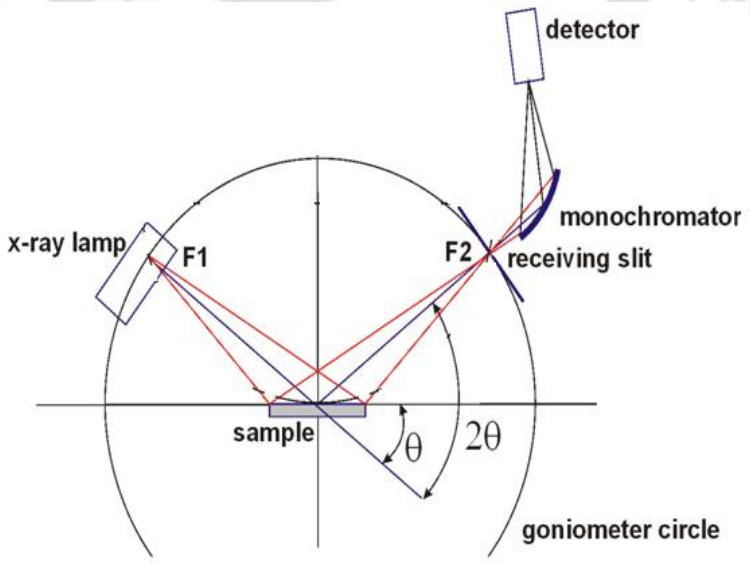

***Fig. 2.4**: Schematic ray diagram of X - ray diffractometer [17].*

Fig.2.5. *Photograph of the X-ray diffractometer (Rigaku RINT 2500, TTRAX III).*

In the present work, two types of X-ray diffractometers were used to characterize the samples. One is Seifert X-ray diffractometer with Cu-Kα (λ = 1.5406 Å) radiation operating at 40 kV and 30 mA (1.2 kW). The other one is Rigaku (TTRAX III, 18 kW) XRD with Cu-Kα (λ = 1.5406 Å) radiation. A photographic view of the XRD instrument (Rigaku) used in the present study is shown in Fig. 2.5. The scanning step size was 0.01°. Calibration using a Si standard was done to account for the instrumental line broadening and the value was approximately 0.005^o. The exact peak position and full-width at half maximum (FWHM) of the XRD peak is obtained from the Lorentzian fitting to the experimental data, using following expression,

$$y = y_o + \frac{2A}{\pi}\frac{w}{4(x-x_c)^2 + x^2} \tag{2.6}$$

where y_o is the offset constant, x_c, w and A are the peak position, FWHM and area, respectively. FWHM gives the average crystallite size (using Scherrer's formula [18]) and lattice strain is calculated from the shift in x_c using Williamson's – Hall plot method [19].

The XRD patterns were also analyzed with the help of Reitveld refinement method using Fullprof program [20]. The background was refined using a polynomial function. Pseudo -Voigt function was chosen for peak shape. The global parameters, such as coefficients of background polynomial, scaling factor, half width parameters (u, v, w) and

lattice parameters (*a, b, c*) were mainly varied during the refinement. In addition to that nuclear structure variables such as fractional atomic co - ordinates (*x, y, z*), isotropic displacement (temperature) parameters and occupancy values were varied. Here, occupancy is the chemical occupancy normalized to the multiplicity of the general position of the group. The occupancy of oxygen was taken as 1 for all the refinements and it was not varied during the refinement. The quality of the refinements are known based on the values of reliability factors such as, R_p, R_{wp}, R_{exp}, R_{Bragg}, R_F and χ^2, which are defined as follows:

$$\text{Profile factor, } R_p = 100\frac{\sum_{i=1,n}\left|y_i - y_{c,i}\right|}{\sum_{i=1,n} y_i} \tag{2.7}$$

Here, y_i is the observed point (experimental) and $y_{c,i}$ is the calculated point and n represents the number of data points.

$$\text{Weighted profile factor, } R_{wp} = 100\left[\frac{\sum_{i=1,n}\omega_i\left|y_i - y_{c,i}\right|^2}{\sum_{i=1,n}\omega_i y_i^2}\right]^{1/2} \tag{2.8}$$

Here, $\omega_i = \frac{1}{\sigma_i^2}$, σ_i^2 is the variance of observation y_i.

$$\text{Expected weight factor, } R_{\exp} = 100\left[\frac{n-p}{\sum_{i=1,n}\omega_i y_i^2}\right]^{1/2} \tag{2.9}$$

where $(n - p)$ is the number of degrees of freedom. n is the total number of experimental points and p is the number of refined parameters.

$$\text{Reduced chi - square, } \chi^2 = \left[\frac{R_{wp}}{R_{\exp}}\right]^2 \tag{2.10}$$

$$\text{Bragg factor, } R_B = 100\frac{\sum_h\left|I_{obs,h} - I_{calc,h}\right|}{\sum_h I_{obs,h}} \tag{2.11}$$

Here, h is the vector which levels the Bragg reflections. $I_{obs,h}$ is the observed integrated intensity and $I_{calc,h}$ is the calculated intensity.

$$\text{Crystallographic } R_F \text{ factor, } \quad R_F = 100\frac{\sum_h\left|F_{obs,h} - F_{calc,h}\right|}{\sum_h F_{obs,h}} \tag{2.12}$$

where, $F_{obs,h}$ and $F_{calc,h}$ are the observed and calculated structural factors respectively. Inter atomic distances (bond length) and bond angles were calculated using the refined fractional coordinates and lattice parameters by using Fullprof software.

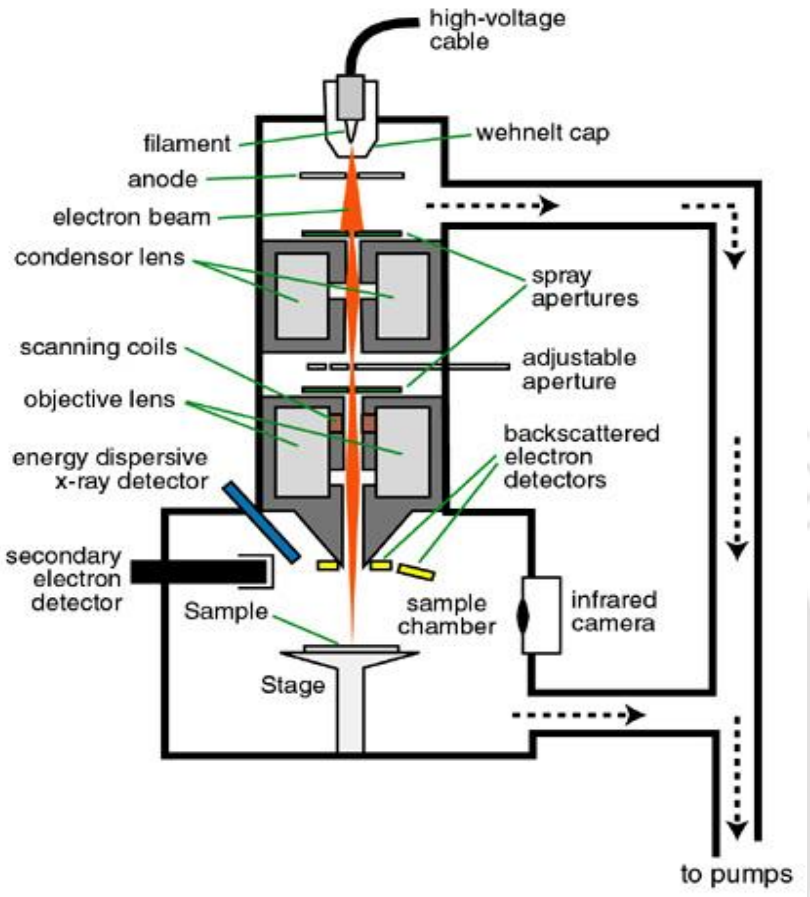

Fig. 2.6 *Schematic view of scanning electron microscopy.*

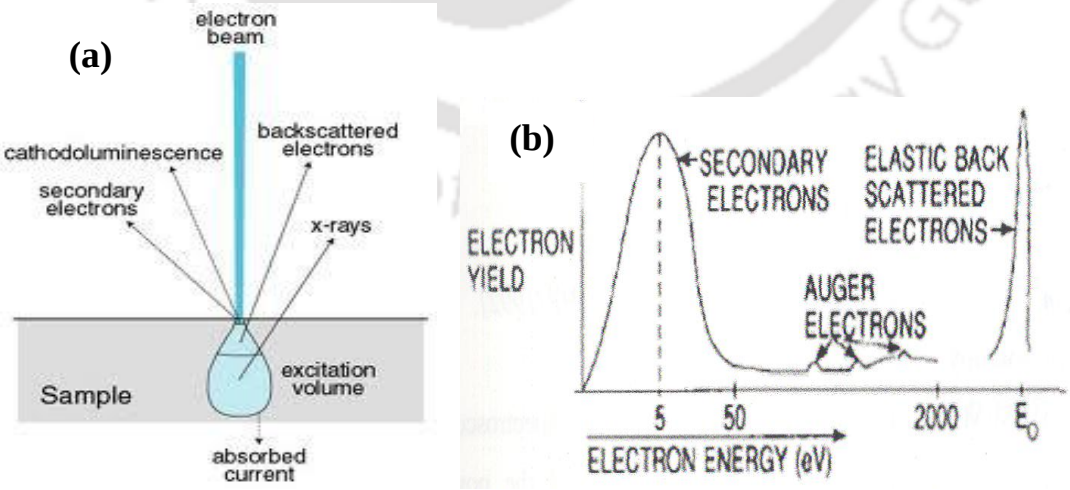

Fig. 2.7 *(a) Electron and photons signals emanating from tear shaped interaction volume during electron beam impingement on specimen surface and (b) Energy spectrum of electrons emitted from the specimen surface.*

2.2.2 Scanning electron microscopy

In the present thesis work all the microstructural images and compositional analysis of the MTO based samples have been carried out by using SEM equipped with Oxford energy dispersive spectrometer (EDS). Basic principles of SEM and EDS analysis are given briefly.

SEM is a type of electron microscope that uses electrons to form an image of objects and to study surface morphology, fractured components, foreign particles, residues, etc. The schematic view of SEM is shown in Fig. 2.6**.** The thermionically emitted electrons from a tungsten filament are drawn towards anode and focused by two successive condenser lenses into a beam with a narrow spot size (~50 Å). The shorter wavelength of electrons permits image magnifications of up to 1,00, 000 times in SEM. Pair of scanning coils located at the objective lens deflect the beam either linearly or in raster fashion over a rectangular area of specimen surface. These primary bombarding electrons on the surface of the specimen dislodge electrons from the specimen. Fig. 2.7 shows the interaction of electrons with the surface of the sample. Upon electron impingement on the surface, the interaction volume assumes a tear drop shape. The electrons dislodged from the surface of the specimen are known as secondary electrons, which are attracted and collected by a positively biased grid or detector, and then translated into signals. These signals are then amplified, analyzed, and translated into images of the topography being inspected.

Apart from secondary electrons, the back scattered electrons (BSE), characteristic X -rays, light (cathode - luminescence), specimen current and transmitted electrons are produced by SEM. These types of signal require specialized detectors. The primary electron beam results in the emission of BSE from the specimen. BSE possess more energy than secondary electrons and have a definite direction. All emissions above 50 eV are considered to be BSE. BSE imaging is useful in distinguishing one material from another, since the yield of the collected BSE increases monotonically with the specimen's atomic number Z (~ 0.05 $Z^{1/2}$). Backscattered imaging can distinguish elements with atomic number difference of at least three. Energy dispersive X - ray spectroscopy (EDS, or EDAX) is an analytical technique used for the elemental analysis or chemical characterization of a sample. Its characterization capabilities originate from the fact that each element has a unique atomic structure, which emits its unique characteristic X - ray. To stimulate the emission of characteristic X - rays from a specimen, a high energy beam

of charged particles such as electrons or protons or a beam of X - rays is focused into the sample being studied. At rest, an atom within the sample contains ground state (or unexcited) electrons in discrete energy levels or electron shells bound to the nucleus. The incident beam may excite and eject an electron from an inner shell and it results in an electron vacancy in the shell. An electron from an outer higher energy shell then fills the vacancy and the difference in energy between the higher energy shell and the lower energy shell is released in the form of an X - ray. The atoms of every element release X - rays with unique amounts of energy during the above process. Thus, we get the EDS spectrum describing how frequently an X - rays is received for each energy level. An EDS spectrum normally displays peaks corresponding to the energy levels for which the X -rays had been received. Each of these peaks is unique to an atom, and therefore corresponds to a single element. The intensity of the peaks depends on the concentration of the elements present.

Fig. 2.8: *Photographic view of the field emission scanning electron microscopy.*

2.2.3 Field-emission scanning electron microscopy

FE-SEM is used to visualize very small topographic details on the surface of densified samples or fractioned objects. Researchers in biology, chemistry and physics apply this technique to observe structures in the range of 1 to 10 nm. In the present thesis work ZEISS made FE-SEM (ΣIGMA) was used to study the surface morphology of

nanocrystalline samples. The resolution of this FE - SEM is 1.3 nm at 50 kV and 2.8 nm at 1 kV. A photographic view of the FE - SEM (M/s Sigma Zeiss, Germany) used in the present study is shown in Fig. 2.8**.**

Field-emission (FE) is an emission of electrons induced by external electromagnetic fields. FE can happen due to the promotion of electrons, from the valence to the conduction band of semiconductors. The related effect is cold electronic emission, i.e., the emission of electrons in strong static (or quasi - static) electric fields. The electron gun is basically a zirconium oxide coated tungsten (ZrO_2 / W) emitter, which operates in a thermally assisted Schottky emission mode. This type of gun provides narrower probing beams as well as high electron energy resulting in both improved spatial resolution and minimized sample charging and damage. Electrons are liberated from a field emission source and accelerated in a high electrical field gradient. Within the high vacuum column, these so called primary electrons are focused and deflected by electronic lenses to produce a narrow scan beam that bombards the object. As a result, secondary electrons are emitted from each spot on the object. The angle and velocity of these secondary electrons depend on the surface structure of the object. A high efficient annular in - lens ac - detector catches the secondary electrons and produces an electronic signal. One more detector, i.e., solid state back scattered detector is used to detect the BSE.

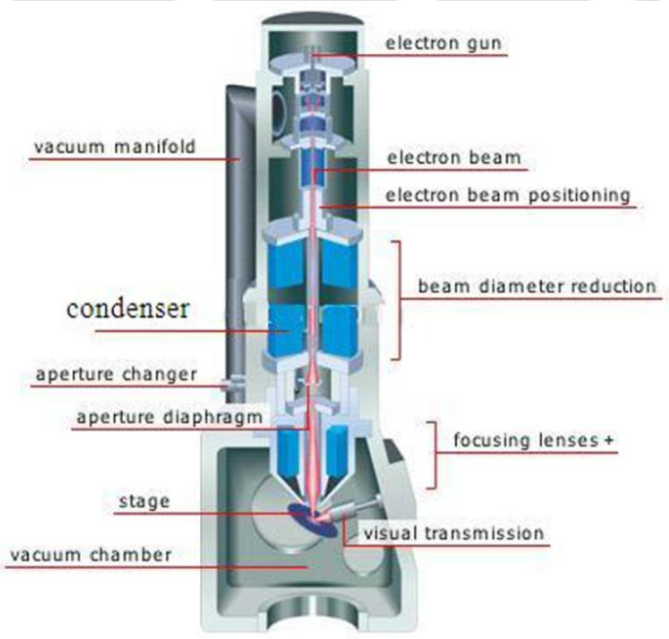

Fig. 2.9: *Schematic diagram of transmission electron microscopy.*

The advantages of FE - SEM over SEM are as follows, (1) FE - SEM produces clearer, less electrostatically distorted images with spatial resolution down to 1 nm. This

is nearly 3 to 6 times better than conventional SEM; (2) Smaller area contamination spots can be examined at electron accelerating voltages compatible with Energy Dispersive X - ray Spectroscopy; (3) Closer to the immediate material surface can be probed due to the reduced penetration of low kinetic energy electrons; (4) High quality, low voltage images are obtained with negligible electrical charging of samples. (Accelerating voltages range from 0.5 to 30 kV).

In order to observe FE - SEM for objects, the sample needs to be coated if it is electrically non - conducting. This can be done by coating them with an extremely thin layer (1.5 - 3.0 nm) of gold or carbon by using respective coater. However, in the present thesis work, the samples were electrically non - conducting and a thin layer of gold was coated over the samples before mounting for the FE - SEM observation.

2.2.4. Transmission electron microscopy

Characterization of nanocrystalline microstructure has been carried out by using TEM. Fig. 2.9 shows the schematic diagram of TEM. Thermionically emitted electrons from the gun are accelerated to 100 keV or higher and are first projected onto the specimen by means of the condenser lens system. The scattering process experienced by these primary electrons during their passage through the specimen determines the kind of information obtained. Elastic scattering, involving no energy loss, when electrons interact with the potential field of the ion core, gives rise to diffraction patterns. Inelastic interactions between beam and matrix electrons at heterogeneities such as grain boundaries, dislocations, secondary phase particles, defects, density variations, etc., cause complex absorption and scattering effects, leading to a spatial variation in the intensity of the transmitted beam. Images can be formed in a number of ways. The bright field image is obtained by intentionally excluding all diffracted beams and only allowing the central beam passing through the specimen. This is done by placing suitably sized apertures in the back focal plane of the objective lens. Intermediate and projection lenses then magnify this central beam. Dark field images are also formed by magnifying a single beam; here one of the diffracted beams is chosen by means of an aperture that blocks the central beam and the other diffracted beams. By selected area (electron) diffraction, abbreviated as SAD (SAED), ring like structure is imaged, which corresponds to the particular plane of that element or compound. If only diffused rings appear then the system must have single amorphous phase. In the present investigation, SAD pattern has been employed to identify the crystalline nature of the mechanically alloyed MTO

samples. Further, high resolution TEM study was applied to analyze the lattice fringes of the milled samples.

2.2.5. Thermogravimetric analysis

Thermogravimetric analysis (TGA) is a technique measuring the weight of the substance in an environment heated or cooled at a controlled rate and is recorded as function of time or temperature. Thus, the basic requirements for the measurement are a heating / cooling set up and a means of weighing. The TGA curve gives the information about [21]: (a) The thermal stability of the material, (b) The procedural decomposition temperature i.e., the lowest temperature at which the cumulative mass change reaches a magnitude that the thermo balance can detect and (c) The temperature at which the reaction is complete and the reaction interval.

2.2.6 Differential scanning calorimetry

Differential scanning calorimetry (DSC) is a thermal technique in which differences in heat flow into a substance and a reference are measured as a function of sample temperature. Both the samples are subjected to a controlled temperature program and maintained a nearly same temperature throughout the experiment. The basic principle is that when the sample undergoes a physical transformation such as phase transitions, more (or less) heat will need to flow to it than the reference to maintain both at the same temperature. Whether more or less heat must flow to the sample depends on the types of the process: exothermic or endothermic. Differential scanning calorimetry can be used to measure a number of characteristic properties of a sample like fusion, crystallization events and glass transition temperatures (T_g), oxidation and other chemical reactions [21]. In the present investigation, DSC is used to determine the melting and crystallization temperature of the dried MTO ceramic powders.

2.2.7. Density measurement

The densities of the sintered samples were measured by Archimedes setup along with weighing machine. According to Archimedes principle, when a body is immersed partially or fully in a fluid, it experiences an upward force (buoyant force) which is equal to the weight of the liquid displaced by it. The relative densities of the sintered pellets calculated using the following expression:

$$\rho_a = \left(\frac{w_1}{w_2 - w_3} \right) \times \rho_w \text{ gm/cm}^3 \qquad (2.13)$$

where, w_1 is the weight of the sintered pellet in air, w_2 is the weight of the sintered pellet immersed in liquid medium (distilled water), w_3 is the weight of the sintered pellet after removed from liquid medium (distilled water) and ρ_w density of liquid medium (water =1 gm / cm^3). The relative densities of sintered pellets were calculated using the formula:

$$\text{Relative density} = \frac{\rho_a}{\text{theoretical density}} \tag{2.14}$$

2.2.8 Microwave characterization

The increasing demand for the development of high - speed, high frequency devices require a complete understanding of the properties of materials functioning at microwave frequencies [22]. In general, the microwave methods for materials characterization fall into two categories: non - resonant methods and resonant methods. Non - resonant methods are often used to obtain a general knowledge of electromagnetic properties over a wide frequency range, while resonant methods are used for low loss dielectric materials to get accurate knowledge of dielectric properties at a single microwave frequency or at several discrete microwave frequencies [23]. The presence of air gaps is one of the most important factors limiting the measurement accuracy of high permittivity solid materials, unless the electric field of the mode of interest does not have a component perpendicular to the surfaces of the sample. This is the situation for TE_{0np} modes of cylindrical cavities and dielectric resonators. Therefore, methods employing these modes are considered to be among the most accurate [24]. The quasi -$TE_{01\delta}$ mode of operation (often called the TE_{011} - mode) is the mode most commonly used by manufacturers of dielectric materials for making dielectric loss tangent measurements.

The important characteristics of a dielectric resonator (DR) are dielectric constant, loss tangent and temperature dependence of resonant frequency. The permeability of most of these materials is equal to that of free space, as they are nonmagnetic materials. A parallel plate dielectric resonator structure known as Courtney set up is used to measure the dielectric constant of the bulk dielectric material. The principle involved in the measurement is rather simple. The resonant frequency of a $TE_{01\delta}$ mode is measured for a dielectric resonator radius '*a*' and height '*L*'. Afterwards, the dielectric constant is computed using the Courtney procedure [24]. Hakki and Coleman first introduced the procedure. The error analysis and investigation of temperature effects were later made by Courtney [25]. Another cylindrical cavity made of invar is used to measure the

temperature coefficient of resonant frequency of the cylindrical DR. The negligible coefficient of thermal expansion of invar material helps to increase the accuracy of this measurement.

2.2.8.1 Vector network analyzer

In microwave engineering, Network Analyser is a major instrument used to investigate a wide variety of materials, components, circuits and systems. A measurement of the reflection from and / or transmission through a material along with knowledge of its physical dimensions provides the information to characterize the permittivity and permeability of the material. Network Analyser is a swept frequency measurement equipment to completely characterize the complex network parameters in comparatively less time without any degradation in accuracy and precision. Two types of network analysers are available: scalar and vector network analysers. Scalar network analyser measures only the magnitude of reflection and transmission coefficients while the vector network analyser measures both the magnitude and phase. Note that magnitude and phase of a component can be critical to the performance of a communication system. A vector network analyser can provide information on a wide range of these devices, i.e., from active devices such as amplifiers and transistors to passive devices such as capacitors and filters.

A basic network analyser is designed to show graphically a plot of the voltage gain or loss of a network versus frequency. The network analyser measures the magnitude, phase and group delay of two - port networks to characterize their linear behaviour. A vector network analyser consists of a signal source, a receiver and a display. The source launches a signal at a single frequency to the material under test. The receiver is tuned to that frequency to detect the reflected and transmitted signals from the material. The measured response produces the magnitude and phase data at that frequency. The source is then stepped to the next frequency and the measurement is repeated to display the reflection and transmission measurement response as a function of frequency. The ratio of the output to the input level is displayed as dB which is the voltage gain or loss of the network.

Consider a circular cylindrical rod of relative dielectric constant ε_r, permeability μ_0, length L, and radius a placed between two large perfectly conducting plates. If the dielectric material is isotropic, then the characteristic equation for this resonant structure operating in the TE_{0nl} mode is

$$\alpha \frac{J_0(\alpha)}{J_1(\alpha)} = -\beta \frac{K_0(\beta)}{K_1(\beta)} \tag{2.15}$$

where $J_0(\alpha)$ and $J_1(\alpha)$ are the Bessel functions of the first kind of orders zero and one, respectively, $K_0(\beta)$ and $K_1(\beta)$ are the modified Bessel functions of the second kind of orders zero and one, respectively. The parameters α and β depend on the geometry, the resonant wavelength and dielectric properties. Thus,

$$\alpha = \frac{2\pi a}{\lambda_0}\left[\varepsilon_r - \left[\frac{c}{\nu_p}\right]^2\right]^{1/2} \tag{2.16}$$

$$\beta = \frac{2\pi a}{\lambda_0}\left[\left(\frac{c}{\nu_p}\right)^2 - 1\right]^{1/2} \tag{2.17}$$

c is the velocity of light and ν_p the phase velocity in the structure so that

$$\frac{c}{\nu_p} = \left(\frac{l\lambda_0}{2L}\right) \tag{2.18}$$

where l is the number of longitudinal variations of the field along the axis, L is Length of the DR, D is Diameter of the DR, λ_0 is free space resonant wavelength. It is seen that the characteristic equation is a transcendental equation and hence, a graphical solution is necessary. The resulting mode charts are given by Hakki et al. [24] where each value of β_l corresponds α_n. The characteristics equation and the resulting charts are universal as per as permittivity concerned.

In the present investigation, a vector network analyzer (VNA, Rohde & Schwarz, Model no: ZVA24) was used for the measurement of microwave dielectric properties of MTO ceramics.

2.2.8.2 Measurement of dielectric constant (ε_r)

This can be done by using transmission method introduced by Hakki and Coleman and modified by Courtney [25]. This setup is having two parallel plates with an adjustment for varying distance between the two plates. Two bent monopoles (rigid coaxial cables) are provided for coupling electromagnetic waves to the DR and are suitably mounted to move in any of the *x*, *y* and *z* directions. One can identify the modes of the DR by moving the bent monopoles in all three directions. The number of standing waves in *z* - directions indicates the third subscript of resonant mode. By rotating the rigid coaxial cables around

its own axis, it is possible to find the maximum field in horizontal direction or vertical direction. Subsequently, the first subscript can be found by placing the coaxial cable at different angles in the plane of parallel plates. Once the resonant frequency of $TE_{01\delta}$ mode is measured, the relative dielectric constant for the dielectric resonator with known dimensions can be calculated using the equations (2.19) and (2.20).

$$\beta_l = \frac{2\pi a}{\lambda_0}\left[\left(\frac{l\lambda_0}{2L}\right)^2 - 1\right]^{\frac{1}{2}} \tag{2.19}$$

$$\varepsilon = \left(\frac{\alpha_n \lambda_0}{2\pi a}\right)^2 + \left(\frac{l\lambda_0}{2L}\right)^2 \tag{2.20}$$

where β_l corresponds to α_n, which can be obtained from the mode chart given in [25] one of the characteristic equation.

2.2.8.3 Measurement of unloaded quality factor (Q_u)

To measure the *Q* factor of microwave resonators, various methods are applied [27-29]. However, all the methods do not consider practical effects produced by a real measurement system such as noise, crosstalk, coupling losses, transmission line delay and impedance mismatch. Inadequate accounting of these effects may lead to significant uncertainty in the measured *Q* factor of the DR.

The *Q* factor measured for the DR under end shorted condition using parallel plate resonant method is very low, since the losses occur due to conducting plates, radiation etc. Therefore, to reduce these effects, in our present study, we have used a transmission mode cavity proposed by Krupka et al. [23] to measure unloaded quality factor of the DR. This measurement is done using reflection method by placing the sample over a low loss quartz spacer with height 4 mm inside a cylindrical copper cavity having 10 mm height and 24 mm diameter (inner dimensions). The inner side of the cavity was finely polished and silver plated to reduce radiation loss. The use of low loss single quartz spacer reduces the effect of losses due to the surface resistivity of the cavity. Samples with diameter / length (D/ L) ratio of 1.8 – 2.2 are preferable to get maximum mode separation and to avoid interferences from other modes. Microwaves are fed into the sample using the loop coaxial antennas, which provides a magnetic coupling to excite the transmission mode resonance spectrum of dielectric cylinder. The rigid coaxial cable is provided at the center of the cavity (as shown in Fig. 2.10 (a)) for electromagnetic field coupling and it can be moved in and out for adjusting between weak and strong coupling.

The cavity is connected to the VNA through a rigid coaxial cable with connectors on both the ends (THRU). The network analyzer is set in S_{21} mode and performs calibration. The coaxial cable is adjusted in such a way that weak coupling exists between the rigid coaxial cable and DR. By identifying the $TE_{01\delta}$ mode, the resonant frequency can be obtained. The 3 dB bandwidth of the spectrum to calculate loaded *Q* factor (Q_l), from the resonance spectrum (Fig. 2.10 (b)) is given by,

$$Q_l = \frac{f_0}{\Delta f} \tag{2.21}$$

One can assume that the unloaded *Q* factor is equal to loaded *Q* factor if coupling is weak (S_{21} at resonance < 45 dB, and couplings are symmetric). The unloaded Q_u value is calculated using the coupling coefficient β_c, and loaded Q_l value using the relation [30],

$$Q_u = \frac{Q_l}{(1-\beta_c)} \tag{2.22}$$

where β_c is the coupling coefficient is equal to $10^{\frac{-S_{21}}{20}}$. Further rigorous electromagnetic analysis must be performed to evaluate the dielectric constant of the sample under test. Rayleigh - Ritz's method has been used in the computer program for calculating the dielectric constant.

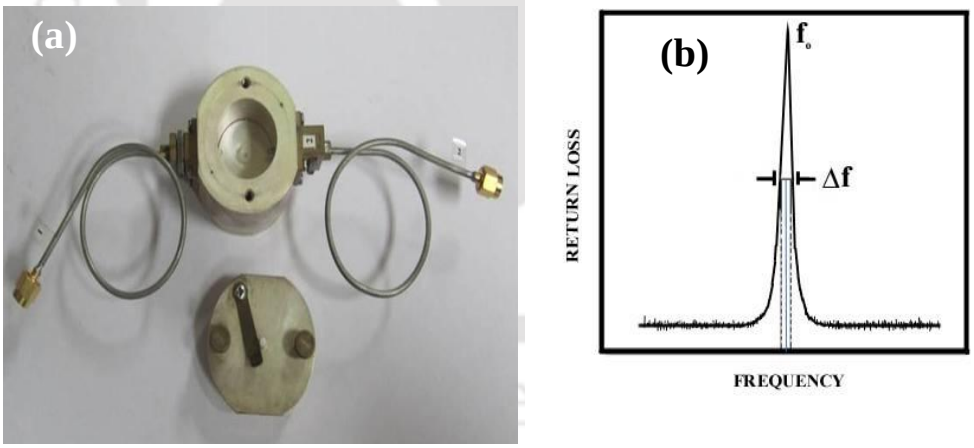

Fig. 2.10: (a) *QWED Krupka resonator cavity used to measure the Q- factor and dielectric constant (b) the method of calculating Q- factor from resonant mode using Eq. 2.21.*

2.2.8.4 Measurement of temperature coefficient of resonant frequency (τ_f)

The temperature coefficient resonant frequency (τ_f) is an important parameter to determine the performance of the device. Since the resonators are used in communication systems, temperature stability is an important factor and should nearly be zero.

The temperature dependent resonant frequency can be measured using the cavity made up of invar material having least thermal expansion coefficient. The cavity is kept on a hot plate and the entire system is insulated in an isothermal enclosure. The setup is then slowly heated (1° per min.) from room temperature to 80 °C to obtain the temperature coefficient of resonant frequency defined as,

$$\tau_f = \frac{1}{f_0}\frac{\Delta f}{\Delta T}\ ppm/^oC \tag{2.23}$$

where f_o is the resonant frequency at room temperature and Δf is the change in resonant frequency for a variation in temperature of ΔT .

2.2.8.5 Low temperature dielectric measurement

The experimental system consists of vector network analyzer (E8356B, Agilent Technology, Palo Alto, CA), a closed cycle refrigerator (ARS Cryo), a temperature controller (LTC 340, Lakeshore, CA), custom made vacuum dewar, a personal computer and a TE_{011} mode dielectric resonator. The resonator containing the dielectric material was cooled from room temperature to approximately 6.5 K. The TE_{011} mode resonance is identified around 10.2 GHz. The S_{21}, S_{11} and S_{22} parameter data around the resonance were measured at the lowest temperature [31, 32]. The Transmission mode *Q* Factor (TMQF) technique [33] has been used to eliminate all kinds of parasitic losses and to precisely compute coupling coefficients k_1 and k_2 [34]. The S_{21} parameter is measured as a function of temperature from 6.5 to 290 K. The coupling coefficient for each measurement temperature is calculated using a simplified TMQF and hence the unloaded *Q* factor. The perpendicular component of the real part of the relative permittivity and loss tangent (tan δ) of MTO was computed from the measured resonant frequency and calculated unloaded *Q* factor, respectively.

2.2.8.6 RF impedance analyzer

In the present thesis work, the broadband dielectric properties of the MTO based samples were measured in the frequency range of 1 MHz – 3 GHz using RF impedance / Material Analyzer (Agilent E 4991A equipped with BDS 2200, 2300, Concept 7, M/s Novocontrol (GMbH) equipped with dielectric cell and temperature controller. The temperature of the system can be varied from -160 °C to 400 °C with maximum heating / cooling rate of 20 °C / min.

2.2.8.7 Low frequency dielectric measurement

It is well - known that LCR meters are generally used for measurement of the capacitance and dissipation factor of capacitors in the radio frequency region (low frequency) by parallel plate capacitor method. This will give an approximate idea of ε_r and loss tangent (tan δ) which in turn helps to calculate the approximate resonant frequency and size of the DR to measure the *Q* factor. The parallel plate capacitor method involves sandwiching a thin sheet of the material between two electrodes to form a capacitor. The capacitance of a parallel plate capacitor in vacuum is compared with one in the presence of the material for which the dielectric properties are to be measured. Then relative permittivity is calculated using the following relation [35],

$$C = \frac{\varepsilon_r \varepsilon_o A}{d} \tag{2.24}$$

where ***C*** is the capacitance of the material and ε_r and ε_o are the relative permittivities of the material and free space, respectively. In the present study, the low frequency dielectric properties at zero direct current (DC) bias from 100 Hz to 1 MHz were performed by using LCR meter (Wayne Kerr Electronics Pvt. Ltd., Model 1J43100).

2. (B) Fabrication and characterization of Mg_2TiO_4 thin films

These materials have been commonly used in bulk form and hence most of the research works were focused to study of bulk properties. Mg_2TiO_4 is an excellent microwave dielectric material with wide bandgap and high refractive index suitable for optical and electronic applications. Therefore, its practical applications in optical response are very promising. To the best of our knowledge, the growth of thin films using Mg_2TiO_4 microwave dielectric ceramics as target materials has not been reported so far. Therefore, a brief history of various thin film fabrication techniques is discussed below.

2.3 Thin film preparation techniques

Thin films are three dimensional solids, on which one dimension called the thickness which is several orders of magnitude lower than the other two dimensions. Thin films have a thickness range from a monolayer to several hundreds of nanometers. The properties of thin films are governed by the deposition method. In general, the preparation techniques of thin films are broadly classified into two categories: (a) Chemical vapor deposition (CVD) and (b) Physical vapor deposition (PVD).

2.3.1 Chemical vapor deposition

This method is suitable when a volatile compound of the substance needs to be deposited. The material to be deposited as thin film is vaporized to produce atoms or molecules and reacted with other gases, vapors or liquids on the substrate surface to yield non - volatile reaction products on the substrate.

2.3.2 Physical vapor deposition

This is a general term used to describe any of a variety of methods to deposit thin films by the condensation of a vaporized form of the material onto various surfaces. The coating method includes purely physical processes such as high temperature vacuum evaporation or plasma sputter bombardment. PVD is divided into two major categories: (i) Thermal evaporation and (ii) Sputtering.

2.3.2.1 Thermal evaporation

The solid materials vaporize when heated to sufficiently high temperatures. The condensation of vapor on to a substrate yields a thin solid film. Thermal evaporation of a material can be achieved by a variety of physical methods: (a) Molecular beam epitaxy (MBE) (b) Resistive heating, (c) RF heating (d) Exploding wire technique, (e) Arc evaporation, (f) Flash evaporation and (g) Electron beam evaporation.

2.3.2.2 Sputtering

The ejection of atoms from the cathode surface (target) when bombarded with energetic positive ions of noble gases (such as helium, argon, neon and krypton) under low pressure environment is called sputtering. This process involves a momentum transfer between the impinging positive ions and the cathode surface atoms and as a result of which a physical removal of atoms takes place. In 1852, Sir W. R. Grove first discovered the sputtering phenomenon.

A simple source of ions for sputtering is provided by the glow discharge due to an applied electric field between two electrodes at low pressures [36]. The gas breaks down to conduct electricity when a certain value of voltage is reached. The glow discharge maintains itself at a constant voltage and referred to as a normal glow. The region where voltage and current increase together are called abnormal glow. A luminous layer, which covers the cathode partially in the normal glow and completely in the abnormal glow, is known as a cathode glow. A fairly well - defined region of relatively low luminosity known as Crookes or cathode dark space is found next to it. A bright negative glow region, Faraday dark space and then a positive column region follows this in sequence.

The cathode dark space is the most important region. Most of the applied voltage is dropped (cathode fall) across it. Ions and electrons created at the breakdown are accelerated across this region. The different regions in the discharge are illustrated in Fig. 2.11. The energetic electrons produce more ions by collision with the gas atoms in the negative glow and the energetic ions strike the cathode to produce sputtered flux and secondary electrons, which are essential to sustain the glow. The effective sputtering is possible only when both the number of ions and their energy are large and controllable. There are four different types of sputtering techniques (DC, radio frequency (RF), magnetron and reactive sputtering) proposed for thin film deposition [36].

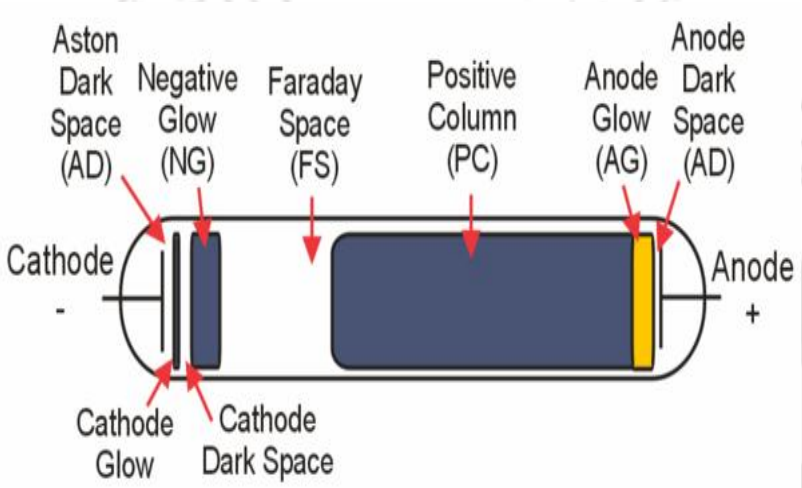

Fig. 2.11: *Different regions in a typical glow discharge [36].*

(i). DC sputtering

This technique is the simplest among the sputtering techniques. In this method, the system consists of a pair of planar electrodes (cathode and anode). The front part of the cathode is covered with a target material, which is to be deposited, and the substrate is placed at an anode. The sputtering chamber is filled with an inert gas (in general argon gas) and the glow discharge is maintained under the application of DC voltage between the electrodes. The Ar^+ ions generated in the glow discharge are accelerated towards cathode to eject the atoms from the target resulting in the deposition of the thin film on to the substrate. DC sputtering suffers from two major drawbacks as compared to conventional evaporation: (i) low deposition rates and (ii) high thermal load of the substrate due to bombardment of secondary electrons. Further, for DC sputtering the target should be conducting materials to avoid building up positive charges on the target, which eventually stop sputtering.

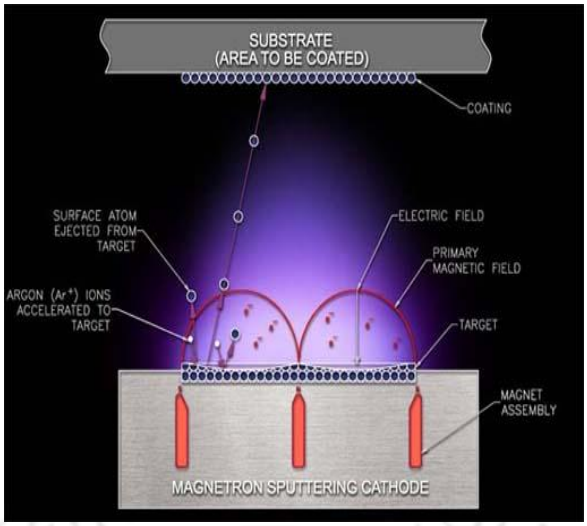

Fig. 2.12: *Schematic presentation of magnetron sputtering gun assembly* [37].

(ii). Mechanism of magnetron sputtering

In a magnetron sputtering configuration, both an electric field (*E*) and a magnetic field (*B*) are used to confine the electrons near the cathode surface. An electron moving with a component of velocity perpendicular to the magnetic field will spiral around the magnetic field lines and will be confined by the magnetic field. Both the frequency and the radius of spiral motion depend on the strength of the magnetic field. The interaction of an electron with the electric and magnetic fields depends on the magnitude and the orientation of the field as $E \times B$. If the magnetic field is parallel to the cathode surface and the electric field is normal to the surface, an electron leaving the surface will be accelerated towards the anode and will spiral around the magnetic field lines. The magnetic field is oriented such that these drift paths for electrons form a closed loop. This electron trapping effect increases the collision rate between the electrons and the sputtering gas molecules. The sputtering collision on the target surface is shown in the Fig.2.12. The chief reasons of its success are (1) increased sputtering rates (~ 5 - 10 times) due to high plasma density around target, (2) low discharge voltages of 300 to 1000 V due to the reduced plasma impendence resulting from high plasma density and (3) low thermal load of the substrate due to deflection of secondary electrons by the magnetic field [37].

(iii). Reactive magnetron sputtering

When a reactive gas species such as oxygen or nitrogen is introduced in to chamber, thin films of compounds such as oxides and nitrides are deposited by the sputtering of the

appropriate metal targets. This process is known as reactive magnetron sputtering. This process is used in practice for high rate of deposition of insulating metal oxide films.

Fig. 2.13: *Photographic view of the RF magnetron sputtering system.*

(iv). RF magnetron sputtering

When insulating / dielectric targets (such as oxides or nitrides) are sputtered using DC voltages, the negative charge applied to the target is neutralized by the *Ar* ions. Eventually, due to positive charge built - up on the cathode (target), the *Ar* ions will not be attracted any more by the target to carry out sputtering. Very high potential differences (around 10^8 volts) between the electrodes are required to sputter insulators, which creates practical difficulties. To overcome this, an alternating current in the radio frequency (RF) regime is used. Since the ions are heavy and less mobile as compared to electrons, they cannot follow radio frequencies. On the other hand, the electrons follow RF and acquire sufficient energy to cause ionizing collisions in the space between the electrodes and thus maintain the plasma. When an electrode is capacitively coupled with the RF source, an alternating (positive and negative) potential appears on the surface. In the one-half cycle, at which the target is negative, the ions are accelerated towards the target with sufficient energy to cause sputtering while, in the next positive half cycle; the electrons reach the target surface to prevent any charge built - up. Since the substrate and chamber make a very large electrode, not much sputtering occurs at the substrate. RF sputtering can be performed at lower *Ar* pressures (1 to 15 mTorr). The processing parameters such as substrate temperature, RF power, deposition time, target to substrate distance, Ar/O_2 flow

ratio and working pressure significantly affects the thickness of the film and consequently thin film properties.

In the present study, we have chosen RF magnetron sputtering (Advanced Process Technologies, India) to deposit Mg_2TiO_4 based thin films. Fig. 2.13 depicts the typical set up of RF magnetron sputtering unit used in the present work. This consists of vacuum system, which is equipped with conventional mechanical pump and turbo-molecular pump and mass flow controllers.

2.4 Thin film characterization techniques

XRD and FE-SEM techniques were used to find out the crystalline phase and microstructural analysis of the films as discussed earlier.

2.4.1 Optical properties

The optical constants of the thin films were calculated using the envelope technique [38]. The spectral transmission characteristics in the wavelength range of 190 - 1200 nm were measured using a UV - VIS - NIR spectrophotometer (UV 3101 PC, SHIMADZU). When the light is incident on a film of refractive index *n*, coated on to a substrate of refractive index *s*, then at the air - film, film - substrate and substrate - air interfaces, part of the incident light is reflected and part of it is transmitted. Since the reflected and transmitted beams originate from a single coherent source, the beams exhibit interference effects. The condition for constructive interference in such a case is given by,

$$2nd = m\lambda \tag{2.25}$$

where n is the refractive index of the film at a wavelength λ and m is the order of interference and d is the thickness of the film that can be calculated from the derived values of refractive indices. Generally, the transmission T, is given by the expression,

$$T = \frac{Ax}{B - Cx\cos\phi + Dx^2} \tag{2.26}$$

where, $A = 16n^2s$, $B = (n+1)^3 (n+s)^2$, $C = 2(n^2-1) (n^2-s^2)$, $D = (n-1)^3 (n-s^2)$, $\phi = 4\pi nd/\lambda$ and $X = e^{-\alpha d}$. For such a system, at the points of constructive and destructive interference the transmittance T_M and T_m, respectively are given by,

$$T_M = \frac{Ax}{B - Cx + Dx^2} \tag{2.27}$$

and $$T_m = \frac{Ax}{B + Cx + Dx^2} \tag{2.28}$$

For simplicity, it can be assumed that the transmission is a continuously varying function of wavelength which can be approximated by drawing the envelope across the spectrum, connecting all the maximas and minimas as shown in the Fig. 2.14.

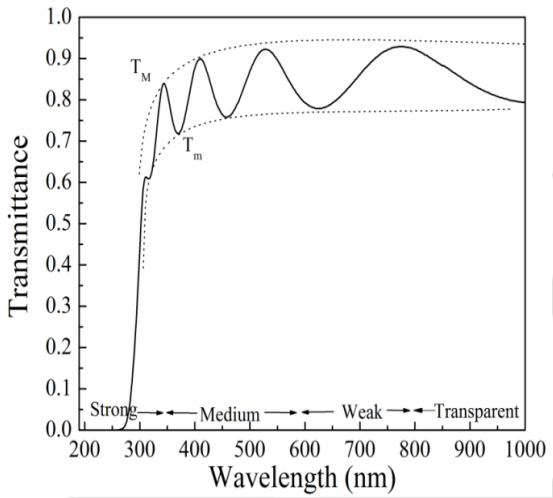

Fig. 2.14: *Typical transmittance spectrum of the film [38].*

The refractive index of the films was derived by employing the envelope method [38] on the basis of following expression:

$$n = \left[N + \left(N^2 - n_S^2\right)^{1/2}\right]^{1/2} \tag{2.29}$$

where N is a constant, n_s is the refractive index of the substrate used and n is the refractive index of the film at that particular wavelength.

$$N = 2n_S\left[\frac{T_M - T_m}{T_M T_m} + \frac{n_S^2 + 1}{2}\right] \tag{2.30}$$

On adding the reciprocals of the equations (2.26) and (2.27) yields,

$$\frac{2T_M T_m}{T_M + T_m} = \frac{Ax}{B + Dx^2} \tag{2.31}$$

and solving for x we get,

$$x = \frac{F - F\left[F^2 - \left(n^2 - 1\right)\left(n^2 - n_S^4\right)\right]^{1/2}}{\left(n-1\right)^3\left(n - n_S^2\right)} \tag{2.32}$$

where $$F = \frac{8n^2 n_S}{T_i} \quad (2.33)$$

and $$T_i = \frac{2T_M T_m}{T_M + T_m} \quad (2.34)$$

where T_M is the maximum of the transmission on the envelope at a wavelength λ and T_m is the minimum in transmission on the envelope at the same wavelength. The T_M and T_m at each wavelength can therefore be read off from the envelope and the refractive index can be derived at each wavelength. From the equation of constructive interference, it can be seen that for two successive maxima occurring at λ_1 and λ_2, the equation becomes

$$2n_1 d = m_1 \lambda_1 \quad (2.35)$$

and $$2n_2 d = m_2 \lambda_2 \quad (2.36)$$

Also $|m_1 - m_2| = 1$.

Therefore, $$d = \frac{\lambda_1 \lambda_2}{2(n_1 \lambda_2 - n_2 \lambda_1)} \quad (2.37)$$

In the strong absorption region, from Beer - Lambert's law given by

$$I = I_0 e^{-\alpha d} \quad (2.38)$$

where, I_0 is the incident intensity =1, I is the intensity at a given wavelength λ, d is the thickness of the film and α is the absorption coefficient in cm^{-1}. Since d is known from previous calculations and I is a measured quantity (i.e. transmission at a wavelength λ), the absorption coefficient α can be calculated. Knowing α from the expression for the so-called "***Tauc gap***", the fundamental absorption edge of the material can be determined by using the expression for the Tauc gap as given by,

$$\alpha h\nu = const.(h\nu - E_g)^{1/2} \quad (2.39)$$

The intercept of the extrapolation of the linear region in a plot of $(\alpha h\nu)^2$ *vs.* $h\nu$ on the x-axis will give the value of bandgap E_g. The error associated with the measurement of k, n and d is ± 0.005, ± 0.02 and ± 10 nm, respectively.

2.4.2 Surface profilometer

The thickness of the films deposited on to transparent substrates were calculated using envelop technique and verified using the surface profilometer. The thickness of the thin films deposited on platinized silicon substrates were measured using stylus profiler

(Veeco - Dektak 150). A diamond - tipped stylus is used to measure the thickness of the films. A precision *x* - *y* stage moves the sample under the stylus, and vertical displacements in the stylus are converted into an electrical signal corresponding to the dimensions of the feature. These electrical signals are then converted to a digital format where they can be displayed on a computer screen and manipulated to determine various analytical information about the surface of the substrate. Scan length and scan speed can be fine-tuned to increase or decrease analysis time and resolution.

2.4.3 Atomic force microscopy

The topography of the deposited films was analyzed using atomic force microscope (AFM). AFM consisting of a microscale cantilever with a sharp tip (probe) at its end is used to scan the specimen surface. The cantilever is typically silicon or silicon nitride with a tip radius of curvature of the order of nanometers. When the tip is brought into the proximity of a sample surface, forces between the tip and the sample lead to a deflection of the cantilever according to Hooke's law. Depending on the situation, forces that are measured in AFM include mechanical contact force, Vander-Walls force, capillary force, chemical bonding, electrostatic forces, magnetic force, casimir force, solvation force etc. Typically, the deflection is measured using a laser spot reflected from the top of the cantilever into an array of photodiodes. The AFM can be operated in a number of modes depending on the application. The primary modes of operation are static (contact) mode and dynamic mode [39]. In the static mode operation, the static tip deflection is used as a feedback signal. As the measurement of a static signal is prone to noise and drift, low stiffness cantilevers are used to boost the deflection signal. However, close to the surface of the sample, attractive forces can be quite strong, causing the tip to 'snap - in' to the surface. Thus static mode AFM is almost always done in contact where the overall force is repulsive. Consequently, this technique is typically called 'contact mode'. In contact mode, the force between the tip and the surface is kept constant during scanning by maintaining a constant deflection through feedback circuit.

In the dynamic mode, the cantilever is externally oscillated at or close to its resonance frequency. The oscillation amplitude, phase and resonance frequency are modified by tip - sample interaction forces. These changes in oscillation with respect to the external reference oscillation provide information about the sample's characteristics. Schemes for dynamic mode operation include frequency modulation and the more common amplitude modulation. In frequency modulation, changes in the oscillation

frequency provide information about tip -sample interactions. Frequency can be measured with very high sensitivity and thus the frequency modulation mode allows for the use of very stiff cantilevers. In the present study, the AFM images were obtained using Agilent AFM **(**Agilent technologies, Model 5500 series**)** and analyzed using WSXM software [40].

2.4.4 Electrical measurements

For the electrical characterizations, metal-insulator-metal (MIM) type test structures were fabricated. All the oxide thin films were deposited on Pt coated Si substrates. 100 nm thick *Ag* top electrodes were deposited on top of the oxide layer through a shadow mask to define a capacitor structure (diameter of a top electrode is 1.0 mm). In the present thesis work, the low frequency dielectric properties were performed at zero DC bias from 100 Hz to 1 MHz by using an LCR meter (Wayne Kerr Electronics Pvt. Ltd., 1J43100).

2.4.5 Microwave dielectric properties of thin films using split post dielectric resonator method

The microwave dielectric properties of thin films were determined using a vector network analyzer Agilent 8722 ES by employing the split post dielectric resonator based measurement technique (SPDR) [41]. Split - post dielectric resonator measurement technique is a highly accurate technique for measurement of complex permittivity of dielectric substrates and thin films at spot frequencies in the frequency region of 1- 20 GHz. This method is attractive for accurate non - destructive measurements of low - loss substrates. Low loss materials are nearly non dispersive so that the dielectric constant and loss tangent will stay constant over a range of frequencies. The required thickness of sample depends on dielectric constant of material. Material with high dielectric must have less thickness. The fixture air gap and the active area dimension of the fixture depend on the operating frequency of resonator. It is possible to measure the relative permittivity with uncertainty of approximately ± 0.5% or better and the dielectric loss tangent with a resolution of 2×10^{-5} for properly chosen sample thickness. The cross section view of the SPDR is shown in Fig. 2.15.

For thin films deposited on a substrate, the frequency shift due to the film has to be separated from the overall frequency shift of the film substrate. For this purpose one has to measure the resonance frequency and quality factor (f_{01}, Q_{01}) of the empty resonator and do the same (f_0, Q_0) with the substrate. After the film deposition, the resonance frequency and quality factor of the (f_s, Q_s) substrate coated with the film have to be

measured again. The SPDR typically operates in the $TE_{01\delta}$ mode that has only an azimuthal electric field component, so that the electric field remains continuous on the dielectric interfaces. This makes the system insensitive to the presence of air gaps perpendicular to the z - axis of the fixture. The real part of permittivity of the sample is found on the basis of the measurements of the resonant frequencies and thickness of the sample as an iterative solution to Eq. (2.40).

$$\varepsilon' = \frac{1+(f_0 - f_s)}{hf_0 K_s(\varepsilon', h)} \tag{2.40}$$

Here, h is the sample thickness, f_0 is the resonance frequency of the SPDR with the substrate, and f_s is the resonance frequency of the SPDR with the film coated substrate. K_s is a function of the sample's dielectric constant ε_r and thickness h. Since K_s is a slowly varying function of ε_r and h, the iterations using the formula (2.40) converge rapidly.

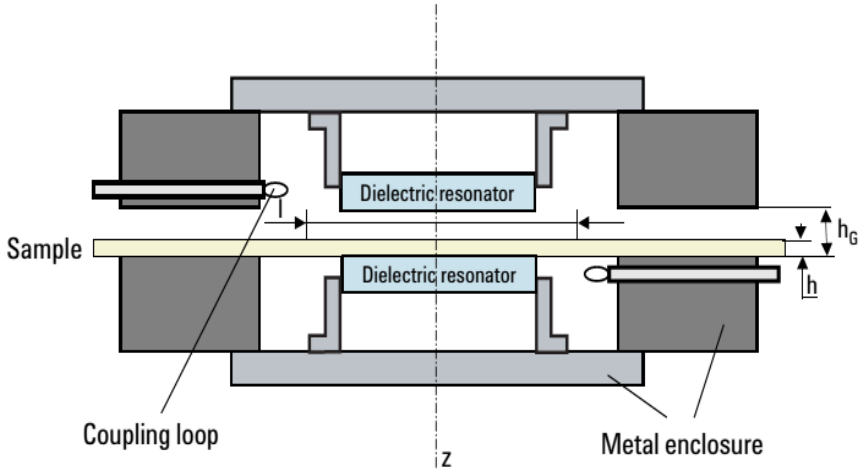

Fig. 2.15: *Cross sectional view of SPDR fixture [41].*

The loss tangent is computed using the Eq. (2.41):

$$\tan\delta = \frac{Q^{-1} - Q_{Dr}^{-1} - Q_c^{-1}}{P_{es}} \tag{2.41}$$

where, Q is the unloaded quality factor of the SPDR containing the dielectric sample and Pes is the electrical energy-filling factor of the sample. Q_c is the Q factor depending on the metal losses for the SPDR containing the dielectric sample and Q_{Dr} is the Q - factor depending on the dielectric losses in the dielectric resonators. The unloaded Q - factors depends on conductor and dielectric lossess and all other related parameters. The dielectric parameters can be derieved using basis of measurements for high frequency applications.

2.5 References

[1] R. E. Carter, *J. Chem. Phys*. **34** (1961) 2010.

[2] M. N. Rahaman, *Ceramic processing and sintering*, Marcel Dekker, Inc, New York (2003).

[3] D. Seagal, *Chemical synthesis of advanced ceramic materials*, Cambridge University Press, Cambridge (1991).

[4] J. S. Benjamin, *Metall. Trans.* **1** (1970) 2943.

[5] J. S. Benjamin, *Advances in powder Metallurgy and particulate materials*, E. D. Capus, R. M. German (Eds.), Metal Powder Industry Federation, Princeton, **7** (1970) 155.

[6] C. Suryanarayana, "*Mechanical Alloying and Milling*", Marcel Dekker, New york, (2004).

[7] L. B. Kong, J. Ma, W. Zhu, and O. K. Tan, *J. Alloys Compd.*, **322** (2001) 290.

[8] C. Suryanarayana, *Prog. Mater. Sci*. **46** (2001) 1.

[9] S. Penn and N. Alford, *Handbook of low and high dielectric constant materials and their applications phenomena, Properties and Applications*, (Editor Hari Singh Nalwa), Academic Press, (1999).

[10] X. K. Wu, D. W. Whitman, W. L. Kaufell, W. C. Finch and D. l. Cumbers, *Ceram. Eng. Sci. Proc.*, **18** (1997) 422.

[11] P. Winiewski, M. Szafran and G. Rokicki, *Key Eng. Mater. Euro Ceram.-VIII*, **264** (2000) 428.

[12] S. J. Kang, *Sintering, densification, grain growth and microstructure*, *Elsevier*, Amesterdam, (2002).

[13] R. L. Coble, *J. Appl. Phys.*, **32** (1961) 787.

[14] M. W. Barsoum, *Fundamentals of Ceramics*, CRC Press, New York, (2003).

[15] W. D. Kingery, and M. Berg, *J. Appl. Phys.*, **26** (1955)1205.

[16] W. D. Kingery, H. K. Bowen, D. R. Uhlmann, *Introduction to ceramics*, John Wiley and Sons, New York (1975).

[17] D. Cullity, *X-ray Diffraction*, Addison-Wesley, Reading, MA (1956).

[18] K. Ishikawa, K. Yoshikawa, N. Okada, *Phys. Rev. B*, **37** (1988) 5852.

[19] G. K. Williamson and W. H. Hall, *Acta Metallurgica*, **1** (1953) 22.

[20] R. A. Young, *The Rietveld Method*, Oxford university press, New York, (1996).

[21] A. John Dean, *The Analytical Chemistry Handbook*, McGraw Hill Inc., New York, (1995).

[22] D. Kajfez, P. Guillon (eds.), Dielectric Resonators Norwood, MA, *Artech House* (1986).

[23] J. J. Krupka, K. Derzakowskiz, B. Riddlex, J. B. Jarvisx, *Meas. Sci. Technol*. **9** (1998) 1751.

[24] B. W. Hakki, and P. D. Coleman, *IEEE Trans. Microwave Theory Technol*., **8** (1960) 402.

[25] W. E. Courtney, *IEEE Trans. Microwave Theory Technol*. **18** (1970) 476.

[26] Y. Kobayashi, M. Katoh, *IEEE Trans. Microwave Theory Technol*., **33 (**1985)586.

[27] E. L. Ginzton, *Microwave Measurements*, McGraw Hill Book Co., Boston, (1957).

[28] E. J. Vanzura, J. E. Roger, *Proc. IEEE Conference on instrumentation and Measurement Technology*, May 15-16, Atlanta, (1991).

[29] T. Miura, M. Kobayashi, *IEICE Transactions on Electronics*, **E7** (1994) 900.

[30] M. T. Sebastien, *Dielectric Materials for Wireless Communications*, Elsevier Science Ltd, Netherlands (2008).

[31] M. V. Jacob, J. Mazierska, D. Ledenyov and J. Krupka; *J. Euro. Ceram. Soc.* **23** (2008) 2617.

[32] M. V. Jacob; *Sci. Technol. Adv. Mater.*, **6** (2005) 944.

[33] E. L. Ginzton; *Microwave Measurements*; McGraw-Hill Book Co, New York (1995).

[34] M. V. Jacob, J. Mazierska, K. Leong and J. Krupka; *IEEE Trans of Microwave Theory Technique.*, **49** (2001) 2401.

[35] W. D. Kingery and M. Berg, *J. Appl. Phys.*, **26** (1955) 1205.

[36] K. Wasa, M. Kitabatake, and H. Adachi, *Thin film materials technology*: Sputtering of compound materials" *Springer, Verlag*, Berlin (2004).

[37] www.angstromsciences.com.

[38] R. Swanpoel, *J. Phys. E: Sci. Instrum*. **16** (1983) 1214.

[39] http://www.siint.com.

[40] Horcas, R. Fernandez, J. M. Gomez-Rodriguez, J. Colchero, J. Gomez-Herrero, A. M. Baro, *Rev. Sci. Instrum*., **78** (2007) 013705.

[41] J. Krupka, A. P. Gregonry, O. C. Kochard, R. N. Clarke, B. Riddle, and J. Baker-Jarvis. *J. Eur. Ceram. Soc*., **21** (2001) 2673.

Chapter 3

Effect of mechanical alloying on structural, microstructural and microwave dielectric properties of Mg_2TiO_4 ceramics

3.1 Introduction

The growing importance of ceramic dielectrics for the applications in microwave oscillators, amplifiers, filters etc. has led to great advances in the material research and development of dielectric systems [1-4]. Although the demand for dielectric materials in different areas are increased, but recently, the primary need of such materials is focused for developing low loss materials with higher permittivity to miniaturize the device [3-5]. However, the dielectric loss of most of the high permittivity materials is extremely high and hence it is ideal to use medium / low permittivity materials in circuit and devices. Low permittivity can not only minimize cross coupling with conductors but also shorten the time for the electronic signal transition. In addition, a high-quality factor ($Q \times f_o$) has been playing a more prominent role because of the rise of the carrier frequency and nearly a zero temperature coefficient of resonant frequency (τ_f) is needed to ensure stability of the frequency against the change in temperature. Numbers of microwave dielectrics were proposed to meet this requirement for high-frequency applications [5-12]. Accordingly, the search on new high Q dielectric materials such as MgO – TiO_2 binary system has brought much more attention for high – frequency applications. Recently, the intense development of high Q microwave materials based on low - cost raw oxides from the MgO – TiO_2 system has been initiated. There are basically three stable phases ($MgTiO_3$, Mg_2TiO_4 and $MgTi_2O_5$) in the MgO – TiO_2 system has been reported in the literature [13, 14]. Among these, Mg_2TiO_4 ceramic is one of the leading dielectric material with excellent microwave dielectric properties: modest dielectric constant (ε_r) ~ 14, high-quality factor ($Q \times f_o$) ~150,000 GHz and a negative temperature coefficient of resonant frequency (τ_f) ~ - 50 ppm / ^oC [13, 14].

However, there is a major disadvantage in preparing Mg_2TiO_4 (MTO) ceramics by solid state reaction method as it requires high sintering temperature is about 1450 ^oC. Achieving maximum densification at lower temperatures without additives is very difficult and these additives may degrade the microwave dielectric properties. Nevertheless, there are several methods used to reduce the sintering temperature of microwave dielectric ceramics such as addition of a low-softening glass or liquid phase sintering aids [15, 16], chemical processing [17] and reduction of initial particle sizes using mechanical synthesis [18]. Extensive research works revealed that mechanical activation could simplify or accelerate solid state reaction, which normally occurs at high temperature and / or high pressure [19].

On the other hand, nanomaterials have generated a lot of interest due to their unique physical and chemical properties that are significantly different from bulk counterparts. Reducing the particle size into nanometer range, without changing the chemical composition can change the fundamental properties of the materials [20]. In the present study, MTO nanoceramics were prepared by mechanical synthesis method. This is a convenient method for the synthesis of wide range of nanosized metallic and ceramic powders in an efficient and economical manner [21]. It has many advantages: simplicity, relatively inexpensive to produce nanoparticles and applicable to any class of materials [22]. The most valuable advantage of this technique is that the solid-state reaction is activated via mechanical energy rather than of heating energy (high temperature). Hence, this method does not require the calcination step, which is necessary in the conventional solid-state method and the initial reaction takes place slightly above the room temperature in a sealed container. Furthermore, the mechanically derived powders possess a higher sinterability than those synthesized by a conventional solid-state reaction and most of the wet-chemical processes [23]. Mechanical synthesis not only makes the material finer but also includes structural changes, phase transformations and even solid-state reactions among the solid reagents. These physicochemical changes occur due to the efficient transformation of the mechanical energy of the grinding media to the particles and the intensive mechanical force during the milling process [24].

Taking all this into account, we have chosen mechanical synthesis method to prepare the MTO nanoceramics. Further, to see the influence of mechanical alloying on phase composition, crystal structure, microstructure, as well as on thermodynamics of MgO-TiO_2 system before and after sintering process. Also, the dielectric loss mechanisms are discussed on the basis of densification and microstructure of the MTO ceramics and

the obtained results are compared with the earlier reports. In addition, the low frequency dielectric properties are studied extensively.

3.2 Experimental details

Mg_2TiO_4 (MTO) ceramics were synthesized by mechanical alloying (MA) process from individual high - purity oxide powders MgO and TiO_2 (99.99%) from Sigma Aldrich (St. Louis, MO). The starting materials were mixed according to desire stoichiometry ratio and the powders were ball milled for 35 hours (hr) to reach steady state condition (using Fritsch Germany, planetary ball mill) with the following parameters: (i) ball-to-powder ratio of 10:1; ball diameters of 8 and 16 mm; ball and vial materials: Tungsten carbide; milling speed of 350 rpm. The ball milling process was stopped periodically for 5 minutes for every 10 minutes of milling to avoid significant temperature rise. After drying and sieving, the samples were uniaxially pressed into pellets with dimensions of 10 mm in diameter and 4 - 5 mm in thickness under a pressure of 200 MPa. The pellets were sintered in the range of 1250 -1400 ^oC for 3 hr in air. The heating and cooling rates were controlled to be 8 ^oC / min and 1 ^oC / min, respectively.

The bulk densities of the sintered samples were calculated by Archimedes method. Crystal structures of the as prepared samples were analyzed by using high powder X-ray diffraction (XRD) technique with Cu-Kα radiation. Further, XRD patterns were refined by using Rietveld refinement technique and Full Proof program [25]. Thermal decomposition behavior of the milled MTO powders was analyzed by a thermogravimetric analyzer (TGA) and a differential scanning calorimeter (DSC). Surface morphology and microstructural analysis were performed using SEM, AFM and TEM, respectively. Spectral transmission characteristics were measured in the wavelength range 200-1000 nm using a UV-VIS-NIR spectrophotometer. Photoluminescence (PL) measurements were performed at room temperature through thermo-spectronic double monochromator coupled to GaAs photo-multiplier with a conventional photon counting system. The dielectric properties ε_r and Q_u of the materials were measured in the microwave frequency range using resonance technique as described in Chapter 2.

3.3 Results and discussion

3.3.1 The effect of milling time on the structural properties of MTO powders

In order to monitor the effect of mechanical alloying on the initial powders, XRD patterns were recorded for the samples milled for different durations. The XRD patterns of MgO-

TiO_2 systems milled for 5, 20, 30 and 35 hr are illustrated in Fig. 3.1. It was observed that the MTO ceramics milled for 5 hr exhibited the peaks corresponding to MgO and TiO_2 oxides only. As the milling time increases, the intensities of the parent oxide peaks decrease gradually and the formation of $MgTi_2O_5$ phase was observed. After 30 hr of milling, all the parent oxides peaks are disappeared completely, resulting a strong diffraction peak of MTO phase along with low intense peaks of $MgTiO_3$ and $MgTi_2O_5$. However, after 35 hr milling the intensity of MTO peak gets stronger along with a low - intensity $MgTiO_3$ peak, suggesting that there is an increase of crystallite of the MTO phase. The formation of the heterogeneous phases comprising $MgTi_2O_5$ and $MgTiO_3$ in the MgO -TiO_2 system is mainly due to the difference in the degree of the incipient mechanical reaction. This can be explained as follows: during the ball milling process, the mechanical energy of the grinding media transforms into the parent oxide particles resulting a structural destruction followed by reduction in particle size.

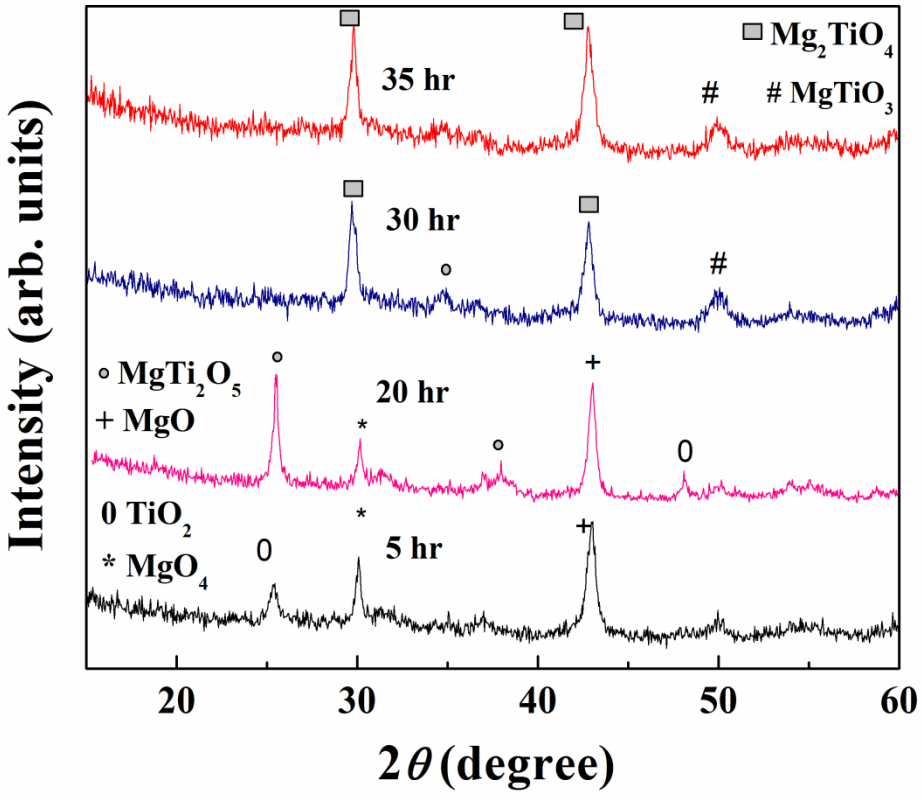

Fig. 3.1: *XRD patterns of the MgO and TiO_2 oxides milled for 5, 20, 30 and 35 hr.*

3.3.2. Calculation of average crystallite sizes

The crystalline size of nanoparticles can be determined with several techniques that rely upon the peak width of the X- ray diffraction patterns. In the present study, we have

chosen the Williamson-Hall (W-H) method in order to understand the origin of the broadening in the XRD peaks. According to W-H method [26], the peak broadening due to lattice strain can be calculated using the following formula:

$$\beta\cos\theta = \left[\frac{k\lambda}{D_{WH}}\right] + 4e\sin\theta \tag{3.1}$$

where β is the full width at half maximum (FWHM) of the Bragg peaks (in radians), θ is the Bragg's angle of the analyzed peaks, λ is the wavelength of the X-ray (λ = 0.154056 nm for Cu-K_α), D_{WH} is the average crystallite size and e is the effective strain associated with mechanical alloying. According to Debye-Scherrer's equation the broadening due to small crystallite size may be expressed as:

$$\beta_c = \frac{k\lambda}{D\cos\theta} \tag{3.2}$$

where β_c is the FWHM, D is the crystallite size, k is the shape factor taken as 0.9 for spherical particles, λ is the wavelength of Cu-K_α radiation.

Fig.3.2 (a) depicts the variation of average crystallite size as a function of milling time determined from Eqs. (3.1) and (3.2). It is apparent from the Fig. 3.2(a) that the average crystallite size decreased rapidly up to 30 hr of milling and then attained a saturated value. The average crystallite size of the as-mixed powder was nearly 2.5μm. After 20 hr of milling, the crystallite size reduced to 80-100 nm and further to 40-60 nm for 35 hr of milling. But, according to Scherrer method the average crystallite size for MTO powder after 20 and 35 hr of milling are 28 nm and 17 nm, respectively. Thus the crystallite size obtained using Scherrer equation is smaller than that computed by W-H method. The difference is mainly due to the fact that the Scherrer's equation does not take into lattice strain effect on the peak broadening. Inset Fig. 3.2(a) illustrates the variation of lattice parameter as a function of milling time. It reveals that with increase of milling time the lattice constant decreases from 8.436 Å to nearly a stable value of 8.412 Å, after 35 hr of milling. The changes in lattice constant indicate the occurrence of atomic disorder by milling process.

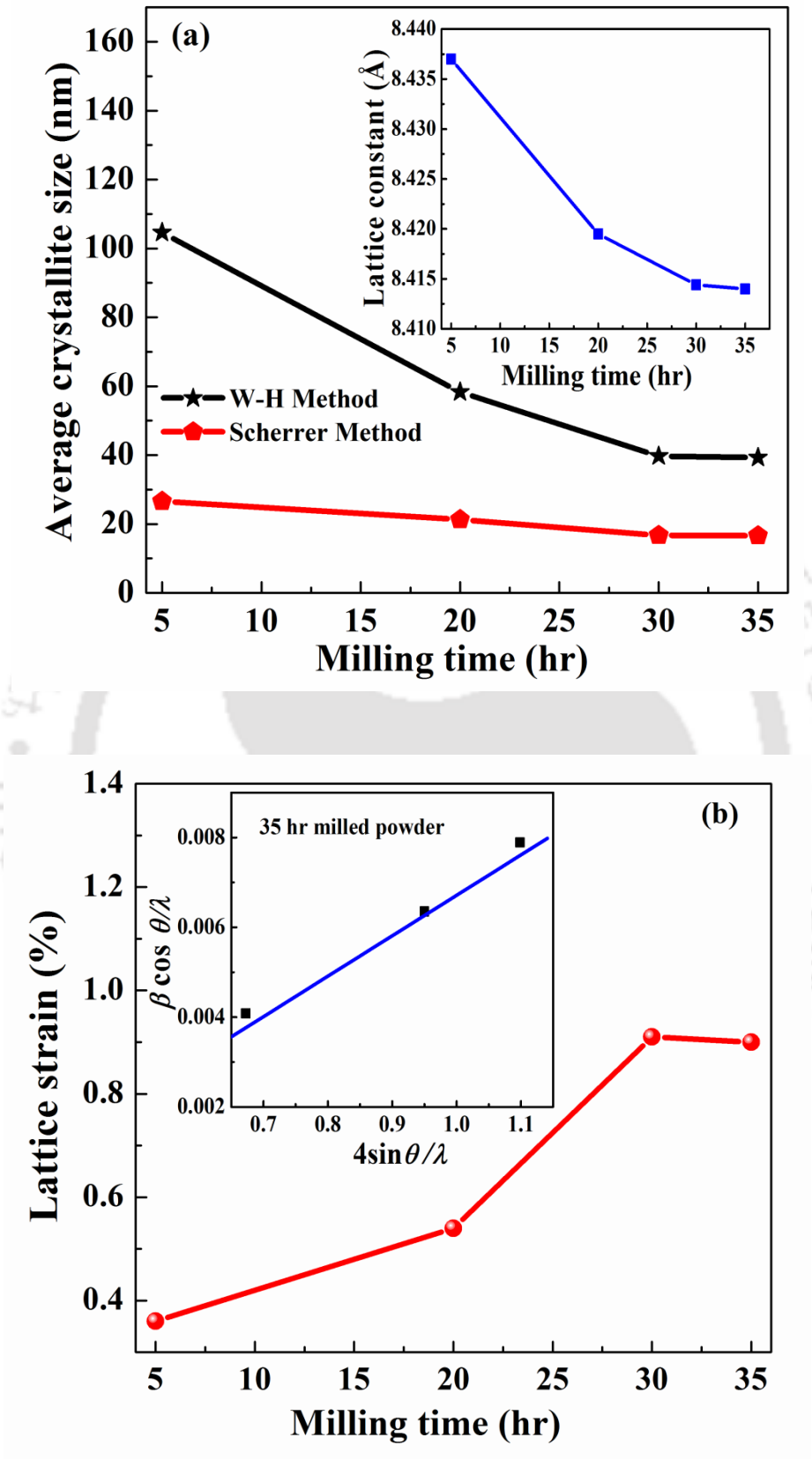

Fig. 3.2: ***(a)*** *Variations of average crystallite size and lattice parameter (**inset**) with milling time and* ***(b)*** *Variation of lattice strain with milling time.* ***Inset:*** *W-H plot for 35 hr milled powders.*

The mechanical alloying process not only reduces the crystallite size of the concerned powders into nanometric size but also causes an increase of lattice strain. The total broadening of the XRD peaks is mostly caused due to reduction of crystallite size, lattice strain and the instrumental effects. Crystallite size is a measure of the size of a coherently diffracting domain. When the crystallites of the materials are very smaller (less than 100 nm), they have less number of parallel diffraction planes producing broadened diffraction peaks. Likewise, the non-uniform strains arising out of heavy plastic deformation during mechanical alloying process cause broadening of the diffraction peaks. The other sources of strain are the grain boundary triple junctions, crystal imperfections, such as lattice dislocation, contact or sinter stresses etc. The milling dependence of internal microstrain (e) of mechanically alloyed MTO powders was calculated and depicted in Fig. 3.2 (b). A plot is drawn between $4\sin\theta/\lambda$ along the x- axis and $\beta_{hkl}\cos\theta/\lambda$ along y-axis (known as W-H plots) for selected diffraction peaks of 35 hr milled MTO nano-powders and is shown in inset Fig. 3.2 (b). The deviation in the data points from the straight line suggests that the strain is anisotropy. From the linear fit to the data, the average crystallite was estimated from the y-intercept and the strain (e) from the slope of the fit as 9.01×10^{-3} and 38 nm, respectively, for 35 hr milled powders. From the W-H analysis, it is clearly seen that the broadening of the peaks in X-ray diffraction is due to the contribution of small crystallite size and the anisotropic strain. It was also observed that the internal strain increased with increasing milling time and subsequently attains saturated values.

3.3.3 Morphological study on mechanically alloyed MTO powders

3.3.3.1. SEM analysis

To investigate the effect of mechanical activation on the evolution of microstructure of MTO powders, SEM micrographs were obtained and depicted in Fig. 3.3 for as-mixed and milled MTO powders. It is well-known that during mechanical attrition by ball milling, the evolution of materials phases is coupled to the mechanical properties of the powders and therefore to their microstructures [27, 28]. It has been established that the microstructure evolution is controlled by the temperature, milling intensity and composition. From our microstructural analysis, it was observed that the initial powders consisted of spherical particles with agglomerated morphology. After 5 hr of milling, the particle morphology was found to be spherical, but the particle size was distributed over a wide range from sub-micrometer to few micrometers. With increasing milling time, the

particle size reduces into nanometer range with more distinct grains compared to early stages of milling along with the presence of new phases in shape of agglomerates covered with many smaller nanosized particles of starting powders. These aggregates are typical of mechanically alloyed powders resulting from repeated cold welding and fracture of powder during ball milling.

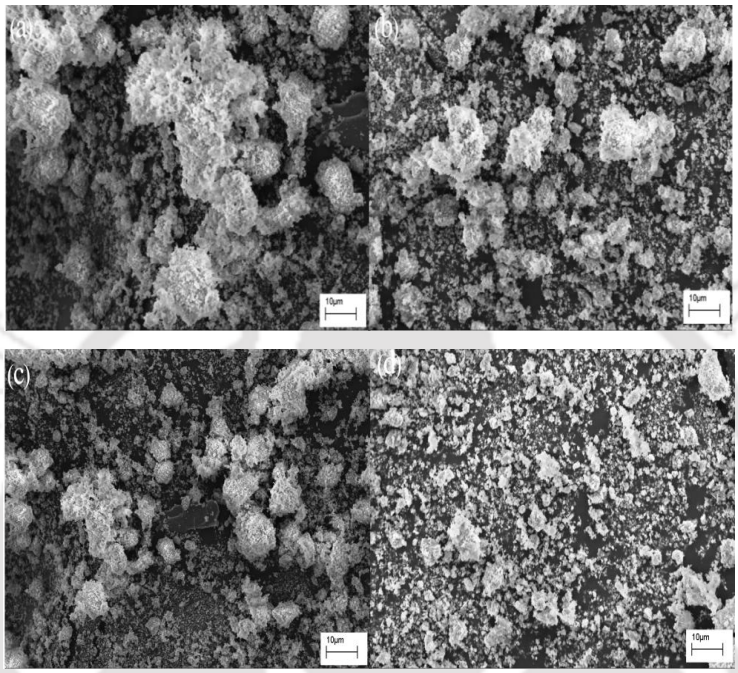

Fig. 3.3: *SEM micrographs of MTO powders milled for (a) 0 (b) 5 (c) 20 and (d) 35 hr.*

3.3.3.2 TEM analysis

Fig. 3.4 shows the bright field TEM micrographs of MTO powders milled for 20 and 35 hr. It was observed that the powders milled for 20 hr did not exhibit distinct particle size, whereas the powders milled for 35 hr exhibited a clear nanosized particle. The initial particle size of the parent oxides was greater than 2μm and as the milling time increases the initial particle sizes of the powders decreased, and the average particle size of the powders milled for 35 hr was found to be around 60 -100 nm. This crystalline size is nearly consistent with the calculated data by Williamson-Hall plot method. Fig. 3.4 (c) shows the selected area electron diffraction (SAED) pattern of the 35 hr milled powder. The ring pattern corresponds to various interplaners spacing (*d*-spacing) of the spinel MTO phase suggesting the crystalline nature of the sample. High resolution TEM (HRTEM) study was carried out to analyze the lattice fringes for the 35 hr milled samples, as shown in Fig. 3.4 (d). The clear lattice fringes were obtained, implying that

the as-grown samples are highly crystalline. The *d*-spacing of the crystal plane is calculated as 2.968 Å for 35 hr milled powders, indicating the preferable crystal growth plane is (220), which corresponds to the highest intensity peak in the XRD pattern of the 35 hr milled powders (shown in Fig. 3.1). Therefore, it can be concluded that a solid-state reaction at ambient temperature between MgO and TiO_2 took place during the ball milling process.

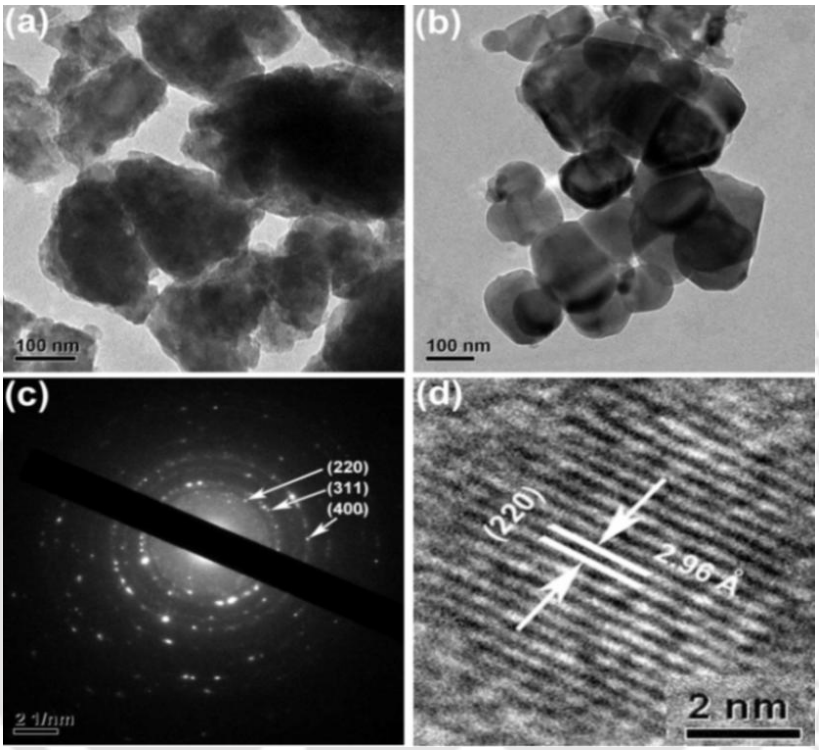

Fig.3.4*: Bright field TEM micrographs of (a) 20 and (b) 35 hr milled MTO powder (c) SAED pattern and (d) HR-TEM for 35 hr milled powder.*

3.3.4 Thermal analysis

The influence of mechanical activation on the behavior of the MgO -TiO_2 system during thermal treatment is analyzed for different milled samples. Fig. 3.5 shows the weight loss of MgO-TiO_2 system milled for 20 and 35 hr during heating. With the increase of the activation time, the reaction occurs at a lower temperature in comparison with non-activated samples. This confirms that the basic material changes during mechanical alloying are related to physical - chemical surface parameters, resulting in the occurrence of changes in the materials reactivity. Thus, with increase of milling time, ceramic powder increases their reactivity and accelerates solid-state reactions. It is observed that up to 100 ^{o}C, the weight loss is about 5 -7%, which is attributed to the evaporation of water. Mechanical activation supports hygroscopic. Therefore, the weight loss is highest

for the sample with longest period of milling, i.e., the powders milled for 35 hr has more weight loss compared to 20 hr milled powders. Further, the weight loss around 350 - 400 ^oC is more prominent due to the formation of secondary phases ($MgTiO_3$ and $MgTi_2O_5$) for both the systems. The formation of secondary phases was also confirmed by the XRD results.

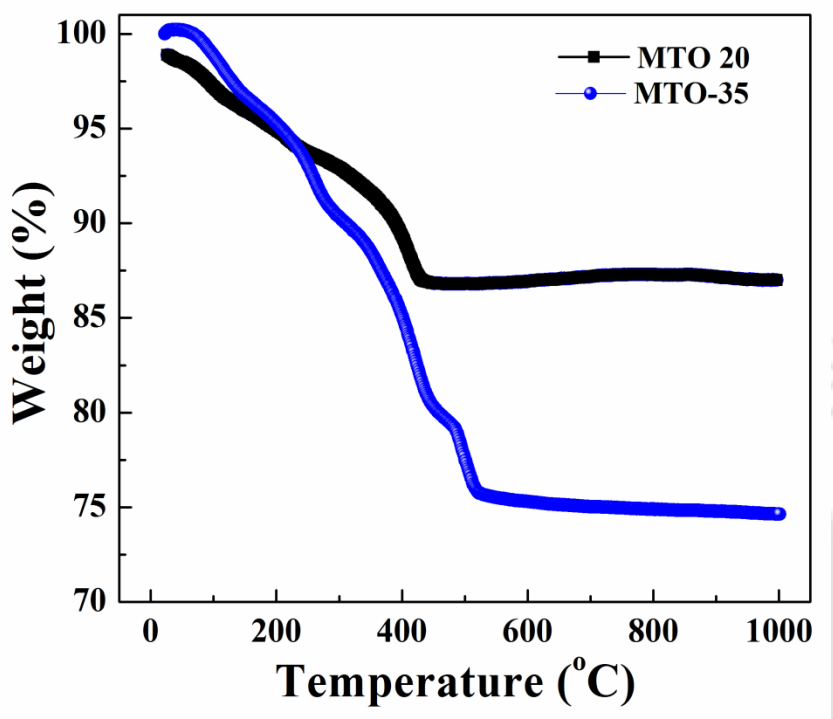

Fig. 3.5: *Weight loss verses temperature curves for 20 and 35 hr milled MTO powders.*

3.3.5 Optical studies of mechanically alloyed MTO powders

3.3.5.1 UV-Vis and PL analysis

The effect of milling time on the optical bandgap of the mechanically alloyed MTO nanoparticles was analyzed by obtaining absorption spectrum using UV-Vis Spectrometer for all the as-prepared samples and shown in Fig. 3.6 (a). It was found that there is strong band gap absorption at around 356 nm for un-milled MTO powders. With the increase of milling time, the peak slightly shifted to 352 nm for 35 hr milled powders. A clear blue-shift in the absorption peak is observed with the reduction of average crystallite size of the MTO powders. This indicates the increase in bandgap with particle size reduction. However, the enhanced absorption in nanoparticles can be attributed to a large surface to volume ratio and increased oscillator strength with size reduction.

The optical bandgap of all the samples was determined using Tauc relation [32], which is given as, $\alpha h\upsilon = \beta\,(h\upsilon - E_g)^n$, where $h\upsilon$ is the photon energy, β is a constant which

is a measure of crystalline order of the samples and n =1/2 was taken for direct band gap structure (since inverse spinel structures exhibits a direct band gap). The variation of bandgap with milling time was plotted and is shown in inset of Fig 3.6 (a). This optical bandgap (E_g) is determined by the extrapolation of the best fit line between $(\alpha h\upsilon)^2$ and $h\upsilon$ to intercept the $h\upsilon$ axis (α = 0) as shown in Fig. 3.6 (b). The plot indicates that with increasing milling time from 0 hr to 35 hr the bandgap increases from 3.26 eV - 3.78 eV. This is comparable with the previously reported results [30-32]. Fig.3.6 (b) shows the dependence of the absorption coefficients $(\alpha h\upsilon)^2$ with photon energy for the 35 hr milled powders. The position and slope of the optical absorption edge makes this material as a suitable UV light absorber.

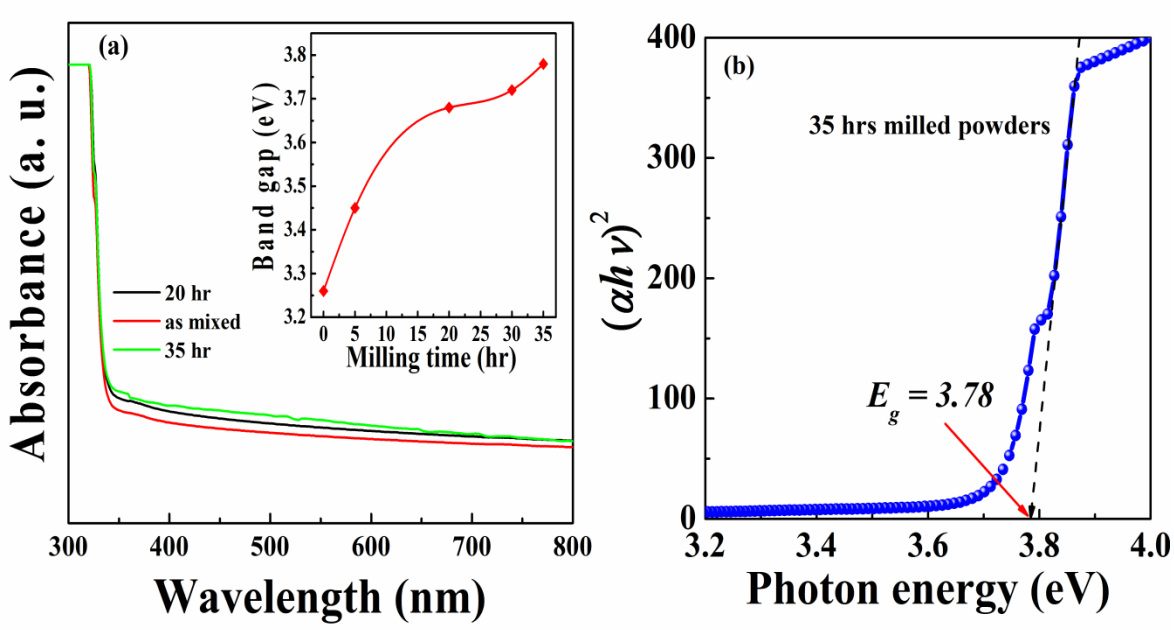

***Fig. 3.6**: (a) Room temperature UV – Visible spectra of pure and milled MTO powders, **Inset:** Variation of bandgap with milling time, and (b) variation of $(\alpha h\nu)^2$ versus photon energy for the 35 hr milled powders.*

Photoluminescence (PL) is the spontaneous emission of light from a material under optical excitation. Fig. 3.8 illustrates the room temperature PL spectra of as - milled samples. It was observed that the broadening increases with an increase in milling time and there is only one characteristic peak at 357 nm for all the milled powders corresponding to the near shortest visible blue-emission. The PL spectra also indicate that the MTO powders milled for 35 hr exhibited highest intensity with a characteristic peak at 357 nm without any significance of peak shifting. These emissions were found to be

extremely broad and may be due to phonon assisted transition and large surface to volume ratio of the nanosized powder.

In addition, our PL results compliment with the optical bandgap values that the increase in milling time results the highest intensity of the peaks, which can be attributed to the high degree of structural order and disorder in the lattice [33]. Recently, in our previous study, a broad UV- blue PL emission with characteristic peaks around 357 and 409 nm were observed in our sputtered MTO thin films [34], which ultimately support our bulk (nano-powders) counterpart. The inset Fig. 3.7 shows the variation of PL intensity with milling time. It was observed that with increasing milling time the PL intensity increases, which can be attributed to a large surface to volume ratio of the MTO nanoparticles and increased oscillator strength with size reduction.

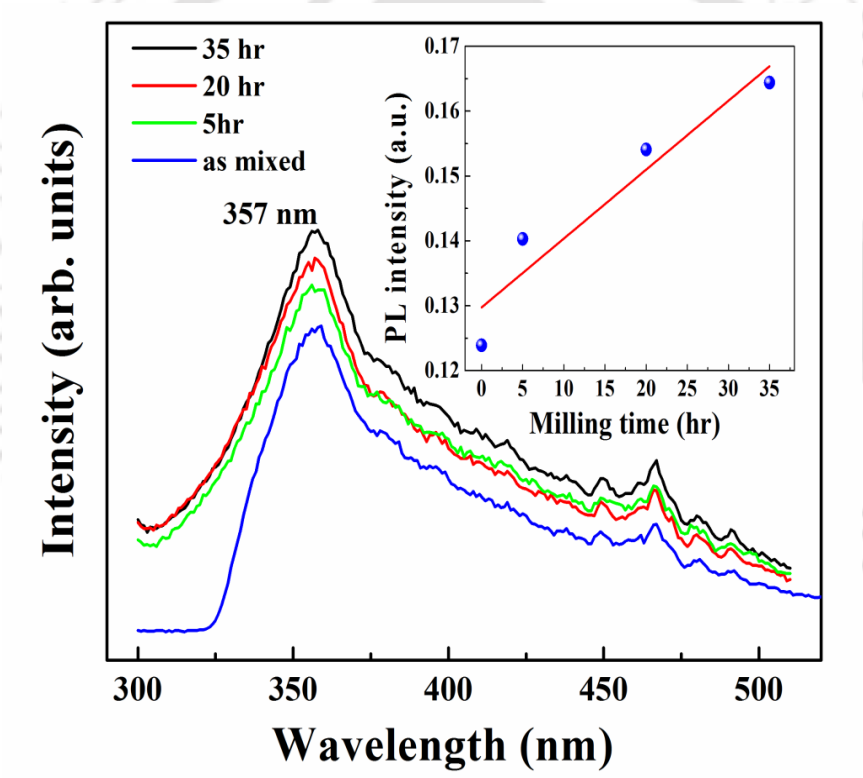

Fig. 3.7: *Room temperature photoluminescence spectrum of pure and milled MTO powders,* ***Inset:*** *Variation of PL intensity versus milling time.*

3.3.6 Influence of sintering temperature on the crystal structure microstructure and relative density of MTO ceramics

3.3.6.1 Crystal structure analysis

To monitor the effect of sintering temperature on the crystal structure of the MTO ceramics, XRD patterns of the samples were recorded. Fig.3.8 (a) shows the XRD patterns of the MTO ceramics sintered at different temperatures for a constant sintering duration of 3 hr. It is observed that all the MTO ceramics exhibit single spinel phase (ICSD-PDF # 06-5792) without the evidence of any additional secondary phase over the entire compositional range. These patterns could be refined by using *Fd-3m* space group in cubic cell. The typical XRD patterns along with the Rietveld refinement for the sample sintered at 1325 ^{o}C for 3 hr is shown in Fig.3.8 (b). The refinement was carried out by varying cell parameters, position of the Mg, Ti, and O atoms, occupancy and thermal parameters. The typical values of lattice parameters are found to be $a = b = c = 8.4544$ (15) (Å). The values of $\chi 2$, R_{Brag} factor and R_f factor were found to be 0.86, 10.3 and 6.6, respectively. The metal-oxygen bond lengths between <Mg_1-O> and <Mg_2-O> were found to be 1.8222 Å and 3.5050 Å, respectively. The derived Rietveld refinement data was well set with the standard data of MTO ceramics [13].

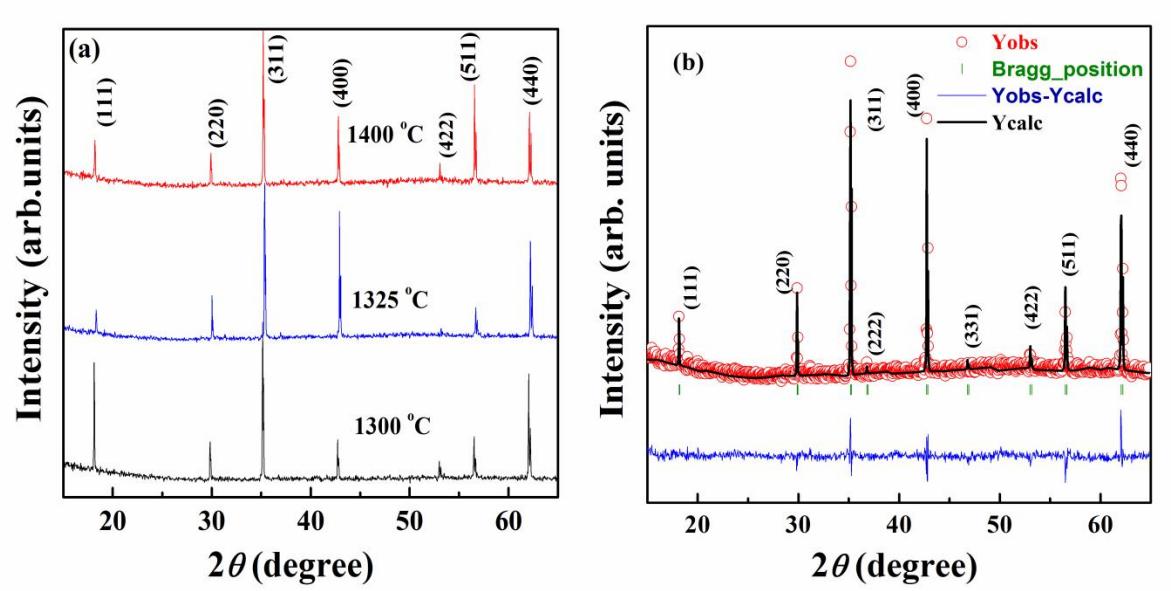

Fig. 3.8: (a) *XRD patterns of the MTO ceramics sintered at different sintering temperatures.* ***(b)*** *XRD pattern along with Rietveld refinement of MTO ceramics sintered at 1325* ^{o}C. *The circles and solid line represent the experimental and the refined data, respectively. The blue line at the bottom shows the difference between the experimental and the refined data. The vertical bars correspond to the allowed Bragg's peaks.*

The average crystallite size estimated using Williamson- Hall plot method is found to be 70 nm for the sample sintered at 1325 ^{o}C for 3 hr. There are no secondary phases

observed from the XRD patterns, suggesting the optimized processing parameters using mechanical synthesis techniques. It is interesting to note that the $MgTiO_3$ secondary phase presented in the powders milled for 35 hr was suppressed completely during the sintering process.

3.3.6.2 Microstructural analysis

The SEM micrographs of MTO ceramics sintered at different sintering temperatures for 3 hr are illustrated in Fig. 3.9. The samples sintered between 1250 ^{o}C and 1300 ^{o}C revealed porous microstructures with small average grains. The increase in the sintering temperature promoted the grain growth and an enhancement in the grain size was achieved for the specimen sintered at 1325 ^{o}C. However, the inhomogeneous grain growth was observed, for the sample sintered at temperature 1400 ^{o}C due to higher sintering temperature [35]. The average grain size of MTO ceramics sintered at 1325 ^{o}C was found to be about 5μm.

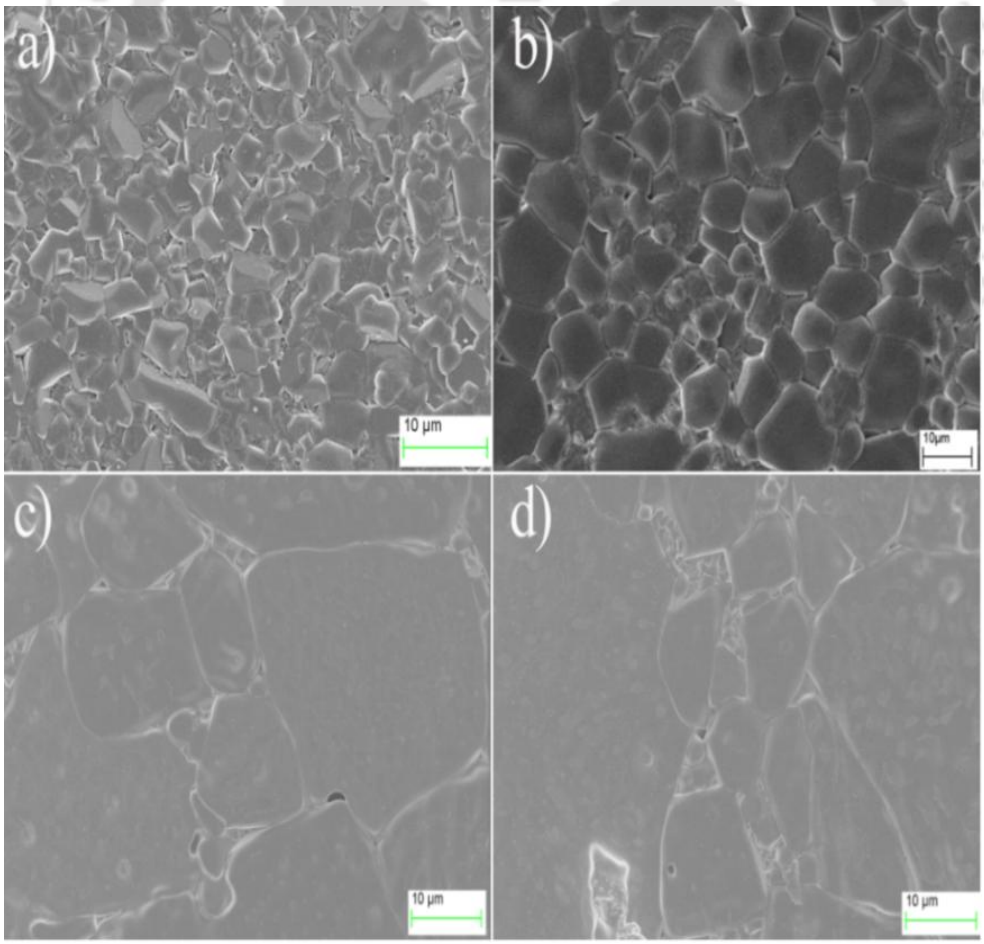

Fig. 3.9: *SEM micrographs of MTO ceramics sintered at different temperature (a) 1250 ^{o}C (b) 1300 ^{o}C (c) 1325 ^{o}C and (d) 1400 ^{o}C.*

3.3.6.3 Relative density

The variation in relative density of the samples sintered at 1325 ^oC as a function of milling time is shown in Fig. 3.10(a). It was found that the density of the MTO ceramics increases linearly with increasing the milling time. To optimize the sintering temperature of MTO ceramics, the variation of relative density as a function of sintering temperature was carried out as illustrated in Fig. 3.10(b). It was observed that the density for the specimen sintered at 1250 ^oC was low, but increases with increasing sintering temperature up to 1325 ^oC and then reduces significantly for 1400 ^oC. The maximum relative density of 97.75 % or 3.47 g/cm^3 (theoretical density of MTO is 3.545 g/cm^3) was obtained for the sample sintered at 1325 ^oC for 3 hr. This confirms that the MTO ceramics exhibited highest density at 1325 ^oC.

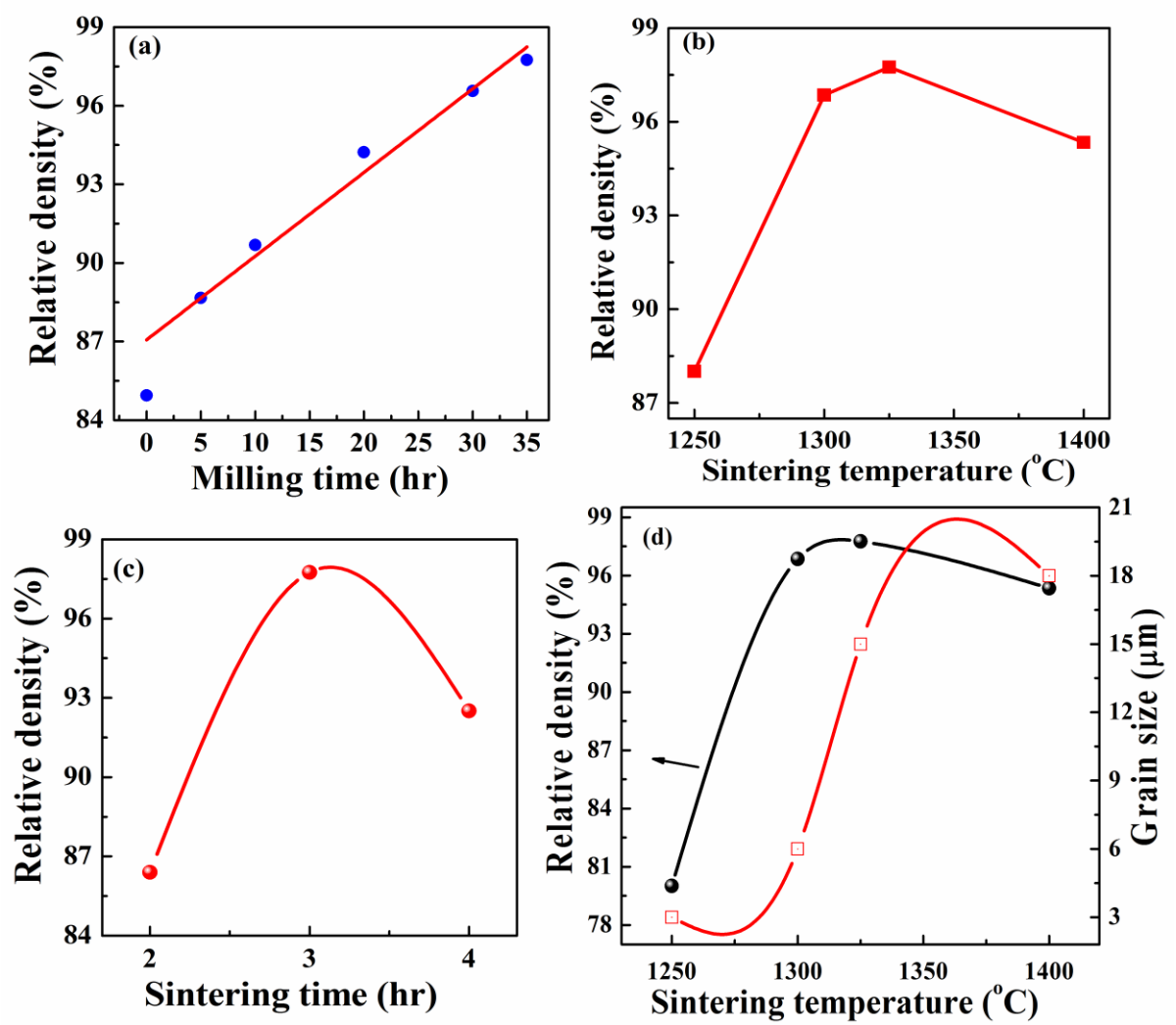

Fig. 3.10: *Dependence of relative density on (a) milling time, sintered at 1325 ^oC, (b) sintering temperature (c) sintering time, sintered at 1325 ^oC and (d) Variation of relative density and grain size as a function of sintering temperature.*

The increase in the density is mainly due to initial small particle size and uniform grain-growth. On the other hand, the decrease in the density of the sample might be caused by the presence of the pores induced during sintering process.

The initial particle size plays an important role on the densification of MTO ceramics and it is well-known that the microwave dielectric properties are heavily influenced by the density of the ceramics. During the mechanical milling, the MTO powders are heavily deformed, resulting in an increase of the internal energy of the powders. These highly reactive powders can easily diffuse during sintering and hence promotes the densification. The lower densities and porous microstructure obtained at 1250 ^{o}C may be due to the insufficient sintering temperature. Similarly, the observation of low densities at higher sintering temperatures may be correlated to abnormal grain growth as observed from SEM microstructure shown in Fig.3.9 (c). It is known that finer particles have tremendous surface areas and surface energy. The finer the particle the higher is the surface energy, which leads to a faster densification rate.

Fig. 3.10 (c) shows the dependence of relative densities on sintering time. It is evident that 3 hr of sintering is sufficient enough to prepare the single phase MTO (synthesized by mechanical alloying process) with higher density. The plot of relative density and grain size as a function of sintering temperature depicted in Fig.3.10 (d) reveals that both relative density and grain size increases with increasing sintering temperature up to 1325 ^{o}C. The sintering mechanism and increase in uniform grain size observed in this study can be explained as follows: It is known that the sintering velocity is inversely proportional to particle size, i.e., sintering is faster for finer particles. Sintering velocity can be enhanced when the diffusion increases across grain boundary and within grains [36]. Therefore, the larger grains and higher densities obtained in the present study can be correlated to uniform mixing of the powders and smaller particle sizes.

3.3.7 Microwave dielectric properties

To understand the influence of mechanical activation on MTO ceramics, microwave dielectric properties were measured. Fig. 3.11 shows the dependence of microwave dielectric constant (ε_r) and $Q\times f_o$ values on sintering temperature (for 3 hr) and sintering time (at 1325 ^{o}C) of MTO ceramics. Both the dielectric constant and $Q\times f_o$ followed a similar trend as that of relative density versus sintering temperature. This suggests that the microwave dielectric properties of the MTO ceramics were influenced by the relative

densities. It is known that the relative density plays an important role in controlling the dielectric loss, as has been shown for other microwave dielectric materials. The ε_r values of MTO ceramics were ranged between 12.6 - 13.6. The increase in ε_r values can be attributed to the increase in the relative density of the MTO ceramics, because higher the density means lower the porosity.

In order to see the effect of porosity on the dielectric constant, the measured values of the microwave dielectric constants corrected for porosity using the following equation:

$$\varepsilon_r = \varepsilon_m\left(1-\frac{3P(\varepsilon_m-1)}{2\varepsilon_m+1}\right) \tag{3.3}$$

where ε_m is the dielectric constant corrected for porosity, ε_r is the experimental dielectric constant and P is the fractional porosity [37]. The porosity corrected values were significantly higher than the experimental values and tabulated in **Table 3.1**.

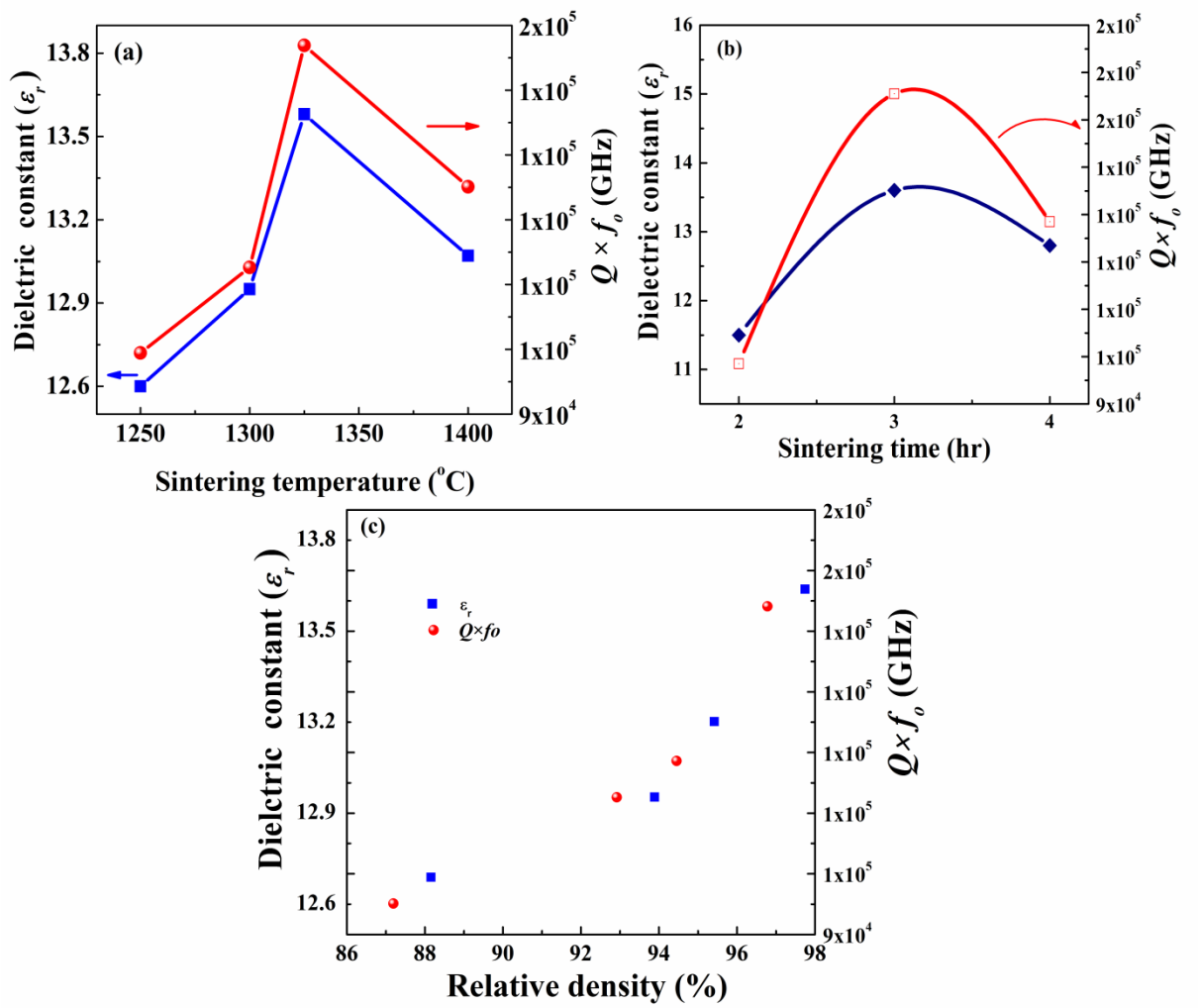

Fig. 3.11: *Dependence of dielectric constant (ε_r) and $Q \times f_o$ values on (a) sintering temperature for 3 hr and (b) sintering time at 1325 ^{o}C and (c) density of MTO ceramics.*

The product of the quality factor (Q) and resonant frequency (f_o) is considered as a tool for evaluating the quality of dielectric materials. The microwave dielectric properties and relative density obtained at different sintering temperatures were tabulated in **Table 3.1**. The maximum $Q \times f_o$ value of 155,000 GHz (at 10.4 GHz) obtained for the sample sintered at 1325 ^oC. The increase in $Q \times f_o$ values can be attributed to the increase in relative density and uniform grain size and the degradation in $Q \times f_o$ value at higher sintering temperature can be attributed to the inhomogeneous grain growth resulted in a reduction in the density as shown in Figs. 3.9 (d) and 3.10(b). The microstructure and microwave dielectric properties of the MTO ceramics were improved even at lower sintering temperatures. The specimen with large grain size is expected to have a high $Q \times f_o$ value due to the reduction in the grain boundary region. Hence, it can be concluded that under favorable conditions, grains grow uniformly to larger sizes leading to the well-densified MTO ceramics behaving like a single crystal and show that the $Q \times f_o$ (dielectric loss) values were strongly dependent both on the uniform grain size and relative density. Moreover, the $Q \times f_o$ values obtained in the present study are much higher than the values reported by Belous et al. [13, 41].

Table 3.1: *Relative density, dielectric constant corrected for porosity (ε_m) and microwave dielectric properties of MTO ceramics sintered at different temperatures.*

Sintering temperature	**Relative density(%)**	**ε_r (measured)**	**ε_m (corrected)**	**$Q \times f_o$ (GHz)**
1250 ^oC	80.01	12.60	17.37	99,430
1300 ^oC	96.85	12.97	13.53	112,600
1325 ^oC	97.75	13.60	14.02	155,500
1400 ^oC	95.34	13.07	13.94	125,000

It may be noted that there are several factors such as density, lattice vibration modes, porosity, grain boundaries, impurities, secondary phases, lattice defects and inclusions in real homogeneous ceramics that contribute to the dielectric loss at microwave frequencies [38-40]. But in our present investigation, we observed that the variation of $Q \times f_o$ showed a similar trend with that of density, suggesting that the $Q \times f_o$ of the MTO ceramics was mainly influenced by the relative density. Moreover, MTO ceramics sintered at 1325 ^oC showed a relatively uniform microstructure compare to other

sintering temperature. This indicates that the sintering temperature might also have significant effect on the dielectric-loss of the ceramics. Generally, the factors that influence the microwave dielectric loss fall into two categories: (i) intrinsic and (ii) extrinsic losses [41, 42]. Intrinsic losses in crystals arise from anharmonic lattice forces that mediate the interaction between crystal and phonons. This leads to damping of the optical phonons and therefore of the microwave field. On the other hand the extrinsic losses are dominated by extended dislocations, grain boundaries, porosity, oxygen vacancies and secondary phases, which are heavily dependent on the processing conditions. These losses are caused by either dipole relaxations of impurities concentrated at interfaces or relaxations of space charge polarizations present at the interfaces. Interfacial polarization was thought to play an important role in porous materials.

The variation of ε_r and $Q \times f_o$ values as a function of relative density are plotted in Fig. 3.11 (c). It was observed that the dielectric constant and $Q \times f_o$ increases with increasing in relative density especially at higher values of relative density. This reveals that the relative density plays an important role in controlling the microwave dielectric loss. From all of the studies, it can be concluded that the mechanical synthesis promoted the favorable conditions in the preparation of MTO ceramics with the improvement in the relative density at lower sintering temperatures, uniform microstructure, which exhibited better microwave dielectric properties as compared to the samples prepared by solid-state reaction method [43].

3.3.8 Low frequency dielectric properties

The low frequency dielectric properties of MTO ceramics in the frequency range of 5 kHz to 1 MHz from room temperature to 500 ^oC were measured. Fig. 3.12 illustrates the variation of dielectric constant and dielectric loss as a function of frequency at different temperatures for the MTO ceramics sintered at 1325 ^oC for 3 hr. From the plots, it is observed that at lower temperature both the dielectric permittivity (ε_r) and dielectric loss decreases monotonically with increasing frequency up to a certain limiting range (~ 35 kHz), and above that it becomes frequency - independent. This may be due to the inability of electric dipoles to follow the fast variation of the alternating applied electric field. The higher values of ε_r at lower frequencies and at higher temperatures indicate that the polarization in the test materials is larger. This is due to simultaneous presence of all types of polarizations like space charge, dipolar, ionic and electronic, which is found to decrease with the increase in frequency. This also signifies that the resistive grain

boundaries become conducting at these temperatures and that grain boundaries are not relaxing even at higher frequency and temperature.

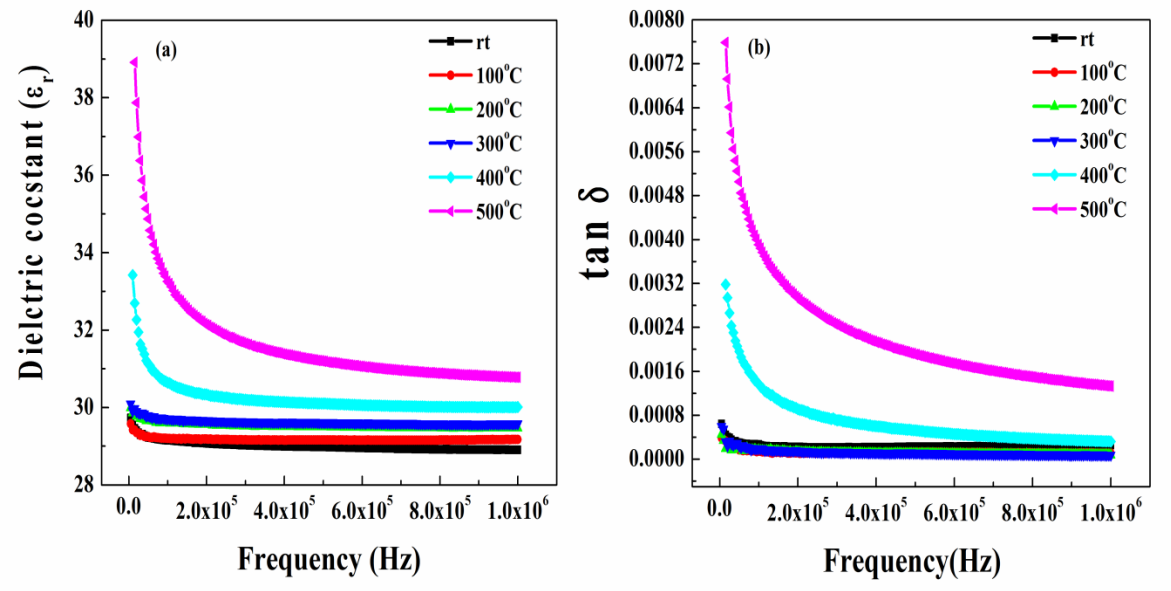

Fig. 3.12: *Frequency dependence dielectric properties of MTO ceramics sintered at 1325 ^oC for 3 hr.*

The decrease in dielectric permittivity with frequency observed in such type of materials can be explained on the basis of Maxwell-Wagner model [44] in agreement with Koop's phenomenological theory [45]. According to Koop's model, the dielectric materials can be imagined as a heterogeneous structure consisting of high conducting grains with ε_1, σ_1 and thickness d_1 separated by thin layers of poorly conducting grain boundaries with ε_2, σ_2 and thickness d_2. These grain boundaries could be formed during the sintering process either by superficial reduction or oxidation of crystallites in the pores materials due to their direct contact with the firing atmosphere. Koop's assumed that, $y = d_2 / d_1 << 1$, $\sigma_2 << \sigma_1$, $\varepsilon_1 \approx \varepsilon_2$, and the dielectric constant of the sample ε_r, is given by,

$$\varepsilon_r = \varepsilon_1 / y \approx \varepsilon_2 / y \qquad (3.4)$$

Thus the grain boundaries control the behavior of ε_r at lower frequencies, but at higher frequencies only grains are more active in electrical conduction. The thinner the grain boundary layers, the higher the value of ε_r.

The dielectric loss shows almost a similar behavior of dielectric constant as seen from Fig. 3.12 (b). This loss factor curve is considered to be caused by ion migration

losses, electron polarization losses and dipolar relaxation losses. At lower temperatures, the monotonic decrease of dielectric loss indicated that at lower temperatures, the relaxation is absent in the materials, i.e., relaxation species are immobile defects and the orientation effects may be associated. Also the decreasing magnitude of ε_r and dielectric loss with increasing frequencies implied that relaxation in the materials is temperature dependent. The dielectric constant and dielectric losses are in the range of 28.1 to 38.9 and 2.0×10^{-4} to 7.5×10^{-3} in the temperature range of room temperature to 500 ^{o}C, respectively.

To know the conduction mechanism in MTO samples, the ac conductivity is studied. The dielectric conductivity in ceramics is mainly controlled by the migration of charge species under the action of electric field and the defect-ion complexes, the polarization field, the relaxation etc. The ac conductivity (σ_{ac}) of the MTO ceramics is calculated from the dielectric data by using the relation:

$$\sigma_{ac} = \varepsilon' \varepsilon_o \omega \tan\delta \tag{3.5}$$

where $\omega = 2\pi f$ (f being the frequency used); ε_o is the permittivity of vacuum (8.85×10^{-12} F/m) and tan δ is the dielectric loss factor. Thus, σ_{ac} is directly related to the dielectric properties of the materials.

The ac conductivity of the system depends on the dielectric properties and sample capacitance. Fig. 3.13 (a) shows the variation of ac conductivity as a function of frequency at different temperatures. It is observed that the ac conductivity increases not only with the frequency but also with the measurement temperature. Frequency dependent of ac conductivity indicates that conduction occurs due to hoping of charge carriers among the localized states. As the frequency of the applied field increases, the conductive grains become more active and thereby promoting electron hopping between two adjacent sites. At lower frequencies, the grain boundaries are more active and hence the electron-hopping between Ti^{+4} and Ti^{+3} ions is less. But at higher frequencies, the electron-exchange between Ti^{+4} and Ti^{+3} ions might not be able to follow the alternation of the applied ac electric field frequencies and therefore lags behind. Thus the conductivity decreases at higher frequencies. This behavior can be attributed to the relaxation process associated with the domain reorientation, domain wall motion and the dipolar behavior.

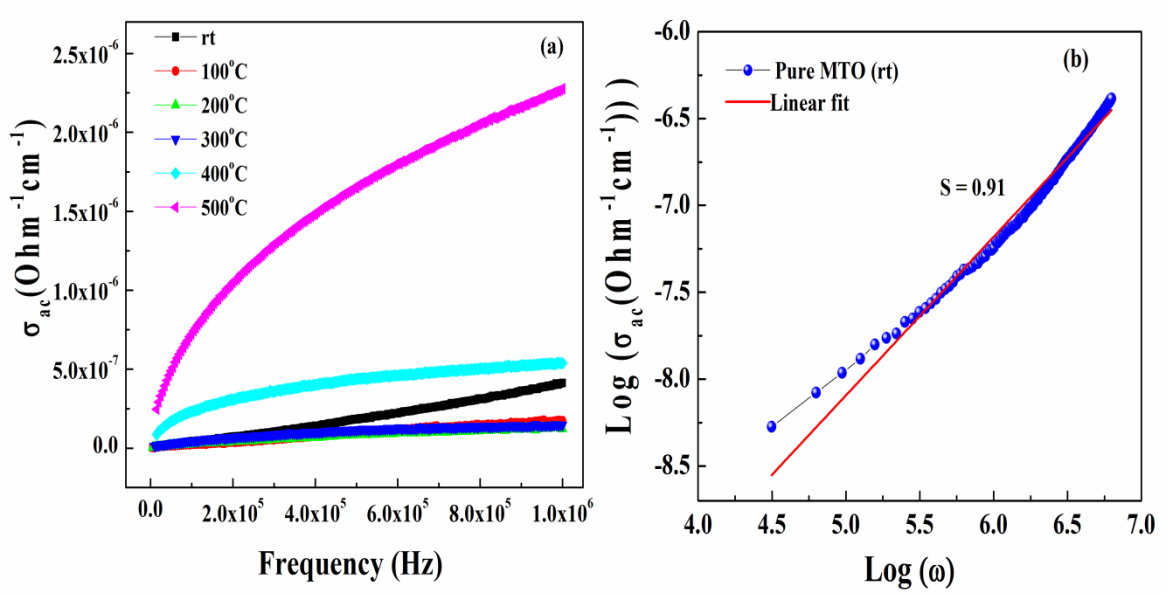

Fig. 3.13: *Variation of (a) σ_{ac} as a function of frequency for different temperatures and (b) log (σ_{ac}) as a function of frequency for MTO ceramics sintered at 1325 ^oC for 3 hr.*

Generally, for oxide ceramic materials, the frequency dependence of ac conductivity can be expressed by the empirical formula [46-48],

$$\sigma(\omega) = A\omega^s \tag{3.6}$$

where *s* is a dimensionless parameter (power law exponent) which varies between 0 and 1 depending on the temperature, A is a temperature dependent constant having unit of conductivity and ω is the angular frequency at which the conductivity was measured. The exponent *s* is a measure of the degree of correlation, i.e., *s* should be zero for random hopping and tends to be one as the correlation of charge carrier increases. In the present work, the value of *s* was calculated from the relation log (σ_{ac}) versus logω, over the studied range of frequency using eqn. (3.6), at room temperature and depicted in Fig. 3.13(b). In the present systems, *s* values have been found to be 0.91~1, which clearly indicated that there are strong correlations between the charge carriers in the systems, i.e., long range motion of the carriers.

Fig.3.14 illustrates the variation of dielectric constant (ε_r) and loss tangent (tan δ) as a function of temperature of the MTO sample measured at 10^6 Hz. It is observed that both the dielectric constant and tan δ increases linearly with increasing temperature. The observed behavior of the dielectric constant with temperature can be explained as follows: at room temperature, the ions cannot oriented themselves with respect to the direction of

the applied filed, therefore, they possess a week contribution to the polarization and hence to the dielectric constant. As the temperature increases, the conduction relies on the formation of the lattice defects under the action of thermal excitation

This creates vacancies through which ions motion may proceed under the action of external electric field. Therefore, with increasing temperature the ions gain enough thermal energy to follow the change in the external field quite easily. This enhances their contribution to the polarization leading to an increase in the dielectric constant of the materials. The value of the loss tangent is very small and nearly constant up to 300 ^{o}C. At high temperatures, the dielectric losses caused by the dipole mechanism reach their maximum value and the degree of dipole orientation increases. Apart from dipole losses, electrical conduction also increases with increase temperature. These factors would cause the increase in both dielectric constant and dielectric loss of MTO ceramics with increasing temperature.

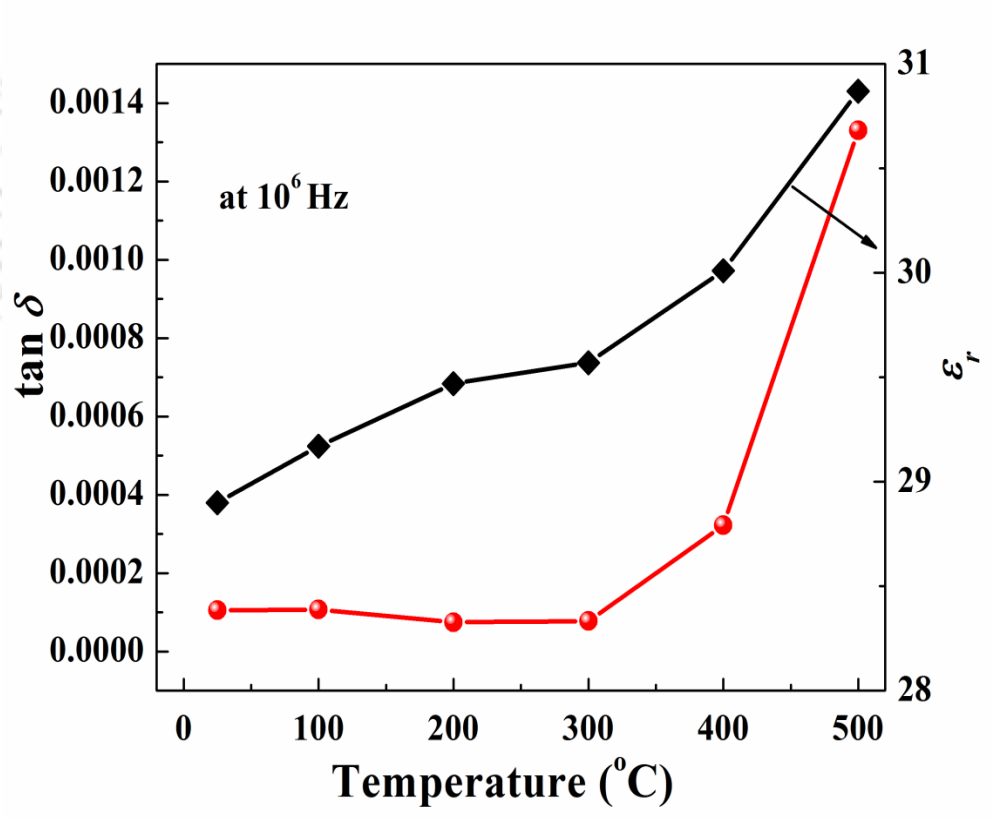

Fig. 3.14: *Variation of dielectric constant and loss tangent (tan δ) as a function of temperature of MTO ceramics, measured at 10^6 MHz*

3.4 Conclusions

The effect of mechanical alloying on structural, microstructural, optical and the microwave dielectric properties of pure MTO ceramics was studied systematically in this chapter. The salient features of the MTO ceramics from the current investigations are as follows:

- The single phase Mg_2TiO_4 ceramics were successfully prepared by mechanical alloying process and the processing parameters were optimized to reduce the sintering temperature of MTO ceramics.
- A maximum relative density of 97.75 % was obtained for the MTO sample sintered at 1325 ^oC for 3 hr. In addition, the effect of milling time on particle size, crystal structure and the microstructure was studied through XRD, SEM, and TEM analysis.
- Williamson-Hall (W-H) method was carried out to understand the origin of the broadening in the XRD peaks. The microstructural analysis reveals the nanocrystallinity nature of MTO ceramics prepared by mechanical alloying method.
- The thermal decomposition behavior of the milled powders was examined by a thermo-gravimetric analyzer (TGA) in argon atmosphere.
- The best microwave dielectric properties of ε_r ~ 13.68, $Q \times f_o$ ~ 155,000 GHz (measured at 10.4 GHz) were obtained for the MTO ceramics sintered at 1325 ^oC for 3 hr. The increase in $Q \times f_o$ values was attributed to the increase in uniform grain size and increase relative density.
- The low frequency dielectric behaviors of MTO ceramics in the frequency range of 5 kHz to 1 MHz from room temperature to 500 ^oC were measured.
- The Mg_2TiO_4 ceramic prepared by mechanical synthesis and having a high-quality factor promising material suitable for commercial high-frequency applications.

3.5 References

[1] C. L. Huang, J. J. Wange, *J. Am. Ceram. Soc.*, **90** (2007) 858.

[2] C. L. Huang, S. S Liu, *J. Am. Ceram. Soc.*, **91** (2008) 3428.

[3] C. L. Huang, J. Y Chen, *J. Am. Ceram. Soc.*, **92** (2009) 675.

[4] C. L. Huang, J. Y Chen, *J. Alloys Compd.*, **485** (2009) 706.

[5] L. Li, X. Ding, Q. Liao, *Ceram. Inter.*, **38** (2012) 1937.

[6] C. L. Huang, C. E. Ho, *Int. J. Appl. Ceram. Technol.*, **7** (2010) E163.

[7] C. L. Huang, S. S. Liu, S. H. Chen, *J. Alloys Compd.*, **480** (2009) 794.

[8] P. S. Anjana, M. T. Sebastain, M. N. Suma, P. Mohanan, *Int. J. Appl. Ceram. Technol*., **5** (2008) 325.

[9] C. L. Huang, J. F. Tseng, *Mater. Lett.*, **58** (2004) 3732.

[10] R. J. Cava, *J. Mater. Chem.*, **11** (2001) 54.

[11] R. K. Bhuyan, T. Santhosh Kumar, A. R. James, D. Pamu, *Inter. J. Appl. Ceram. Technol.*, **10** (2013) E18.

[12] C. L. Huang, C. E. Ho, *Int. J. Appl. Ceram. Technol*., **7** (2010) E163.

[13] A. Belous, O. Ovchar, D. Durilin, M. M. Krzmanc, M. Valant, D. Suvorov, *J. Am. Ceram. Soc.*, **89** (2006) 3441.

[14] Wechsler, R. B. Von Dreele, *Acta Cryst*., B45 (1989) 542.

[15] T. Takada, S. F Wang, S. Yoshikawa, S. T. Jang, R. E. Newnham, *J. Am. Ceram. Soc.*, **77** (1994) 2485.

[16] D. Pamu, G. Lakshmi Narayana Rao, K. C. James Raju, *J. Alloys Compd*., **475** (2009) 745.

[17] H. Lu, C. C. Tsai, *Mater. Sci. Eng. B.*, **55** (1985) 95.

[18] M. H. Liang, S. Y. Wu, C. T. Hu, I. N. Li, *Mater. Chem. Phys*., **79** (2003) 276.

[19] N. Stubicar, A. Tonejc, M. Stubicar, *J. Alloy Compd*., **370** (2004) 296.

[20] M. Kamruddin, P. K. Ajit Kumar, R. Nithya, A. K. Tyagi, B. Raj, *Scripta Materialia*, **50** (2004) 417.

[21] H. Yang, Y. Hu, A. Tang, S. Jin, G. Qiu, *J. Alloy. Compd*., **363** (2004) 271.

[22] K. T. Paul, S. K. Satpathy, I. Manna, K. K. Chakraborty, G. B. Nando, *Nanoscale Res. Lett*., **2** (2007) 397.

[23] L. B. Kong, J. Ma, W. Zhu, O. K. Tan, *J. Alloys Compd*., **322** (2001) 290.

[24] Suryanarayana, *Mechanical Alloying and Milling*, Marcel Dekker, (2004).

[25] R. A. Young, "The Rietveld Method" *International Union of Crystallography*, Oxford University Press, London (1996).

[26] G. K. Williamson, W. H. Hall, *Acta Mater.*, **1** (1953) 22.

[27] J. Xu, G.S. Collins, L. Peng, M. Atzmon, *Acta Mater.*, **47** (1999)1241.

[28] N. Obradovic, N. Labus, T. Sreckovic, M. M. Ristic, *Mat. Sci. Forum*, **518** (2006)131.

[29] J. C. Tauc, "*Optical Properties of Solids"*, North-Holland, Amsterdam, 1972.

[30] H. Kominami, M. Tanaka, K. Hara, Y. Nakanishi, Y. Hatanaka, *Phys. Status Solidi C.*, **3** (2006) 2758.

[31] A. Golubovic, M. Radovic, *J. Serb. Chem. Soc.*, **76** (2011) 1561.

[32] J. Stade, D. Hahn, R. Dittmann, *J. Lumin.*, **8** (1974) 308.

[33] A. V. Ferri, J. C. Sczancoski, L. S. Cavalcante, E. C. Paris, J. W. M. Espinosa, A. T. de Figueiredo, P. S. Pizani, V. R. Mastelaro, J. A. Varela, and E. Longo, *Mater. Chem. Phys.*, **117** (2009) 192.

[34] R. K. Bhuyan, T. S. Kumar, A. Perumal, P. Saravanan, D. Pamu, *J. Exper. Nano. Sci.*, **8** (2013) 371.

[35] Pamu, G. Lakshmi Narayana Rao, K. C. James Raju, *J. Am. Ceram. Soc.*, **95** (2012) 126.

[36] S.-J. L. Kang "*Sintering*" Elsevier, Burlington, MA 2005.

[37] S. J. Penn, N. M. Alford, A. Templeton, X. Wang, M. Xu, M. Reece, K. Schrapel, *J. Am. Ceram. Soc.*, **80** (1997) 1885.

[38] B. D. Silverman, *Phys. Rev.*, **125** (1962) 1921.

[39] H. Tamura, *J. Eur. Ceram. Soc.*, **26** (2006) 1775.

[40] J. D. Breeze, J. M. Perkins, D. W. McComb, N. McN. Alford, *J. Am. Ceram. Soc.*, **92** (2009) 671.

[41] W. S. Kim, T. H. Hong, E. S. Kim, K. H. Yoon, *Jpn. J. Appl. Phys.*, **37** (1998) 5367.

[42] J. Petzelt, S. Pacesova, J. Fousek , S. Kamba, V. Zeleny, V. Koukal, J. Schwarzbach, B. P. Gorshunov, A. A. Volkov, *Ferroelectrics*, **93** (1989) 77.

[43] A. Belous, O. Ovchar, D. Durilin, M. Valant, M. M. Krzmanc, D. Suvorov, *J. Euro. Ceram. Soc.*, **27** (2007) 2963.

[44] J. Maxwell, "*Electricity and Magnetic"*, V-1 section 328, Oxford University Press, London (1873).

[45] C. Koops, *Phys. Rev.*, **83** (1951)121.

[46] S. R. Elliiott, *Adv. Phys*., **36** (1987) 135.

[47] A. Ghosh, *Phys. Rev. B*, **45** (1992) 11318.

[48] J. Suchanicz; *Ferroelectrics*, **209** (1998) 561.

Chapter 4

Microwave dielectric properties of Mg_2TiO_4 ceramics added with CeO_2 nanoparticles

4.1 Introduction

With the tremendous increase in the development of microwave and millimeter wave based communication technologies, the production of dielectric resonators has emerged as one of the most rapid growth areas in electro ceramic manufacturing [1, 2]. However, as the carrier frequency of communication systems extends to a higher frequency region, the materials with high quality factor and low dielectric constant would play a major role on controlling the dielectric loss and allowing a fast communication of the electronic signal at ultrahigh frequencies. For instance, low loss dielectrics with different dielectric constants become the most popular materials due to their applications in today's Global Positioning Systems (GPS) and patch antennas with different sizes. In addition, these materials should have nearly a zero temperature coefficient of resonant frequency (τ_f), as they affect broadness and stability of the resonant frequency [2, 3].

Mg_2TiO_4 is one of the promising low loss and low cost dielectric ceramic material suitable for microwave and millimeter wave frequency applications [4]. It is well-known that MTO based ceramics have wide applications such as dielectric resonator, heat resistor, microwave integrated circuit, wave guides, capacitors for temperature compensation and antennas [5]. It possesses excellent microwave dielectric properties ($\varepsilon_r \approx 14$, $Q \times f_o$ = 150,000 GHz at 10 GHz and $\tau_f \approx -50$ ppm / ^oC) [6, 7]. However, MTO ceramics prepared by solid - state route require higher sintering temperatures which restrict these materials for practical applications. Further, it is difficult to densify the material at lower sintering temperatures without any sintering aids. Therefore, to reduce the sintering temperature of the ceramics, three methods were generally adopted: (a) addition of low softening glass or liquid phase sintering aid [8, 9], (b) chemical processing [10] and (c) the use of smaller particles as the starting material [11]. Out of these processes, the later one is found to be one of the effective

and inexpensive methods to achieve higher densities at lower sintering temperatures. At the same instant, the additives, which are used to improve sinterability, should not degrade the microwave dielectric properties. Hence, it is necessary to optimize the concentration, additive materials and the processing parameters to achieve best microwave dielectric properties at lower sintering temperatures. There are only a few reports on the synthesis of MTO ceramics at lower sintering temperature by adding the impurities with low melting temperature [12-14] and by chemical processing methods [15, 16].

Recently, ceramic nanoparticles have attracted much attention, as they are effectively acting as a bridge between bulk materials and atomic structures. A sole aspect of nanoscale materials is the tremendously increased ratio of surface area to volume, which opens new possibilities on the surface dependent phenomena. At these reduced dimensions, they provide an enormous driving force during the sintering especially at elevated temperatures and hence the surface energy of the nanoparticles substantially affects the interior bulk properties of the host materials. With these smaller particles, the sintering can take place at reduced temperatures over shorter time scales than for the larger particles. As discussed in chapter 3, the physical properties of the ceramics are very much sensitive to their density and the microstructures. Therefore, the understanding on the control of the above properties of the ceramics with respect to processing parameters such as initial powder natures, types of additives and the sintering temperature is very much essential. It was reported that CeO_2 and Nd_2O_3 forms flux and improves the sintering ability in the case of ZST ceramics [17]. Chen et al. [18] reported a reduction in the sintering temperature from 1500 ^oC to 1200 ^oC with the addition of ultrafine CeO_2 powders. Similarly, Takagi et al. [19] reported the occurrence of the particle size dependent melting, when the average particle size is on the order of nanometers. More recently, Santhosh et al. [20] reported the reduction of sintering temperature of $MgTiO_3$ ceramic from 1400 to 1300 ^oC with the addition of 0.5 wt.% of CeO_2 nanoparticles which showed good microwave dielectric properties.

The dielectric loss is the factor that primarily limits these materials as dielectric resonators in microwave devices [21, 22]. Therefore, the understanding of nature of such dielectric loss in these materials is essential to enable them in devices. Minimization of the dielectric loss is one of the important tasks to improve the material performance. Thus, it is

essential to comprehend the fundamental mechanism of the dielectric loss at microwave frequencies. In general, the microwave dielectric loss originates from intrinsic and extrinsic loss mechanisms [23]. The intrinsic loss occurs primarily due to the anharmonicities of the lattice vibration and the extrinsic loss is associated to factors such as impurities, secondary phases, non - uniform grain growth and porosity. However, there is no clear understanding of the mechanisms themselves as well as the relationships between these mechanisms. Dielectric measurements at cryogenic temperatures can provide important insights about the dynamics of molecular and ionic matter, which allows advancement in the understanding of the intrinsic loss mechanisms [24, 25].

In order to find suitable materials for cryogenic electronic devices, the microwave dielectric properties at cryogenic temperatures is necessary. Currently there is very limited data available regarding the dielectric properties of microwave materials at cryogenic temperatures. There is no systematic study with the addition of CeO_2 nanoparticles to MTO ceramics. This motivated us to study and understand the microwave dielectric properties of the MTO ceramics at room temperature and at cryogenic temperatures. In this chapter, we have chosen very small amounts of CeO_2 nanoparticles as sintering aid and to see its effect on the sintering ability, densification, crystal structure, microstructure and the microwave dielectric properties of MTO ceramics. Further, the microwave dielectric properties of pure MTO and MTO ceramics added with different concentration of CeO_2 nanoparticles measured at cryogenic temperatures are reported.

4.2 Experimental details

MTO ceramics were synthesized by conventional solid - state reaction method from individual high purity oxide powders (> 99.99%, M/s Sigma Aldrich) MgO and TiO_2. The starting materials were mixed in accordance with the desired stoichiometry of the MTO ceramics and then the powders were grounded in distilled water for 10 hours (hr) by using a planetary ball mill (M/s Fritsch, GmBH, Germany) at higher speeds. All mixtures were dried and calcined at 900 ^oC for 3 hr. The calcinated powders were remilled for 10 hr. Subsequently, a different weight percent (wt.%) of CeO_2 nanoparticles was added to the milled powders and further milled for 1 hr. The CeO_2 nanoparticles with an average particle size of 80 nm were procured from M/s Alfa Aesar, USA. Finally, the as milled powders were

uniaxially pressed into pellets with dimensions of 10 mm in diameter and 4 - 5 mm in thickness under a pressure of 200 MPa. The samples were sintered at 1250 -1400 ^oC for 3 hr. The heating and cooling rates were set as 10 ^oC / min and 1 ^oC / minute respectively.

The thermal decomposition behavior of the dried powder was examined by a thermogravimetric analyzer and a differential scanning calorimeter at a heating rate of 10 ^oC / minute in argon atmosphere. The bulk densities of the sintered samples were calculated by Archimedes method. Structural phases were identified by XRD technique using Cu-Kα radiation. Surface morphology of the powders was characterized using scanning electron microscope. The dielectric properties ε_r and Q_u of the materials were measured in the microwave frequency range using resonance technique as described in Chapter 2. Dielectric properties in the temperature range of 6.5 K to 295 K were measured by placing the copper cavity on the cold head of a closed cycle refrigerator (ARS Cryo), connected with a Vector Network Analyzer (E8356B, Agilent Technologies, Palo Alto, CA).

4.3 Results and discussion

4.3.1 Thermal and phase analysis

Fig. 4.1 shows the DTA and DSC curves of the pure MTO powders. The initial weight loss of 5 % was attributed to the evaporation of moisture at 100 ^oC. The weight loss observed in the temperature around 400 ^oC is very prominent and confirmed to the formation of $MgTi_2O_5$ [26]. Further, two endothermic peaks around 120 and 600 ^oC, representing the weight loss of ~ 5 % caused by evaporation of molecular water and 7 % due to the formation of secondary phase of $MgTiO_3$, respectively were observed. The formation of secondary phases was also confirmed by the XRD results as discussed in the next session. On further increasing the temperature, we observed an exothermic peak around 900 ^oC corresponding to the crystallization of MTO phase and removal of all secondary phases.

To confirm the crystallization of MTO powders calcined at different temperatures, XRD patterns were recorded and illustrated in Fig.4.2. It is clearly evident that when the calcination temperature is below about 700 ^oC, the powders have $MgTi_2O_5$ and $MgTiO_3$ as major phases along with a significant MTO phases. With increasing the calcination temperature to 800 ^oC, the $MgTi_2O_5$ and MTO phases are increased at the expense of $MgTiO_3$ phase and the powders contains only the MTO phases (Mg_2TiO_4) with a cubic

structure for the powders calcined at 900 ^{o}C. The average crystallite size estimated using Scherrer's formula from the (311) reflection increases with increasing the calcination temperatures. The observed results are in good agreement with these results obtained using DSC / TGA analysis.

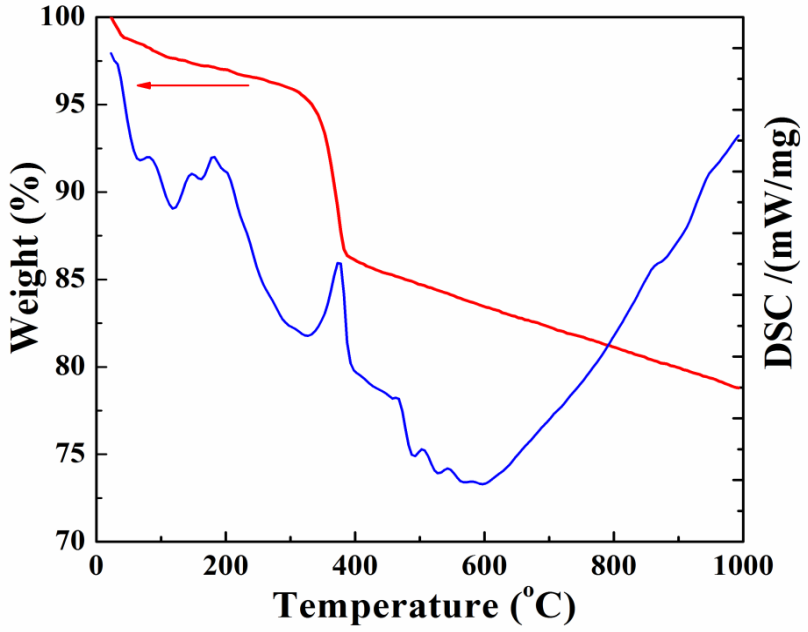

Fig. 4.1: *DSC / TGA curves of the pure MTO powders.*

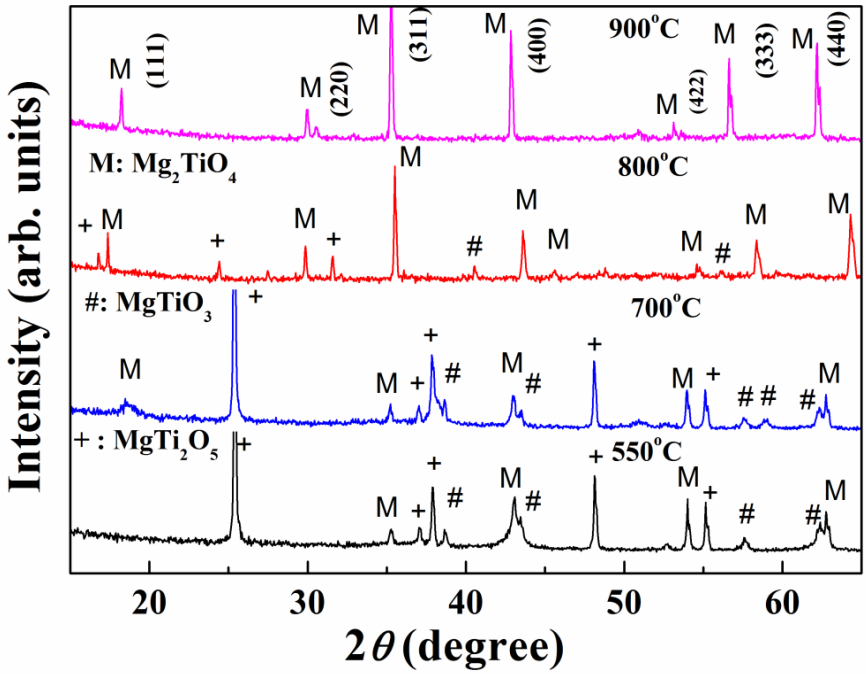

Fig. 4.2: *XRD patterns of MTO powders calcined at different temperatures for 3 hr.*

4.3.2 Structural analysis of sintered MTO ceramics

To study the effect of CeO_2 nanoparticles on the crystal structure of MTO ceramics, room temperature XRD patterns were recorded for all the samples. Fig.4.3 (a) illustrates the XRD pattern of the pure MTO ceramic sintered at 1400 ^oC and MTO + x CeO_2 (x = 0.5, 1.0 and 1.5 wt.%) ceramics sintered at 1300 ^oC for 3 hr. All samples exhibit an inverse spinel type crystal structure (ICSD – PDF # 06-5792) and there is no evidence of additional phases up to 1.5 wt.% of CeO_2. It may be noted that, it is difficult to suppress the secondary phases such as $MgTiO_3$ and $MgTi_2O_5$ in the MTO ceramics prepared by solid - state reaction method. In contrast, in the present study, no appearance of such secondary phases is observed. This might be due to the effect of ball milling and smaller initial particle sizes. The average crystallite size of the MTO ceramics was ranged between 50 and 80 nm. Although the ionic radii of Ce^{4+} (0.87 nm) is larger than Mg^{2+} (0.72 nm) and Ti^{4+}(0.605 nm), the determined values of the lattice constants of the CeO_2 added MTO ceramics revealed that there is no deviation in the lattice constants as compared to the pure MTO ceramics [27]. This confirms that the mixed CeO_2 nanoparticles do not enter into crystal lattice of the MTO, but remain at the grain boundary.

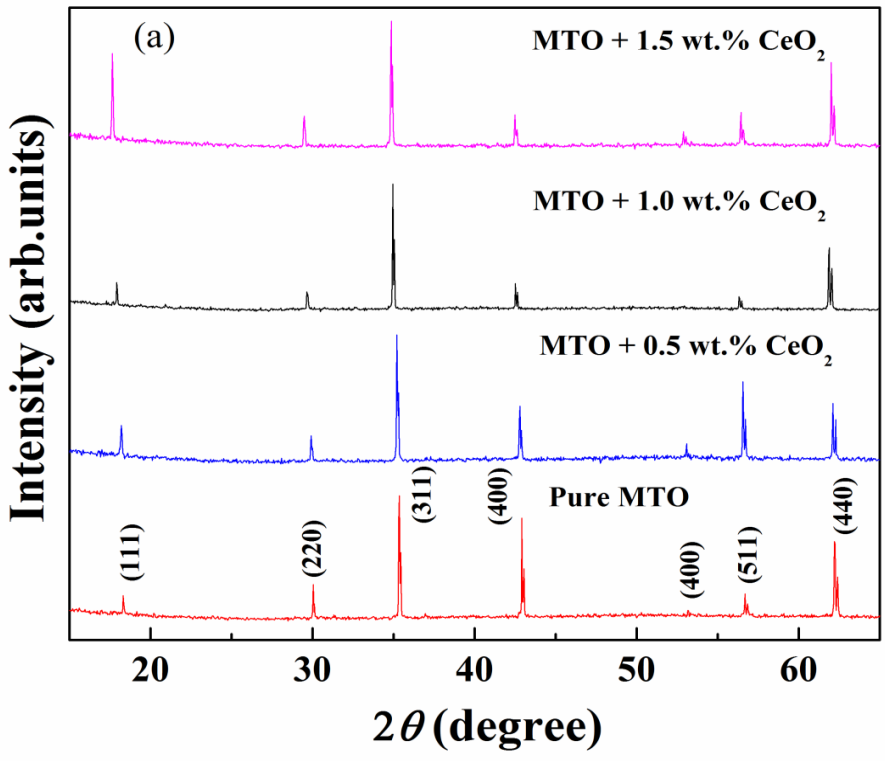

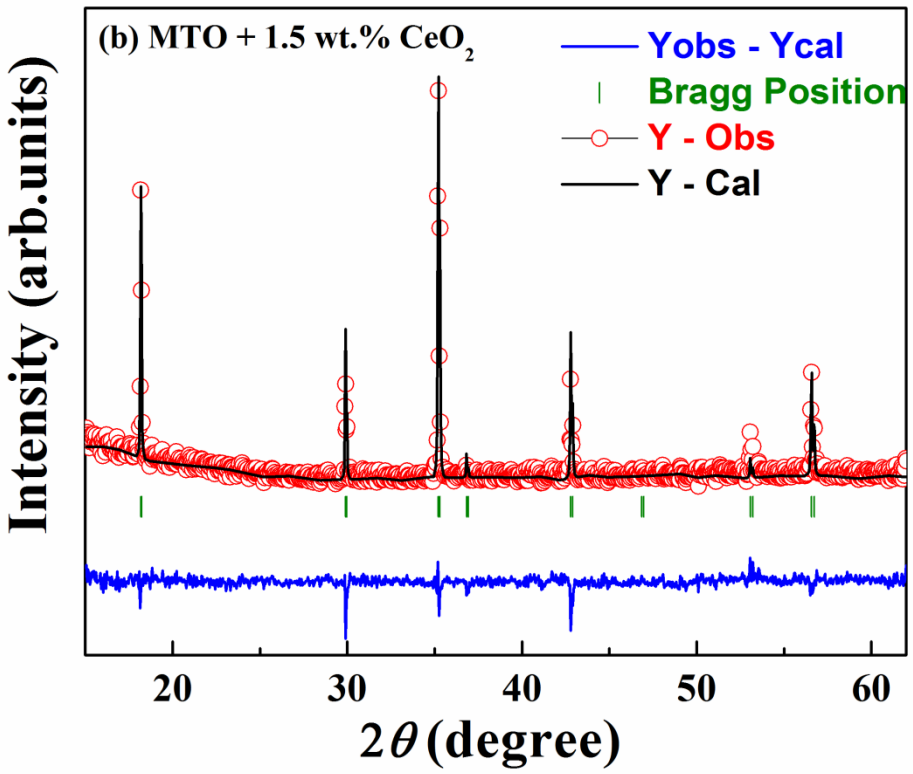

Fig.4.3 (a) *XRD patterns of the pure MTO ceramic sintered at 1400 ^oC and MTO + x CeO_2 (x wt.%) ceramics sintered at 1300 ^oC for 3 hr and* ***(b)*** *XRD pattern along with Rietveld refinement of the MTO+1.5 wt.% CeO_2 ceramics, sintered at 1300 ^oC for 3 hr.*

The XRD patterns of all samples could be refined by taking *Fd-3m* space group in cubic cell. The typical XRD pattern along with the Rietveld refinement of MTO + 1.5 wt.% of CeO_2 nanoparticles sample sintered at 1300 ^oC for 3 hr is shown in Fig.4.3 (b). The refinement was carried out by varying cell parameters, position of the Mg, Ti, and O atoms, occupancy and thermal parameters. The refined parameters with lattice constants obtained from Rietveld analysis of the 1.5 wt.% added MTO sample are $a = b = c = 8.4462$ Å, with $\chi 2$, R_{Brag} factor and R_f factor were found to be 0.66, 12.46 and 11.84, respectively. The derived lattice constant from Rietveld refinement was well set with the standard lattice constants of MTO ceramics prepared with solid - state reaction method. Hence, it indicates that CeO_2 nanoparticles are not forming a solid solution with MTO matrix but possibly segregated at the grain boundary.

4.3.3 Surface morphology and average grain size

To determine the effect of CeO_2 nanoparticles on morphological nature of MTO ceramics, SEM micrographs were obtained for all the samples. Fig. 4.4 depicts the SEM micrographs of pure MTO ceramics sintered at 1400 ^oC and MTO + *x* CeO_2 (*x* wt.%) ceramics sintered at 1300 ^oC for 3 hr. It was observed that the microstructure of pure MTO ceramics contains pores and non - uniform grain structure. On the other hand, the CeO_2 mixed MTO ceramics exhibit a uniform grain structure with increased grain size from 3.5 μm to 6.5 μm for the increase of *x* from 0.5 to 1.5, respectively. The addition of CeO_2 nanoparticles improves the sintering ability even at reduced sintering temperature as compared to pure MTO ceramics [6]. Since, the MTO + *x* CeO_2 (*x* wt.%) samples exhibited a large and uniform grain size, we have extended the investigation of the microstructure for the samples sintered at different sintering temperatures

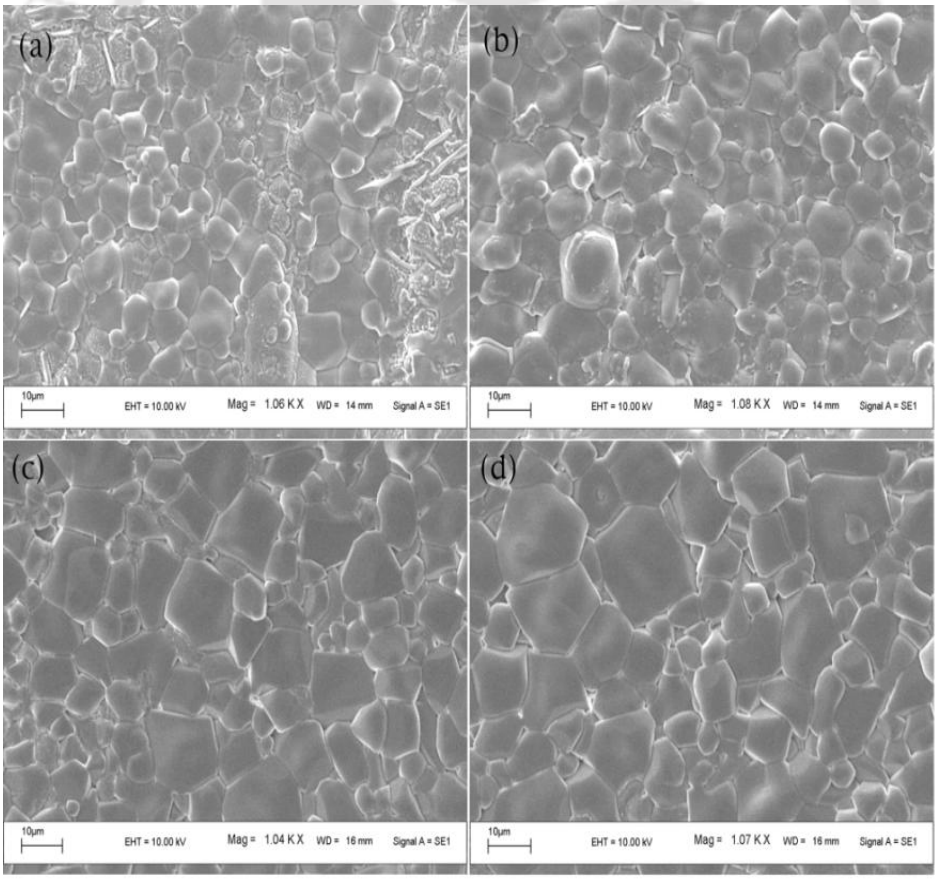

Fig. 4.4: *SEM images of (a) Pure MTO ceramics sintered at 1400 ^oC and MTO + x CeO_2 (x wt.%) ceramics with (b) x = 0.5, (c) x = 1 and (d) x = 1.5, sintered at 1300 ^oC for 3 hr.*

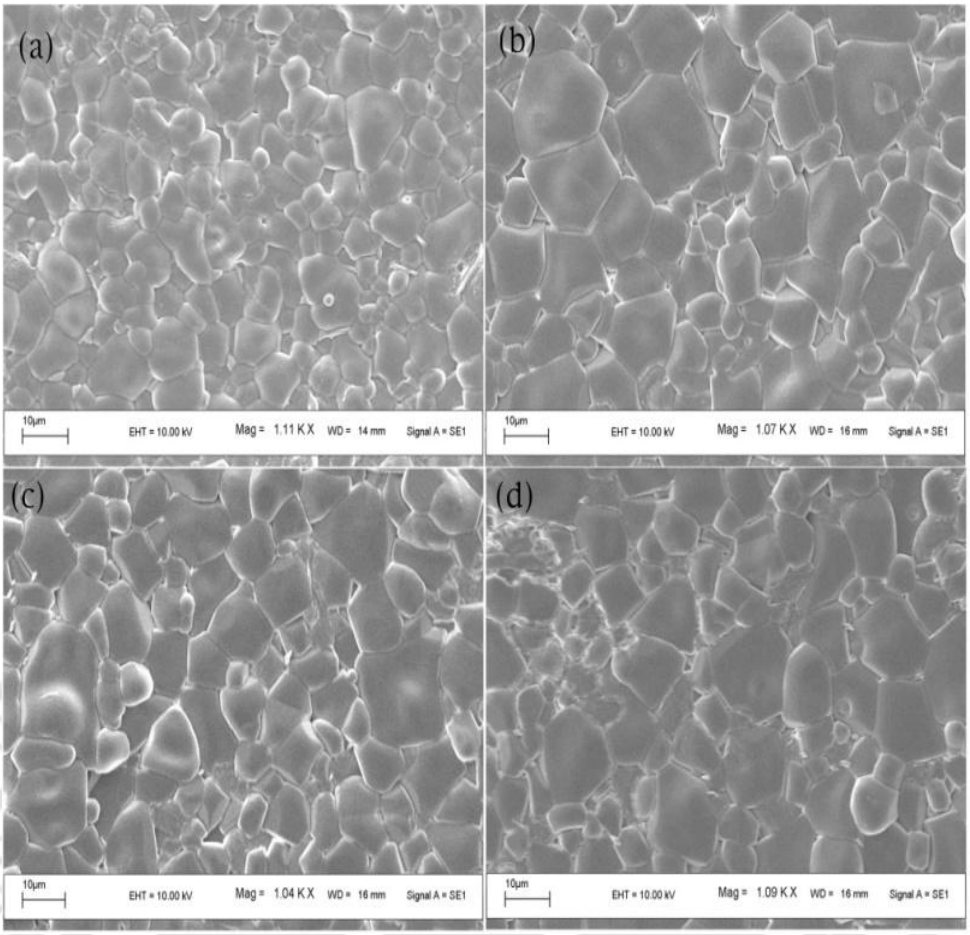

Fig. 4.5: *SEM micrographs of MTO + x CeO_2 (1.5 wt.%) ceramics sintered at (a) 1250 ^oC, (b) 1300 ^oC, (c) 1350 ^oC and (d) 1400 ^oC for 3 hr.*

The SEM micrographs of the MTO + x CeO_2 (x = 1.5 wt.%) samples sintered at different sintering temperatures for 3 hr are illustrated in Fig. 4.5 and the extracted value of the average grain sizes as a function of the sintering temperature are displayed in Fig. 4.6. With increasing sintering temperatures up to 1300 ^oC, it is not only observed that the average grain size of MTO ceramic increases (see Fig. 4.6) due to the aggregation of already existing crystals, but also the microstructure turns out to be quite uniform. On further increasing sintering temperatures the non - uniformity of the grain morphology in the microstructure increases along with the development of fine pores structure (see Fig. 4.5(d)) at these higher sintering temperatures. Therefore, the average grain size decreases with increasing the sintering temperature above 1300 ^oC. This can be attributed to the evaporation of CeO_2 nanoparticles, which causes significant reduction in density and the average grain size.

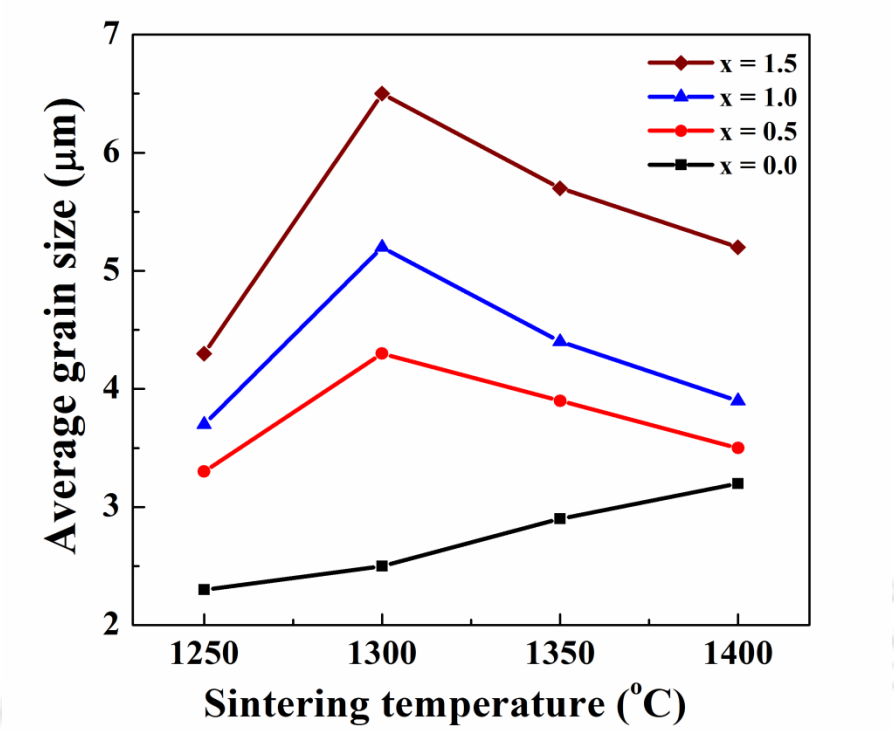

Fig.4.6: *Average grain size of MTO+xCeO_2 (x wt.%) ceramics sintered at different temperatures.*

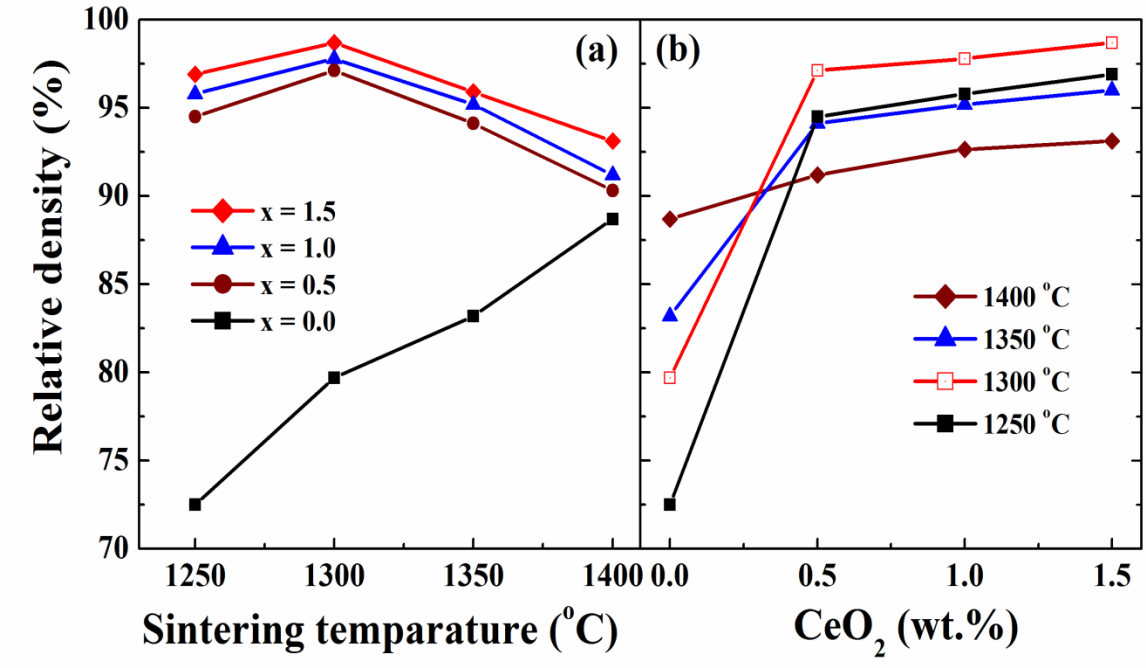

Fig. 4.7: *(a) Variations in relative densities as a function of (a) sintering temperatures and (b) weight percentage of CeO_2 nanoparticles for MTO + x CeO_2 (x wt.%) ceramics.*

4.3.4 Relative density

To understand the effect of CeO_2 nanoparticles on the densification properties of MTO ceramics, the relative density of the MTO ceramics mixed with different weight percentage of CeO_2 nanoparticles was estimated using Archimedes method. Fig. 4.7 shows the variation of relative density for the MTO + *x* CeO_2 (*x* wt.%) samples as a function of sintering temperature (a) and weight percentage of CeO_2 (b). While the pure MTO ceramic shows a continuous increase from 72 to 88 % with increasing sintering temperature from 1250 to 1400 ^oC and attains a maximum of 88 % of the theoretically predicted value, the MTO + *x* CeO_2 (*x* wt.%) ceramics reveal an enhanced densification of 98.7% even at lower sintering temperature. In addition, the densification is also found to increase with increasing the concentration of CeO_2 nanoparticles at a given sintering temperature (see Fig. 4.7(b)). These results confirm that the densification of MTO ceramics without the sintering aid is substantially difficult and at the same time, the sintering of the MTO + *x* CeO_2 (*x* wt.%) ceramics at higher temperatures (>1300 ^oC) not only degrades the densification but also the microstructure (see Fig. 4.5(d)).

The effects of additive elements and the sintering temperature on the improvement of the density and microstructure can be described by the following mechanism: It is well known that the sintering velocity is inversely proportional to the particle size, i.e., sintering is faster for the finer particles. In addition, the sintering velocity enhances when the diffusion across the grain boundaries increases [28]. When the fine CeO_2 powders of average size of 80 nm are dispersed into the matrix of 0.7 μm MTO powder, the reinforcing fine powders contain substantial surface energy due to large surface area. Furthermore, the fine particles have many defects including vacancy, aberration and local stress [29]. Therefore, during sintering, surface and defect atoms of powders tend to become normal atoms with lower energy within the crystalline grains and the high temperature provides the external activation energy to release the internal energy contained in powders enabling mass transfer and reduction in surface energy [30, 31]. In the present case, it is proposed that the extra energy of the fine CeO_2 particles enhances the effective coalescence of the MTO particles, resulting in a uniform microstructure with larger grains. This is in good agreement with the earlier reports on similar systems [32].

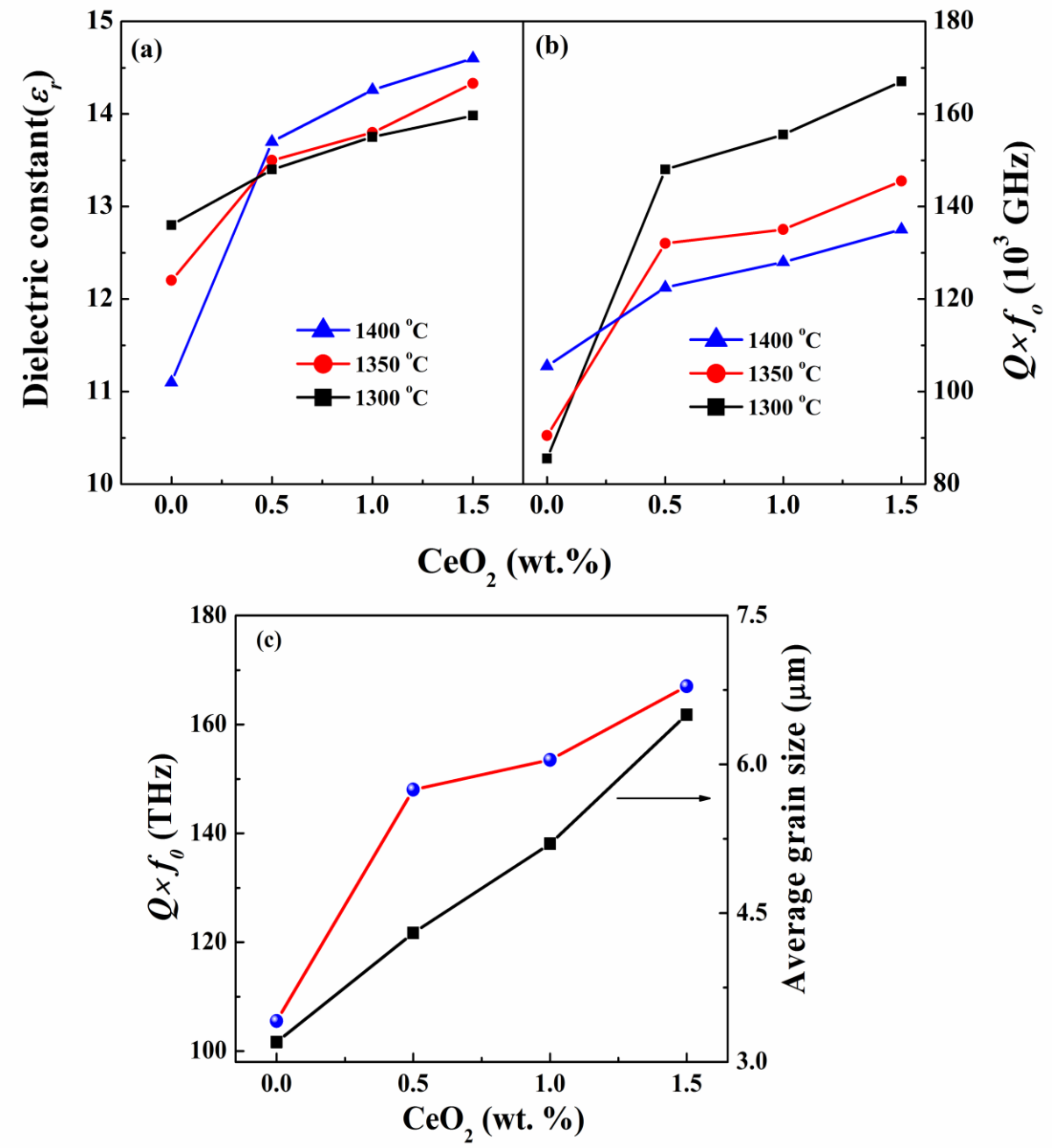

Fig. 4.8: *Variation in (a) ε_r and (b) $Q\times f_o$ as a function of different wt.% of CeO_2, sintered at different temperatures (c) Dependence of $Q\times f_o$ and average grain size on wt.% of CeO_2.*

4.3.5 Microwave dielectric properties

To study the effect of concentration of the CeO_2 nanoparticles on the microwave dielectric properties of MTO ceramics, we obtained the dielectric constant and the quality

factor for all the samples as depicted in Fig. 4.8. It is clearly seen that both the dielectric constant and quality factor increases rapidly for the low value of x followed by an almost linear variation for the weight concentration between 0.5 and 1.5. The values of ε_r of the MTO + x CeO_2 nanoparticles were in the range of 13.4 - 14.6, whereas the pure MTO exhibits only between 11 and 12.8. The variation of the dielectric constant with x shows a similar trend with the density of the MTO ceramics suggesting that the dielectric constant of the presently investigated samples can be improved by increasing the densification of the MTO ceramics, which results a reduction in the porosity. Further, to see the effect of porosity on the dielectric constant, the measured values of the microwave dielectric constants were corrected for porosity using the Eq. 3.3 as described in chapter 3 [33]. The porosity corrected values were slightly higher than the experimental values and is tabulated in **Table 4.1.**

The product of the quality factor (Q) and resonant frequency (f_o) is considered as a major tool for evaluating the performance of the microwave dielectric materials. A maximum value of $Q \times f_o$ of 167,000 GHz (at 10.4 GHz) is obtained for the x = 1.5 samples sintered at 1300 ^oC. The degradation in the $Q \times f_o$ values at higher sintering temperatures can be attributed to the lowering of densities and the non - uniform microstructure. The variation of the $Q \times f_o$ with x shows a similar trend with the density and the average grain size of the MTO ceramics (see Fig. 4.8(c) and 4.9(b)), suggesting that the increase in grain size and densification strongly influences the microwave dielectric properties. Similarly, Li et al. [12] and Huang et al. [34] have reported that the microwave dielectric properties of ceramics are strongly dependent on the densifications, the microstructure as well as sintering temperature of the specimens. This is in good agreement with our present study. Moreover, the $Q \times f_o$ values obtained in the present study are much higher than the values reported by Belous et al. [4, 6], Li et al. [12], Yao et. al. [13], Huang et al. [34] and Chen et.al. [35, 36]. It may be noted that there are several other factors such as crystal defects, grain boundary, secondary phases and pores also affects the microwave dielectric loss of ceramics. For instance, Chen [14] reported the enhanced dielectric properties of Mg_2TiO_4 ceramics by minimizing the extrinsic losses upon the substitution of Zn^{2+} and Co^{2+} in Mg site. Similarly, Huang et al. [7, 37, 38] showed the improved microwave dielectric properties of Mg_2TiO_4 ceramics due to the enhancement in maximum density (i) by replacing Mg^{2+} with Co^{2+}, (ii) by substituting Mn^{2+} in Mg sites and (iii) with partial substitution of Sn^{4+} in Ti^{4+} sites. They also studied the variation in

microwave dielectric properties of $(Mg_{0.95}Co_{0.05})_2TiO_4$ and $(Mg_{0.95}Zn_{0.05})_2TiO_4$ ceramics with $SrTiO_3$. Although, the sintering temperature of the MTO ceramics was reduced, the microwave dielectric properties are inferior as compared to the pure MTO ceramics [39, 40].

***Table 4.1**: Relative density, measured dielectric constant (ε_r) and porosity corrected dielectric constant (ε_m) values of pure MTO and MTO ceramics added with CeO_2 nanoparticles*

Material composition	Sintering temperature	% of relative density	ε_r (measured)	ε_m (corrected)
Mg_2TiO_4	1400 °C	88.54	11.20	13.22
	1350 °C	85.22	10.82	13.95
	1300 °C	78.75	10.60	14.88
	1250 °C	72.53	10.42	16.71
Mg_2TiO_4+ 0.5 wt.% CeO_2 nanoparticles	1400 °C	90.32	13.40	15.43
	1350 °C	94.12	13.52	14.69
	1300 °C	97.13	13.70	14.25
	1250 °C	94.50	12.82	13.84
Mg_2TiO_4+ 1.0 wt.% CeO_2 nanoparticles	1400 °C	91.20	13.72	15.58
	1350 °C	95.22	13.85	14.79
	1300 °C	97.80	14.26	14.69
	1250 °C	95.81	13.00	13.77
Mg_2TiO_4+ 1.5 wt.% CeO_2 nanoparticles	1400 °C	93.12	13.98	15.40
	1350 °C	95.90	14.33	15.17
	1300 °C	98.73	14.60	14.85
	1250 °C	96.90	13.24	13.81

It is generally understood that the increase in the average grain size decreases the grain boundary area and hence the reduction in the lattice imperfections. This leads to low dielectric losses. Therefore, the sample with large grains is expected to reveal a high *Q* value

[41, 42]. So, for better understanding the correlation between the structural properties and improvement in microwave dielectric properties with the addition of CeO_2 nanoparticles, we also plotted the dependence of average grain size as a function of different wt.% of CeO_2 nanoparticles along with quality factor as is shown in Fig. 4.8 (c). It is interesting to note that both the quality factor and average grain size follow the same trend as a function of wt% of CeO_2 nanoparticles. These results also revealed that achieving larger grains could be a means to have higher $Q \times f_o$ values if no secondary phase are introduced. However, for a given grain size, the value of $Q \times f_o$ depends strongly the formation of grain size with different additives. Hence, it can be concluded that the suitable additive elements are needed to improve the density and attain uniform microstructure with the larger grains by enlightening the recrystallization process and thereby reducing extrinsic loss mechanisms. This would result in the enhancement of the microwave dielectric properties of MTO ceramics. Furthermore, to correlate the dependence of dielectric properties on relative density for the presently investigated samples, the variations of both the dielectric constant and $Q \times f_o$ were plotted as a function of relative density as depicted in Fig. 4.9. It is clearly evident from the figure that the microwave dielectric properties are strongly dependent on the density and the average grain size (see Fig. 4.8(c) and Fig. 4.9 (a-b)).

In the present study, the addition of CeO_2 nanoparticles modifies the microstructure and microwave dielectric properties along with reduction in sintering temperatures. The modification in microstructure and sintering temperature show that CeO_2 nanoparticles influence the recrystallization process and thereby reduces extrinsic loss mechanisms which is commonly found in ceramics. A similar type of arguments was reported by Shanker et al. [43] that the addition of $BaTiO_3$ nanoparticles added with the microsized $BaTiO_3$ particles improved the microwave dielectric properties with reduction in sintering temperature using polymeric citrate route.

In the present investigation, a slow cooling rate of 1 ^oC / min in the cooling phase is employed to absorb more oxygen and to develop ordered structure. Note that the ordered structure tends to exhibit less anharmonicities and hence reduced losses and temperature dependence [44, 45]. In the present study, the increase in Q value is primarily attributed to the increase in density. But, the slow cooling rate can also play a role in the dielectric

properties of MTO [44, 45]. This is also consistent with the earlier results reported by Petzelt et al. [46] and Wang et al. [47] that annealing and slow cooling could decrease the dielectric loss.

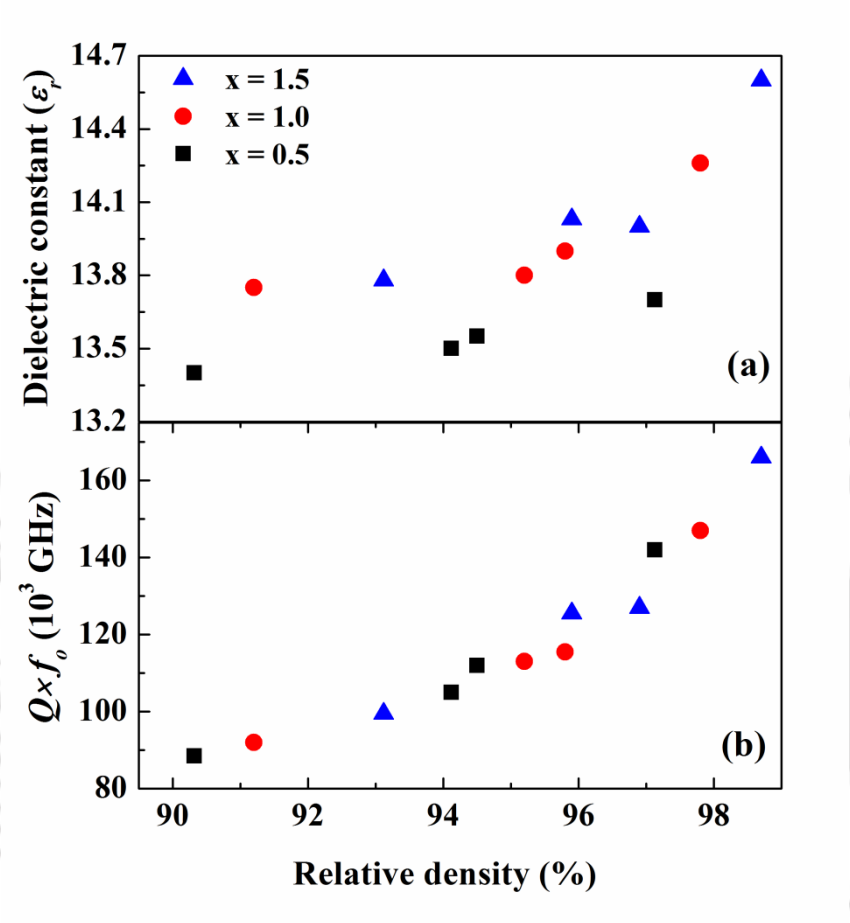

Fig.4.9: *Variation of (a) dielectric constant and (b) $Q \times f_o$ values as a function of relative density for MTO + x CeO_2 (x wt.%) ceramics.*

4.3.6 Low temperature microwave dielectric properties

4.3.6.1 Dielectric studies

To study and understand the dielectric loss mechanisms, the dielectric properties of the MTO ceramics with *x* wt.% of CeO_2 nanoparticles were measured at cryogenic temperature in the microwave frequency range. The variation in resonant frequency of the pure MTO ceramics and MTO ceramics added with different wt.% of CeO_2 nanoparticles was measured as a function of temperature and depicted in Fig. 4.10 (a). It is observed that the pure MTO

ceramics and the MTO ceramics added with CeO_2 nanoparticles exhibited different resonant frequencies. The difference in the resonant frequencies is due to the differences in the real permittivity of the samples and slight variations in the dimensions of the prepared MTO ceramics with and without the addition of CeO_2 nanoparticles.

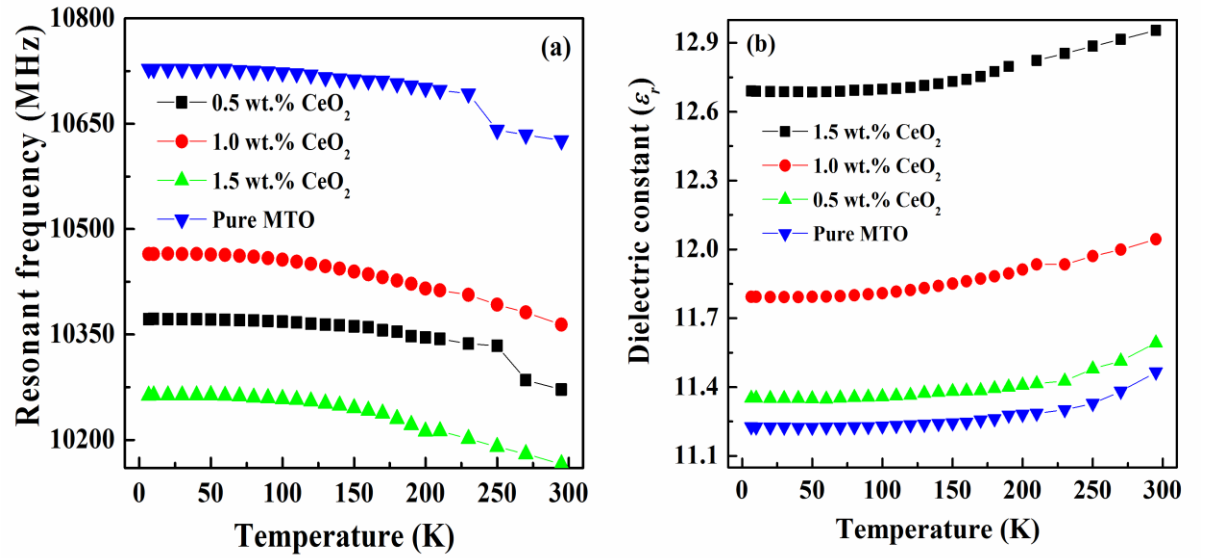

Fig. 4.10: *Variation in (a) resonant frequency and (b) dielectric constants as a function temperature of MTO + x CeO_2 (x = 0.0 - 1.5 wt.%) ceramics.*

Fig. 4.10(b) shows the variations in the dielectric constants as a function of temperature of the MTO ceramics with and without the addition of CeO_2 nanoparticles. The variations in the dielectric constants over the measured temperature range are very minimal. For example, MTO ceramics added with 1.5 wt.% of CeO_2 nanoparticles exhibited the dielectric constant of 12.7 at 6.5 K and 12.95 at 295 K and the pure MTO exhibited 11.2 at 6.5 K and 11.4 at 295 K. It was observed that the MTO ceramics added with CeO_2 nanoparticles exhibited higher dielectric constants as compared to the pure MTO ceramics. This is due to the differences in the densities of the samples, i.e., doped MTO samples have higher densities than the pure MTO samples. Further, there is a slight variation in the dielectric constants measured at cryogenic temperatures and measured at ambient temperature, which may be due to the different experimental setups used to measure the dielectric constants (see **Table 4.2**).

Fig. 4.11(a) shows the temperature dependence of the unloaded Q_u factor of the pure and CeO_2 added MTO ceramics at approximately 10.35 GHz. The actual resonance

frequencies vary slightly depending on the size of the sample and temperature. It is found that the unloaded Q_u factor first increases slightly up to 150 K and then decreases with increasing temperature. The non - monotonous temperature dependences of unloaded Q_u factor below 150 K are seen in most samples, which are caused obviously by extrinsic loss factor and are discussed in later part. In the present case, for the MTO samples added with different concentrations of CeO_2 nanoparticles, the unloaded Q_u factor is higher as compared with pure MTO samples at cryogenic temperature. In addition, the sample added with x =1.5 wt% of CeO_2 showed higher value of Q_u as compared with the rest of the samples. The maximum Q_u is 22,000 at 150 K for the sample with x = 1.5 wt.% CeO_2 and minimum is 13260 at 295 K. The minimum in unloaded Q_u factor is due to dielectric relaxations, which slow down upon cooling. On the other hand, the unloaded Q_u factor of the MTO ceramics measured at ambient conditions (at f_o = 10.44 GHz) increases with the increase in (x wt.%) concentration of CeO_2 nanoparticles [48]. But the values are less as compared to cryogenic measurement (see Table 4.2).

***Table 4.2**: Variation of average grain size, density, dielectric constant and $Q\times f_o$ values of the MTO + x CeO_2 (x wt.%) ceramics, sintered at different temperatures for 3 hr.*

X	**Sintering temperature**	**Relative Density (%)**	**Average grain size (μm)**	ε_r	$Q\times f_o$ **(×10^3GHz)**
0	1400	88.7	3.2	12.8	105.5
0.5	1300	96.6	4.3	13.7	148.0
1	1300	98.2	5.2	14.2	155.5
1.5	1300	98.7	6.5	14.6	167.0

Fig. 4.11(b) shows the temperature dependent of $Q\times f_o$ of the pure and CeO_2 added MTO ceramics. In all samples, $Q\times f_o$ increases first slightly up to 150 K and then decreases with increasing temperature. In comparison with pure MTO, the results substantiate that the dielectric properties are improved as a result of addition of CeO_2 nanoparticles.

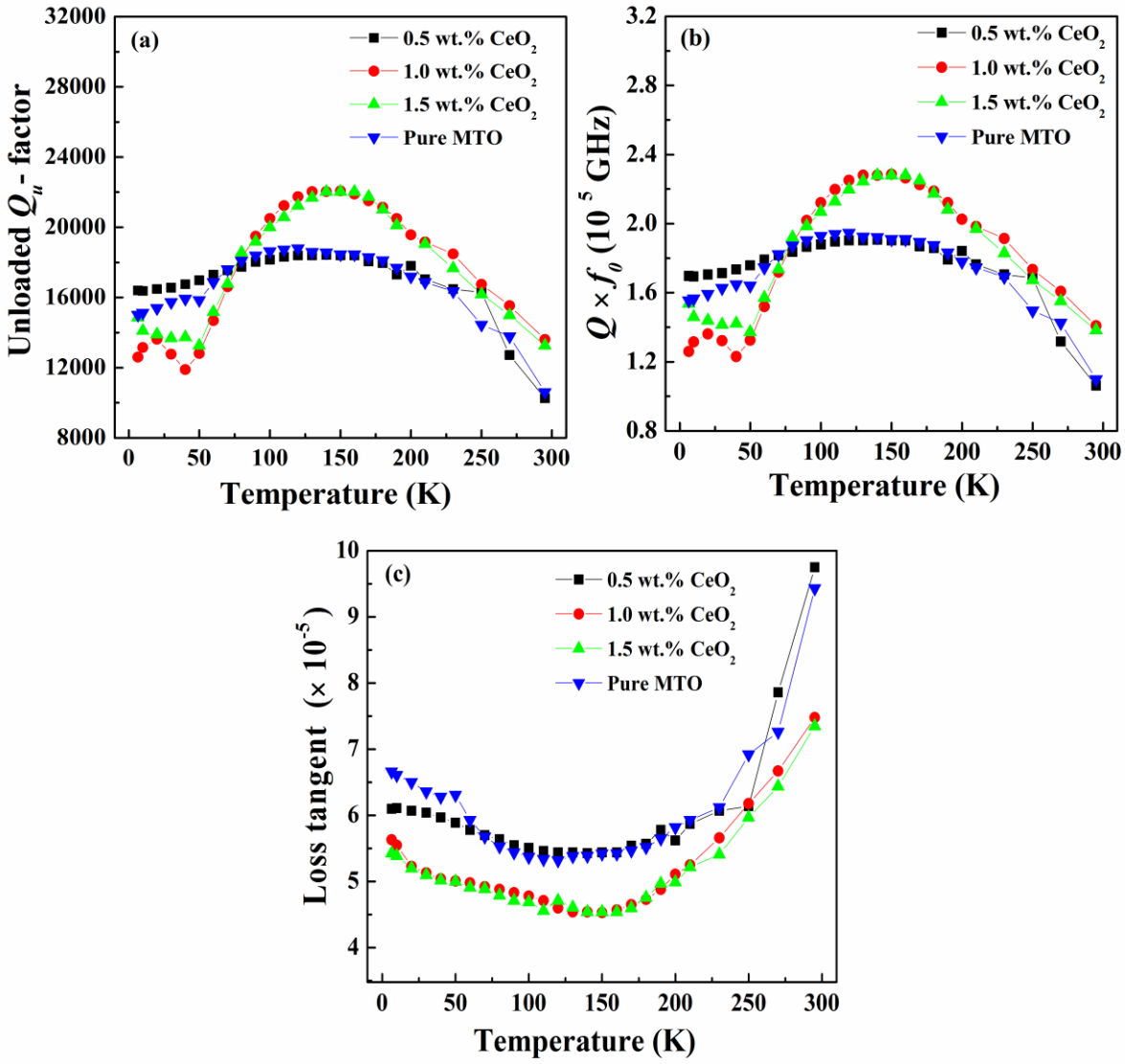

Fig. 4.11: *Variation in (a) unloaded Q_u factor, (b) $Q \times f_o$ and (c) loss tangent as a function of temperature of the MTO + x CeO_2 (x = 0.0 - 1.5 wt.%) ceramics.*

The variation in the loss tangent of the pure MTO and MTO ceramics added with different wt.% of CeO_2 as a function of temperature was measured and are illustrated in Fig. 4.11(c). It is observed that as the temperature increases from 6.5 K to 295 K, the loss tangent of the MTO ceramics decreases initially up to 150 K and then increases with increasing temperature. The loss tangent values for pure MTO ceramics at 6.5 K is found to be 6.66×10^{-5} and at 295 K is 9.43×10^{-5} where as MTO ceramics added with x = 1.5 wt.% exhibited 5.43×10^{-5} at 6.5 K and 7.35×10^{-5} at 295 K. The MTO ceramics added with higher amounts of

CeO_2 nanoparticles exhibited lower loss tangent as compared to the pure and 0.5 wt.% CeO_2 added MTO ceramics. This demonstrates that the higher concentration of CeO_2 nanoparticles may be reducing the intrinsic losses, to some extent, extrinsically. The samples with higher CeO_2 exhibited higher relative densities and larger grain sizes. So, the obtained low loss tangent is attributed to the reduction in both extrinsic and intrinsic loss mechanisms. The higher loss tangent in the pure and x = 0.5 wt.% can be attributed to the lower relative densities and smaller average grain sizes.

The smaller size of the grains increases the grain boundary area, causing an increase in loss tangent. The dielectric loss arises due to the intrinsic and extrinsic factors. Extrinsic loss occurs due to the secondary phases, chemical inhomogeneity, porosity, abnormal grain growth and oxygen deficiency. The extrinsic loss mechanisms are governed by the dipole relaxation of the defect oriented polarization segregated at the grain boundaries. Conversely, intrinsic loss mechanism is influenced by the anharmonic forces, which facilitates/mediates the interaction between crystal lattice modes and electromagnetic field leading to the damping of optical phonon modes and lattice imperfections result an increase in the damping factor [49]. Further, with the decrease in temperature, the damping of the optical phonon modes or the anharmonicity reduces. The dependence of the loss tangent is expressed as,

$$\tan\delta = \frac{\omega\gamma}{\omega^2_T} \tag{4.1}$$

where γ the damping constant and ω_T is the resonant frequency of the transverse optical mode which suggests that the intrinsic loss is heavily influenced by the temperature [50]. However, in this study, it is clear that the MTO ceramics with x = 1.5 wt.% exhibited low loss tangent showing that the addition of CeO_2 nanoparticles reduces both extrinsic and intrinsic loss mechanisms. The $Q\times f_o$ values for the x = 1.5 wt.% CeO_2 added MTO ceramics measured at microwave frequencies and measured at room temperature also exhibited higher values as compared to the other samples. This could be attributed to the enhanced relative density and large size grains. This reduces the grain boundary area [51] and exhibits highest Q value (low loss tangent).

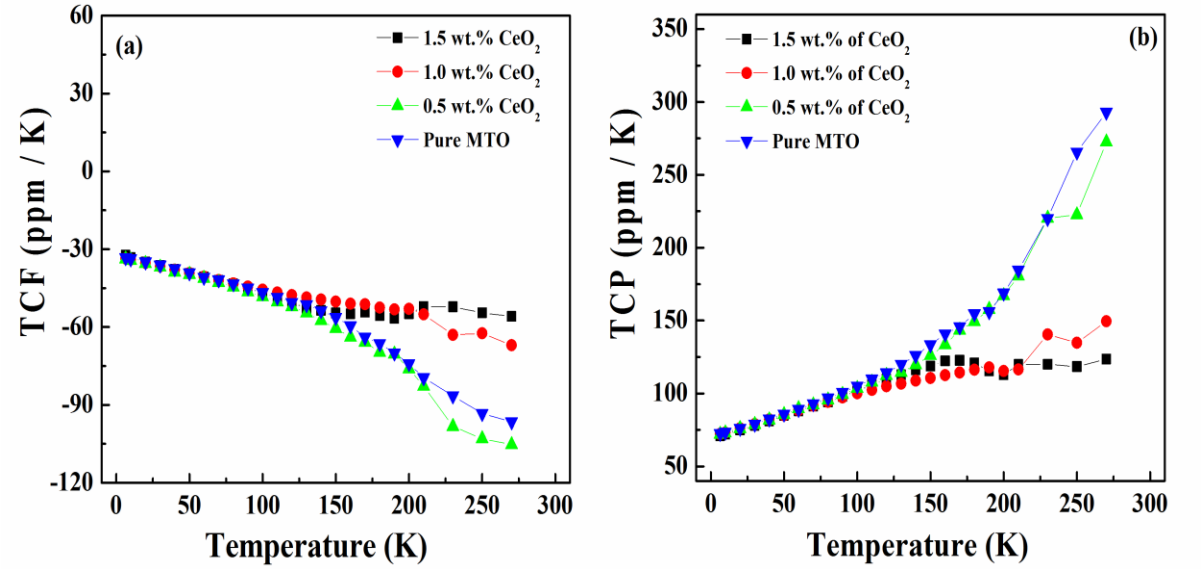

Fig. 4.12: *Variation of temperature coefficient of frequency (a) and the temperature coefficient of permittivity (b) of the MTO + x CeO_2 (x = 0.0 - 1.5 wt.%) ceramics as a function of temperature.*

The temperature coefficient of resonant frequency of the ceramics is estimated using the following expression:

$$\tau_f = \frac{f_0 - f_{0T}}{f_0}\frac{10^6}{\Delta T} \tag{4.2}$$

where f_0 and f_{0T} are the resonant frequencies measured at room temperature and at temperature T, respectively. The temperature coefficient of resonant frequency of the ceramics is known to be influenced by the chemical composition and the secondary phases present within the material. The variation in the temperature coefficient of frequency of the pure and doped MTO ceramics measured at cryogenic temperatures is shown in Fig. 4.12(a). It is observed that the temperature coefficient of frequency of the MTO ceramics decreases weakly up to 150 K and exhibits a considerable deviation beyond 150 K. Further, MTO ceramics added with higher concentrations of CeO_2 exhibit lower values as compared to other samples. From this study, it is clear that the addition of CeO_2 nanoparticles does not cause much change on the temperature stability. These results complement with the XRD results

that there are no secondary phases present in the MTO ceramics up to x = 1.5 wt.% of CeO_2 nanoparticles.

The temperature coefficient of permittivity can be calculated using the following equation:

$$\tau_\varepsilon = \frac{\varepsilon_0 - \varepsilon_{0T}}{\varepsilon_0}\frac{10^6}{\Delta T} \tag{4.3}$$

where ε_0 and ε_T are the permittivity at room temperature and at temperature T. Fig. 4.12(b) shows the temperature coefficient of permittivity of the pure MTO ceramics and MTO ceramics with the CeO_2 nanoparticles measured at cryogenic temperatures. It is observed that the temperature coefficient of permittivity of all the samples increases with the increase in temperature. Moreover, the pure MTO ceramics and the MTO ceramics with x = 0.5 wt.% of CeO_2 nanoparticles show lower values as compared to the MTO ceramics added with higher percentage of CeO_2 nanoparticles. From this study, it is clear that the addition of CeO_2 nanoparticles up to 1.5 wt.% not only improves the uniform microstructure with larger average grain sizes and high relative densities at lower sintering temperatures, but also significantly improves the microwave dielectric properties, especially, the loss tangent.

4.4 Conclusions

A systematic study on the structural, microstructural and the microwave dielectric properties of pure MTO and MTO ceramics added with CeO_2 nanoparticles prepared by solid state reaction method has been carried out in this chapter. The salient features of the MTO ceramics from the current investigations are as follows:

- The addition of CeO_2 nanoparticles effectively reduces the sintering temperature of MTO ceramics from 1450 to 1300 ^oC along with the significant improvement in the density and formation of uniform microstructure.
- The enhancement in the sintering is discussed based on surface energy and defect energy of the fine powders activated by the temperature.
- Highly densified MTO + x CeO_2 (x =1.5 wt.%) sample (98.7%) showed a maximum dielectric constant of 14.6 and $Q \times f_o$ value of 167,000 GHz (at 10.4 GHz) which

makes it a very promising dielectric for various practical applications in microwave and millimeter wave regimes.

- The microwave dielectric properties of the MTO ceramics measured at cryogenic temperatures (6.5 - 295 K), revealed that the loss tangent (tan δ) of all the samples increases with increasing temperature. The loss tangents of the pure MTO ceramics and MTO ceramics added with 1.5 wt.% of CeO_2 nanoparticles measured at 6.5 K are found to be 6.6×10^{-5} and 5.4×10^{-5}, respectively. The addition of CeO_2 nanoparticles in MTO ceramics reduces the loss tangent significantly.
- The addition of CeO_2 nanoparticles in MTO did not cause any change on the temperature stability of the MTO ceramics. However, the temperature coefficient of the permittivity increases with the increase in temperature and CeO_2 content. The obtained lower loss tangent values at cryogenic temperatures can be attributed to the decrease in both intrinsic and extrinsic losses in the MTO ceramics.
- Moreover, it was found that with the variation of temperature the resonant frequency of each sample was slightly vary, which is an important characteristic property for a DR. Therefore, the proposed DR material can be used for commercial high frequency applications.

4.5 References

[1] C. L. Huang, J. J. Wange, Y. P. Chang, *J. Am. Ceram. Soc.*, **90** (2007) 858.

[2] C. L. Huang, J. Y. Chen, B. J. Li, *J. Alloys Compd*., **509** (2011) 4247.

[3] Y. B. Chen, *J. Alloys Compd.*, **509** (2011) 1050.

[4] Belous, O. Ovchar, D. Durilin, M. M. Krzmanc, M. Valant, D. Suvorov, *J. Am. Ceram. Soc.*, **89** (2006) 3441.

[5] M. J. M-Lope, M. P. B. Pena, M. E. G-Clavel, *Thermochim. Acta.*, **194** (1992) 59.

[6] A. Belous, O. Ovchar, D. Durilin, M. Valant, M. M. Krzmanc, D. Suvorov, *J. Eur. Ceram. Soc.*, **27** (2007) 2963.

[7] C.L. Huang, J. Y. Chen, *J. Am. Ceram. Soc*., **92** (2009) 2237.

[8] T. Takada, S. F Wang, S. Yoshikawa, S. T. Jang, R. E. Newnham, *J. Am. Ceram. Soc.*, 77 (1994) 2485.

[9] D. Pamu, G. Lakshmi NarayanaRao, K. C. James Raju, *J. Alloys Compd*., **475** (2009) 745.

[10] H. Lu, C. C. Tsai, *Mater. Sci. Eng. B*, **55** (1985) 95.

[11] M. H. Liang, S. Y. Wu, C. T. Hu, I. N. Li, *Mater. Chem. Phys.*, **79** (2003) 276.

[12] J. Li, J. Y. Chen, G. S. Huang, C. Y. Jiang, C. L. Huang; *J. Alloys Compd.*, **505** (2010) 291.

[13] G. G. Yao, P. Liu, *J. Ceram. Proces. Res*., **13** (2012) 235.

[14] Y. B. Chen, *J. Alloys Compd*., **513** (2012) 481.

[15] M. R. S. Silva, *et al*., *J. Therm. Analy. Calorim*., **79** (2005) 421.

[16] J. Zabicky, G. Kimmel, E. Goncharov, F. Guirado, *Z. Kristallogr. Suppl*., **30** (2009) 347.

[17] D. Pamu, G. Lakshmi Narayana Rao, K. Venkatasarvanan, K. C. James Raju, *J. Int. Ferroelctrics*., **117** (2010) 118.

[18] P. L. Chen, I. W. Chen, *J. Am. Ceram. Soc*., **76** (1993)1577.

[19] M. Takagi, *J. Phys. Soc. Jpn*., **9** (1954) 359.

[20] T. Santhosh Kumar, D. Goswami, D. Pamu, *Ceramic. Inter*., **40** (2014) 1125.

[21] X. Kuang, X. Jing, Z. Tang, *J. Am. Ceram. Soc*., **89** (2006) 241.

[22] M. V. Jacob, J. G. Hartnett, J. Mazierska, J. Krupka, M. E. Tobar, *Cryogenics*, **46** (2006) 730.

[23] V. M. Ferreira, J. L. Baptista, S. Kamba, J. Petzelt, *J. Mater. Sci.*, **28** (1993) 5894.

[24] Pamu, G. L Narayana Rao, K. C James Raju, M. V. Jacob, *Sci. Technol. Adv. Mater.*, **8** (2007) 469.

[25] Subodh, R. Ratheesh, M. V. Jacob, M. T. Sebastian, *J. Mater. Res*., **23** (2008)1551.

[26] V. Petrovic, *Sci. Sint.*, **38** (2006) 287.

[27] R. D. Shannon and C.T. Prewitt, Acta Crystallographic- Section B, *Struct. Sci.*, **25** (1969) 925.

[28] Suk-Joong L. Kang, "*Sintering*" Elsevier, Burlington, MA 2005.

[29] Y. Qingrui, Z. Binghe, Z. Huarong, "*Microstructure, Property and Processing of functional ceramics"*, Springer, GmbH, Berlin Heidelberg, 2009.

[30] P. Buffat, J. P. Borel, *Phys. Rev. A*, **13** (1976) 2287.

[31] Y. Champion, J. Bigot, *Nanostruct. Mater*., **10** (1998) 1097.

[32] D. Pamu, G. Lakshmi Narayana Rao and K. C. James Raju, *J. Am. Ceram. Soc*., **95** (2012) 126.

[33] S. J. Penn, N. M. Alford, A. Templeton, X. Wang, M. Xu, M. Reece, K. Schrapel, *J. Am. Ceram. Soc.*, **80** (1997) 1885.

[34] C. L. Huang, J. Y Chen, C. Y. Jiang, *J. Alloys Compd.*, **487** (2009) 420.

[35] J. Y Chen, C. L. Huang, *J. Alloys Compd.*, **496** (2010) L10.

[36] J. Y Chen, C. Y. Jiang, C. L. Huang, *J. Alloys Compd.*, **502** (2010) 324.

[37] C. L. Huang, W. Y. W. Tseng, Y. C. Kuo, *J. Am. Ceram. Soc.*, **94** (2011) 2963.

[38] C. L. Huang, J. Y Chen, *J. Am. Ceram. Soc.*, **92** (2009) 675.

[39] C. L. Huang, J. Y Chen, *J. Alloys Compd.*, **485** (2009) 706.

[40] C. L. Huang, S. S Liu, S. H. Chen, *J. Alloys Compd.*, **480** (2009) 794.

[41] S. Hirano, T. Hayashi, A. Hattori, *J. Am. Ceram. Soc.*, **74** (1991)1320.

[42] D. Pamu, G. Lakshmi Narayana Rao, K. C. James Raju, *Adv. Appl. Ceram.*, **108** (2007) 202.

[43] V. Shanker, T. Ahmed, I. Henry, A. K. Ganguli, *J. Mater. Res.*, **21** (2006) 816.

[44] R. Chistoffersen, P. K. Davies, *J. Am. Ceram. Soc*., **75** (1992) 563.

[45] A. E. McHale, R. S. Roth, *J. Am. Ceram. Soc*., **69** (1986) 827.

[46] Petzelt, S. Pacesova, J. Fousek, S. Kamba, V. Zeleny, V. Koukal, J. Schwarzbach, B. P. Gorshunov, A. A. Volkav, *Ferroelectrics*, **93** (1989) 77.

[47] C. L Wang, H. Y. Lee, F. Azough, R. Feer, *J. Mater. Sci.*, **32** (1997)1693.

[48] R. K. Bhuyan, T. S. Kumar, D. Goswami, A. R. James, A. Perumal, D. Pamu, *Mater. Sci. Eng. B*, **178** (2013) 471.

[49] M. V Jacob, D. Pamu, K. C James Raju, *J. Am. Ceram. Soc*., **90** (2007)1511.

[50] Wakino, M. Murata, H. Tamura, J. Am. Ceram., *J. Am. Ceram. Soc*., **69** (1986) 34.

[51] C. L. Huang, M. H. Weng, H. L. Chen, *Mater. Chem. Phys.*, **71** (2001) 17.

Chapter 5

Effect of additives on microwave dielectric properties of Mg_2TiO_4 ceramics

5.1 Introduction

Mg_2TiO_4 (MTO) is one of the most promising dielectric material being used for producing type - I ceramic multilayer capacitors and microwave resonators. However, the sintering temperature of the pure MTO ceramics is higher than 1400 ^oC. This demands the use of expensive noble metals as electrodes. Noble metals have been widely used as metallic electrodes due to their high conductivities and the low melting temperatures ($\leq$1050 ^oC). However, most of the commercial materials used for these applications have a processing temperature above 1300 ^oC. Therefore, it is necessary to reduce the sintering temperatures of microwave dielectrics to fabricate the multilayer capacitors. Moreover, sintering aids affect the ceramics in many ways by changing density, microstructure, defect structure and possibly crystal structure. These changes brought about by the sintering aids affect the resulting dielectric properties as well. As discussed in earlier chapter, it therefore requires an addition of low melting point materials or additives having fine particles, which do not degrade the microwave dielectric properties. Hence, it is very much essential to optimize the concentrations, additives and the processing parameters to achieve best microwave dielectric properties at lower sintering temperatures. Therefore, the present study focuses to investigate the effect of different additive concentrations of V_2O_5, La_2O_3 and Bi_2O_3 on the sinterability, microstructure and microwave dielectric properties of MTO ceramics.

5.2 Experimental details

Samples of Mg_2TiO_4 ceramics were synthesized by conventional solid - state reaction method from individual high purity oxide powders of MgO and TiO_2 with 99.9% purity (M/s Sigma Aldrich, USA). The starting materials were mixed according to the stoichiometry of MTO ceramics and ground in distilled water for 5 hr in planetary ball mill (M/s Fritsch GmbH, Germany). The prepared mixture was dried and calcined at 1100

^oC for 3 hr in air. The calcined powders were added with 0.5-1.5 wt.% of La_2O_3 (x = La_2O_3 = 0.5, 1.0 and 1.5 wt.%) or V_2O_5 (y = V_2O_5 = 0.5, 1.0 and 1.5 wt.%) and again milled at high speeds for 15 hr. After drying, the powders were added with 4 wt.% of Poly Vinyl Alcohol (PVA) as organic binder. It was dried again and ground into very fine powder. Cylindrical ceramic pucks of 10 mm in diameter and 4 - 5 mm in height were formed under a uniaxial pressure of 2000 Kg/cm^2. The samples of La_2O_3 or V_2O_5 added MTO samples were sintered at an optimum temperature range of 1200 ^oC – 1400 ^oC with a constant duration of 3 hr. Similarly, the calcined powders of MTO ceramics were added with 0.5 - 1.5 wt.% of Bi_2O_3 and remilled at high speeds for 15 hr. After that the powders were dried and added with 4 wt. % of PVA as binder. It was dried again and ground into very fine powder. Cylindrical ceramic pucks of 10 mm in diameter and 4 - 5 mm in height were formed under a uniaxial pressure of 2000 Kg/cm^2. The samples were subsequently sintered in the range of 1150 - 1350 ^oC for 3 hr in air. The heating and cooling rates were set at 10 ^oC / min and 1^oC / min, respectively.

The bulk densities of the sintered samples were calculated by Archimedes method. Phase purity of the materials was identified by powder X - ray diffraction with Cu-K_α radiation. Surface morphology of the materials was characterized using SEM. The dielectric properties (ε_r and Q_u) of the materials were measured in the microwave frequency range using the Hakki and Colemann resonanator technique as described in chapter 2. Dielectric properties in the temperature range of 6.5 K to 295 K were measured by placing the copper cavity on the cold head of a closed cycle refrigerator (ARS Cryo) connected with a Vector Network Analyzer (M/s Agilent Technologies Pvt Ltd, Palo Alto, CA, Model # E8356B,). The broadband dielectric properties were measured in the frequency range of 1MHz - 2 GHz at room temperature using a computer control impedance analyzer (M/s Agilent Technologies Pvt Ltd, Model # E4991A) attached with a Novocontrol temperature controller.

5.3 Effect of La_2O_3 and V_2O_5 additions on microwave dielectric properties of MTO ceramics

5.3.1 Structural analysis

The MTO ceramics prepared with the La_2O_3 and V_2O_5 as sintering aids showed a change in the color from white to light brown with an increase in additive concentrations. To

study the effect of these additives on the crystal structure of the MTO ceramics, XRD patterns were recorded.

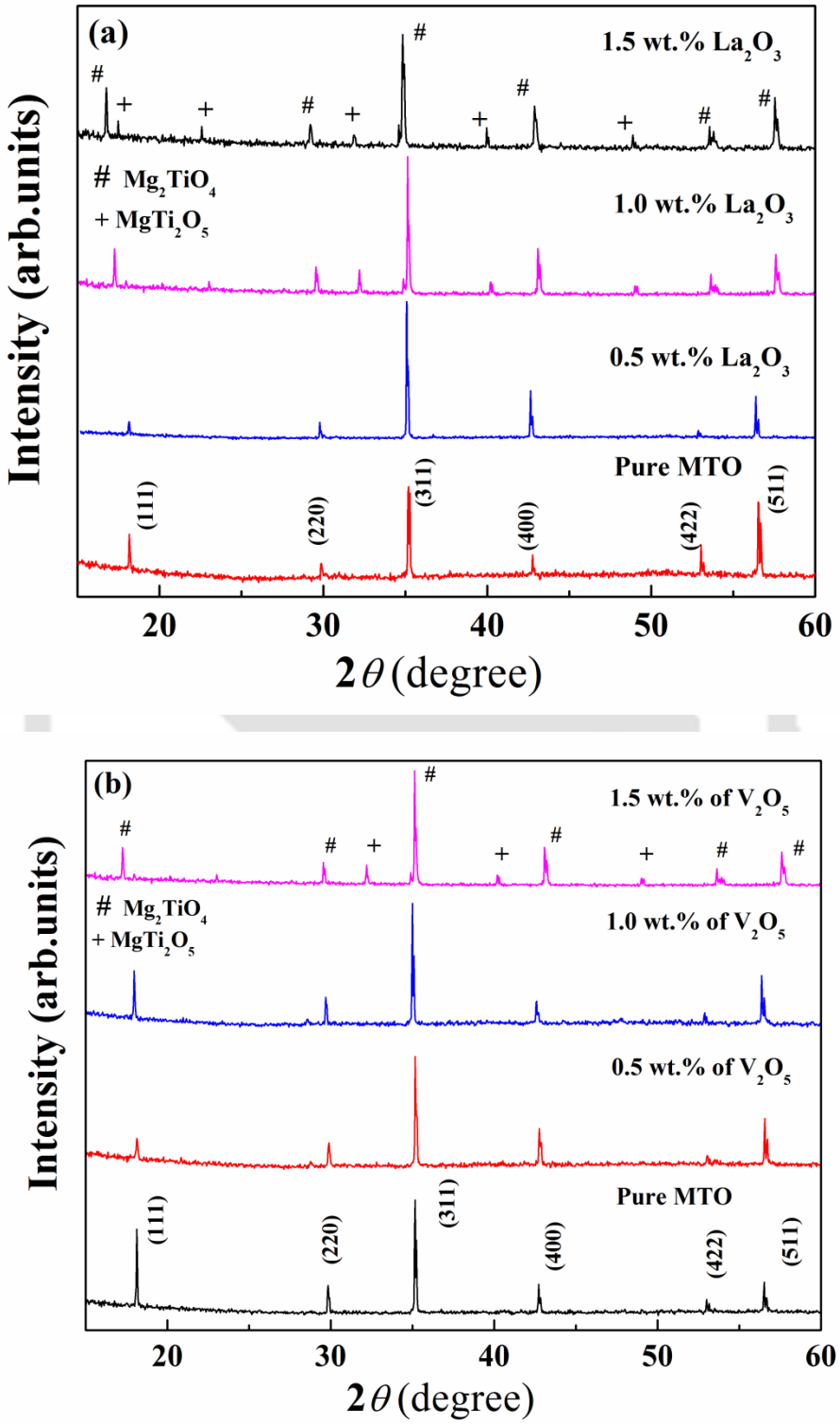

Fig. 5.1: *XRD patterns of the MTO ceramics added with different wt.% of (a) La_2O_3, sintered at 1300 °C for 3 hr and (b) V_2O_5, sintered at 1250 °C for 3 hr.*

Fig. 5.1 illustrates the XRD patterns of pure MTO ceramics sintered at 1400 ^oC and MTO ceramics added with different amounts of La_2O_3 and V_2O_5 additives sintered at 1300 ^oC and 1250 ^oC for 3 hr, respectively. The XRD patterns of the samples added with La_2O_3 upto x = 0.5 wt.% revealed that MTO as a main crystalline phase. On further, increasing La_2O_3 addition, $MgTi_2O_5$ phase was detected as a secondary phase along with major MTO phase. Generally, the formation of $MgTiO_3$ and $MgTi_2O_5$ as intermediate phases is difficult to eliminate from the samples prepared by mixed oxide route. It is expected that La_2O_3 forms a secondary phase at the grain boundary. However, no secondary phase was detected from the XRD patterns within the resolution limit of XRD. With increasing La_2O_3 content, the amount of $MgTi_2O_5$ phase is enhanced.

On the other hand, for the V_2O_5 added MTO samples (see Fig. 5 (b)) the secondary phase was not found up to y = 1 wt.%. It has been reported that the excess Ti and V_2O_5 forms solid solution of $(Ti_{1-x}V_x)_2O_3$ [1], which might possibly suppress the formation of $MgTi_2O_5$. In this study, such $(Ti_{1-x}V_x)_2O_3$ phase was not observed up to y =1.5 wt.%. Nevertheless, the fraction of second phase of $MgTi_2O_5$ was enhanced at y =1.5 wt.%. For both the cases, the full width at half maximum (FWHM) of the most intense diffraction peaks increases with increasing La_2O_3 or V_2O_5 contents up to 1.5 wt.%. This could be attributed to the decrease in average crystallite size with increasing additive elements.

5.3.2 Microstrctural analysis

To study the influence of these additives on microstucture of MTO ceramics, SEM micrographs were obtained. The microstucture of the pure MTO ceramics sintered at 1400 ^oC and MTO ceramics added with different concentrations of La_2O_3 additives sintered at 1300 ^oC for 3 hr were illustrated in Fig.5.2. It was observed that the pure MTO samples show non -uniform microstructure along with a few isolated particles and wide range of grains. With the addition of La_2O_3, densification of MTO ceramics is clearly observed at lower sintering temperature. It is found that the average grain size of x = 0.5 wt.% added MTO sample is larger than the pure MTO sample. However, the average grain size decreases with increasing La_2O_3 content above 0.5 wt.%. In addition, there is some distortion of grain growth for 1.0 and 1.5 wt.% La_2O_3 added MTO samples. A similar distortion effect was observed by Kudesia et al. [2] on the addition of La_2O_3 / ZnO and by Huang and Weng [3] on the addition of CuO / ZnO to ZST ceramics. The average grain size is ranged between 2.1 and 5.7μm. Fig. 5.3 demonstrates the microstructures of V_2O_5 added MTO ceramics sintered at 1250 ^oC. With the addition of V_2O_5, the grain size

distribution becomes more regular and the average grain size was ranged between 5 and 9 *μm*. Further, MTO ceramics added with *y* = 0.5 wt.% of V_2O_5 sintered at 1250 ^oC revealed a quite uniform microstucture with larger sized grains. However, the grain uniformity decreases with the increase in the wt.% of V_2O_5. A similar study was observed by Huang et al. [4] by the addition of V_2O_5 to ZST system. They have found that the low level addition of ZnO and V_2O_5 could significantly improve the densification and the dielectric properties of ZST ceramics. From all these observations, it can be concluded that the La_2O_3 and V_2O_5 additive concentrations play an important role on the densification and enhancement of grain size of the MTO ceramics.

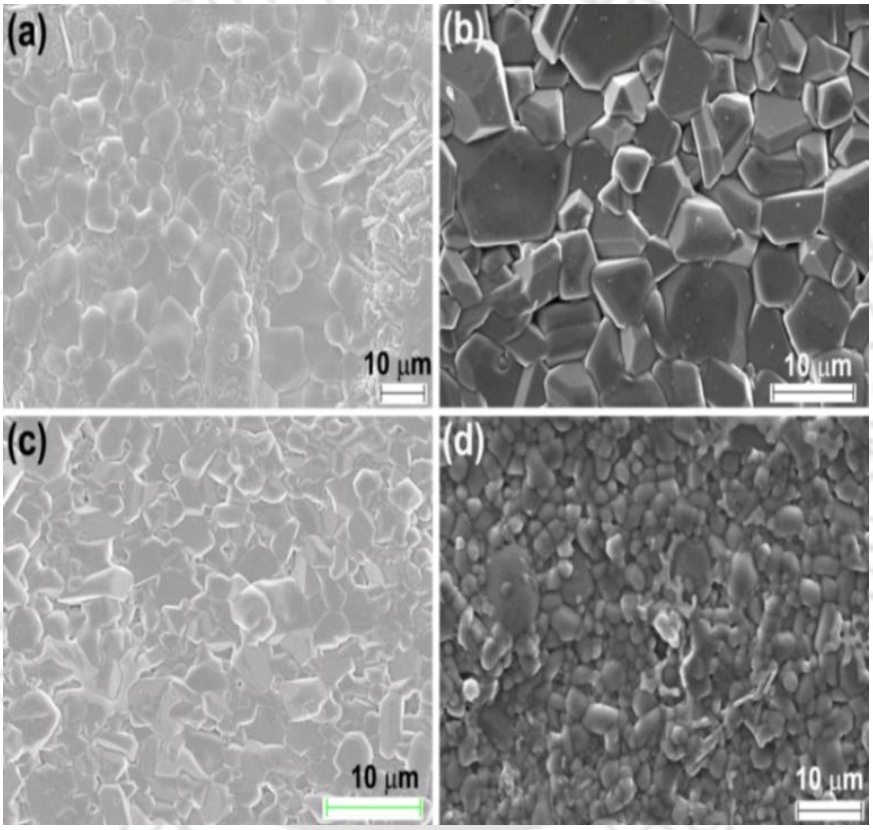

***Fig. 5.2**: SEM micrographs of (a) Pure MTO ceramics sintered at 1400 ^oC and MTO+x La_2O_3 (x wt.%) ceramics with (b) x = 0.5 (c) x = 1.0 and (d) x = 1.5 sintered at 1300 ^oC.*

Fig.5.4 illustrates the dependence of average grain size of MTO ceramics extracted from SEM micrographs added with La_2O_3 and V_2O_5 additives sintered at 1300 ^oC and 1250 ^oC, respectively. As explained earlier, MTO ceramics added with *x* = *y* = 0.5 wt.% of additives show larger grain size as compared to higher concentrations of additives. The reduction in grain sizes at higher concentration of additives can be attributed to the formation of non - uniform grain growth due to the liquid phase effect. The average grain

size of MTO ceramics added with V_2O_5 was larger than those of La_2O_3. Therefore, it is believed that the grain wetting ability of V_2O_5 addition was better than that of La_2O_3 addition in MTO ceramics.

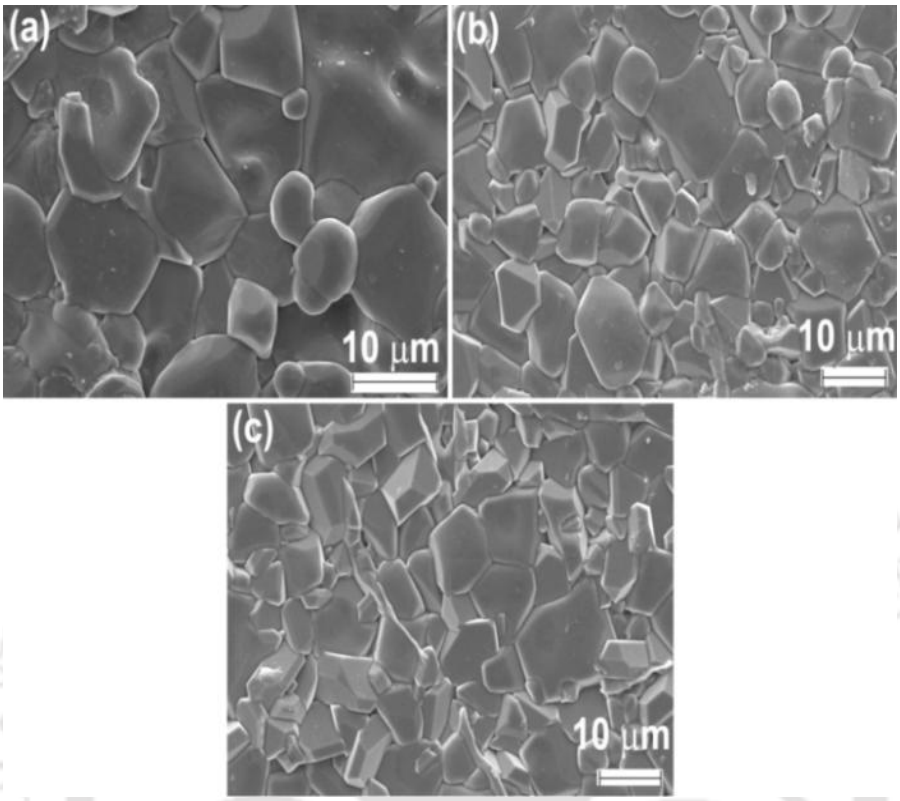

Fig. 5.3: *SEM images of MTO ceramics added with (a) y = 0.5, (b) y =1.0 and (c) y =1.5 wt.% V_2O_5 sintered at 1250 °C for 3 hr.*

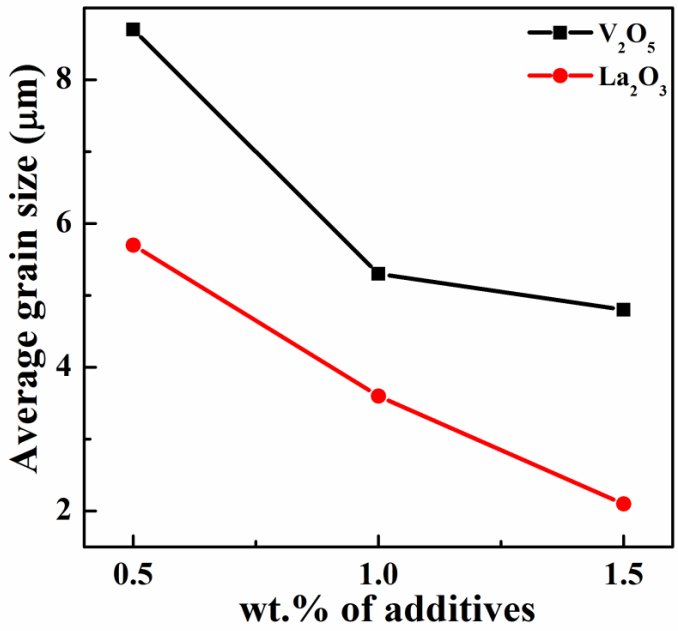

Fig. 5.4*: Dependence of average grain size on different wt.% of La_2O_3 and V_2O_5 additive MTO ceramics, sintered at 1300 °C and 1250 °C, respectively.*

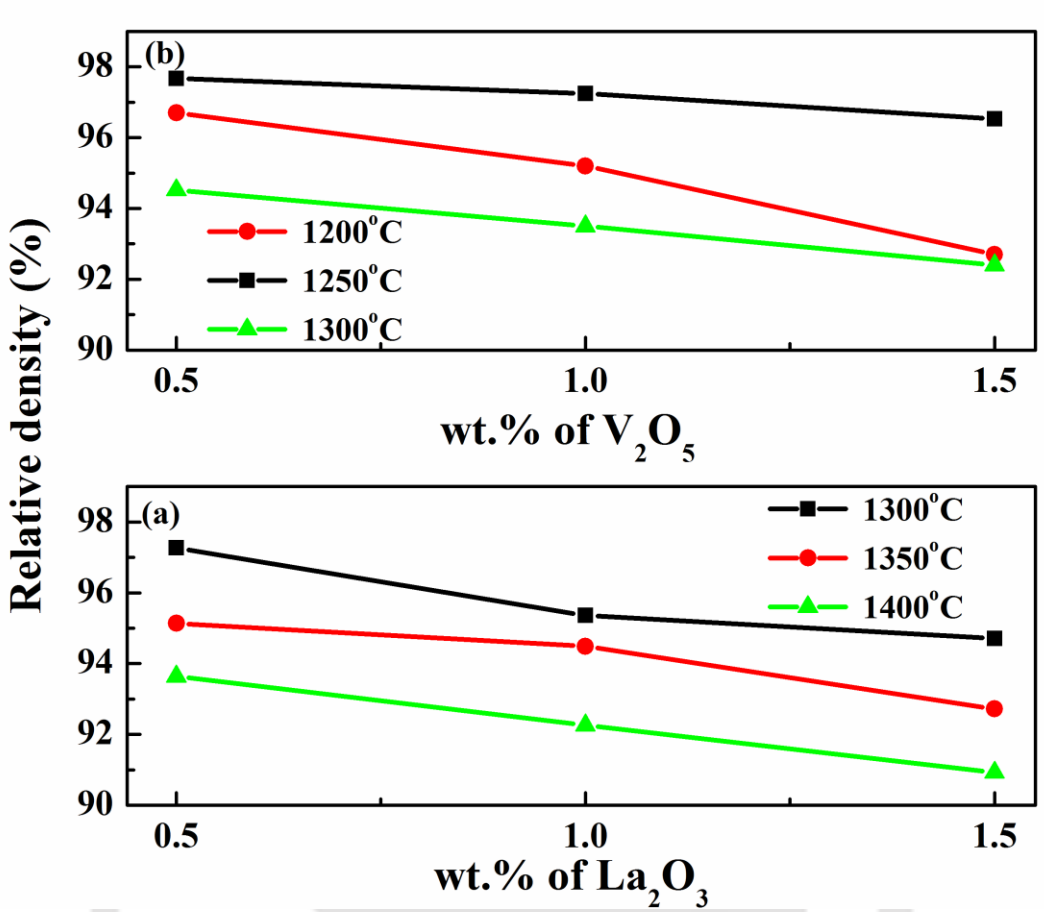

***Fig.5.5**: Variation in relative density as a function of different wt.% of (a) MTO + x La_2O_3 and (b) MTO + y V_2O_5, (x = y = 0.5 - 1.5 wt.%) sintered at different temperatures for 3 hr.*

5.3.3 Relative density

Fig. 5.5 illustrates the diversity of relative density as a function of wt.% of La_2O_3 and V_2O_5 sintered at different temperatures for 3 hr. For of La_2O_3 added samples, with increasing sintering temperature and the wt.% of the La_2O_3, the density of the MTO ceramics decreases. The maximum density of 97.6% was obtained for the MTO samples added with x = 0.5 wt.% of La_2O_3 sintered at 1300 ^oC. The reduction in the density with the higher amounts of La_2O_3 was attributed to the presence of liquid phase effect and the minor secondary phase, which causes the decrease in the average grain size of the samples (see Fig. 5.2(c-d)).

On the other hand, for V_2O_5 added MTO samples, as the sintering temperature increases, the density increases up to 1250 ^oC and then decreases. With increasing amount of additives the relative density of MTO ceramics also decreases. The reduction in relative density at higher sintering temperatures may be due to the evaporation of V_2O_5,

non-uniform grain growth and the formation of secondary phases. As V_2O_5 has lower melting temperature than the La_2O_3 additive, it would be more effectively lower the sintering temperature of the MTO ceramics. In general, the density of the ceramics improved with the increase in sintering temperature upto a critical temperature. In the present case, MTO ceramics with different additives were sintered at constant temperatures for comparison and the sintering temperatures of 1300 ^oC and 1250 ^oC were selected, since all the samples exhibited densities higher than 96 %. In addition, it could be clearly observed that the relative densities of La_2O_3 and V_2O_5 added MTO ceramics sintered at above 1250 ^oC were higher than that of the undoped MTO ceramics which are sintered at 1400 ^oC. This clearly evidences that the addition of La_2O_3 and V_2O_5 in MTO ceramics effectively reduces the sintering temperature nearly by 150 ^oC.

The decrease in sintering temperature in both cases can be attributed to the liquid phase effect. During the sintering process, the liquid spreading to cover the surface of the solid surfaces is separated by the liquid bridge. This decreases the friction between the MTO particles and exerts capillary force, which can be used to rearrange the particle more easily and enhances the densification process to get the maximum packing. During liquid phase sintering, the contact pressure between particles will be improved to promote mass transfer through dissolution and precipitation as well as plastic deformation and vapor transfer resulting in grain growth. When a powder compact is sintered in the presence of a liquid phase, the relative bulk density of the compact increases and at the same time grains grow. The phenomenon in which the average grain size increases via growth of large grains and dissolution of small grains in a matrix is referred as Ostwald ripening. As the capillary pressure exerted on a particle, its solubility in the matrix increases with decreasing particle size. Therefore, the atoms dissolved in the matrix from small particles are transported to large particles, resulting in growth of large grains [5].

5.3.4 Microwave dielectric properties

In order to comprehend the impact of these additives on the microwave dielectric properties, ε_r and $Q \times f_o$ were measured at microwave frequencies. Fig. 5.6 depicts the microwave dielectric constant of MTO ceramics with different wt.% of La_2O_3 and V_2O_5 addition as a function of sintering temperature. In all the cases, it is observed that the relationship between dielectric constant and wt.% of additives reveals the same trend as the relation between relative density and wt.% of additives. In both the cases, with the increase in wt.% of additives, the dielectric constant decreases. The dielectric constants of

the MTO ceramics added with La_2O_3 and V_2O_5 ranged between 12.3 - 14.3 and 12.2 - 14.4, respectively. The decrease in dielectric constant with higher concentration of additives can be attributed to the inferior densities and non - uniform microstructure.

The quality factor ($Q \times f_o$) values of the MTO ceramics as a function of different amounts of La_2O_3 and V_2O_5 are plotted in Fig. 5.7. It is observed that in all the cases, $Q \times f_o$ verses wt.% of the additives followed a similar trend as density verses wt.% additives. The maximum $Q \times f_o$ values for the MTO ceramics supplemented with 0.5 wt.% of La_2O_3 and V_2O_5 are found to be 157,550 GHz and 168,000 GHz, respectively. The lower $Q \times f_o$ values with an increase in the concentration of La_2O_3 and V_2O_5 are due to the presence of minor secondary phase segregated at the grain boundary and the non - uniform grain growth as clearly observed from the SEM pictures. Since, the grain boundary is a plane defect; it probably decreases the $Q \times f_o$ value. Therefore, the specimens with large grains are expected to have high $Q \times f_o$ value as the grain growth decreases the grain boundary area effectively.

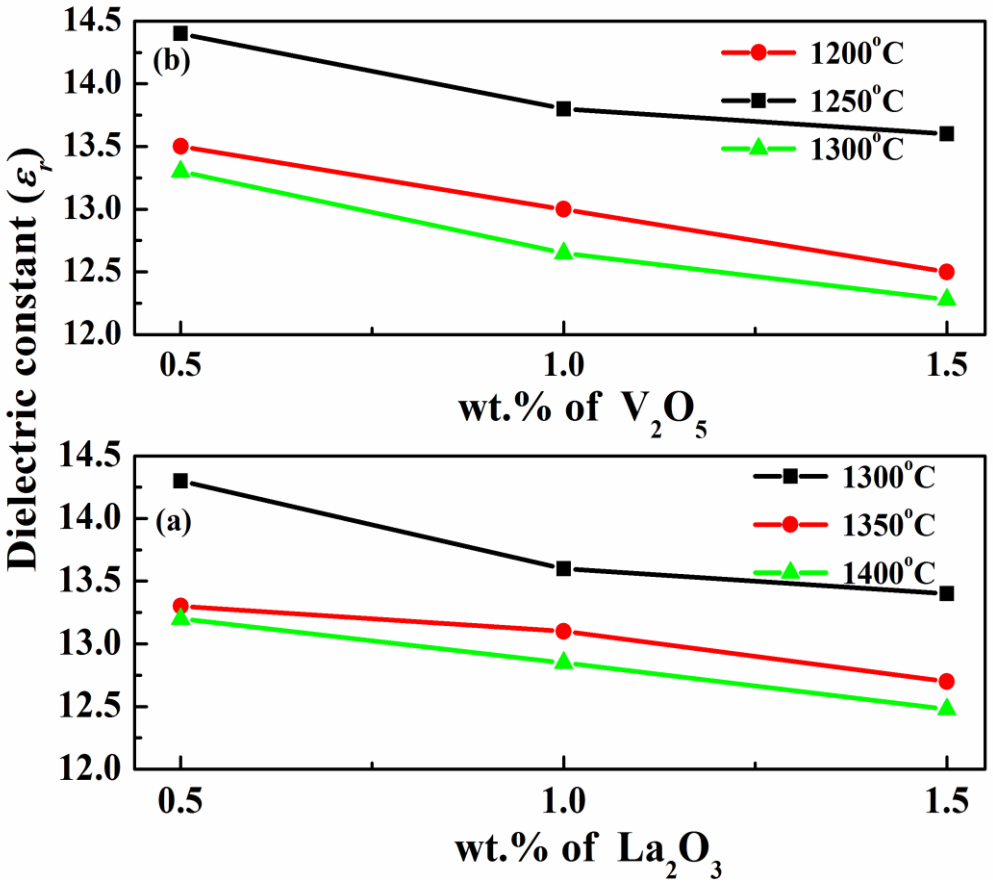

***Fig. 5.6**: (a) Variation in dielectric constant as a function of (a) MTO + x La_2O_3, (b) MTO + y V_2O_5, (x = y = 0.5- 1.5 wt.%), sintered at different temperatures.*

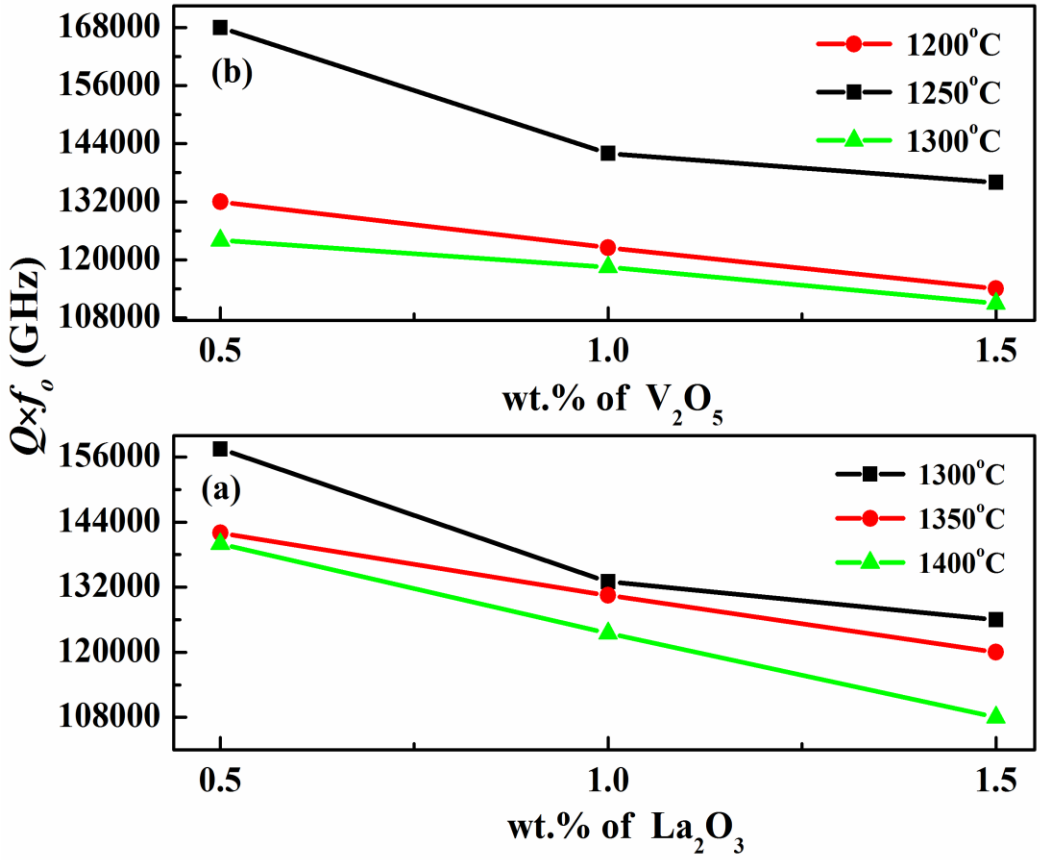

***Fig. 5.7**: (a) Variation in $Q\times f_o$ as a function of (a) MTO + x La_2O_3, (b) MTO + yV_2O_5, (x = y = 0.5- 1.5 wt.%) sintered at different temperatures.*

As the density of all the samples is greater than 95 %, it may be concluded that the $Q\times f_o$ value not only depends on densification but it also strongly depends on grain size of the samples. Grain sizes were suggested to affect the $Q\times f_o$ values of microwave ceramics [6]. Larger sized grains reduce the grain boundaries, and hence lower dielectric loss. The variations in dielectric constant and $Q\times f_o$ as a function of grain size of MTO ceramics added with La_2O_3 and V_2O_5, sintered at 1300 ^oC and 1250 ^oC, respectively are plotted in Fig. 5.8. It shows that both dielectric constant and $Q\times f_o$ values followed the same trend as a function of grain size, in which the dielectric constant and $Q\times f_o$ increasing with the increase in the grain sizes. Furthermore, it is observed that the MTO ceramics added with 0.5 wt.% contain no secondary phases and exhibit higher grain sizes. Therefore, it can be concluded that the increase of dielectric constant and $Q\times f_o$ value at low temperatures with low wt.% of additives was mainly due to the increase of density as well as uniformity of grain growth.

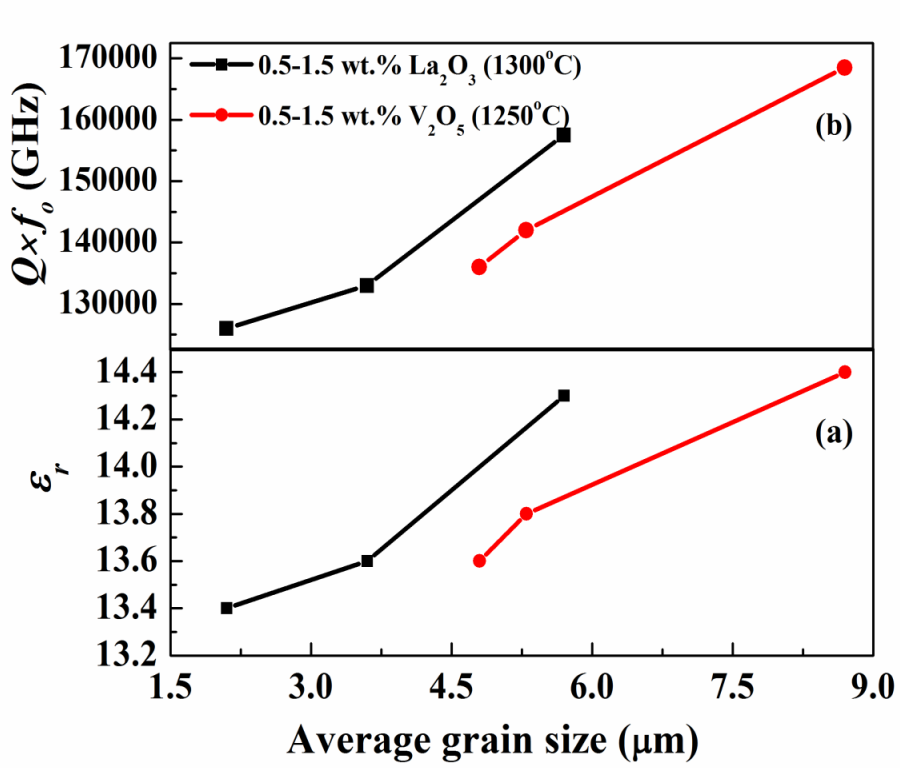

***Fig.5.8**: (a) Variation in (a) ε_r and (b) $Q \times f_o$ values as a function of grain sizes for MTO + x La_2O_3 and MTO + y V_2O_5, (x = y = 0.5 - 1.5 wt.%) ceramics sintered at different temperatures for 3 hr.*

Various factors are postulated to influence the microwave dielectric loss mechanisms and these factors are mainly divided into two types (i) intrinsic and (ii) extrinsic losses [6, 7]. Intrinsic losses in crystals arise due to anharmonic lattice forces that mediate the interaction between crystal and phonons. This leads to damping of the optical phonons and therefore of the microwave field. On the other hand, the extrinsic losses are dominated by extended dislocations, grain boundaries, porosity, oxygen vacancies, abnormal grain growth and secondary phases, which are heavily dependent on the processing conditions. These losses are caused by either dipole relaxations of impurities concentrated at interfaces or relaxations of space charge polarizations present at the interfaces. Interfacial polarization was thought to play an important role in porous materials.

It is well known that the grain boundaries act as two dimensional defects and may contribute significantly into extrinsic dielectric loss. The total number of the grain boundaries decreases with increasing average grain size. It is also known that the long range ordering improves the *Q* factor of the dielectric materials. Since, the grain boundary

interrupts the perfect symmetry of the crystal, the sample having small grains can be viewed as the one with the low degree of ordering. Therefore, it is concluded that the grain size contributes to the $Q \times f_o$ value of MTO ceramics added with different amounts of La_2O_3 and V_2O_5 as evidenced in Fig. 5.8. In addition, the MTO samples added with V_2O_5 exhibited higher $Q \times f_o$ values as compared to the MTO samples added with La_2O_3. La^{3+} ions in MTO matrix act as acceptor. Therefore, the existence of oxygen vacancies in MTO ceramics was due to the oxygen deficiency or trivalent impurity. Since La^{3+} ions act as an acceptor, the reaction could be expressed as

$$La_2O_3 \rightarrow 2\ La'_{Ti} + 3\ O_o + V^{\cdot\cdot}_o \qquad (5.1)$$

The decrease in $Q \times f_o$ values with the increase in wt.% of La_2O_3 can be attributed to the rise in oxygen vacancies which increase the anharmonic interaction. Moreover, the observed $MgTi_2O_5$ is found to influence the $Q \times f_o$ values compared to the oxygen vacancies. On the other hand, the improvement in the $Q \times f_o$ values with the addition of V_2O_5 may be due to reduction in oxygen vacancies. Since, V^+ acts as a donor, the reaction can be expressed as:

$$V_2O_5 + V^{\cdot\cdot}_o \rightarrow 2\ V^{\cdot}_{Ti} + 5O_o \qquad (5.2)$$

The reduced oxygen vacancies influence the anharmonic interaction. Consequently, there is an increase in $Q \times f_o$ value. The decreased $Q \times f_o$ values with the increase in V_2O_5 wt.%, would be attributed to the lower densities, smaller grain size, minor secondary phases and the abnormal grain growth.

Table: 5.1 *Variations of relative density, grain size and $Q \times f_o$ for the doped and undoped MTO ceramics sintered at different temperatures for 3 hr.*

Sintering additives	**Sintering temperature (^{o}C)**	**Grain size (μm)**	**Relative density (%)**	**$Q \times f_o$ (GHz)**
Pure MTO	1400	2.5	89.75	115,000
MTO+0.5 wt.% La_2O_3	1300	5.7	97.23	157,500
MTO+1.0 wt.% La_2O_3	1300	3.6	95.36	133,000
MTO+1.5 wt.% La_2O_3	1300	2.1	94.71	126,500
MTO+0.5 wt.% V_2O_5	1250	8.7	97.67	168,000
MTO+1.0 wt.% V_2O_5	1250	5.3	97.25	142,000
MTO+1.5 wt.% V_2O_5	1250	4.8	96.53	136,500

The $Q \times f_o$ values obtained in the present study are much higher than the $Q \times f_o$ values reported by Belous et al. [8]. The additive La_2O_3 and V_2O_5 contents are greatly influenced the microwave dielectric properties of MTO ceramics, especially $Q \times f_o$ values, but there is not much variation in dielectric constants. For comparison between undoped and doped - MTO ceramics along with their sintering temperature, relative densities, grain size and microwave dielectric properties are given in **Table 5.1**. From this study, it is clear that the additives can effectively reduce the extrinsic losses of the MTO ceramics.

5.3.5 Effect of porosity

To see the effect of porosity on the dielectric constants measured at room temperature using Hakki and Coleman's dielectric resonator method, as modified and improved by Courteny [9, 10], the porosity corrected dielectric constants were calculated using the measured microwave dielectric constants for the MTO + x La_2O_3 and MTO+ yV_2O_5 (x = y = 0.00 -1.5 wt.%) ceramics by using the Eq. 3.3 as described in chapter 3 [11]. The porosity corrected values were slightly higher than the experimental values and are tabulated in **Table 5.2** and **Table 5.3**.

***Table 5.2**: Relative density, measured microwave dielectric constant (ε_r) and dielectric constant corrected for porosity (ε_m)values of pure and La_2O_3 added Mg_2TiO_4 ceramics.*

Samples name	Sintering temperature	Relative density (%)	ε_r (measured)	ε_m (corrected)
Mg_2TiO_4	1400 ^oC	88.54	11.20	13.22
	1350 ^oC	83.27	10.82	13.95
	1300 ^oC	78.75	10.60	14.88
Mg_2TiO_4+0.5 wt.% La_2O_3	1400 ^oC	93.64	13.20	14.43
	1350 ^oC	95.14	13.32	14.25
	1300 ^oC	97.27	14.30	14.88
Mg_2TiO_4+ 1.0 wt.% La_2O_3	1400 ^oC	92.26	12.85	14.36
	1350 ^oC	94.48	13.12	14.20
	1300 ^oC	95.36	13.64	14.55
Mg_2TiO_4+ 1.5 wt.% La_2O_3	1400 ^oC	90.93	12.48	14.19
	1350 ^oC	92.72	12.70	14.08
	1300 ^oC	94.71	13.41	14.23

***Table 5.3**: Relative density, measured microwave dielectric constant (ε_r) and dielectric constant corrected for porosity (ε_m)values of pure and V_2O_5 added Mg_2TiO_4 ceramics.*

Samples name	Sintering temperature	Relative density (%)	ε_r (measured)	ε_m (corrected)
Mg_2TiO_4	1400 °C	88.54	11.20	13.22
	1350 °C	83.27	10.82	13.95
	1300 °C	78.75	10.60	14.88
Mg_2TiO_4+0.5 wt.% V_2O_5	1300 °C	94.52	13.30	14.35
	1250 °C	97.67	14.42	14.86
	1200 °C	96.72	13.51	14.12
Mg_2TiO_4+ 1.0 wt.% V_2O_5	1300 °C	93.52	12.65	13.85
	1250 °C	97.25	13.80	14.33
	1200 °C	95.20	13.02	14.41
Mg_2TiO_4+ 1.5 wt.% V_2O_5	1300 °C	92.41	12.28	13.67
	1250 °C	96.53	13.60	14.26
	1200 °C	92.72	12.55	13.90

5.3.6 Low temperature dielectric properties

To study and understand the dielectric loss mechanisms, the dielectric properties of the MTO ceramics added with different *y* wt.% of V_2O_5 (*y* = 0.0, 0.5 and 1.0 wt.%) were measured as a function of temperature at microwave frequencies. Since the MTO + 1.5 wt.% V_2O_5 sample shows the presence of secondary phases, lower relative density and non - uniform grain growth, this sample was excluded from the cryogenic measurements. Fig. 5.9 shows the variations in resonant frequencies and dielectric constant of the pure MTO and MTO with *y* = 0.5 and 1.0 wt.% as function of temperature from 6.5 K to 290 K. It is noticed that the pure and MTO with *y* wt.% revealed different resonant frequencies. The distinctions in the resonant frequencies can be referred to the differences in the permittivity of the samples and slight variations in the dimensions of the prepared MTO ceramics with and without additives. The dielectric constants of the MTO with *y* wt.% slightly higher as compared to pure MTO and this can be attributed to the lower relative densities. The obtained dielectric constants of the MTO samples added with 0.5 and 1.0 wt.% V_2O_5 were in the rage of 12.0 - 12.2 and 12.2 - 12.4, respectively, while the dielectric constants of pure MTO were in between 11.3 and 11.5.

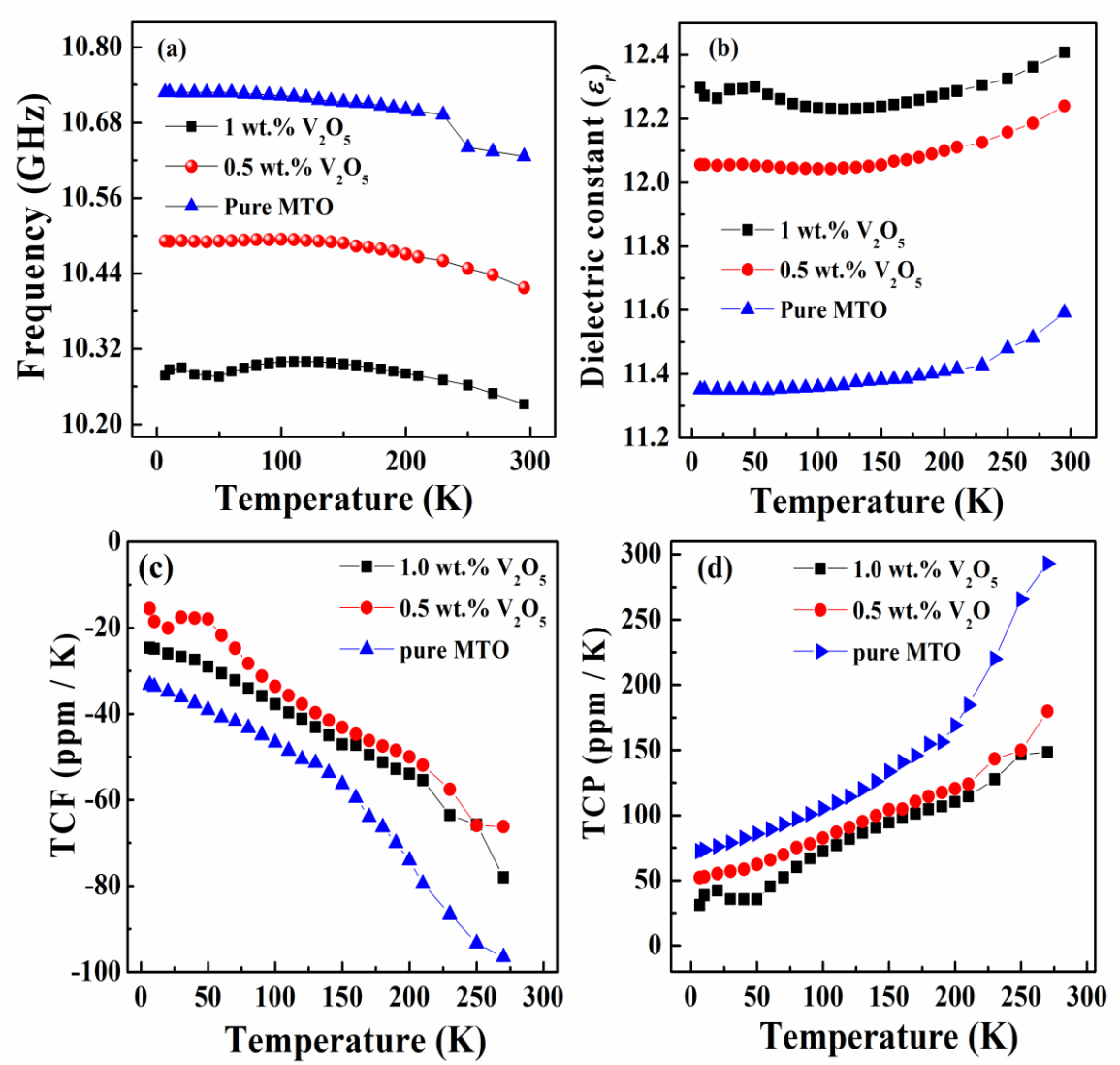

Fig. 5.9: *Variations in the (a) Resonant frequencies, (b) Dielectric constants and (c) Temperature coefficient of frequency and (d) Temperature coefficient of permittivity of the of the MTO ceramics added with and without V_2O_5 as a function of temperature.*

The temperature coefficient of resonant frequency (TCF) of the MTO ceramics is estimated using the following expression,

$$\tau_f = \frac{f_0 - f_{0T}}{f_0}\frac{10^6}{\Delta T} \tag{5.4}$$

where f_0 and f_{0T} are the resonant frequencies measured at room temperature and at temperature T, respectively. The temperature coefficient of resonant frequency of the ceramics is known to be influenced by the additives and the secondary phases present in the material. The variation in the temperature coefficient of frequency of the pure MTO

and MTO with additives measured at cryogenic temperatures is shown in Fig. 5.9 (c). It is observed that the temperature coefficient of frequency of the samples decreases with the increase in temperature and the MTO with *y* wt.% exhibited higher values as compared to pure MTO ceramics. The temperature coefficient of frequency of the MTO ceramics with *y* = 0.5 and 1.0 wt.% were in the range of -66.2 to -15.5 ppm / K and -24.6 to -77.8 ppm / K, respectively, while the values of pure MTO were in between -33.2 to 96.5 ppm / K. This study reveals that the addition of V_2O_5 moderately improved the stability of the MTO ceramics. Similarly, the temperature coefficient of permittivity (τ_ε = TCP) of the MTO ceramics can be estimated using the following expression:

$$\tau_\varepsilon = \frac{\varepsilon_0 - \varepsilon_{0T}}{\varepsilon_0}\frac{10^6}{\Delta T} \tag{5.5}$$

where, ε_0 and ε_{0T} are the permittivity at room temperature and at temperature T, respectively. Fig. 5.9 (d) demonstrates the variation in the temperature coefficient of permittivity of pure MTO and MTO with additives measured at cryogenic temperatures. It was observed that the temperature coefficient of permittivity of all the samples rises with increasing in temperature. Further, pure MTO ceramics exhibit higher values as compared to MTO with *y* wt.%.

Fig. 5.10 (a) shows the temperature dependent dielectric loss of the pure MTO and V_2O_5 added MTO ceramics in the temperature range of 6.5 K to 295 K at 10.2 GHz. It is observed that as the temperature increases from 6.5 K to 295 K, the loss tangent of the pure MTO ceramics increases slightly. On the other hand, the loss tangent of the MTO with *y* = 0.5 and 1.0 wt.% is higher in the temperature range of 6.5 - 90 K and gradually decreases with an increase in measurement temperature. Similar types of result was reported by Shimada et al. [12] in the $Ba(Mg_{1/3}Ta_{2/3})O_3$ ceramics systems measured in the temperature range of 20 -300 K with an loss peak at 40 K. They suggested that the loss peak was caused by the local orientation polarization having dispersion at the microwave frequency. This peculiar frequency dependence of the dielectric loss is well described by Zuccaro et al. [13], by taking into two contributions: (i) microwave absorption by two phonon difference process and (ii) orientation polarization resonance occurring at the microwave frequency. The contribution of the dielectric loss of the two phonon difference process was discussed by Aupi et al. [14]. They were successful in analysis of the

temperature dependent of dielectric loss and suggested that the microwave absorption should simply occur at the Brillouin zone boundary.

On the other hand, the decrease in dielectric loss with the increase in temperature in the V_2O_5 added MTO systems may be due to reduction in oxygen vacancies. Since V^+ acts as a donor, this helps to reduce the oxygen vacancies. The reduced oxygen vacancies influence the anharmonic interaction. Hence, there is a decrease in dielectric loss. Similar argument was reported by Templeton et al. [15] and they found that pure high densified TiO_2 showed very poor dielectric loss at 300 K. On cooling, the pure TiO_2 showed a dramatic reduction in the dielectric loss at around 100 K and this was interpreted as carrier freeze out. In order to prevent the reduction of Ti^{4+} to Ti^{3+} the pure TiO_2 was doped with 2^+ and 3^+ ions with ionic radii in the preferred range 0.5 - 0.95 Å. The dielectric loss measured at 3 GHz of such materials was reduced considerably and dropped smoothly as a function of temperature from 6×10^{-5} at 300 K to a value of 5×10^{-6} at 15 K. Further, the intensity of the loss tangent peak increases with increase in *y* wt.%. Alford et al. [16] have investigated the dielectric loss of single crystals and polycrystallline analogues in the temperature range of 10 to 320 K and they found that impurities, porosity, grain size and grain boundaries are responsible for the losses in the dielectric materials. Therefore, the observed peak of loss tangent in the temperature range of 6.5 – 290 K may be due to the presence of secondary phase, porosity, grain size and liquid phase segregated at the grain boundary of the samples as confirmed from SEM images (see Fig.5.3 (c)). It is generally understood that impurities are swept to the grain boundaries by diffusion and at the grain boundaries, there may be a relaxation of space charges or dipoles. The two - phonon acoustic and quasi - Debye relaxation can occur at the grain boundaries due to relaxation of the conservation of quasi - momentum rules and a breakdown of time reversal symmetry [17]. The observed loss tangent values for pure MTO ceramics at 6. 5 K is 6.6×10^{-5} and at 295 K is 9.4×10^{-5} whereas the loss tangent for the MTO with y = 0.5 wt.% at 6.5 K is 0.0021 and at 295 K is 1.3×10^{-4}. The loss tangent of the MTO with y = 1.0 wt.% measured at 6. 5 K and 295 K found to be 0.0021 and 6.7×10^{-4}, respectively. This study demonstrates that the addition of V_2O_5 significantly affects the loss tangent in MTO ceramics. The samples with higher concentrations of V_2O_5 exhibited lower relative densities and smaller grain sizes. The microwave dielectric properties of pure and MTO with *y* wt.% measured at room temperature were given in **Table 5.1**. It was found that the MTO with y = 0.5 wt.% exhibited the lowest loss tangent

as compared to pure MTO, but at the cryogenic temperature, the same sample is exhibiting somewhat higher loss tangent as compared to pure MTO.

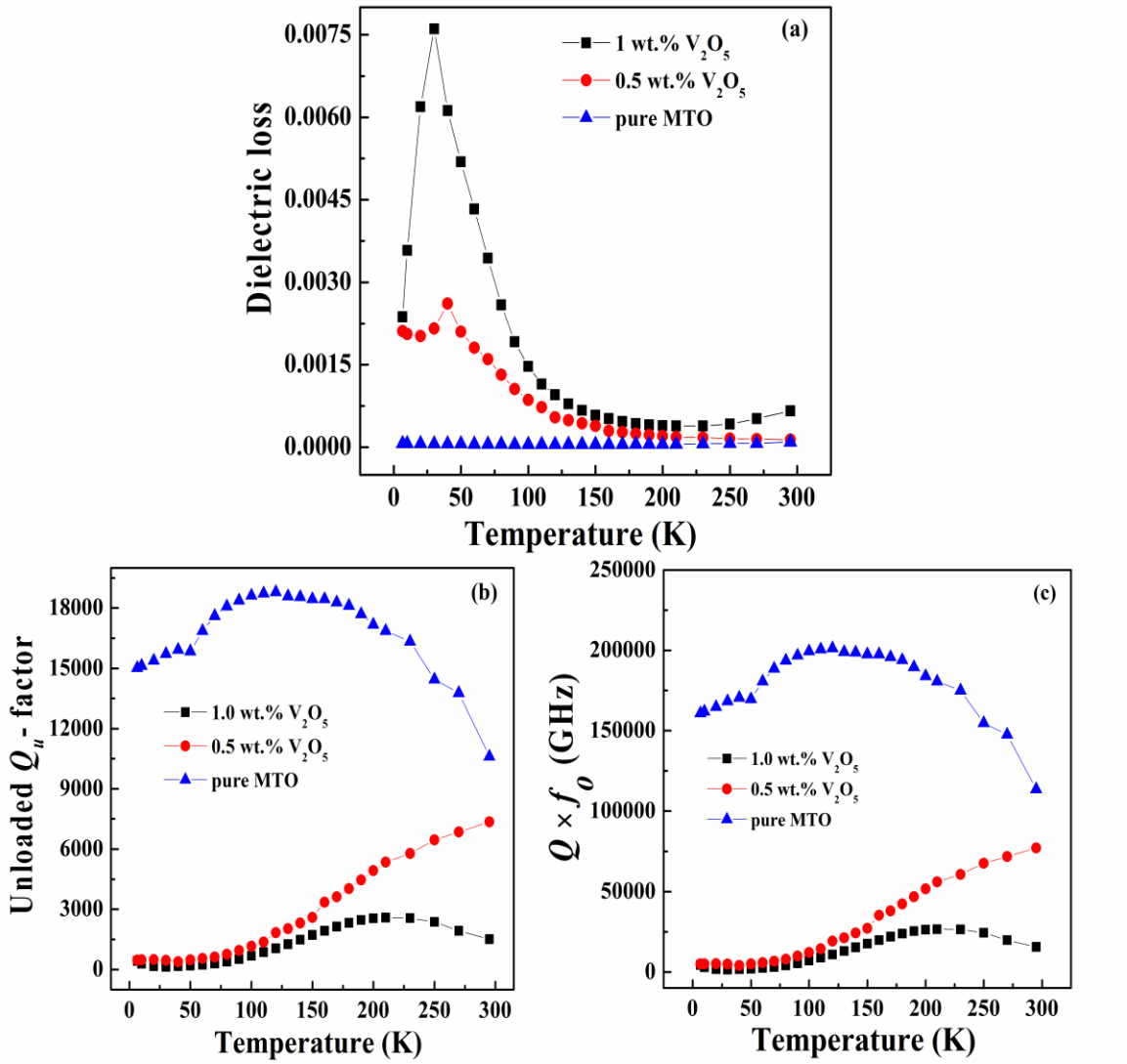

Fig. 5.10: *Variation in the (a) loss tangent, (b) unloaded Q factor and (c) $Q \times f_o$ of the MTO ceramics added with and without V_2O_5 as function of temperature.*

Fig. 5.10 (b) shows the temperature dependent of the unloaded Q_u factor of the pure and added MTO ceramics. The resonance frequencies may vary slightly depending on the size of the sample and temperature. It is found that the unloaded Q_u factor increases with increasing temperature for all the V_2O_5 added samples, while for pure MTO, the Q_u values first increases and then decreases above 120 K. In the case of pure MTO, the unloaded Q_u factor is higher as compared with 0.5 and 1 wt.% V_2O_5 added MTO samples. The maximum unloaded quality factor (Q_u) of the pure MTO is 18797 at 120 K and

minimum at 10604 at 295 K. The product of the quality factor and resonant frequency is considered as a tool for evaluating the quality of the dielectric materials.

Fig. 5.10 (c) shows the temperature dependence of $Q \times f_o$ of the pure and V_2O_5 added MTO ceramics. It was observed that the $Q \times f_o$ values for 0.5 and 1.0 wt.% V_2O_5 added samples increase with increasing temperature, while for pure MTO, the $Q \times f_o$ values first increases up to 120 K and then decreases. In comparison with pure MTO, the results substantiate that the dielectric properties are affected as a result of addition of V_2O_5. It is interesting to note that the obtained loss tangent and $Q \times f_o$ values at cryogenic temperatures were independent of relative densities and average grain sizes and significantly influenced by the secondary phase and liquid phase effect. The increase in dielectric loss at low temperatures for the samples doped with V_2O_5 can be attributed to the following factors: (i) V_2O_5 is a powerful oxidizing agent and undergo reduction in stages depending on the conditions of the process. We propose that at low temperatures there is a possibility of going to trivalent state, (ii) Ti and V_2O_5 is known to form a solid solution of $(Ti_{1-x}V_x)_2O_3$ and (iii) slight reduction in the volume of unit cell. These factors may enhance the dielectric loss at low temperatures. However, there is no report available on the dielectric properties of V_2O_5 at low temperatures. Therefore, the obtained low loss tangent and $Q \times f_o$ values are attributed to both the extrinsic and intrinsic loss mechanisms.

The dielectric loss originates due to the extrinsic and intrinsic factors. Extrinsic loss occurs due to the secondary phases, non - stoichiometry, porosity, impurities, non - uniform grain growth and oxygen vacancies. The extrinsic loss mechanisms are also influenced by the dipole relaxation of the defect oriented polarization segregated at the grain boundaries. Conversely, intrinsic loss mechanism is impacted by the anharmonic force which facilitates / mediates the interaction between crystal lattice modes and electromagnetic field leading to the damping on optical phonon modes and lattice imperfections, increasing the damping factor. Further, with the decrease in temperature, the damping of the optical phonon modes or the anharmonocity reduces, i.e., damping factor is proportional to the temperature [18, 19]. In most cases of practical dielectric ceramics, the extrinsic dielectric loss due to impurities, grain boundaries, stress or electrical conductivity is higher than the intrinsic dielectric loss. Measurements of dielectric properties in a broad frequency and temperature range can assist in distinguishing between intrinsic and extrinsic dielectric loss. Therefore, it is important to analyze the lattice vibration of spectrum of the crystals as the intrinsic dielectric loss is

directly related to the lattice vibration of the materials. A complete theory of intrinsic dielectric losses was developed by Gurevich and Tagantsev [20]. The theory calculates the losses due to the interaction of the electromagnetic field with the phonon system of the crystal and the theory was found to agree well with the earlier experimental results [21]. The temperature dependent of dielectric loss of V_2O_5 added MTO systems are found to be in good agreement with the theory of intrinsic losses. From this study, the addition of V_2O_5 significantly improves the uniform microstructure with larger average grain sizes and high relative densities at lower sintering temperatures but could not improve the microwave dielectric properties, especially the loss tangent and $Q \times f_o$ values as compared to pure MTO at cryogenic temperatures.

5.3.7 Broadband dielectric properties

Fig. 5.11 illustrates the frequency dependence of dielectric constant (ε_r) and loss (tan δ) measured at room temperature in the frequency range from 1 MHz to 2.0 GHz for the pure MTO and MTO + y wt.% V_2O_5 (y = 0.5 and 1.0) samples sintered at 1400 ^oC and 1250 ^oC for 3 hr, respectively. It is observed that (i) the value of ε_r is found to be higher for V_2O_5 added MTO ceramics, (ii) ε_r remains almost constant up to 0.04 GHz for all the samples, (iii) the rate of decrease of ε_r with frequency at a higher frequency range is significantly reduced for V_2O_5 added MTO ceramics, i.e., the stability of ε_r in V_2O_5 added MTO is better at the higher frequency range. A sharp peak (around 1.8 GHz) is observed in the ε_r values of all the samples. The peak is much sharper for the pure MTO but broadened for V_2O_5 added samples. (iv) On the other hand, the values of tanδ remains constant for pure MTO ceramics up to 0.01 GHz, which is shifted to 1.10 GHz and 0.08 GHz for the samples doped with 0.5 and 1.0 wt.% of V_2O_5, respectively (v) In the case of pure MTO ceramics tanδ increases rapidly with increasing frequency above 0.01 GHz. (vi) The V_2O_5 added MTO exhibits a lower tanδ at higher frequencies confirming the low loss as compared to pure MTO ceramics and (vi) A sharp peak in the tanδ of the pure MTO is drastically suppressed for V_2O_5 added samples. The increment in both ε_r and tanδ values around 1.8 GHz may be attributed to the relaxation of the dipole mechanism.

The dielectric behavior observed in such type of materials can be explained with interfacial polarization predicted by the Maxwell - Wagner model [22] in agreement with Koop's phenomenological theory [23]. According to these models, the dielectric materials can be imagined as a heterogeneous structure consisting of well conducting grains

separated by thin layers of poorly conducting grain boundaries. These grain boundaries could be formed during the sintering process either by superficial reduction or oxidation of crystallites in the pores materials as a result of their direct contact with the firing atmosphere. The grain boundaries dominate at lower frequency, while grains dominate at higher frequencies. The observed broadband dielectric properties complement the microwave dielectric properties measured at room temperature.

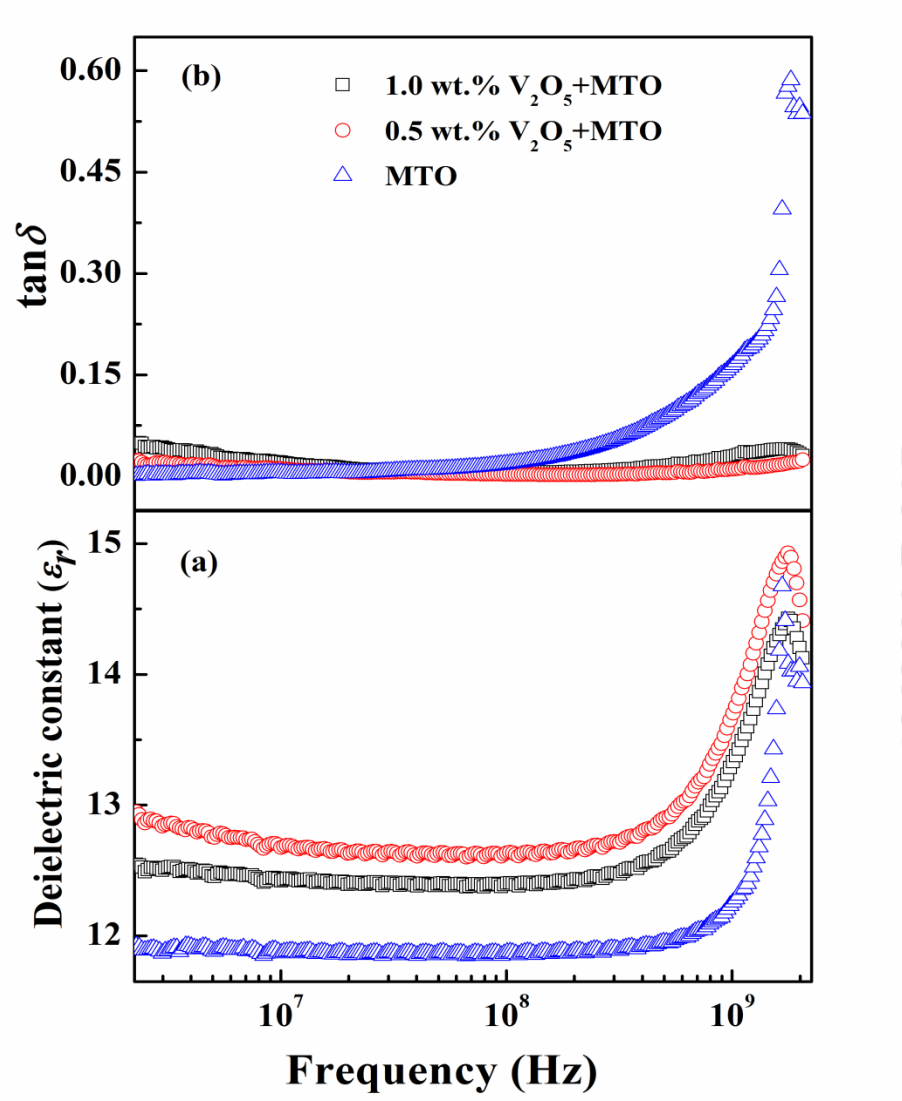

Fig. 5.11*: Broadband dielectric properties of MTO ceramics measured as a function of frequency.*

5.4 Effect of Bi_2O_3 on microwave dielectric properties of MTO ceramics

5.4.1 Structural analysis

Fig. 5.12 (a) illustrates the XRD patterns of MTO ceramics added with 0.5 - 1.5 wt.% of Bi_2O_3 sintered at 1250 ^oC for 3 hr and pure MTO ceramics sintered at 1400 ^oC. It

is confirmed that for all the samples peaks indicating the presence of Mg_2TiO_4 as a main crystalline phase (ICSD – PDF # 06-5792) and $MgTiO_3$ as minor secondary phase. The formation of the secondary phase was attributed to the fact that MgO is hygroscopic leading to a *Ti* rich compound. It is well known that in MTO based ceramics, it is quite difficult to eliminate the formation of $MgTiO_3$ and $MgTi_2O_5$, where the presence of $MgTi_2O_5$ detoriates the overall dielectric response and especially the quality factor of MTO ceramics. But, the addition of Bi_2O_3 suppresses the presence of $MgTi_2O_5$ and formed $MgTiO_3$ as a secondary phase. Usually, $MgTiO_3$ formed as an intermediate phase in the MgO - TiO_2 system and is difficult to eliminate completely from the samples prepared by mixed oxide route. Interestingly, the microwave dielectric properties of $MgTiO_3$ are similar to those of MTO and hence the presence of finite $MgTiO_3$ phase will not affect the overall response of the MTO ceramics.

Petrova et al., [24] proposed the following thermal decomposition mechanism to further explain the formation of $MgTiO_3$ as a secondary phase.

$$Mg_2TiO_4 = Mg_{2+2\delta}Ti_{1-\delta}O_4 + MgTiO_3 \qquad (5.6)$$

where δ is a function of temperature. However, the thermal decomposition of MTO becomes negligible at temperatures exceeding 1400 ^oC.

The XRD patterns of all the samples could well be refined by taking *Fd-3m* space group in cubic cell. The typical XRD patterns along with the Rietveld refinement of pure MTO and MTO + *x* wt.% Bi_2O_3 (*x* = 0.5 and 1.0) samples sintered at 1400 ^oC and 1250 ^oC for 3 hr, respectively are shown in Fig. 5.12 (b - d). The refinement was carried out by varying cell parameters, position of the Mg, Ti, and O atoms, occupancy and thermal parameters. The calculated lattice constants of pure MTO and MTO + *x* wt.% Bi_2O_3 ceramics were found to be nearly same. This is expected due to the differences of ionic radii of Bi^{3+} ions (1.03 Å) with Mg^{2+}(0.72 Å) and Ti^{4+} (0.605 Å) ions. Hence, the Bi^{3+} ion cannot be substituted in the Mg^{2+} and Ti^{4+} sites. This suggests that Bi_2O_3 contents cannot form solid solution with the MTO matrix, but remain at the grain boundary. The mean crystallite sizes of Bi_2O_3 added MTO ceramics calculated from the Williamson-Hall plot method ($\beta\ Cos\theta$ *verses* $Sin\theta$) was found to be around 45 nm.

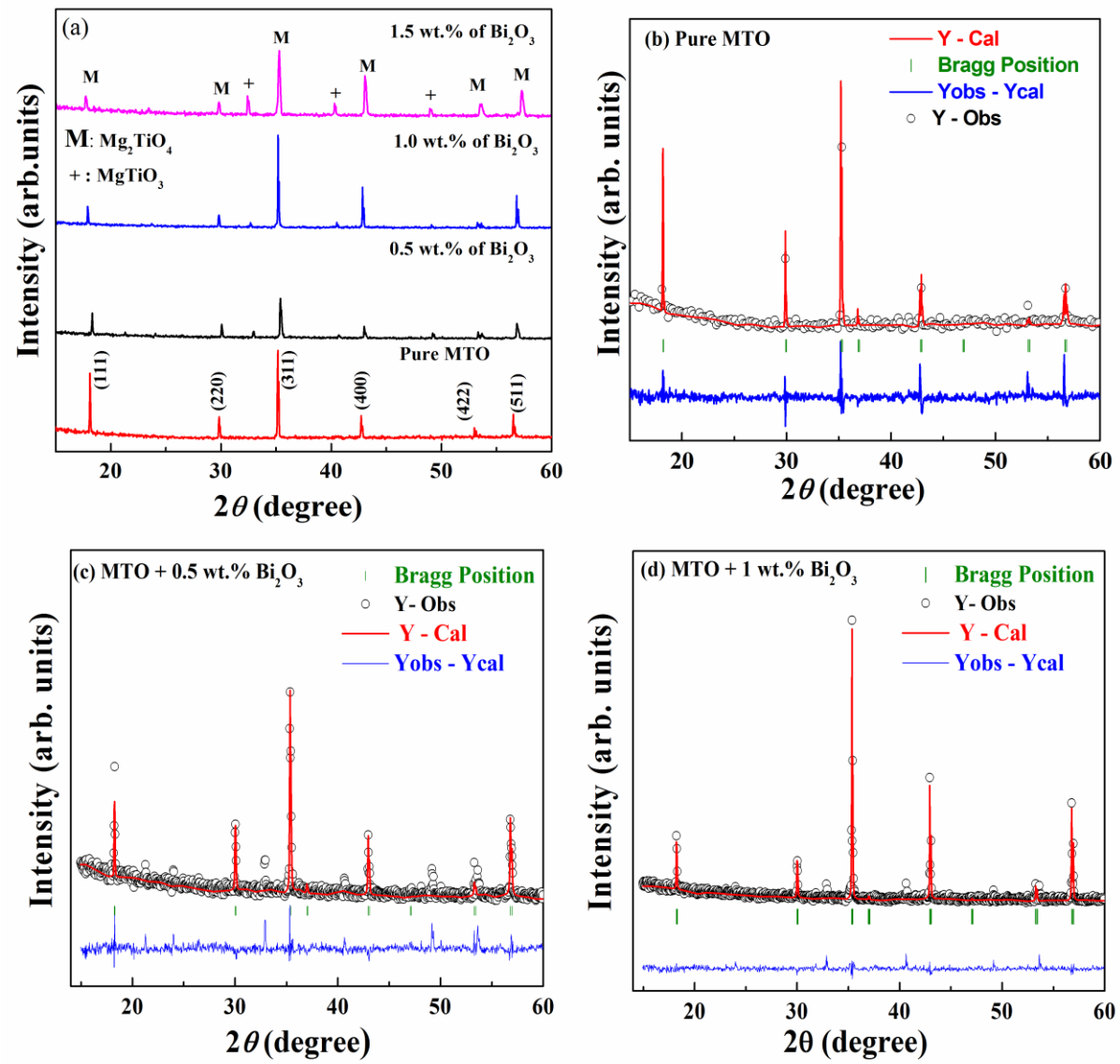

***Fig. 5.12**: (a) XRD patterns of the MTO ceramics added with different wt.% of Bi_2O_3 sintered at 1250 ^oC for 3 hr and XRD pattern along with Rietveld refinement of (b) pure MTO (c) MTO + 0.5 wt.% Bi_2O_3 and (d) MTO + 1.0 wt.% Bi_2O_3 ceramics.*

5.4.2 Microstructural analysis

To understand the effect of Bi_2O_3 addition on the evolution of microstructure of MTO ceramics, surface morphology of sintered MTO ceramics pellets was analysed by using FE -SEM. Fig. 5. 13 illustrates the microstucture of the pure MTO ceramics sintered at 1400 ^oC and MTO ceramics incorporated with different concentrations of Bi_2O_3 additives sintered at 1250 ^oC for 3 hr. Compared to the microstructure of pure MTO ceramics, the MTO ceramics added with different amounts of Bi_2O_3 exhibit larger grain size with well-defined microstructure at lower sintering temperature. This confirms that the sintering aid

prompted the densification of ceramics and inhibited the grain growth due to liquid phase effect. Moreover, the average grain size first increases linearly up to 1 wt.% of Bi_2O_3 content and then decreases gradually with abnormal grain growth. The average grain size was ranged from 3.4 to 10 μm and a maximum grain size with uniform grain growth was appeared for 1 wt.% of Bi_2O_3 added samples.

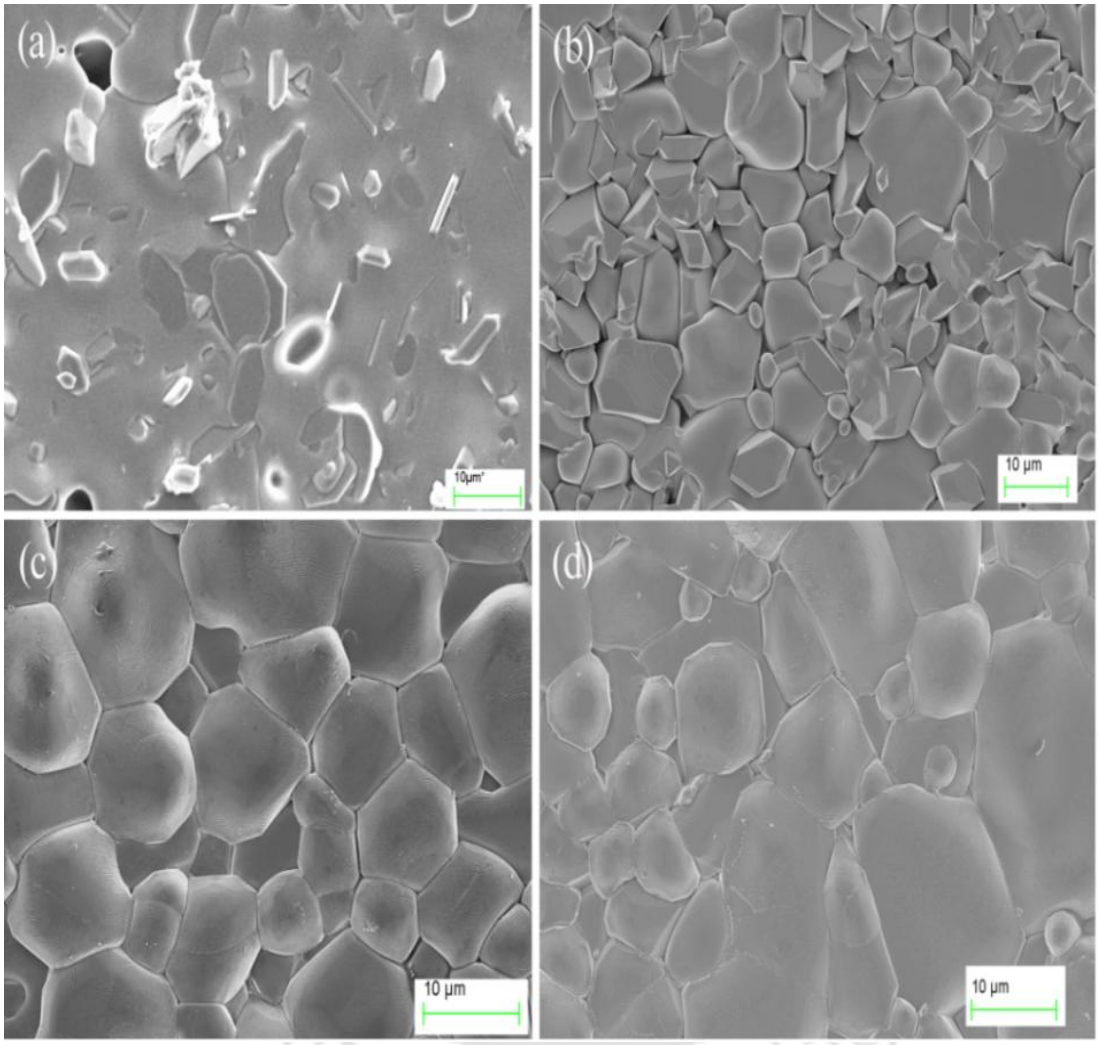

Fig.5.13: *FE-SEM micrographs of (a) pure MTO ceramics sintered at 1400 ^oC and MTO ceramics added with (b) 0.5 wt.%, (c) 1.0 wt.% and (d) 1.5 wt.% Bi_2O_3 sintered at 1250 ^oC.*

Fig. 5.14 illustrates the FE - SEM micrographs of the MTO samples incorporated with 1 wt.% of Bi_2O_3 sintered at different temperatures for 3 hr. It was found that the samples sintered at 1150 ^oC have porous microstructure with non - uniform grain growth and the grain size of the samples was small. This may be due to the insufficient sintering temperature. With increasing the sintering temperature to 1200 ^oC, the grain size increases significantly, but the uniform microstructure with large grain size with porous

free was observed only at 1250 ^oC. On the other hand, non - uniform grain growth was observed for the samples sintered at 1300 ^oC and the grains are relatively large. The non - uniform grain growth observed for the samples sintered above 1250 ^oC could be possibly due to the presence of secondary phases and segregation of liquid phase at the grain boundaries. Microstructure analysis reveals that the optimization of the additive contents and the sintering temperature play an important role during the development of uniform microstructure and the average grain sizes of the MTO ceramics.

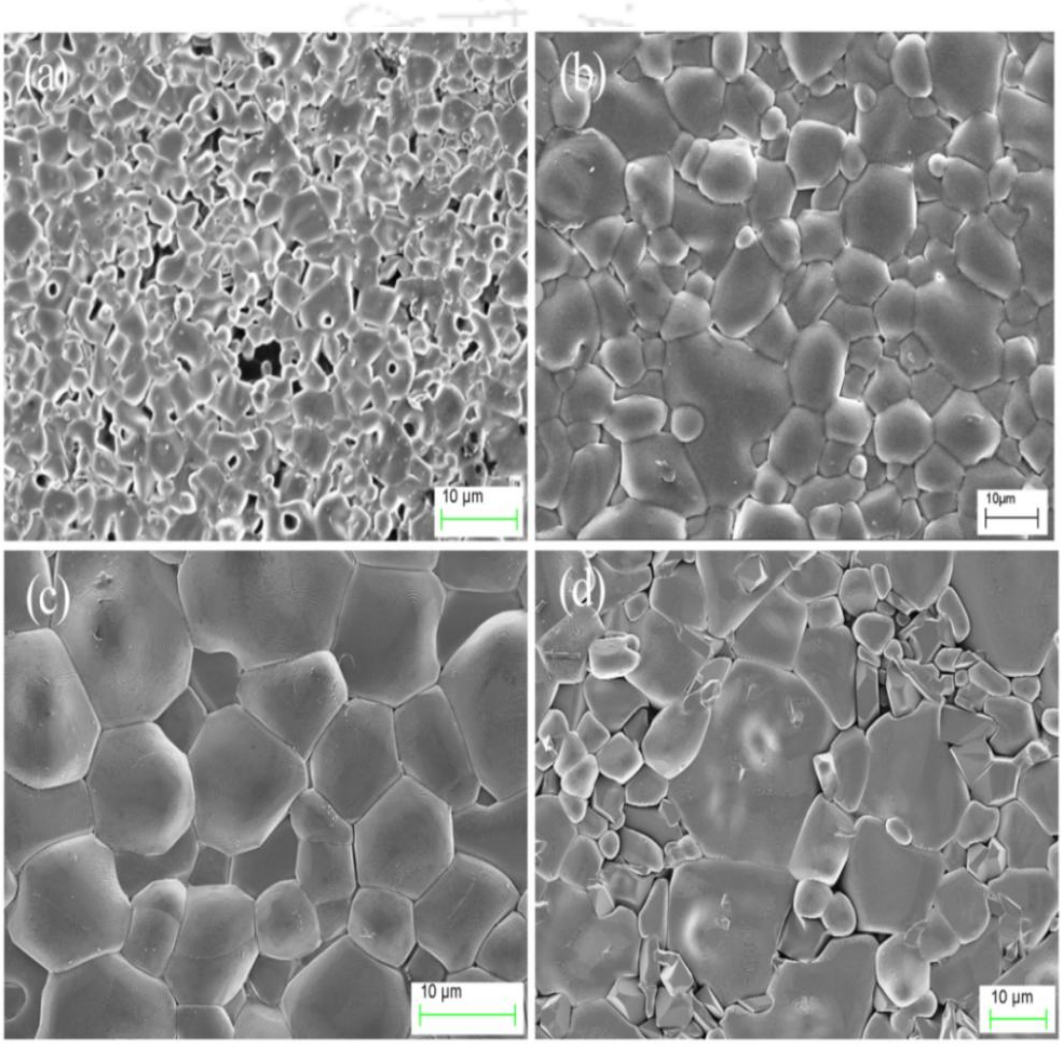

***Fig.5.14**: FE - SEM micrographs of MTO ceramics added with 1.0 wt% of Bi_2O_3 sintered at (a) 1150 ^oC (b) 1200 ^oC and (c) 1250 ^oC (d) 1300 ^oC for 3 hr.*

5.4.3 Relative density

Fig. 5.15 illustrates the variation of average grain size and relative density of the pure MTO and Bi_2O_3 added MTO ceramics as a function of sintering temperature. The Fig.

5.15 (a) reveals that in case of pure MTO ceramics, the average grain size increases almost linearly with the increase of sintering temperature. But, for the Bi_2O_3 added MTO samples the average grain size increases with increasing sintering temperature up to 1250 ^oC and then decreases significantly due to the abnormal grain growth. The reduction in average grain sizes at higher concentration of additives can be attributed for the decrease in density due to liquid phase effect.

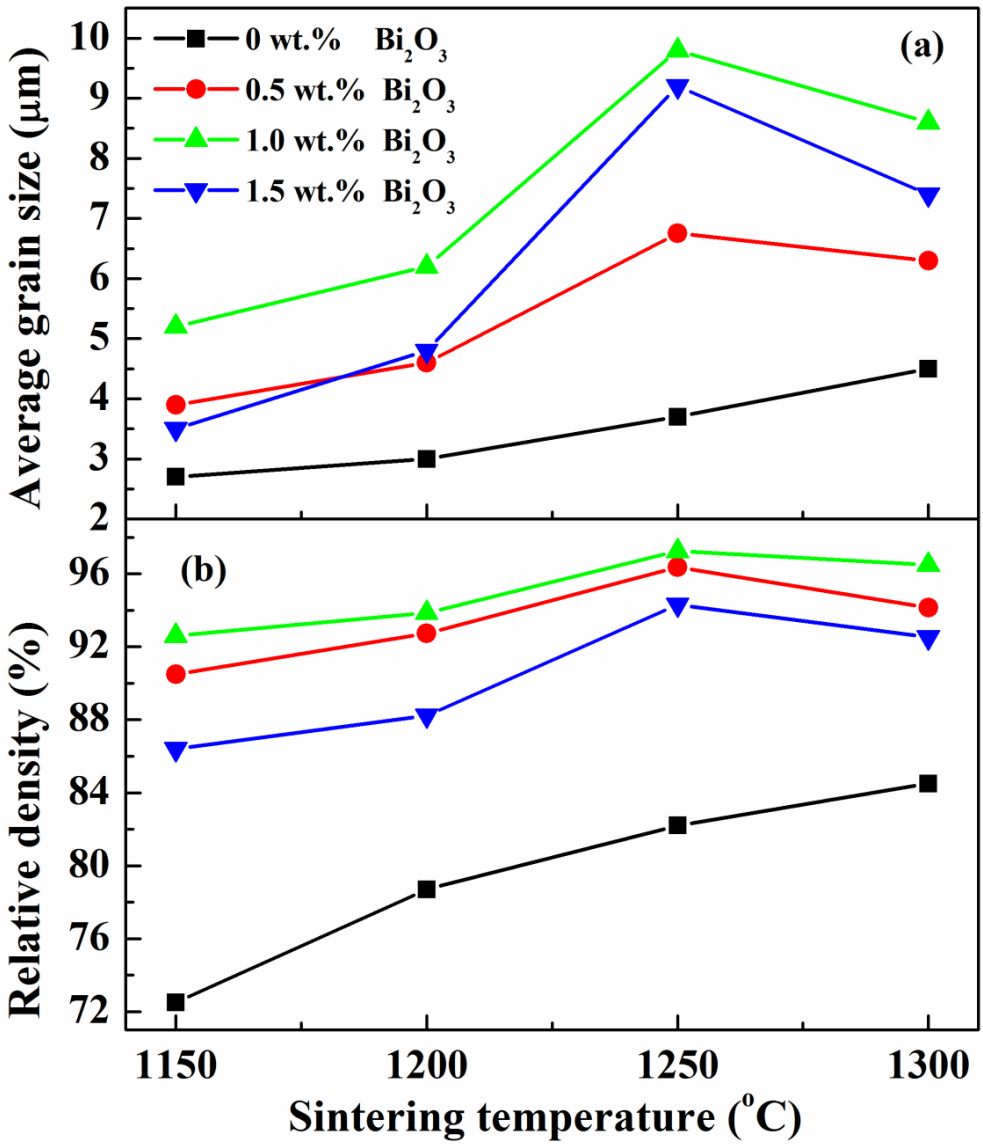

Fig.5.15: *Variation of (a) average grain size and (b) relative densities of MTO+ x Bi_2O_3 (x = 0 to 1.5 wt.%) ceramics as a function of sintering temperature.*

To study the effect of Bi_2O_3 addition on the densification of MTO ceramics the relative densities of MTO ceramics mixed with different wt.% of Bi_2O_3 was measured using Archimedes method and shown in Fig. 5.15(b). It is observed that the density of the

undoped MTO ceramics steadily increased from 72 to 84% of the theoretical density with increasing temperature from 1150 to 1300 ^oC, respectively. Although pure MTO samples contain only the MTO phase, the relative density would not be enhanced largely. When Bi_2O_3 was added as sintering aid, the density of the MTO ceramics increases up to 1 wt.%, and then slightly decreases. The reduction in density with higher amounts of Bi_2O_3 was due to appearance of pores resulted from an inhomogeneous grain growth (Fig. 5.13(d)) and secondary phases, as confirmed from XRD patterns. Nevertheless, the decrease in density above 1250 ^oC may be correlated to the evaporation of Bi_2O_3, which causes abnormal grain growth (Fig. 5. 14(d)). The maximum relative density of 97.2% was obtained for the Bi_2O_3 (1 wt.%) added MTO sample sintered at 1250 ^oC. These results suggested that higher amount of Bi_2O_3 in MTO is not suitable for producing dense MTO ceramics.

The densification temperature of pure MTO ceramics is 1400 ^oC. However, with the addition of Bi_2O_3 content, the MTO ceramics were easily densified at lower temperature of 1250 ^oC. It is wel-known that Bi_2O_3 is one of the flux formers with low melting temperatures (at around 750 ^oC). Therefore, it can be understood that the densification of temperature tends to shift down to lower temperature with increasing Bi_2O_3 content. This fact is attributed to the liquid phase formation during sintering process, which assists the densification through particle rearrangement, solution precipitation and solid skeleton processes [25]. Therefore, it can be concluded that the Bi_2O_3 additive concentrations could not only decrease the sintering temperature, but also could play an important role on the densification and enhancement of grain growth.

5.4.4 Microwave dielectric properties

To understand the influence of Bi_2O_3 addition on the dielectric response of MTO ceramics, microwave dielectric properties were measured. Fig. 5.16(a) illustrates the microwave dielectric constant (ε_r) of MTO ceramics incorporated with different wt.% of Bi_2O_3 at different sintering temperatures. It is observed that the relationship between dielectric constant and wt.% of Bi_2O_3 reveals the same trend in the relation between relative density and wt.% of Bi_2O_3. With the increase in the concentration of Bi_2O_3 wt.%, the dielectric constant increases up to 1 wt.% and then decreases slightly. The dielectric constant values of Bi_2O_3 added MTO ceramics were ranged between 10.6 - 13.2. Even though $MgTiO_3$ was present as secondary phase, no evidence of detoriation of the microwave dielectric properties of the MTO ceramics was observed. This could be due to

similar dielectric properties ($\varepsilon_r \approx 17$ and $Q \times f_o \approx 160{,}000$ GHz) [26] of $MgTiO_3$ as compared to MTO ceramics. Since the volume fraction of secondary phase concentration was very less (only 3 - 4%), so the decrease in dielectric constant with higher concentration of additives (above 1wt.%) can be correlated to the inferior densities, non - uniform grain growth and formation of liquid phase at the grain boundary. To see the effect of porosity on the dielectric constant, the measured values of the microwave dielectric constants corrected for porosity using the Eq. 3.3. The porosity corrected values were bit higher than the experimental values and are tabulated in **Table 5.4**.

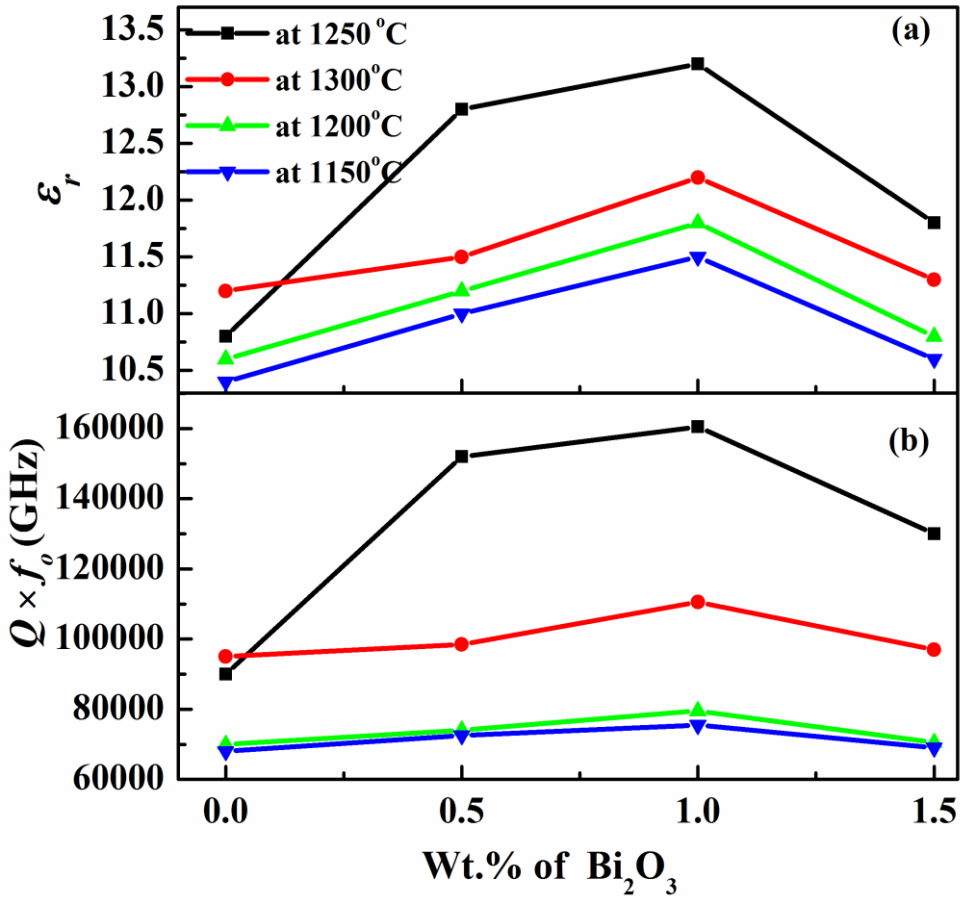

Fig. 5.16: Variation in (a) dielectric constant (ε_r) and (b) $Q \times f_o$ as a function of different wt.% of Bi_2O_3, sintered at different temperatures for 3 hr.

Fig. 5.16 (b) demonstrates the quality factor ($Q \times f_o$) values of the MTO ceramics as a function of different amounts of Bi_2O_3 sintered at different temperatures for 3 hr. It was observed that with increasing Bi_2O_3 content, the $Q \times f_o$ value was significantly increased up to 1 wt.% and decreases significantly. A maximum $Q \times f_o$ value of 160,500 GHz (at 10.48 GHz) was obtained for the 1 wt.% Bi_2O_3 added MTO sample sintered at 1250 ^oC. This

behavior is similar to the variation of density verses wt.% of additives as shown in Fig.5.15. It is considered that the abnormal distribution of the grain growth and formation of liquid phases in the samples with higher wt.% of additives causes the decrease in the relative density. This results in the decrease of $Q \times f_o$ values. Li et al. [27] reported that the microwave dielectric properties of ceramics are strongly dependent on both the densifications and microstructure of the specimens, which is in good agreement with the present study.

***Table 5.4**: Relative density, measured microwave dielectric constant (ε_r) and dielectric constant corrected for porosity (ε_m) values of pure MTO and Bi_2O_3 added MTO ceramics.*

Material composition	Sintering temperature	% of relative density	ε_r (measured)	ε_m (corrected)
Mg_2TiO_4	1400 °C	88.54	11.20	13.22
	1350 °C	85.22	10.82	13.95
	1300 °C	78.75	10.60	14.88
	1250 °C	72.53	10.42	16.71
Mg_2TiO_4+ 0.5 wt.% Bi_2O_3	1300 °C	94.14	11.53	12.50
	1250 °C	96.36	12.80	13.45
	1200 °C	92.74	11.22	12.42
	1150 °C	90.50	11.00	12.58
Mg_2TiO_4+ 1.0 wt.% Bi_2O_3	1300 °C	96.49	12.23	12.82
	1250 °C	97.25	13.24	13.75
	1200 °C	93.86	11.85	12.90
	1150 °C	92.60	11.51	13.18
Mg_2TiO_4+ 1.5 wt.% Bi_2O_3	1300 °C	92.12	11.32	12.56
	1250 °C	94.31	11.84	12.80
	1200 °C	88.23	10.80	12.83
	1150 °C	86.40	10.63	12.98

The value of quality factor ($Q \times f_o$) not only affected by the lattice vibrational modes, but also by densification, grain morphology, impurity and secondary phases, etc. The increase in sintering temperature is helpful to promote the densification as well as average uniform grain growth of the samples until the $Q \times f_o$ value reaches the maximum. On further increasing the sintering temperature, resulted in the appearance of abnormal grain growth with porous microstructure and secondary phases, which leads to the reduction of the $Q \times f_o$ values [28]. Note that the $Q \times f_o$ value reaches a maximum of 160,500 GHz, when the sintering temperature is equal to 1250 ^oC, which lower than the densification temperature of the pure MTO ceramics by about 200 ^oC as reported by Belous et al. [8].

It is well known that the grain boundaries act as two dimensional defects and may contribute significantly into extrinsic loss. The total number of the grain boundaries decreases with an increase in the average grain size. It is also known that the long range ordering improves the Q factor of the dielectric materials. Since, the grain boundary interrupts the perfect symmetry of the crystal, the sample having small grains can be viewed as the one with the low degree of ordering. Hence, it can be concluded that $Q \times f_o$ not only affected by relative density but also by average grain sizes. Therefore, the sample with large grains is expected to reveal a high Q value [29, 30]. In order to correlate this property for the presently investigated samples, the variations of both dielectric constant and $Q \times f_o$ were plotted as a function of relative density sintered at different temperatures as shown in Fig. 5.17. It was found that the dielectric constant and $Q \times f_o$ increases with increasing the relative density of the MTO ceramics. Generally, microwave dielectric loss mechanisms are correlated with intrinsic and extrinsic losses of the samples [6, 7].

The dielectric loss of MTO ceramics can be explained in terms of oxygen vacancies. Since, Bi^{3+} ions in the MTO matrix act as acceptor, the existence of oxygen vacancies in MTO ceramics may be due to the oxygen deficiency or trivalent impurity. The reaction could be expressed as:

$$Bi_2O_3 \rightarrow 2\,Bi'_{Ti} + 3O_o + V^{\cdot\cdot}_o \qquad (5.8)$$

The decrease of $Q \times f_0$ values above the 1 wt.% of Bi_2O_3 can be related to the increase in oxygen vacancies which increases the anharmonic interaction. Moreover, the significant decrease of $Q \times f_o$ value in the case of 1.5 wt.% Bi_2O_3 added MTO ceramics could be due to the inferior relative density and presence of liquid phase effect.

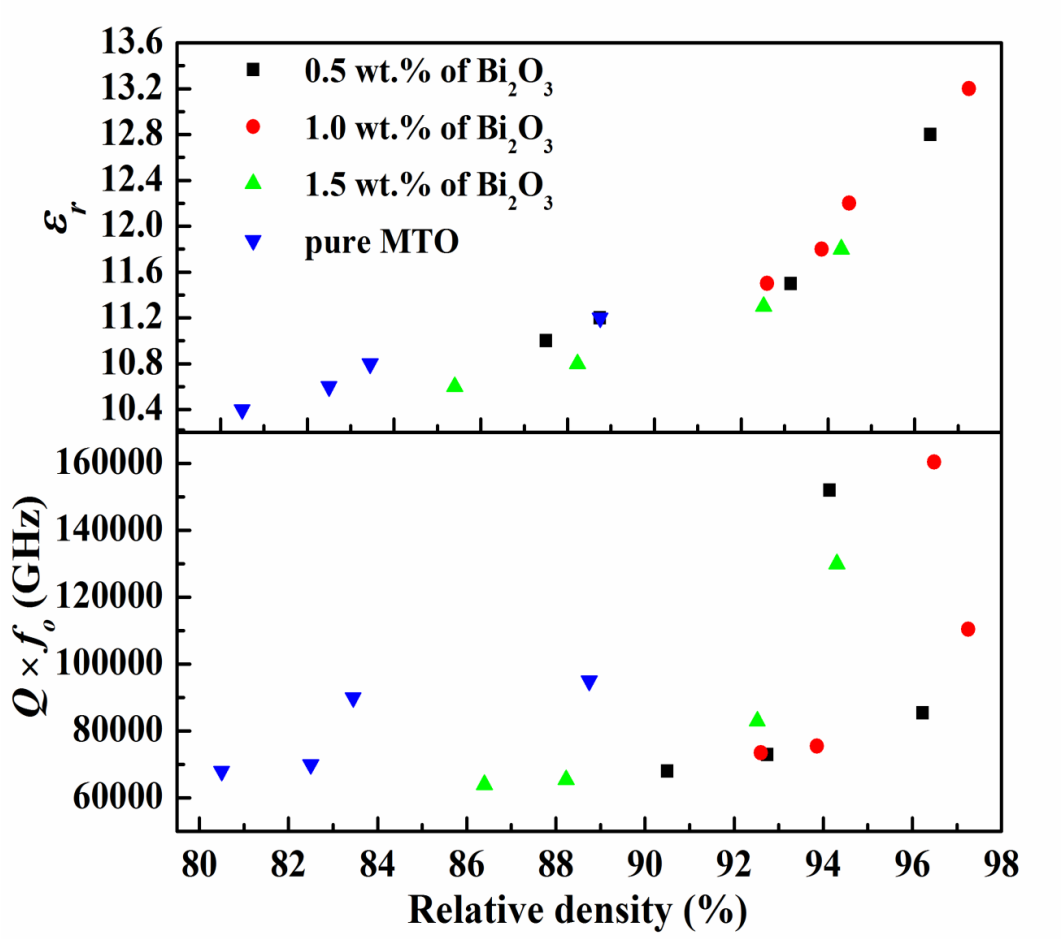

***Fig.5.17**: Variation in (a) dielectric constant (ε_r) and (b) $Q \times f_o$ values as a function of relative density, for the Bi_2O_3 added MTO samples.*

***Table 5.5**: The variation of density, average grain size, dielectric constant and quality factor of the MTO + xBi_2O_3 (x = 0 - 1.5 wt.%) ceramics sintered at different temperatures for 3 hr.*

X	**Sintering temperature**	**% of relative density**	**Average grain size (μm)**	ε_r	$Q \times f_o$ **(THz)**
0	1400	88.75	3.2	11.2	105.5
0.5	1250	96.36	6.5	12.8	152.0
1	1250	98.25	9.7	13.2	160.5
1.5	1250	98.31	8.6	11.8	130.0

Compared with pure MTO ceramics sintered at 1450 ^oC with ε_r ~ 14 and a $Q \times f_o$ ~150,000 GHz [8], the Bi_2O_3 added MTO ceramics have more excellent sinterability and

$Q \times f_o$ value. For comparison between pure MTO and Bi_2O_3 added MTO ceramics along with their sintering temperature, densities, grain size and microwave dielectric properties are given in **Table 5.5**. From the Table 5.5, it is clear that the 1 wt.% Bi_2O_3 added MTO samples exhibited better microwave dielectric properties as compared to the pure MTO and other Bi_2O_3 added samples.

5.5 Conclusions

The liquid phase effect of La_2O_3, V_2O_5 and Bi_2O_3 on the densification, microstructure and microwave dielectric properties of the MTO ceramics was studied systematically in this chapter. The salient features of the MTO ceramics from the current investigations are as follows:

- MTO ceramics with low content of these additives could be sinter at reduced sintering temperature. The reduction of sintering temperature is mainly due to liquid phase sintering effect.
- The addition of different additives in MTO ceramics not only reduces the sintering temperature, but also improves the microwave dielectric properties.
- The microstructure of the MTO ceramics has been improved with low concentrations of these additives. In all the cases, relative density and dielectric constant follows the same trend as a function of temperature as well as amount of additives.
- MTO ceramics added with 0.5 wt.% of La_2O_3 or V_2O_5 possessed excellent microwave dielectric properties: ε_r = 14.3, $Q \times f_o$ = 157,550 (at 10 GHz) and ε_r = 14.4, $Q \times f_o$ = 168,000 (at 10 GHz), sintered at 1300 ^oC and 1250 ^oC, respectively.
- Similarly, Bi_2O_3 (1.0 wt.%) added MTO samples, exhibited best microwave dielectric properties: ε_r = 13.2, $Q \times f_o$ = 160,500 (at 10.48 GHz) sintered at 1250 ^oC.
- The decreases in $Q \times f_o$ value with the increase of additives was correlated to the lowering of densities and reduction of grain size.
- In addition, the oxygen vacancy is also considered as an important factor for the dielectric loss in MTO ceramics for all additives.
- The microwave dielectric properties were also measured in the temperature range of 6.5 K to 295 K for the V_2O_5 added sample. The obtained low loss tangent and $Q \times f_o$ at these temperatures is attributed to the reduction in intrinsic losses.

- The low loss and moderate dielectric constant with reasonably stable performance with temperature, assurances these materials as a potential candidates to be used in the devices for microwave applications.

5.6 References

[1] C. E. Rice, W. R. Robinson, *J. Solid State Chem.*, **21** (1977) 145.

[2] R. Kudesia, A. E. McHale, R. L. Snyder, *J. Am. Ceram. Soc.*, **77** (1994) 3215.

[3] C. L. Huang, M. H. Weng, *Mate. Res. Bull.*, **35** (2000) 1881.

[4] C. L. Huang, M. H. Weng, C. C. Wu and C. C. Wei; *Jpn. J. Appl. Phys.*, **40** (2001) 698.

[5] Suk-Joong L. Kang "*Sintering*" Elsevier, Burlington, MA 2005.

[6] W. S. Kim, T. H. Hong, E. S. Kim, K. H. Yoon, *Jpn. J. Appl. Phys.*, **37** (1998) 5367.

[7] J. Petzelt, S. Pacesova, J. Fousek , S. Kamba, V. Zeleny, V. Koukal, J. Schwarzbach, B. P. Gorshunov, A. A. Volkov, *Ferroelectrics*, **93** (1989) 77.

[8] Belous, O. Ovchar, D. Durilin, M. M. Krzmanc, M. Valant, D. Suvorov, *J. Am. Ceram. Soc.*, **89** (2006) 3441.

[9] W. Hakki, P. D. Coleman; *IEEE Trans. Microw. Theory Technol.*, **8** (1960) 402.

[10] W. E. Courtney; *IEEE Trans. Microw. Theory Technol.*, **18** (1970) 476.

[11] S. J. Penn, N. M. Alford, A. Templeton, X. Wang, M. Xu, M. Reece, K. Schrapel; *J. Am. Ceram. Soc.*, **80** (1997) 1885.

[12] T. Shimada, K. Ichikawa, T. Minemura, T. Kolodiazhnyi, J. Breeze, N. M. Alford, G. Annino; *J. Euro. Ceram. Soc.*, **30** (2010) 331.

[13] Zuccaro, M. Winter, N. Klein, K. Urban; *J. Appl. Phys.*, **82** (1997) 5695.

[14] X. Aupi, J. Breeze, N. Ljepojevic, L. J. Dunne, N. Malde, A. K. Axelsson, N. McN. Alford; *J. Appl. Phys.*, **95** (2004) 2639.

[15] A. Templeton, X. Wang, S. J. Penn, S. J. Webb, L. F. Cohen, N. McN. Alford; *J. Am. Ceram. Soc.*, **83** (2000) 95.

[16] N. McN. Alford, J. Breeze, X. Wang, S. J. Penn, S. Dall, S. J. Webb, N. Ljepojevic, X. Aupi; *J. Euro. Ceram. Soc.*, **21** (2001) 2605.

[17] S. K. Bose, S. K. Kirkpatrick and W. M. Dennis; *J. Luminescence*, 72 (1997) 422.

[18] M.V. Jacob, D. Pamu, K.C. James Raju; *J. Am. Ceram. Soc.*, **90** (2007) 1511.

[19] K. Wakino, M. Murata and H. Tamura; *J. Am. Ceram. Soc.*, **69** (1986) 34.

[20] V. L. Gurevich, A. K. Tagantsev; *Adv. Phys.*, **40** (1991) 719.

[21] V. B. Braginsky, V. S. Ilchenko, K. S. Bagdassarov; *Phys. Lett. A*, **120** (1987) 300.

[22] J. Maxwell, "*Electricity and Magnetic*:, V-1 section 328, Oxford University Press, London (1873).

[23] Koops, *Phys. Rev.*, **83** (1951) 121.

[24] M. A. Petrova, G. A. Mikirticheva, A. S Novikova, V. F Popova, *J. Mater. Res.*, **12** (1997) 2584.

[25] J. Murbe, J. Topfer, *J. Electroceram.*, **16** (2006)199.

[26] K. Wakino, *Ferroelectrics*, **91** (1989) 69.

[27] B. J. Li, J. Y. Chen, G. S. Huang, C. Y. Jiang, and C. L. Huang; *J. Alloys Compd.*, **505** (2010) 291.

[28] W. Lei, W. Z. Lu, J. H. Zhu, X. -H. Wang, *Mater. Lett.*, **61** (2007) 4066.

[29] S. Hirano, T. Hayashi, A. Hattori, *J. Am. Ceram. Soc.*, **74** (1991) 1320.

[30] Pamu, G. Lakshmi Narayana Rao, K. C. James Raju, *Adv. Appl. Ceram.*, **108** (2007) 202.

Chapter 6

Structural, optical and dielectric studies on nanocrystalline Mg_2TiO_4 thin films

6.1 Introduction

Modern technology is demanding smart materials with advanced properties to incorporate more and more functions in electronic devices, especially for microwave resonator and communications applications because these materials facilitate miniaturization to wireless devices [1]. Among them, dielectric oxides are considered to be one of the best materials for optical thin film applications because they offer various functional properties such as infrared optical sensors, planar waveguides, electro-optic switches and coupling in optical communications [2, 3]. Most of the optical devices use multilayer structures, a stack of high index and low index films coated alternatively for improved performance and efficiency. Recently, microwave dielectric resonator materials have been fascinated much interest among the scientist due to their wide variety of microwave communication applications, such as cellular phones, global positioning systems and satellite applications. From the application point of view; such materials should have a high dielectric constant (ε_r), extremely low dielectric loss, and a small temperature coefficient of resonant frequency (τ_f) for thermally stable circuits [4, 5]. The miniaturization of microwave circuits requires materials with above discussed properties. Fabrication of thin film capacitors using high dielectric constant materials can provide higher charge storage densities when they exhibit lower dielectric losses [6, 7].

Now-a-days, the growth of spinel materials gains particular significance due to their specific physical properties. Among other spinel, Mg_2TiO_4 (MTO) is an excellent microwave dielectric compound [8] which satisfies the requirement of dielectric resonators at microwave frequencies. Moreover, MTO is a wide bandgap and high refractive index material suitable for optical and electronic applications. Therefore, its practical applications in optical response are very promissory. Recently, MTO thin film has become important in optical modulation and protective layer of plasma display panels and in the monolithic microwave integrated circuit technologies (MMIC) [9, 10]. In

addition, MTO based thin films are used as a substrate for growing high temperature superconductor films (HTSC) due to their high chemical, mechanical and thermal stability properties [11, 12].

However, most of the research works were focused to study the bulk properties of the MTO ceramics and only few reports are available on the thin films of pure MTO, which are synthesized by different methods other than RF magnetron sputtering. From literature review: Haefke et al. [11] have reported on the formation of epitaxial layers of Mg_2TiO_4 by solid state reaction between an MgO and TiO_2 vapor, which is used as a substrate for high temperature superconducting thin films. Such spinel layers were grown by topotaxial interface reaction via cation counter diffusion. Zeng et al. [13] have grown MTO thin films on the Si (100) and (111) substrate by using atmospheric pressure metallorganic chemical vapor deposition (MOCVD) method and studied the structural properties. In addition, they correlated a relationship between the substrate temperature and crystallography orientations. More recently, Ho et al. [14] have fabricated MTO thin films on p-type Si (111) substrates by sol-gel method and studied the structural and the red shift photoluminescence (PL) behaviors of the films. Hesse et al. [15] have reported the formation of MTO thin films on MgO by solid state reaction method and investigated the electro-optical properties. Similarly, Hsiao et al. [16] prepared Mg_2TiO_4 / MgO composite thin films on the GaN (001) substrate by RF-sputtering method and studied their structural and dielectric properties. Further, they showed that with the use of oxygen in sputtering and post-deposition annealing increased the (111)-preferring orientation of MTO ceramics. Furthermore, Lee et al. [17] studied the application of MTO thin films as the buffer layer by using ultrasonic spraying MOCVD method.

However, there is no systematic study available on the structural, optical and dielectric properties of pure MTO thin films sputtered from the target which is prepared using the mechanical alloying method. In this chapter, we deposited MTO thin films under different O_2 standard cubic centimeters per minute (SCCM) by RF magnetron sputtering from the homemade sputtering target. Subsequently, the effects of processing parameters and post annealing on the structural, microstructural, optical and dielectric properties were studied systematically.

6.2 Experimental details

Mg_2TiO_4 sputtering target was prepared by mechanical synthesis method from high purity MgO and TiO_2 oxide powders and the detailed experimental procedure was discussed in

Chapter 3. MTO thin films were deposited on to Si (100), quartz and platinized silicon ($Pt/TiO_2/SiO_2/Si$) substrates by using RF magnetron sputtering at ambient temperatures under different oxygen gas pressure in SCCM. The base pressure of the chamber was maintained at 10^{-4} Pa. The process gas was a mixture of high purity argon (Ar) and oxygen (O_2). The target was pre-sputtered in an argon atmosphere for 10 minute to eliminate surface impurities. All the films were deposited at a fixed power of 80 W for 3 hr and the working gas pressure ($Ar + O_2$) during the sputtering was maintained at 38 m Torr. Initially, MTO thin films were deposited at different O_2 SCCM for a constant duration of 3 hr. Subsequently, the thickness of the films was calculated using to envelop method and verified by using the surface profilometer. Then all the as deposited films were subjected to post - deposition annealing in air at 500 ^oC for 1 hr.

The crystal structure and phase purity of the target material and the deposited thin films were analysed by using X - ray diffractometer with Cu-K_α radiation. Surface morphology of the films was studied by using FE-SEM. Scanning probe microscope was used in the contact atomic force microscope (AFM) mode to obtain the surface topography of the MTO films. Spectral transmission characteristics were measured in the wavelength range of 200 - 1400 nm using a UV - VIS - NIR spectrophotometer. PL measurements were performed through thermo - spectronic double monochromator coupled to GaAs photo-multiplier with a conventional photon counting system. Ag-MTO-$Pt/TiO_2/SiO_2/Si$ [Metal-Insulator-Metal (MIM)] capacitor structures were fabricated under different O_2 SCCM. The capacitances of the films were measured from 10 kHz to 1 MHz using LCR meter as described in the Chapter 2. Microwave dielectric properties of the films were determined using Agilent 8722 ES vector network analyser by employing the SPDR based measurement techniques.

6.3 Results and discussion

6.3.1 Characterisation of target material

Fig. 6.1 shows the XRD patterns of the MTO sputtering target along with the Rietveld refinement, sintered at 1325 ^oC for 3 hr. The XRD pattern clearly indicates the formation of single phase MTO without any impurities, which show that the processing parameters in the mechanical synthesis are optimized. The refinement was performed through FULLPROF program [18] by varying cell parameters, position of the Mg, Ti and O atoms, their occupancy and thermal parameters. The lattice parameters derived from the

XRD patterns are found to be $a = b = c = 8.4544(15)$ Å and are good agreement with the earlier reports [8]. The obtained refinement results are tabulated in **Table 6.1**.

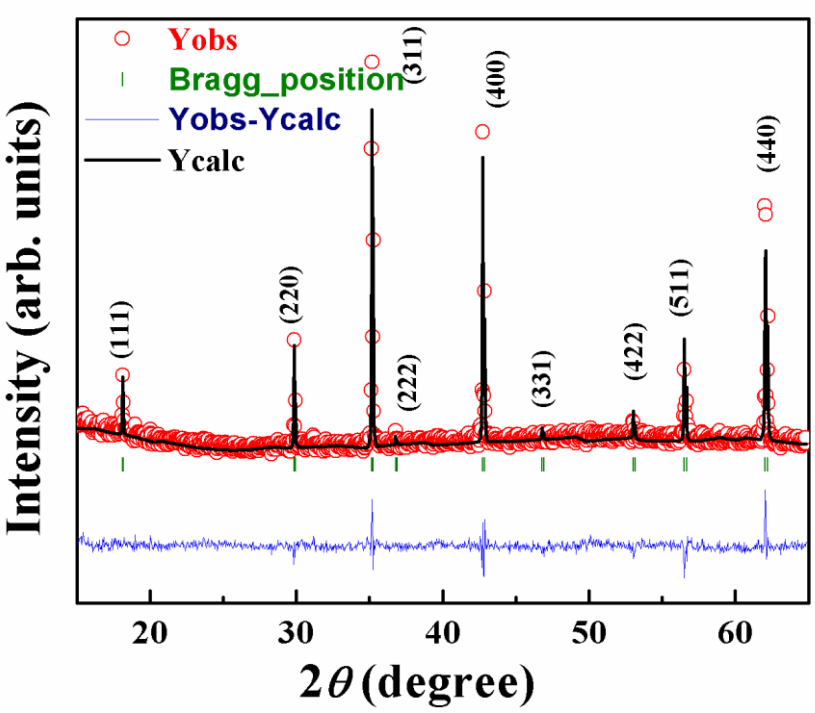

Fig. 6.1: *XRD patterns along with Riveted refinement of MTO target, sintered at 1325 ^oC for 3 hr. The circles and solid line present the experimental and the Rietveld refined data, respectively. The dotted line at the bottom shows the difference between the experimental and the refined data. The vertical bars correspond to the allowed Bragg's peaks.*

Table 6.1*: Parameters obtained from the Rietveld analysis for the MTO target*

Sample parameters	**Values**
Space group	*Fd3-m* (no. 227)
χ^2	0.86
R_{Brag}	10.3
R_f	6.6
$a=b=c$ (Å)	8.4544 (15)
Volume (Å^3)	604.29 (05)
<Mg_1 – O> (Å)	1.8222
<Mg_2 – O> (Å)	3.5050

6.3.2 Crystal structure and microstructure of MTO films

Fig. 6.2 (a) shows the XRD patterns of the MTO thin films deposited on Si substrate at ambient temperature. It is observed that with increasing the O_2 SCCM, the intensities of the peaks corresponding to the cubical (MTO) phase are improved. The average crystallite size of the films was estimated using Scherer's method and is depicted in Fig.6.2 (b) as a function of increasing O_2 pressure. It is clear from the figure that the average crystallite size increases from 8 to 23 nm with increasing O_2 SCCM, suggesting that the oxygen - rich atmosphere during the deposition of MTO thin films promoted the formation of denser and more stable films. Therefore, the formation of nanocrystalline structure in the as - deposited MTO films is mainly due to the plasma - assisted crystallization, as the temperature rise during the deposition is only about 100 ^oC. On the other hand, the MTO films grown over the quartz substrate under the same conditions did not show the formation of any crystalline phase.

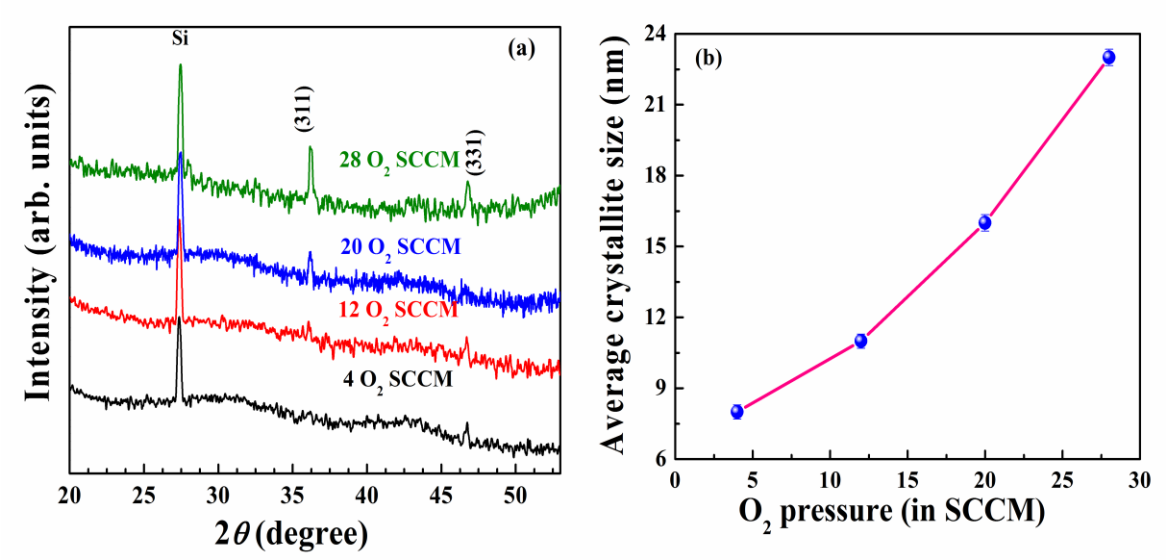

Fig. 6.2: *(a) XRD patterns of MTO thin films deposited on Si substrate at different O_2 SCCMs and (b) Variation of average crystallite size of MTO films as a function of O_2 SCCM.*

It is well - known that the oxide films grow naturally in the amorphous form unless the activation is provided in the form of either the temperature or the ion bombardment. Therefore, the observed results could be attributed to the differences in the surface free energies of the substrates; the thermal diffusivity of the substrates for the growth of the films and lattice mismatch induced strain process between substrate and the film. A careful analysis of the literature results revealed that the Si (100) substrate has higher

surface energy (2007 mJ/m^2) [19] as compared with the quartz substrate (980 mJ/m^2) [20]. As a result, the nucleation of crystalline phase occurs on the substrates having high surface energy, which determines the crystalline or amorphous nature of the films [21]. Similarly, the lattice mismatch induced strain between the substrate, and the films can also promote the nucleation of the crystallites, which is substantially different for crystalline and amorphous substrates. Hence, the formation of nanocrystalline phase in the as - deposited films is mainly due to the intrinsic energies of the process, which are sufficient to cause crystalline phase. However, it is difficult to quantify the exact contribution of various factors to the improvement of the crystallinity of the MTO films.

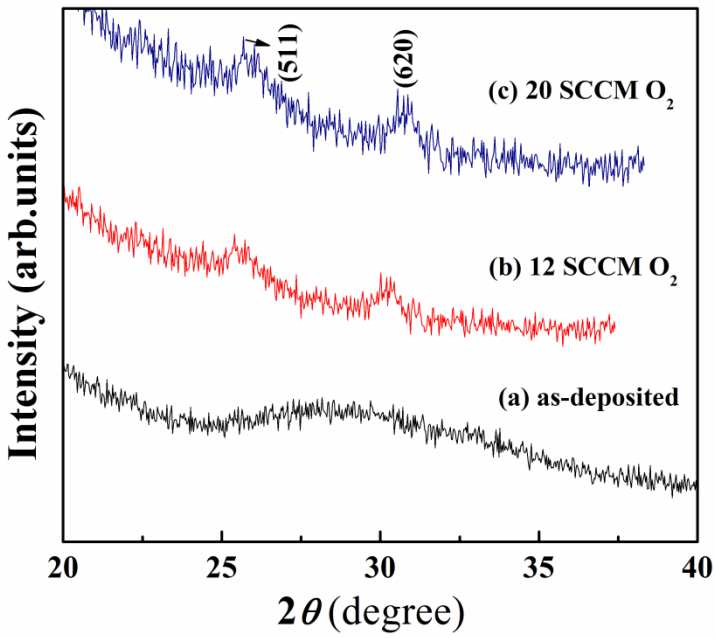

***Fig.6.3**: XRD patterns of MTO films deposited on quartz substrate at different O_2 SCCM for (a) as -deposited films and (b and c) annealed films.*

As all the films deposited on quartz substrate were found to be amorphous and become crystalline after the post - deposition annealing at 500 ^oC for 1 hr. In other words, the presence of diffraction peaks can be used to evaluate the structural order at a long range from the material [22]. Fig. 6.3 shows the XRD patterns of MTO thin films deposited on quartz substrate at various O_2 SCCMs. It was observed that the MTO peaks were enhanced gradually with increasing O_2 SCCM for annealed films. Moreover, the full width at half maximum intensity values of the peaks decreases with increasing O_2 partial pressure. It indicates that larger sized crystal grains and lower concentration of crystal defects are available in the annealed films.

In order to understand the evolution of the surface morphology, SEM micrographs were obtained for the films prepared at different O_2 SCCM are depicted in Fig.6.4. It is clear from the micrographs that the microstructures of the MTO thin films are changed with increasing O_2 SCCM: (i) the films deposited at 4 O_2 SCCM show very shallow dimples on the surface without a distinct grain structure (ii) With increasing O_2 pressure to 12 SCCM, the films exhibiting grain structure, but the grains are smaller in size. (iii) On further increasing the O_2 pressure to 28 SCCM, a clear, more compact and a distinct grain structure was observed. The morphology suggests that the films are crack - free surface having homogeneous distribution of fine particles with an average particle sizes of 25, 40 and 65 nm for the films deposited at 4, 12 and 28 SCCM, respectively. The variation of particle size with the O_2 SCCM can be correlated with the reduction in the deposition rate of the MTO films with increasing O_2 SCCM, which results in a reduced number of high energy bombarding atoms during the deposition. As a result, the crystallinity of the MTO thin films increases with higher O_2 SCCM [23]. Further, to compare the microstructure of the as-deposited film deposited at 12 O_2 SCCM, the FESEM micrograph of annealed film was taken and is depicted in Fig. 6.4 (d). The image reveals that the post - deposition annealing causes an enhancement in the grain growth with more distinct grains. Significantly, by the annealing process, the densification of the films increased along with the decrease of porosity and the later one reflected in the increase of packing density of the films.

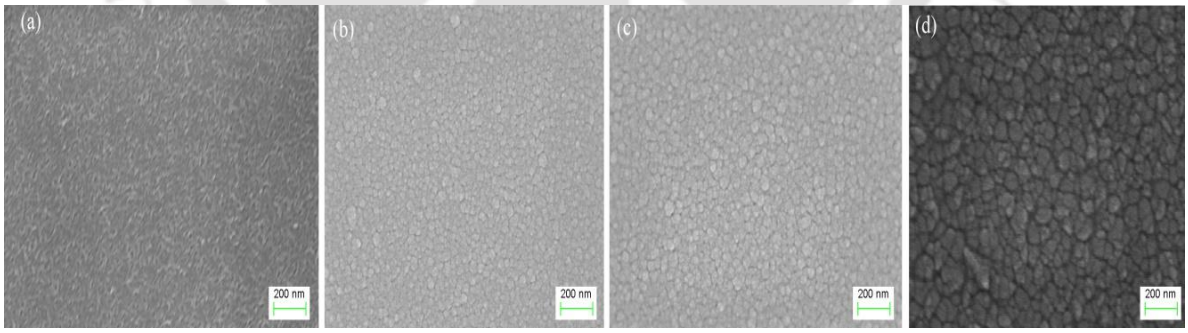

Fig.6.4*: FE - SEM micrographs of MTO thin films deposited at different O_2 SCCMs (a) 4, (b)12, (c) 28 and (d) annealed film deposited at 12 O_2 SCCM.*

Further, to confirm the chemical composition of the deposited MTO films, energy dispersive spectroscopy (EDX) analysis was performed and the results are summarized in **Table 6.2**. It is clearly seen that the composition of the target is almost achieved in the

deposited film within around 2% accuracy, confirming that the films are stoichiometric and minimize the contribution from stacking faults.

Table 6.2: *The required and obtained percentages of elements in MTO film.*

Element	Weight %	Atomic %	Required %	Obtained %
O K	43.11	57. 3	4	4.01
Mg K	30.13	28. 22	2	1.97
Ti K	26.76	14. 48	1	1.01

Fig. 6.5 shows the AFM images of as - deposited and annealed MTO films deposited on quartz substrate. It is evident that the as - deposited film does not show any apparent grain structure. On the other hand, the AFM images of the annealed films reveal the nanosized grain morphology with an average grain size of about 40 - 60 nm. The AFM morphology also indicates that the annealed film is dense and fine grained having no porosity. This fine micro structured thin film with a higher packing density and smaller roughness is more suitable for various optical applications. The AFM analysis of the MTO films is also well consistent with FESEM result.

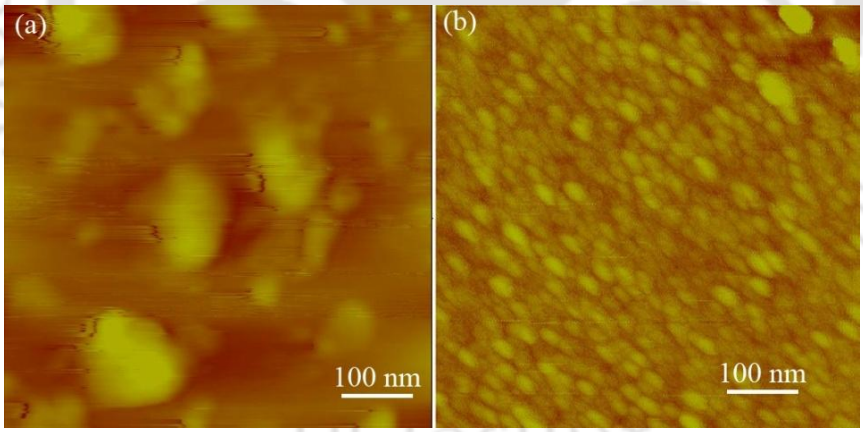

Fig. 6.5: *AFM surface morphology of MTO films deposited on quartz at 12 O_2 SCCM for (a) as -deposited and (b) annealed films.*

6.3.3. Optical characterization

To understand the optical behavior of the MTO thin films, the optical constants were obtained from the transmittance spectrum. Fig. 6.6 (a) depicts the spectral transmittance of as - deposited MTO films deposited at different O_2 SCCMs and Fig 6.6 (b) shows the

as -deposited and annealed MTO films deposited at 12 O_2 SCCM on quartz substrate. It is observed that the as - deposited films were more transparent when compared with the annealed films due to the absence of scattering grain boundaries. All the transmission spectra show interference fringes that originated due to the interference at the air and substrate - film interfaces. The sharp fall in transmission and disappearance of fringes at shorter wavelength are due to the fundamental absorption of the films. It revealed that films deposited at higher O_2 SCCM show lower transmittance. The reduction in the transmittance with the increase in O_2 SCCM can be attributed to the increase in average crystallite size resulting in a higher scattering of light. The average transmittances of the as - deposited films were in the range between 80 - 98% above 300 nm, which indicates the high quality of the deposited thin films. On the other hand, annealed MTO films exhibited lower transmittance compared to as - deposited films. The post deposition annealing causes an increase in average grain size of a film which scatters the light on grain boundaries. As a result the packing density of the films increases. This does not allow the light to pass through and hence the reduction in the transmittance and is also confirmed from FESEM and AFM images. It was also observed that the absorption edge of the annealed films shifted to the lower wavelengths.

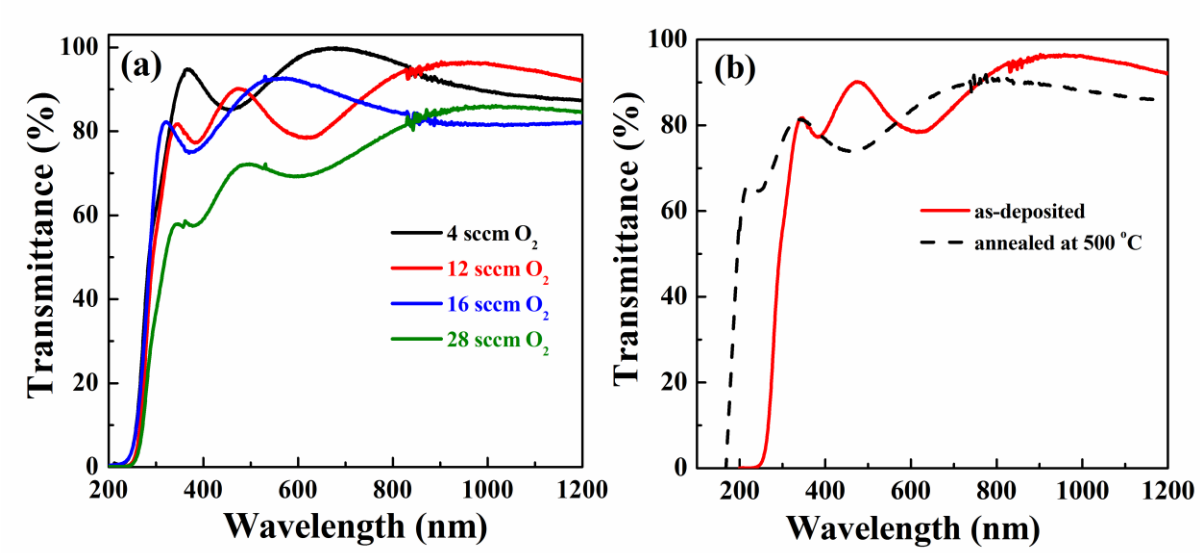

Fig. 6.6: *Optical transmittance spectrum of MTO films (a) deposited at different O_2 SCCMs and for (b) as - deposited and annealed films deposited at 12 SCCM O_2.*

The refractive index (*n*) of the film was derived by employing the envelope method [24] as discussed in Chapter 2, section 2.4.1. The optical packing density (P) of the films is calculated using the relation [25],

$$P = \left(\frac{n_f^2 - 1}{n_f^2 + 2}\right)\left(\frac{n_b^2 + 2}{n_b^2 - 1}\right) \tag{6.1}$$

The porosity ratio (the volume of pores per volume of film) of the films obtained using the following expression [26],

$$P = 1 - \left(\frac{n_f^2 - 1}{n_b^2 - 1}\right) \tag{6. 2}$$

where n_b is the bulk refractive index (2.05) of Mg_2TiO_4 [27] and n_f is the observed film refractive index.

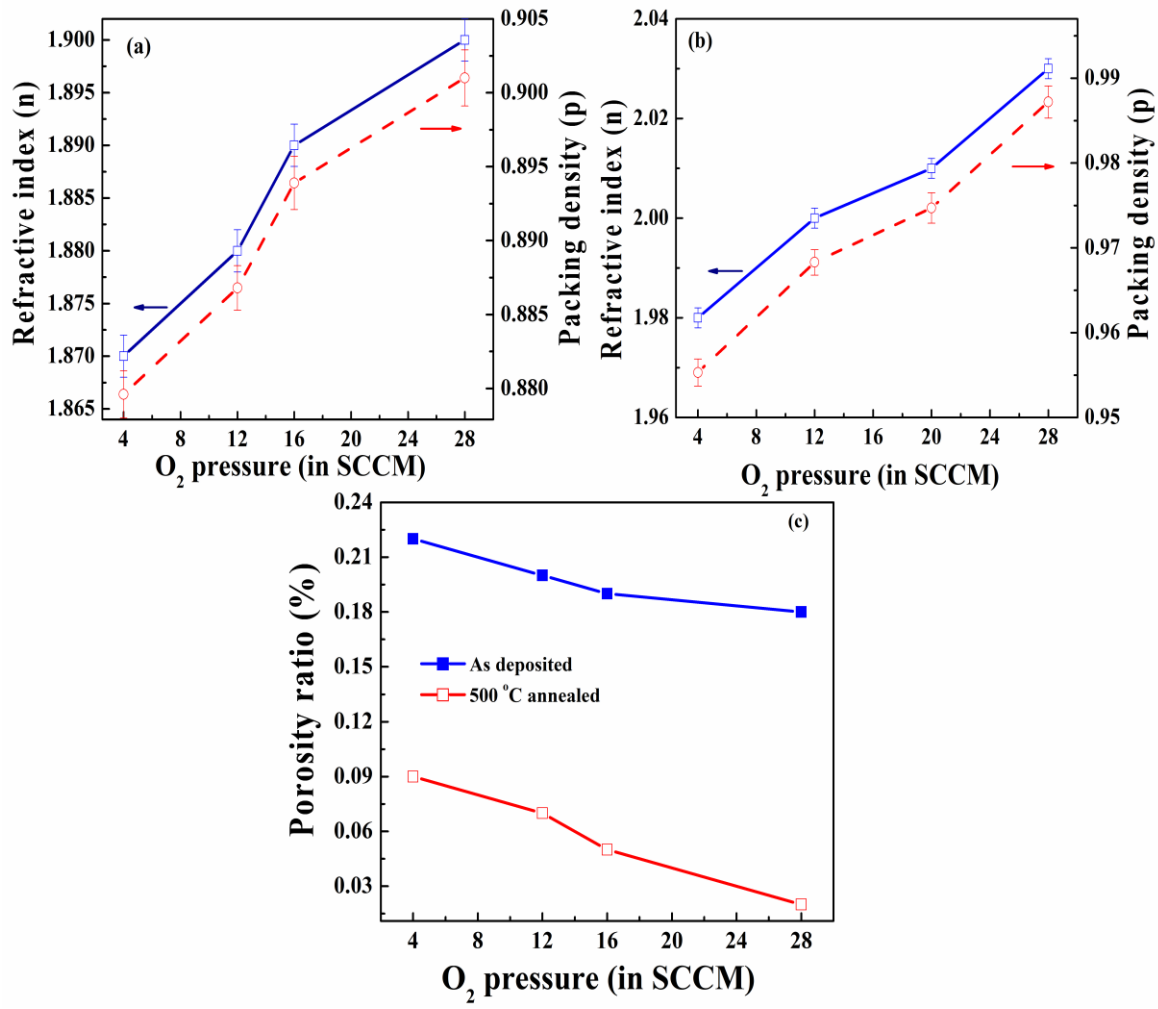

Fig. 6.7: *Variation in (a - b) refractive index and packing density and (c) porosity ratio of as -deposited and annealed films as a function of O_2 SCCM.*

Fig. 6.7 (a - b) illustrates the variation of the refractive index (n) and packing density (P) of the as - deposited and annealed films deposited on quartz substrate as a function of O_2 SCCM. Porosity ratios as a function of O_2 SCCM of the as - deposited and

annealed films are shown in Fig. 6.7 (c). Packing density is defined as volume of the films that is occupied by the solid materials, which is a measure of the porosity. A film with a pore - free microstructure will have a packing density of 1 and the value of which decreases with increasing porosity and the Fig. 6.7 (c) reveals the same. Therefore, the measured refractive index of a film with packing density less than one can be referred as an effective refractive index. The increase in refractive indices with an increase in O_2 SCCM can be related to the increase in the crystallinity and packing density. On the other hand, annealed films showed higher values of refractive index as compared to as - deposited films, which can be attributed to the increase in the packing density, crystallinity, reduction in porosity ratio and the enhancement of microstructure. It was also found that upon annealing the porosity ratio decreases, which complements the increase in refractive index and packing density of the films. The obtained values of refractive index and packing densities of the as - deposited films were in the range of 1.87 - 1.90 (at λ = 550 nm) and 0.88 - 0.90, respectively and on annealing it increases to 1.98 - 2.03 and 0.95 - 0.98, respectively.

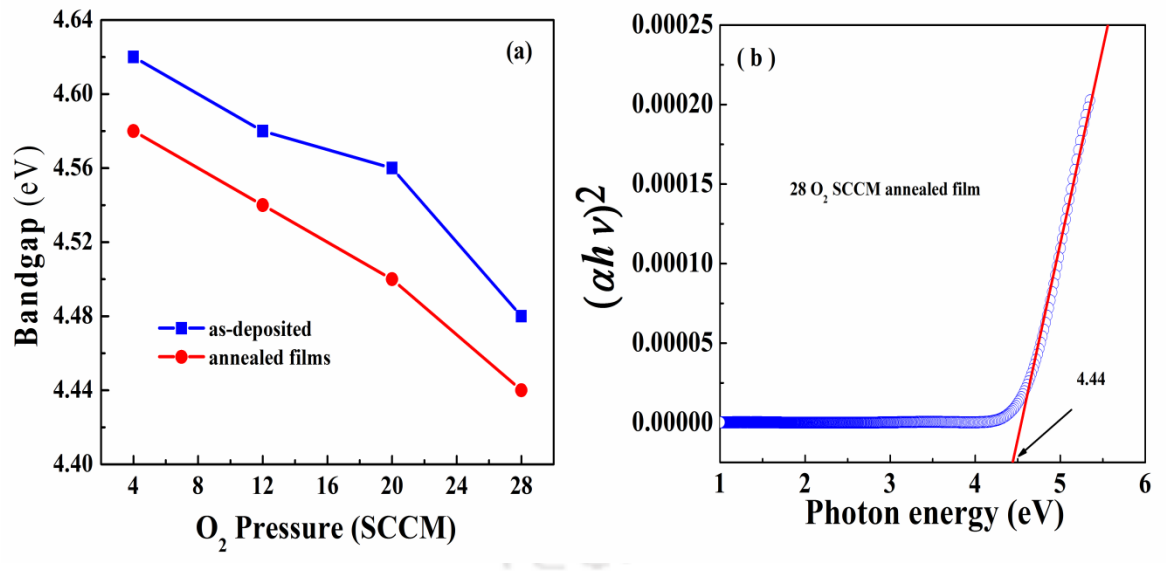

Fig. 6.8: *Variation of optical bandgap as a function of O_2 SCCM for as - deposited and annealed MTO films deposited on quartz substrate. (b): Plot of $(\alpha h\upsilon)^2$ versus $h\upsilon$ for the MTO films deposited at 28 O_2 SCCM.*

It is well - known that the refractive index of a transparent thin film is directly proportional to its electronic polarization, which is inversely proportional to the inter - atomic separation [28]. It should be noted that in the present case, the as - deposited films

are highly disorder due to their amorphous nature resulting in lower film density, which in turn results in the lowering of the refractive index. On annealing, there is a reduction in the interatomic spacing resulting in the densification of the films leading to an increase in the refractive index. Hu et al. [29] also reported that increasing packing density would lead to a higher refractive index for the HfO_2 films. The as - deposited films are highly disordered due to their amorphous nature resultant in lower film density and low adatom mobility, which in turn results in the lower refractive index.

The variation in optical bandgap for the as - deposited and annealed MTO films as a function of O_2 SCCM is shown in Fig.6.8 (a). The optical bandgap (E_g) for all the films was calculated using the Tauc relation [30], which is given by,

$$\alpha h\nu = \beta\left(h\nu - E_g\right)^n \tag{6.3}$$

where $h\upsilon$ is the photon energy, β is a constant which is a measure of crystalline order in the deposited films and n = 0.5, 1.5, 2 or 3 for allowed direct forbidden direct, allowed indirect and forbidden indirect electronic transitions, respectively. In the present case, the bandgap energy (E_g) has been estimated by assuming an allowed direct electronic transition between the highest occupied state of the valence band and the lowest unoccupied state of the conduction band, i.e., n = 0.5 for direct bandgap. It can be seen that optical bandgap of the annealed films found to decrease with O_2 SCCM as compared to as - deposited film. For example, the bandgap of the as deposited film was 4.48 eV, which decreases to 4.44 eV for annealed film deposited at 28 SCCM O_2. This is a direct bandgap transition and is in good agreement with the previously reported results for bulk MTO (E_g= 4.0 - 4.4 *eV*) [31-33]. The values of E_g were determined by the extrapolation of the best fit between $(\alpha h\upsilon)^2$ and $h\upsilon$ (Fig. 6.8 (b)). The optical bandgap values are a good qualitative estimation of stoichiometry. The decrease in optical bandgap with annealing may be attributed to the lowering of porosity, increase of packing density due to better crystallinity and increase in particle size of the films. It is well - known that when a crystalline phase is embedded in a large amorphous matrix, a deviation in the optical bandgap is expected from the bulk values [34].

6.3.4 Photoluminescence studies

Photoluminescence (PL) is the spontaneous emission of light from a material under optical excitation. The intensity of the PL signal provides information regarding the

quality of surfaces and interfaces. Fig. 6.9 illustrates the PL spectra recorded at room temperature for as-deposited and annealed MTO films deposited at different O_2 SCCMs. The characteristic emission sharp peak and shoulder peaks at 357, 409 and 466 nm were detected. The PL spectra indicated that the annealed MTO films, which are deposited at higher O_2 SCCM, exhibited the maximum intensity with a characteristic peak at 357 nm, which corresponds to the intensive UV emission together with two week green emissions. It is noted that after annealing, the intensities of MTO films increases as intensity of the emission peaks strongly depend upon the films density. Furthermore, the effect of annealing and the increase of O_2 SCCM results an enhancement of the grain growth of the films and hence the ratio of the surface area to volume decreases. Consequently, the films become more compact with fewer defects and the number of released photon increases. This causes an increase in intensity and decrease in line width. Nevertheless, it is known that the optical properties of the films are generally related to the grain size and defects in the films. In particular, the later part may be evolving due to (i) lattice mismatch between the substrate and the films, (ii) inter diffusion of atoms between the substrate and film, (iii) deficiency of oxygen vacancy, and (iv) deviation in the stoichiometry. The lattice mismatch induces the strain due to the formation of misfit dislocations, while the inter diffusion of atoms occurring generally at the high processing temperatures leads to the formation of point defects near the interface. Similarly, the presence of oxygen vacancies in the films reduces the optical bandgap. But, the obtained optical bandgap values in the presently investigated samples are higher than the bulk MTO ceramics. This reveals that the deposited films were significantly free from oxygen vacancies.

PL results complement the optical bandgap values that the increase in O_2 SCCM results the highest intensity of the peaks, which can be attributed to the high degree of structural order and disorder into the lattice [35]. From the bandgap calculations, it is observed that for as - deposited and annealed films bandgap decreases with O_2 SCCM. It is known that the order films exhibit lower bandgap values as compared to the disorder films. Furthermore, the characteristic peak of the films shifted slightly with the increase O_2 SCCM due to the grain growth. As observed from transmittance spectra, the highest intensity film exhibited the lowest bandgap. The increase in intensities from PL spectrum and decrease in the bandgap can be attributed to the increase of intermediary energy levels within the bandgap due to the defects in clusters of crystalline structure [36].

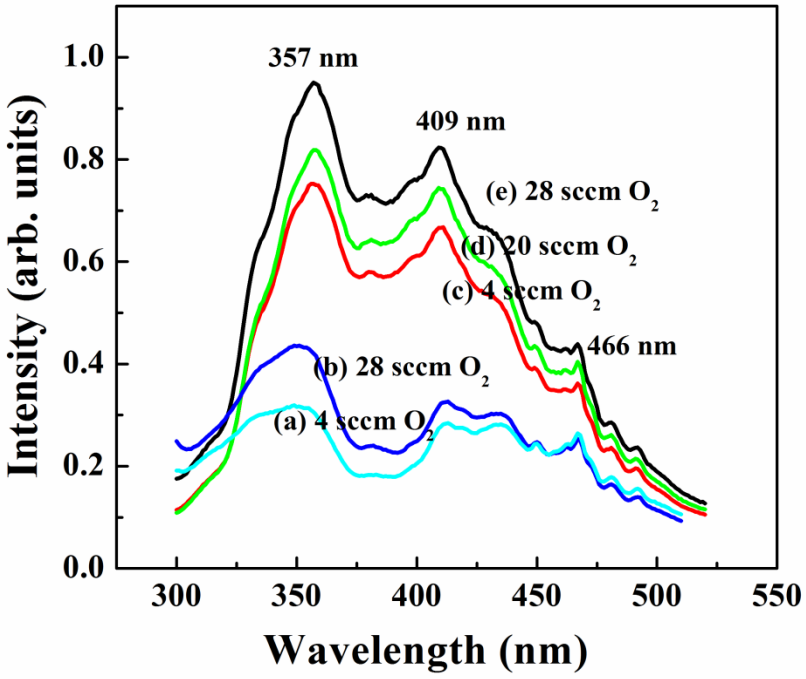

Fig.6.9: *PL spectra of MTO films deposited at different O_2 SCCM for (a - b) as - deposited films and (c - e) annealed film.*

6.3.5 Dielectric studies

To investigate effect of processing parameters on the dielectric response of MTO thin films, MIM capacitors were fabricated and their response is studied in the frequency range of 10 kHz to 1 MHz. Fig. 6.10 (a) and 6.10 (b) shows the variation in dielectric constant (ε_r) and loss tangent (tan δ) of the MTO films deposited under different O_2 SCCM, respectively. Both the dielectric constant and tan δ are found to decrease with an increase in applied frequency. The decrease in dielectric constant with the increase in frequency is a typical characteristic of the linear dielectric. It is observed that the dielectric constant and loss values were found to be higher at low frequencies. The dispersion in dielectric constant with frequency can be explained on the basis of Maxwell - Wagner two layers and Koop's phenomenological theory [37]. These models demonstrate that as the frequency increases, the electrons reverse their direction of motion more often, which decreases the probability of electrons reaching the grain boundary, which results in the reduction in polarization leading to a decrease in the dielectric constant.

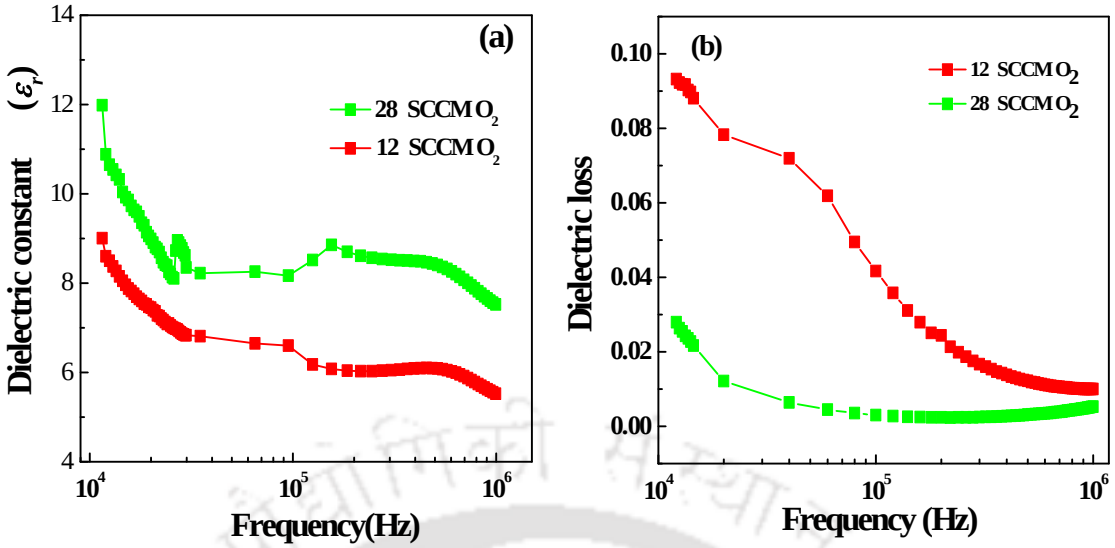

***Fig.6.10**: Variation in (a) dielectric constant and (b) dielectric loss of MTO thin films as a function of frequency deposited at 12 and 28 SCCM O_2.*

It is also observed that as the O_2 SCCM increases, both the dielectric constant and loss tangents are improved, and the films deposited at 28 O_2 SCCM exhibited maximum dielectric constant and lowest loss. It is natural that films deposited at lower O_2 SCCM may have some oxygen vacancies, which lead to a high dielectric loss. The dielectric loss arises from interfacial dead layers, possibly existing at a film - electrode interface and the interface dead layer may occur due to impurities, vacancies and the lattice disorder. The dielectric dispersion at low frequencies occurs due to the space charges arising from vacancies or charged defects and the structural disorder is likely to be the primary cause for dielectric loss. The improvement in dielectric properties with the increase in O_2 SCCM has been correlated to the reduction in oxygen vacancies, increase in crystallinity and grain size of the films. In the present case, the thin films deposited in pure oxygen atmosphere reduce the oxygen vacancies which may cause the improvement of dielectric properties. The optimum values of dielectric constant and loss tangent are in the range between 11.98 - 5.52 and 0.098 - 0.005, respectively.

(a) Microwave dielectric properties of pure MTO thin films

To investigate and to compare the microwave dielectric properties of both bulk and thin films, the microwave dielectric properties of pure MTO films were measured using split post resonator technique (SPDR) [38]. This is a non-destructive and accurate method for measuring the complex permittivity of dielectric substrates and thin films at spot

frequencies. The microwave dielectric properties of MTO thin films deposited on quartz substrates are measured by using SPDR method and are listed in **Table 6.3**. For the first time, the SPDR method was used to measure the microwave dielectric properties (5 - 15 GHz) of MTO thin films. The microwave dielectric properties were investigated for as-deposited and annealed MTO films at different frequencies of 5, 10 and 15 GHz. It is observed that with an increase of O_2 SCCM, the dielectric constant of the films increases whereas the dielectric loss decreases. Furthermore, as compared to annealed films the as-deposited films exhibited higher loss and low dielectric constant. This might be due to the increase in the packing density and refractive index of the films with annealing. On annealing, crystallization occurs by decreases in inter-atomic distances. Consequently, it may be helpful for increasing electron charge transfer between cations and oxygen, resulting in the enhancement of dipoles in the films. This enhancement of dipoles is responsible for an increase in the polarization [39]. Further, with an increase in measurement frequency from 5 GHz to 15 GHz, the dielectric constant is found to decrease whereas dielectric loss increases slightly. This might be due to the decrease in the polarization and high conductivity at microwave frequencies.

Table: 6.3 *Microwave dielectric study of MTO thin films deposited on quartz substrates by using split post dielectric resonator method*

	As-deposited MTO films					
	5 GHz		**10 GHz**		**15 GHz**	
O_2 SCCM(%)	ε_r	tanδ	ε_r	tanδ	ε_r	tanδ
0	12.2	1.9×10^{-1}	11.8	4.5×10^{-2}	8.8	2.9×10^{-1}
50	13.5	3.9×10^{-2}	12.3	6.8×10^{-2}	10.5	5.9×10^{-1}
100	14.6	4.0×10^{-3}	13.2	8.2×10^{-3}	11.7	4.3×10^{-2}

	Annealed MTO films					
	5 GHz		**10 GHz**		**15 GHz**	
O_2 SCCM(%)	ε_r	tanδ	ε_r	tanδ	ε_r	tanδ
0	17.5	1.7×10^{-2}	14.5	6.1×10^{-2}	12.4	7.9×10^{-1}
50	19.5	1.8×10^{-2}	16.4	9.8×10^{-2}	13.5	1.5×10^{-2}
100	24.5	8.0×10^{-3}	17.5	8.9×10^{-3}	14.2	7.3×10^{-2}

The microwave dielectric properties of pure bulk MTO ceramics (ε_r =13.60 and $Q \times f_o$ = 155,500 GHz, measured at 10.4 GHz) were reported by the present author [40]. The obtained results for both bulk and thin films of MTO ceramics are tabulated in **Table 6.4**. From the Table 6.4, it is clear that there is not much change in the dielectric constants of the bulk and thin films of the pure MTO ceramics. However, the dielectric loss is higher in thin films as compared to bulk form. The obtained higher dielectric losses in the films can be explained as follows: The low dielectric losses in the case of bulk MTO ceramics may be due to the large grain sizes and the reduction in strain of the crystallites results from high sintering temperature. In the case of thin films, the small grain sizes results in large grain boundary area and these differences could cause the deviation from the bulk properties. The grain boundary regions are interconnected in all directions and their properties may dominate or severely influence the effective dielectric response of the whole system even if their volume concentration is relatively small [41]. From the present study, it is clear that the obtained optical and dielectric properties of MTO thin films show that these films are one of the potential candidates for applications in integrated circuits and optical devices.

Table 6.4: *The comparison of the microwave dielectric properties of MTO ceramics in both bulk and thin film form.*

	Dielectric constant (ε_r)	**Dielectric loss (tanδ)**	**Measured frequency**
Bulk pure MTO	13.6	1.5×10^{-5}	10.4 GHz
MTO thin film deposited at 100% O_2 SCCM	14.6	3.0×10^{-3}	5 GHz
	13.3	8.9×10^{-3}	10 GHz
	11.7	4.3×10^{-2}	15 GHz

6.4 Conclusions

A systematic study of effect of O_2 pressure and post - deposition annealing on the structural, microstructural, optical and dielectric properties of MTO thin films fabricated by RF magnetron sputtering was carried out in this chapter. The salient features of the MTO thin films from the current investigations are as follows:

- Nanocrystalline MTO thin films were fabricated on quartz, Si (100) and platinized silicon (Pt/ TiO_2/ SiO_2/Si) substrates by using RF magnetron sputtering.
- The as-deposited films on Si substrate are found to be crystalline, but show amorphous nature on a quartz substrate. The difference in the crystallinity of the films was attributed to the differences in the surface free energies and the thermal diffusivity of the substrates.
- Further, post - deposition annealing was carried out at 500 ^oC for 1 hr in air to induce crystallization. It was found that the oxygen - rich atmosphere during the deposition and post - deposition annealing of MTO thin films promoted the formation of denser and more stable MTO films, which is confirmed from FE-SEM and AFM images.
- The variation of refractive index and packing density with O_2 SCCM for the annealed films is attributed to increase in the optical bandgap with increase in crystalline nature.
- The O_2 SCCM and post - deposition annealing significantly influence the PL response of the films. It was found that the annealed films showed higher emission peaks than the as - deposited films. The increase in intensities from PL spectrum and decrease in the bandgap can be attributed to the increase of intermediary energy levels within the bandgap due to the defects in clusters of crystalline structure.
- The MIM structures were fabricated and it was observed that the dielectric constant and loss tangent values were strongly depends on the O_2 SCCM.
- The MTO films deposited under pure oxygen atmosphere exhibited best dielectric properties of dielectric constant of 11.98 and low losses (0.005), attributed to the reduction in oxygen vacancies.
- Microwave dielectric properties of both bulk and thin films are almost comparable.

6.5 References

[1] T. Takada, S. F. Wang, S. Yoshikawa, S. J. Yang, R. E. Newnham, *J. Am. Ceram. Soc*., **77** (1994) 2485.

[2] R. J. Walker, R. A. Mckee, H. W. Yen, D. E. Zelmon, *Appl. Phys. Lett*., **65** (1994)1495.

[3] D. Y. Kim, S. E. Moon, E. K. Kim, S. J. Lee, J. J. Choi, and H. E. Kim, *Appl. Phys. Lett*., **82** (2003)1455.

[4] R. J. Cava, W. F. Peck Jr., J. J. Krajewski, G. L. Reberts, B. P. Barber, *Appl. Phys. Lett*., **70** (1997)1396.

[5] G. C. Ling, R.S. Withers, B.F. Cole, N. Newman, *IEEE Trans. Microwave Theory. Tech*. **42** (1994) 34.

[6] B. D. Lee, H. R. Lee, K. H. Yoon, Y. S. Cho, *Ceram. Int*., **31** (2005) 143.

[7] C. L. Haung, Y. B. Chen, *Surf. Coat. Technol*., **200** (2006) 3319.

[8] Belous, O. Ovchar, D. Durilin, M. M. Krzmanc, M. Valant and D. Suvorov, *J. Am. Ceram. Soc.*, **89** (2006) 3441.

[9] K. Wakino, K. Minai, H. Tamura, *J. Am. Ceram. Soc*., **67** (1984) 278.

[10] D. Pamu, K. Sudheendran, M. G. Krishna, K. C. James Raju, Anil K. Bhatnagar, *Vaccum*, **81** (2007) 686.

[11] H. Haefke, H. P. Lang, R. Sum, H. J. Guntherodt, L. Berthold, D. Hesse, *Appl. Phys. Lett*., **61** (1992) 2359.

[12] D. Hesse, *Patent*, DD 0151828 (1981).

[13] J. Zeng, H. Wang, S. Shang, Z. Wang, C. Lin, *J. Mater. Sci. Elect*., **8** (1997)159.

[14] Y. D. Ho, C. H. Su and C. L. Huang, *J. Am. Ceram. Soc*., **97** (2014) 358.

[15] D. Hesse and H. Bethge, *J. Cryst. Growth*, **52** (1981) 875.

[16] Y. Hsiao, J. C. Wu, H. T. Wu, C.F. Shih, *J. Am. Ceram. Soc*., **95** (2012) 45.

[17] H. Lee, J. H. Yeom, *Jpn. J. Appl. Phys*., **39** (2000) 6716.

[18] H. M. Rietveld, *J. Appl. Crystallogr.*, **2** (1969) 65.

[19] S. Yamauchi, M. Hirai, M. Kusaka, M.Iwami, H. Nakamura, Y. Yokota, H. Watabe, *Appl. Surf. Sci*. **70** (1993) 461.

[20] Yu. K. Shchipalov, *Glass and Ceram.*, **57** (2000) 374.

[21] K. W. Cho, D. W. Kim, S. Yoon, *Macromolecules*, **36** (2003) 7652.

[22] L. S. Cavalcante, V. S. Marques, J. C. Sczancoski, M. T. Escote, M. R. Joya, J. A. Varela, M. R. M. C. Santos, P. S. Pizani, E. Longo. *Chemical Engi. J.*, **143** (2008) 299.

[23] R. B. Zhang, C. S. Yang, G. P. Ding, *J. Matter. Lett*., **59** (2005) 1741.

[24] R. Swanpoel, *J. Phys. E: Sci. Instrum.*, **16** (1983) 1214.

[25] K. Goedicke, J. S. Liebig, O. Zywitzki, *Thin Solid Films*, **377** (2000) 37.

[26] Q. Ye, P. Y. Liu, Z. F. Tang and L. Zhai, *Vaccum*, **81** (2007) 627.

[27] S. Taki, *J. Chem. Soc. Japan-Ind. Chem. Sect*. 59 (1956) 18 (in Japanese); *Engl. Abstr*., **50** (1956) 15308i.

[28] P. Li, J. F. McDonald, T. M. Lu., *J. Appl. Phys*., **71** (1992) 5596.

[29] H. Hu. C. X. Zhu, Y. F. Lu, Y. Liew, M. F. Li, B. J. Cho, W. K. Chio, N. Yakovlev. *J. Appl. Phys*., **94** (2003) 551.

[30] J. C. Tauc, Optical Properties of Solids, *North–Holland, Amsterdam*, 1972.

[31] H. Kominami, M. Tanaka, K. Hara, Y. Nakanishi, Y. Hatanaka, *Phys. Status Solidi (c)*, **3** (2006) 2758.

[32] A. Golubovic, M. Radovic, *J. Serb. Chem. Soc*., **76** (2011)1561.

[33] J. Stade, D. Hahn, R. Dittmann, *J. Lumin.*, **8** (1974) 308.

[34] J. D. DeLoach, G. Scarel, C. R. Aita, *J. Appl. Phys.*, **85** (1999) 2377.

[35] A. V. Ferri, J. C. Sczancoski, L. S. Cavalcante, E. C. Paris, J. W. M. Espinosa, A. T. Figueiredo, P. S. Pizani, V. R. Mastelaro, J. A. Varela, E. Longo, *Mate. Chem. Phys*., **117** (2009) 192.

[36] L. S. Cavalcante, J. C. Sczancoski, F. S. De Vicente, M. T. Frabbro, M. Siu Li, J. A. Varela, E. Longo. *J. Sol-Gel Sci. Technol*., **49** (2009) 35.

[37] J. C. Maxwell, "*Electricity and magnetism"*, vol -1, *Oxford University press*, Oxford, 1929.

[38] G. Balakrishnan, T.N. Sairam, P. Kuppusami, R. Thimurugesan, E. Mohandas, V. Ganesan, D. Sastikumar, *Appl. Surf. Sci*. **257** (2011) 8506.

[39] P. Li, J. F. McDonald and T. M. Lu, *J. Appl. Phys*., 71 (1992) 5596.

[40] R. K. Bhuyan, T. S. Kumar, and D. Pamu, *Int .J. Ceram. Technol.*, **10** (2013) E18.

[41] Pamu, K. Sudheendran, M. Ghanashyam Krishna and K. C. James Raju, *Eur. Phys. J. Appl. Phys*., **44** (2008) 71.

Chapter 7

Summary and future scope

The overall summary of the salient features obtained on the structural, microstructural and microwave dielectric properties of MTO- based bulk and thin films samples is listed in this chapter. Highlights of the current investigations and possibilities of further extension of the work in future directions are also summarized.

7.1 Summary of the works

In summary, dielectric resonators (DR) of single phase Mg_2TiO_4 (MTO) ceramics have been prepared by mechanical alloying and solid-state reaction methods. The effect of various additives, their concentrations and processing parameters on crystal structure, microstructure and on microwave dielectric properties of MTO ceramics are studied systematically. Successful efforts were made to reduce the sintering temperature from 1450 to 1250 ^{o}C without affecting the microwave dielectric properties of the MTO ceramics by reducing the initial particle size and supplementing different types of additives. The investigations performed in my present thesis work are divided into seven chapters.

The first Chapter is a brief introduction and historical development of DRs, with their technological importance at current trends. It also includes the fundamental physical aspects of DRs, the material requirements and the factors affecting the microwave dielectric properties, with their potential use in different practical applications. Further, it also includes the electronic applications of thin films with their importance in various areas of interest in the present technological world. Chapter 2 discusses in detail various preparation techniques used for the synthesis of MTO-based samples. A brief account of structural, microstructural and microwave characterization techniques of samples are also discussed.

In Chapter 3, MTO nanopowders are prepared by mechanical alloying method under different processing conditions and the impact of mechanical alloying on the crystal structure, sintering temperature, densification, microstructure and microwave dielectric

properties of MTO ceramics is discussed. Since MTO ceramics prepared by conventional solid state reaction method needs high sintering temperature is about 1450 ^{o}C. Therefore, the efforts are made in order to improve the densification by reducing the initial particle size. As a result the sintering temperature is significantly reduced from 1450 to 1325 ^{o}C with improved microwave dielectric properties. The dielectric loss mechanisms are discussed on the basis of densification and microstructure of the MTO ceramics and the obtained results are compared with the earlier reports. A maximum relative density of 97.75 % was obtained for the MTO sample sintered at 1325 ^{o}C for 3 hr. The best microwave dielectric properties of ε_r ~ 13.68, $Q \times f_o$ ~ 155,000 GHz (measured at 10.4 GHz) were obtained for the pure MTO ceramics sintered at 1325 ^{o}C for 3 hr.

In Chapter 4 a systematic study on the structural, microstructural and the microwave dielectric properties of pure MTO and MTO ceramics added with CeO_2 nanoparticles prepared by solid state reaction method are presented. With the addition of CeO_2 nanoparticles, the sintering temperature of MTO ceramics is effectively reduced from 1450 to 1300 ^{o}C along with the significant improvement in the density and uniform microstructure. It was found that the MTO sample added with 1.5 wt.% of CeO_2 showed highest density of 98.7% with maximum microwave dielectric properties: $Q \times f_o$ value of 167000 GHz (at 10.4 GHz) and ε_r of 14.6. The microwave dielectric properties of the MTO ceramics were also measured at cryogenic temperatures (6.5–295 K). The results indicated that the loss tangent (tan δ) of all the samples increases with increasing temperature. The loss tangents of the pure MTO ceramics and MTO ceramics added with 1.5 wt.% of CeO_2 nanoparticles, measured at 6.5 K are found to be 6.6×10^{-5} and 5.4×10^{-5}, respectively. The moderation in the loss and temperature dependence of the loss factors with CeO_2 nanoparticles addition in MTO is also attributed to the CeO_2 nanoparticles influencing the intrinsic loss mechanism of MTO.

A systematic study of the effect of different additives concentrations of V_2O_5, La_2O_3 and Bi_2O_3 on the crystal structure, densification, microstructure and microwave dielectric properties of MTO ceramics are presented in Chapter 5. It was found that the addition of these additives the sintering temperature of MTO ceramics significantly reduced without affecting the microwave dielectric properties. MTO ceramics added with 0.5 wt.% of La_2O_3 or V_2O_5 possessed excellent microwave dielectric properties: ε_r = 14.3, $Q \times f_o$ = 157,550 (at 10 GHz) and ε_r = 14.4, $Q \times f_o$ = 168,000 (at 10 GHz), sintered at 1300 ^{o}C and 1250 ^{o}C, respectively. In case of MTO ceramics added with 1.0 wt.% of Bi_2O_3,

exhibited best microwave dielectric properties: ε_r = 13.2, $Q \times f_o$ = 160,500 (at 10.48 GHz), sintered at 1250 ^oC. Further, microwave dielectric properties of pure MTO and MTO ceramics added with 0.5 and 1.0 wt.% of V_2O_5 were measured at cryogenic temperatures (6.5 K to 295 K). It was observed that loss tangent of pure MTO increased with temperature, whereas for V_2O_5 added samples it decreases with rise in temperature. However, MTO ceramics added with 0.5 and 1.0 wt.% of V_2O_5 manifested slightly higher loss tangents as compared to the pure MTO ceramics. The mechanism of the microwave loss is in agreement with the theory of intrinsic dielectric loss derived from the two phonon difference process.

The Chapter 6 describes the optimization processing conditions of the MTO thin films prepared by RF magnetron sputtering. MTO thin films were deposited on various substrates like, Si (100), quartz and on platinized silicon ($Pt/TiO_2/SiO_2/Si$)) from the homemade sputtering target which is prepared from mechanical alloying method. All the films are deposited at ambient temperature under different oxygen gas pressure. The impact of processing parameters (Ar / O_2 ratio) and the post-deposition annealing on structural, microstructural, optical and dielectric properties of MTO films were investigated. For the first-time MTO films were deposited in pure oxygen atmosphere. Interestingly, the as-deposited film on Si substrate was found to be crystalline, while film deposited on quartz substrate showed amorphous nature. Surface morphology and optical transmittance spectra studies revealed that the average particle size in the film increases with increasing O_2 SCCM and the films deposited at higher O_2 SCCM exhibit lower transmittance, respectively. In addition, both the refractive index and packing density increases with increasing O_2 SCCM, leading to a decrease in the optical band gap from 4.62 to 4.48 eV. Further, the post-deposition annealing (at 500°C) resulted in an amorphous –crystalline phase transition in the films (deposited on quartz substrate), which is accompanied by an increase in the refractive index and decrease in the optical bandgap. The annealed films exhibit a refractive index of 1.98-2.03 (at 600 nm) with an optical bandgap values between 4.44 and 4.58 eV. The O_2 SCCM and annealing are also significantly greatly affected the photoluminescence spectra. Metal-Insulator-Metal (MIM) capacitors were fabricated under different O_2 SCCM for the films deposited on platinized silicon substrates. The dielectric properties of MTO films were measured in the frequency range of 1 kHz to 1MHz as a function of O_2 SCCM. The films deposited in pure oxygen atmosphere showed the highest dielectric constant with low loss.

The dielectric properties of MTO films were measured both at low frequency and at microwave frequencies. At lower frequency range, the dielectric constant and loss decreased with an increase in frequency. While at microwave frequencies, the dielectric constant decreases and loss increases with enhancement in frequency. The dielectric constant and loss showed enormous dependence on O_2 SCCM and the resulting variation in crystallite size and bandgap. For the first time, the microwave dielectric properties of pure MTO thin films are reported.

In the present study, DRs and thin films of MTO have been prepared by mechanical alloying, solid state reaction method and RF reactive magnetron sputtering respectively. In bulk form MTO has dielectric constant of 13.60, $Q \times f_o$ of 155,500 GHz observed for the sample sintered at 1325 ^oC where as in thin film form dielectric constant of 13.2 and $\tan\delta = 8.2\times10^{-3}$ were observed at 10 GHz. The dielectric constant of each film is close to the bulk value whereas the dielectric losses of the films are observed to be higher than the bulk value. The detailed observations, discussion and possible explanations are presented in this chapter.

From the present study, the obtained excellent microwave dielectric properties of the MTO based ceramics makes this material appropriate for type -1 capacitor and dielectric resonators for various microwave communication applications. Furthermore, the optimized best optical and dielectric properties of pure MTO thin films are suitable for optoelectronic, antireflection, integrated electronic and CMOS applications.

7.2 Scope for the future work:

To reduce the sintering temperature of the MTO-based ceramics, by improving densification and microwave dielectric properties, we have studied the effect of different types of additives as sintering aids. During this process, the microstructure of MTO ceramics changes significantly. But, to find out whether these additives entered into the matrix of MTO or remained at the grain boundary, a composition analysis across the microstructure with a facility like Electron Probe Micro Analysis (EPMA) will be useful. We have focused on to reduce microwave dielectric losses that are extrinsic in nature by process optimization. However, we have not studied the intrinsic loss mechanisms and can be studied with far IR reflectivity spectroscopy.

It would be interesting to explore the effect of initial particle size on sintering temperature of the MTO ceramics. To study the effect of different types of transition

metal (Co, Zn, Ni etc.) doping on densification and microwave dielectric properties of the MTO ceramics. Further, to produce a temperature stable material suitable for practical use, it is necessary to tune the temperature co-efficient of resonant frequency (τ_f) of the MTO ceramics, by adding positive τ_f materials such as $CaTiO_3$ and $SrTiO_3$.

For the thin films cases, since the crystallinity and microstructure are playing an important role on optical, electrical and microwave dielectric properties, a systematic study of the films by varying the substrate temperature during deposition will be beneficial. A detailed compositional analysis of MTO films deposited at different temperatures and pressure are needed to explain the loss mechanisms of the films. Films deposited with same O_2 SCCM but having different microstructures can be obtained by annealing or heating during deposition. A detailed compositional analysis with independent control over the microstructure will help in interpreting the observed variations in optical and dielectric properties with changes in O_2 SCCM during deposition.

The dielectric properties of these films are measured only at a few spot frequencies in the microwave range. It will be interesting to do a broad - band measurement of dielectric constant and tanδ of these films spanning over a few bands to ascertain the loss mechanisms in these films at such frequencies.

List of Publications

Journals

1. **R. K. Bhuyan**, T. S. Kumar, D. Pamu, J. M. Renehan and M. V. Jacob,
   Low temperature and broadband microwave dielectric properties of V_2O_5 added Mg_2TiO_4 ceramics,
   Materials Express, 4 (2014) 349.

2. **R. K. Bhuyan**, T. S. Kumar, D. Pamu, J. M. Renehan and M. V. Jacob,
   Cryogenic microwave dielectric properties of Mg_2TiO_4 ceramics added with CeO_2 nanoparticles,
   Advances in Materials Research, 3 (2014) 327.

3. **R. K. Bhuyan**, T. S. Kumar, A. R. James and D. Pamu,
   Structural and microwave dielectric properties of Mg_2TiO_4 ceramics prepared by mechanical synthesis method,
   International Journal of Applied Ceramic Technology, 10 (2013) E18.

4. **R. K. Bhuyan**, T. S. Kumar, A. R James, A. Perumal and D. Pamu,
   Enhanced densification and microwave dielectric properties of Mg_2TiO_4 ceramics added with CeO_2 nanoparticles,
   Material Science and Engineering B, 178 (2013) 471.

5. **R. K. Bhuyan**, T. S. Kumar, D. Goswami, A. R. James and D. Pamu,
   Liquid phase effect of La_2O_3 and V_2O_5 on microwave dielectric properties of Mg_2TiO_4 ceramics,
   Journal of Electroceramics, 31 (2013) 48.

6. **R. K. Bhuyan,** T. S. Kumar, A. Perumal and D. Pamu,
   Effect of annealing and atmosphere on the structure and optical properties of Mg_2TiO_4 thin films, obtained by the radio frequency magnetron sputtering method,
   Journal of Experimental Nanoscience, 8 (2013) 371.

7. **R. K. Bhuyan**, T. S. Kumar, A. Perumal, S. Ravi and D. Pamu,
   Optical properties of ambient temperture grown nanocrystalline Mg_2TiO_4 thin

films deposited by RF magnetron sputtering,
Surface and Coatings Technology, 221 (2012) 196.

8. **R. K. Bhuyan**, A. Perumal and D. Pamu,
Dielectric properties of Bi_2O_3 added Mg_2TiO_4 ceramics for microwave applications,
Manuscript under preparation.

9. **R. K. Bhuyan,** A. Perumal and D. Pamu,
Effects of Zn doping on the structural, microstructural and microwave dielectric properties of $(Mg_{1-x}Zn_x)_2TiO_4$ (x = 0.01-0.1) ceramics,
Manuscript under preparation.

10. **R. K. Bhuyan** and D. Pamu,
Importance of low loss and medium to high-K dielectric ceramics used for microwave applications in the 21st century: **a review**
Manuscript under preparation.

Conferences and workshops

1. **R. K. Bhuyan**, A. Perumal and D. Pamu,
Structural, optical and dielectric study of mechanically alloyed nanocrystalline Mg_2TiO_4 powders,
International Conference on Nanoscience and Engineering Applications (**ICONSEA-2014, 26-28 June**), Kukatpally, Hyderabad, India

2. **R. K. Bhuyan**, P. Kalyana Rao, K. Venkateswara Rao, A. R James and D. Pamu, *Influence of Bi_2O_3 additions on densification and microwave dielectric properties of Mg_2TiO_4 Ceramics***,**
17th National Seminar on Ferroelectrics and Dielectrics (**NSFD-2012, 17-19 December**) Odisha, India

3. **R. K. Bhuyan**, T. S. Kumar, D. Goswami and D. Pamu,
Effect of La_2O_3 and V_2O_5 addition on sintering behavior and microwave dielectric properties of Mg_2TiO_4 ceramics,
International Conference (**ICMST-2012, 10-14 June**), Kottayam, India

4. **R. K. Bhuyan**, T. S. Kumar, A. Perumal and D. Pamu,
Effect of annealing on the structural and optical properties of Mg_2TiO_4 nanocrystalline thin films prepared by RF magnetron sputtering,
2nd International Conference on Advance Nanomaterials and Nanotechnology (**ICANN-2011, 10-12 December**), IIT Guwahati, India

5. **R. K. Bhuyan**, T. S. Kumar, A. Perumal, S. Ravi and D. Pamu,
Optical studies of ambient temperture grown nanocrystalline Mg_2TiO_4 thin films deposited by RF magnetron sputtering,
International Thin Films Conference (**TACT-2011, 20-23 November**), Kenting, Taiwan

Outside thesis work

1. T. Santhosh Kumar, **R. K. Bhuyan** and D. Pamu.
Effect of post annealing on structural, optical and dielectric properties of $MgTiO_3$ thin films deposited by RF magnetron sputtering,
Applied Surface. Science, 264 (2013) 184

2. T. Santhosh Kumar, **R. K. Bhuyan** and D. Pamu,
Effect of processing parameters and post annealing temperature on structural and optical properties of $MgTiO_3$ thin films deposited by RF magnetron sputtering,
Springer Proceedings in Physics, 143 (2013) 291

3. T. Bora, A. Nandy, B. Samantaray, **R. K. Bhuyan**, D. Pamu, and S. Ravi,
Magnetic, electrical and optical properties of $Nd_{0.85}K_{0.15}MnO_3$ thin film,
Advanced Nanomaterials and Nanotechnology (Springer Proceeding), 143 (2013) 449

4. T. Bora, A. Nandy, B. Samantaray, **R. K. Bhuyan**, S. Ravi and D. Pamu,
Preparation and characterization of $Nd_{0.8}K_{0.2}MnO_3$ thin films,
AIP Conference Proceeding, 1447 (2012) 1119

5. A. Nandy, T. Bora, **R. K. Bhuyan**, D. Pamu and S. Ravi,
Preparation and characterization of charge ordered $Nd_{0.8}Na_{0.2}MnO_3$ thin films,
AIP Conference Proceeding, 1447 (2012) 1117

Conference Presentations

1. T. S Kumar, **R. K. Bhuyan,** S. Thota, A. R. James and D. Pamu,
   Effect of annealing on the structural and optical properties of nanocrystalline $MgTiO_3$ thin films,
   International Conference on Nanoscience and Technology (**ICONSAT-2012, 20-23 January**) Hyderabad, India

2. T. Bora, A. Nandy, **R. K. Bhuyan**, D. Pamu and S. Ravi,
   Electrical resistivity and magnetic properties of $Nd_{0.85}K_{0.15}MnO_3$ thin films,
   International Thin Films Conference (**TACT- 2011, 20-23 November**), Kenting, Taiwan

3. T. Santhosh Kumar, **R. K. Bhuyan** and D. Pamu,
   Structural and dielectric studies of nanocrystalline $MgTiO_3$ thin films deposited by RF magnetron sputtering,
   International Thin Films Conference (**TACT-2011, 20-23 Nov.**), Kenting, Taiwan

4. T. Bora, A. Nandy, B. Samantaray, **R. K. Bhuyan**, D. Pamu and S. Ravi,
   Preparation and characterization of $Nd_{0.8}K_{0.2}MnO_3$ thin film,
   DAE-SSPS, December-21-23 2011, SRM University, Kattankulathur, India

5. A. Nandy, T. Bora, **R. K. Bhuyan**, D. Pamu and S. Ravi,
   Preparation and characterization of charge ordered $Nd_{0.8}Na_{0.2}MnO_3$ thin films,
   DAE-SSPS, December– 2011 SRM University, Kattankulathur, India

6. T. Santhosh Kumar, **R. K. Bhuyan**, D. Goswami and D. Pamu,
   Effect of CeO_2 nanoparticle addition on microstructure and microwave dielectric properties of $MgTiO_3$ ceramics,
   ICMST-2012, 10-14 June Kottayam, India

7. P. Mahesh, T. Santhosh Kumar, **R. K. Bhuyan** and D. Pamu,
   Raman and dielectric studies on lead free $(K_{0.5}Na_{0.5})NbO_3$ piezoelectric ceramics,
   ICMST-2012, 10-14 June, Kottayam, India